3 cys

GEAP-13049
AEC RESEARCH AND
DEVELOPMENT PROGRAM
MARCH 1970

TWO-PHASE FLOW AND HEAT TRANSFER IN MULTIROD GEOMETRIES:

SUBCHANNEL AND PRESSURE DROP MEASUREMENTS IN A NINE-ROD BUNDLE FOR DIABATIC AND ADIABATIC CONDITIONS

R.T. LAHEY JR.
B.S. SHIRALKAR
D.W. RADCLIFFE

GENERAL ELECTRIC

DISCLAIMER

GEAP-13049
AEC Research and
Development Report
March 1970

TWO-PHASE FLOW AND HEAT TRANSFER IN MULTIROD GEOMETRIES:

SUBCHANNEL AND PRESSURE DROP MEASUREMENTS IN A NINE-ROD BUNDLE FOR DIABATIC AND ADIABATIC CONDITIONS.

R. T. Lahey, Jr.
B. S. Shiralkar
D. W. Radcliffe

Approved:

E. Janssen
Project Engineer

Approved:

F. A. Schraub, Manager
Core Development

Prepared for the
U. S. Atomic Energy Commission
Under Contract Number AT (04-3)-189
Project Agreement 44

Printed in U.S.A. Available from the
Clearing House for General Scientific and Technical Information
National Bureau of Standards, U.S. Department of Commerce
Springfield, Virginia
Price: $3.00 per copy

ATOMIC POWER EQUIPMENT DEPARTMENT • GENERAL ELECTRIC COMPANY
SAN JOSE, CALIFORNIA 95125

6022-Dev Eng-140
100 GRJ-4/70

GENERAL ELECTRIC

LEGAL NOTICE

This report was prepared as an account of Government sponsored work. Neither the United States, nor the Commission, nor any person acting on behalf of the Commission:

A. Makes any warranty or representation, expressed or implied, with respect to the accuracy, completeness, or usefulness of the information contained in this report, or that the use of any information, apparatus, method, or process disclosed in this report may not infringe privately owned rights; or

B. Assumes any liabilities with respect to the use of, or for damages resulting from the use of any information, apparatus, method, or process disclosed in this report.

As used in the above, "person acting on behalf of the Commission" includes any employee or contractor of the Commission, or employee of such contractor, to the extent that such employee or contractor of the Commission, or employee of such contractor prepares, disseminates, or provides access to, any information pursuant to his employment or contract with the Commission, or his employment with such contractor.

TABLE OF CONTENTS

LIST OF ILLUSTRATIONS

LIST OF ILLUSTRATIONS—(Continued)

LIST OF ILLUSTRATIONS—(Continued)

LIST OF ILLUSTRATIONS—(Continued)

LIST OF TABLES

NOMENCLATURE

A_{ch} = Subchannel cross sectional area, ft^2

A_h = Test vessel heated surface area, ft^2

A_p = Projected area of pin spacer, ft^2

A_t = Total flow area, ft^2

C_d = Drag coefficient

C_p = Specific heat, Btu/lb-°F

dB = Increment in quantity B

D_h = Hydraulic diameter = $\frac{4 A_t}{P_w}$, ft

$\frac{dp}{dz}$ = Axial pressure gradient, lb/ft^2-ft

f = Single-phase friction factor

F_{cw} = Cooling-water flow, lb/h

g = Acceleration due to gravity, ft/h^2

g_c = Conversion factor, $\frac{ft}{h^2} \frac{lbm}{lbf}$

$\bar{G}$ = Bundle average mass flux, lb/ft^2-h

$\tilde{G}$ = Average mass flux in two adjacent subchannels, lb/ft^2-h

$\hat{G}$ = Bundle average mass flux calculated from continuity, lb/ft^2-h

G_i = Mass flux in subchannel i, lb/ft^2-h

G_{ch} = Mass flux in a subchannel, lb/ft^2-h

Gr = Grashof Number = $\frac{\rho_{room} - \rho_w}{\rho_{room}} \left(\frac{\rho}{\mu}\right)^2 gL^3$

$\bar{H}$ = Bundle average enthalpy, Btu/lb

$\hat{H}$ = Bundle average enthalpy calculated from energy totals of individual subchannels, Btu/lb

H_{ch} = Subchannel enthalpy, Btu/lb

H_{fg} = Latent heat of evaporation, Btu/lb

NOMENCLATURE—(Continued)

H_{out} = Enthalpy of sample at heat exchanger outlet, Btu/lb

H_{sat} = Saturation enthalpy at system pressure (H_f), Btu/lb

H_{sub} = Subcooling = H_{sat} − local enthalpy, Btu/lb

H_x = Enthalpy associated with flow diversion, Btu/lb

j_f^* $\triangleq$ $\left[\frac{G(1-x)}{\rho_f}\right] \rho_f^{1/2} \left[g_c D_H (\rho_f - \rho_g)\right]^{-1/2}$, nondimensionalized,

superficial liquid velocity

j_g^* $\triangleq$ $\left(\frac{Gx}{\rho_g}\right) \rho_g^{1/2} \left[g_c D_H (\rho_f - \rho_g)\right]^{-1/2}$, nondimensionalized,

superficial vapor velocity

k = Thermal conductivity, Btu/ft-h-°F

L = Total length, ft

ℓ = Running length, ft

L_b = Boiling length, ft

N_i = Number of spacer pins of type i

p = System pressure, psi

P_{ch} = Subchannel friction perimeter, ft

P_h = Subchannel heated perimeter, ft

P_w = Wetted perimeter, ft

P_t = Total power, kW

Pr = Prandtl number = $\frac{C_p \mu}{k}$

Q' = Sample heat loss Btu/h

q'' = Heat flux on heater rod, Btu/ft^2-h

Q_L = Heat loss from test section, Btu/h

Re = Reynolds number = $\frac{G D_h}{\mu}$

NOMENCLATURE—(Continued)

s	=	Rod-to-rod gap spacing, ft
T	=	Temperature, °F
U	=	Internal energy, Btu/lb
$\tilde{V}$	=	Average linear velocity in adjacent subchannels, ft/h
v_f	=	Specific volume of liquid ft^3/lb
v_{fg}	=	Specific volume of evaporation = $v_g - v_f$, ft^3/lb
v_g	=	Specific volume of vapor, ft^3/lb
V_i	=	Velocity in section i, ft/h
V_p	=	Local velocity at spacer pin, ft/h
w'	=	Fluctuating mass flow rate due to turbulent interchange, lb/h-ft
$\overline{w}$	=	Total bundle flow rate, lb/h
w_{ch}	=	Mass flow in a subchannel, lb/h
$\overline{x}$	=	Average quality of a bundle
x_{ch}	=	Quality in a subchannel
x_{flow}	=	Nonequilibrium flow quality
$\hat{x}$	=	Bundle quality calculated from qualities in individual subchannels
z	=	Axial length coordinate, ft
$\alpha(z)$	=	Void fraction at axial location z
β	=	Mixing stanton number
Δp	=	Pressure difference, psi
ΔT	=	Temperature difference, °F
ϵ	=	Turbulent eddy diffusivity, ft^2/h
ρ	=	Density, lb/ft^3
ρ'	=	Momentum density, lb/ft^3

NOMENCLATURE–(Continued)

ϕ_{Lo}^2	=	Martinelli-Nelson friction-pressure-drop multiplier
μ	=	Viscosity, lbf-h/ft^2
τ	=	Shear stress, lbf/ft^2

Subscripts

avg	=	Refers to average
ch	=	Refers to subchannel
e	=	Refers to bundle exit conditions
f	=	Refers to liquid
fg	=	Denotes difference between saturated vapor and liquid values
g	=	Refers to vapor
iso	=	Refers to quantities at isokinetic condition
p	=	Quantity evaluated at or in the vicinity of a spacer pin
room	=	Quantity at ambient temperature
i	=	Refers to subchannel i
x	=	crossflow

ABSTRACT

Extensive subchannel test data have been taken in an electrically heated nine-rod bundle under conditions typical of BWR operating conditions. Uniform and peaked local (radial) power distributions were run in order to determine the effect of the rod-peaking pattern on subchannel conditions. Analysis of the isokinetic and non-isokinetic subchannel data indicate that: (1) variation of flow and enthalpy within a rod bundle is quite pronounced; (2) current ventilated-subchannel codes, such as COBRA, do not accurately predict the trends in the data for two-phase conditions; (3) The crossflow enthalpy transferred during flow diversion is, in general, greater than the enthalpy of the donor subchannel and appears to be a strong function of flow regime; (4) The present data agree in general with previous adiabatic and diabatic subchannel data.

In addition to subchannel data, pressure-drop measurements were made for single-phase and two-phase conditions. Analysis indicates that the single-phase friction factor is higher than the friction factor for a smooth tube and that the classical Martinelli-Nelson, two-phase friction multiplier ϕ_{Lo}^2 *correlates the data quite well.*

1. INTRODUCTION

In order to achieve improvement in the thermal-hydraulic characteristics of nuclear reactor cores, it is necessary to gain a better understanding of the coolant flow and enthalpy distribution in the complex geometries found there. In many reactors, a liquid coolant is employed to remove heat from the reactor core. The coolant exits from the coolant channel as a two-phase mixture of liquid and vapor. Knowing the flow rate of coolant in different parts of the channel and the manner in which the two phases are distributed around the channel provides a more realistic localized basis for the evaluation of thermal performance parameters, such as the critical heat flux (CHF).

The primary purpose of this investigation was to obtain the mass flux and enthalpy distribution in a simulated rod-bundle geometry for a nuclear reactor. Test conditions typical of operating BWR conditions have been studied. Results for both uniformly heated and radially-peaked nine-rod arrays are reported.

Detailed pressure-drop measurements have also been taken in the subchannel under both single-phase and two-phase exit conditions, since this information is of great value both for the designer and in the analysis and prediction of the detailed flow distribution.

At the time these tests were planned, no data of this nature had been reported. Since then, some results of subchannel sampling in slightly different geometries have appeared in the literature. Comparisons have been made with these data as well as theoretical predictions. It is significant that this report gives the only data yet published for true multirod geometries in which all the representative subchannels have been sampled. Hence it is the only multirod data that can be checked for validity from the point of view of conservation of mass and energy.

2. DESCRIPTION OF NINE-ROD TEST SECTION

The test section described here was built specially for subchannel and flow-structure measurements. The salient geometrical features are:

Number of Rods	9
Rod Diameter	0.570 inch
Radius of Channel Corner	0.400 inch
Rod-Rod Clearance	0.168 inch
Rod-Wall Clearance	0.135 inch
Hydraulic Diameter	0.474 inch
Heated Length	72 inches

The rods are of a new type developed by General Electric. Each rod is clad with a nickel tube, insulated from the electrical heater element so that the exterior of the rod is at ground potential thereby eliminating any shorting problems. The rods pass out the bottom end of the test section through watercooled O-ring glands, permitting differential expansion and access to electrical power leads. The power supplied is three-phase a-c power.

Tests were run with all nine rods heated. The local (radial) peaking was either uniform or a peaking pattern

typical of BWR conditions. The peaking of the rods was accomplished with peaking transformers rather than using different cal-rods.

A sectional view of the test section is shown in Figure 1. Subcooled water enters the channel at the bottom. A mixture of steam and water, generally at a bulk flow quality greater than zero, leaves the channel at the top. Rod-rod and rod-wall clearances are maintained in these "clean" channel configurations* by means of 1/8-inch diameter stainless steel pins. Each pin is cut to the length corresponding to the clearance to be maintained, then lightly fusion-welded ("zapped"), and finally secured by silver soldering into place on one of the two surfaces. A set of pins is installed at each of several positions along the channel. These are located on 12-inch centers so that the last set is 10 inches before the top end of the test length.

Provision is made for bringing static pressure lines out through glands in a blind flange located at the same elevation as the inlet flange (Figure 2). These are for measuring the static pressure drop along the channel and for setting the isokinetic condition for subchannel measurements. The lines, shown in Figure 2, run horizontally from the blind flange to seal-pots. It is the static pressures in the seal-pots which are actually measured by means of transducers (Figure 3).

To measure the flow in any given subchannel, that subchannel must be isolated at some point from the rest of the channel. The subchannel flow, also referred to as sample flow (see Figure 3), can then be taken through special ducting to another point outside the test section, where both the flow rate and enthalpy (energy content) can be measured. Figure 1 shows typical provisions for sampling Subchannel No. 1. Thin (0.010 inch) pieces of metal sheet (flow splitters) are installed just past the end of the heated length, to separate Subchannel No. 1 from its neighbors. Similar splitters are used when Subchannels Nos. 2 and 3 are sampled, but the flow is measured for only one subchannel at a time. The splitters, plus continuous segments of rod and channel wall, form a box into which the subchannel flow enters and from which it leaves at the top end via a sample tube. The tube passes out through the top-closure flange, and from there it passes to a heat exchanger (calorimeter), as shown in Figures 3 and 4. The sample flow is monitored by a turbine flowmeter; two turbine meters of different capacity are used in conjunction with the different subchannels being sampled.

A flow control valve (Figure 3) is used to set the sample flow to the desired amount.

The sample flow rate is set so as to obtain a particular value of static pressure difference between pressure taps located inside and outside the subchannel at the same axial location. Four pressure taps, referred to as C1, C2, W1, and W2, are available for this purpose and their peripheral locations are shown in Figure 5. Axially, they are located at the leading edge of the flow splitters. When sampling the corner subchannel, C1 and either C2 or W2 can be used. Similarly, W1 and W2 can be used for the side subchannel.

A special arrangement was required for the center subchannel. Three different schemes were tried, and the one shown in Figure 5 with a horizontal pressure tap line through a side rod was adopted. CC1, a pressure tap in the wall at the same axial location was used as the reference tap. The decision to use this arrangement was based on the single phase data, which can be predicted from analysis and continuity considerations. One method used a pressure tap in one of the splitters, but was found to cause appreciable obstruction in the adjoining side subchannel. Another scheme used two vertical pressure tap lines in two rods as shown in Figure 5, but was found to give erratic results under diabatic conditions.

When the pressure difference is set to the value that exists when the sample tube is removed and the subchannel flow is not drawn off, the sampling is termed "isokinetic." This pressure difference was generally zero or close to it. "Non-isokinetic" data were also taken since they yield additional information, such as estimates of the enthalpy of crossflow between subchannels. The static pressure differences were measured by a 0.2-psi-capacity, Pace Δp cell.

The sample enthalpy was determined by a heat balance on the calorimeter. For this purpose, cooling water from a city water line is used and its flow rate is measured with another turbine flowmeter. The inlet and outlet temperatures of the cooling water are measured by chromel-alumel thermocouples. Three thermocouples are located at each place, and their differential output is also recorded, to obtain better accuracy on the rise in temperature of the cooling water. The outlet thermocouples are inserted beyond a right-angle bend in the piping to ensure good mixing in the water. The outlet temperature of the condensed sample was also measured with three chromel-alumel thermocouples.

Pressure drop measurements were also made during the tests. These were taken with Pace Δp transducers over six 1-foot lengths and with a Pace cell and a manometer over the whole 6-foot heated length.

* By "clean" channel is meant a channel in which the means of holding the rods in their correct positions produces as little disturbance to the flow as possible.

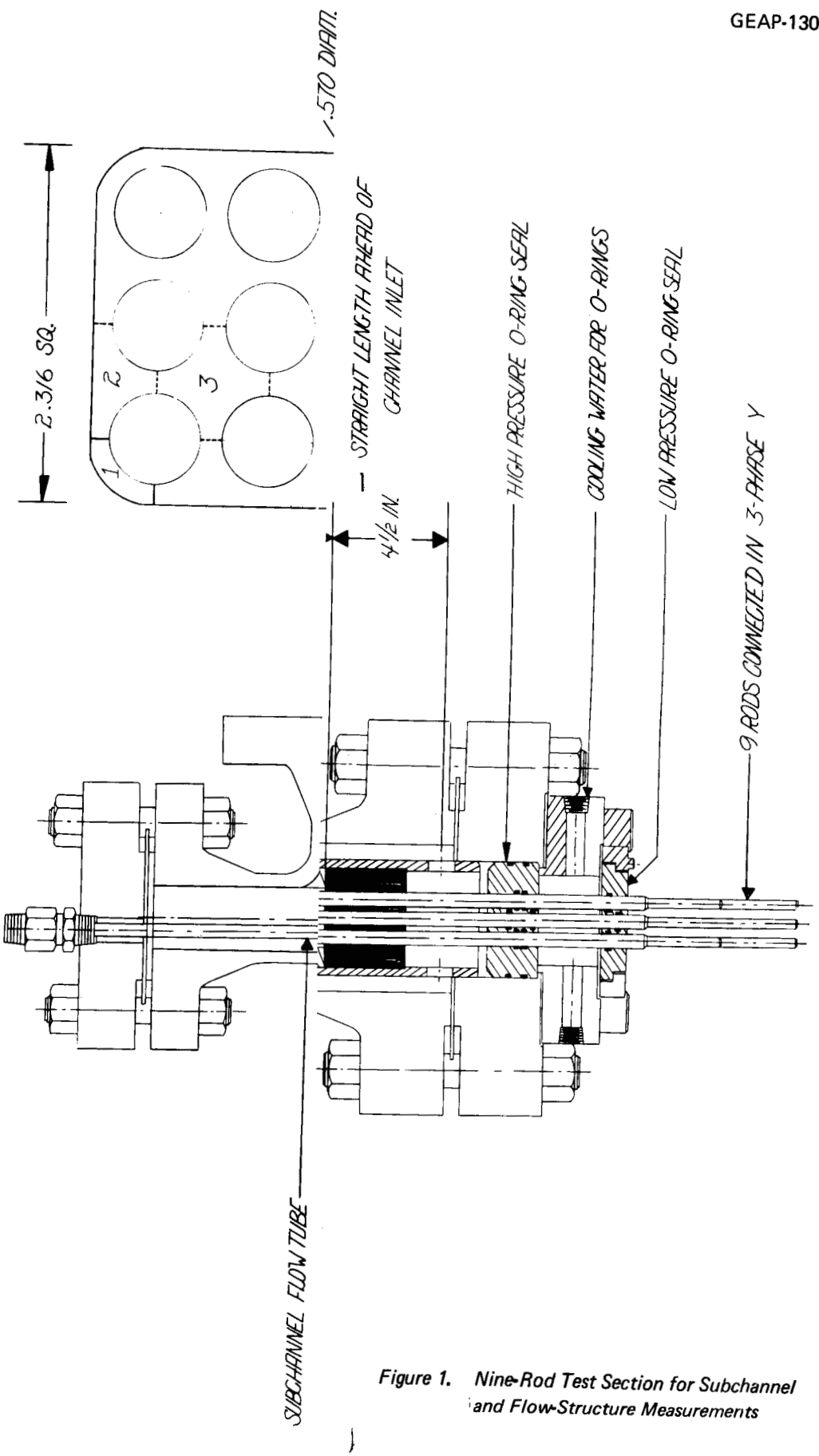

Figure 1. Nine-Rod Test Section for Subchannel and Flow-Structure Measurements

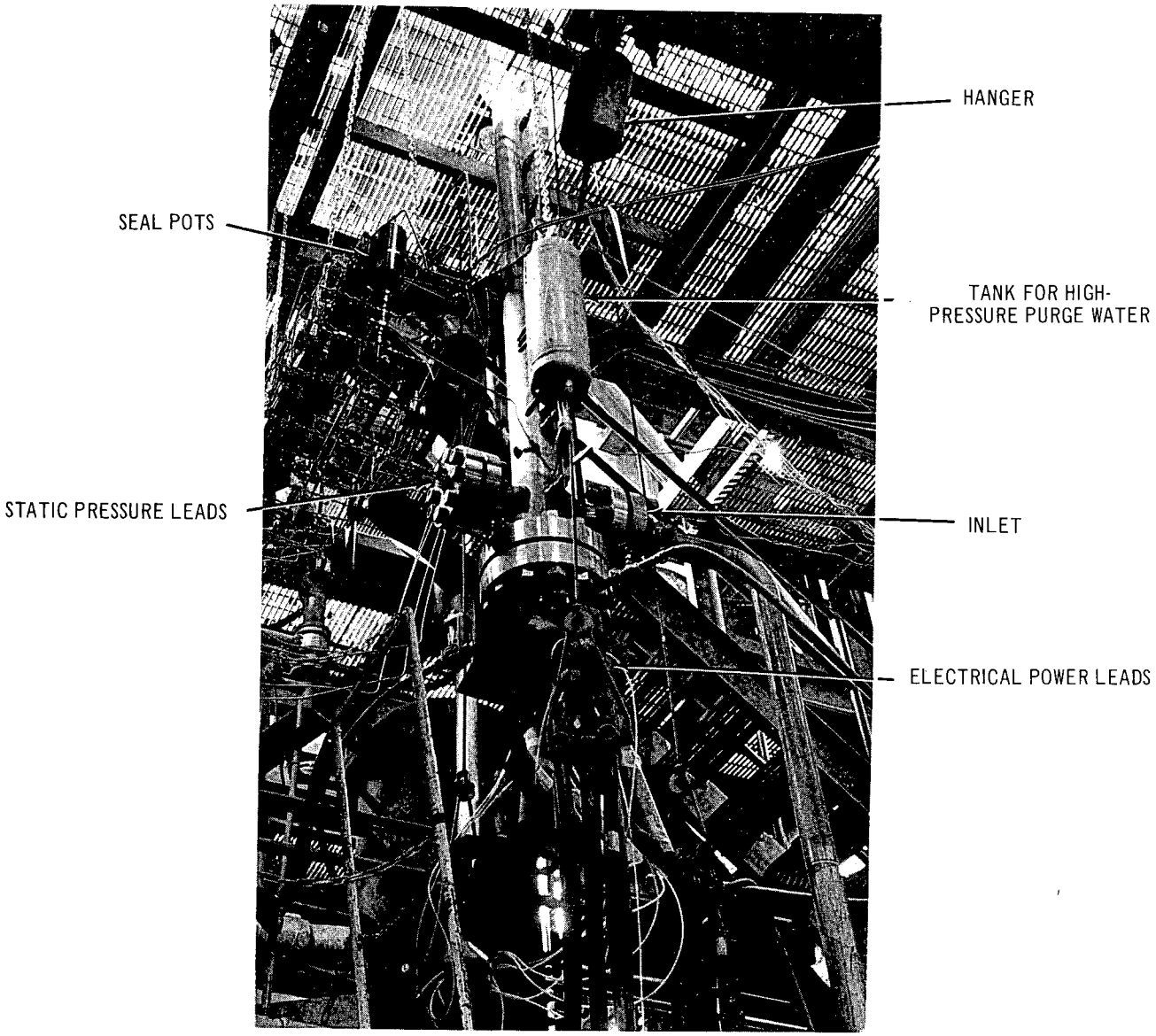

Figure 2. Nine-Rod Test Section Installed in Heat-Transfer Loop

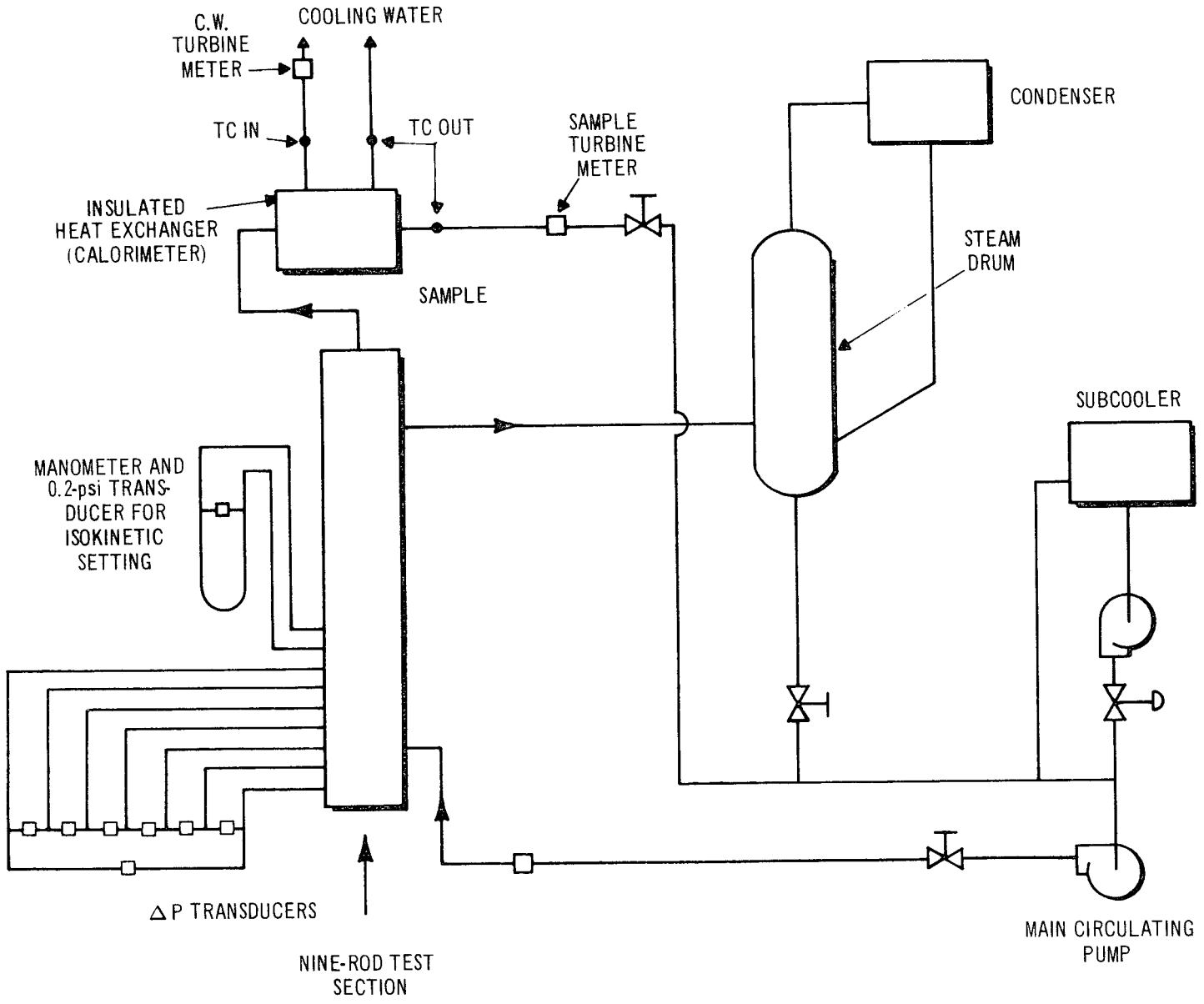

Figure 3. Schematic of Loop Showing Sampling Circuit

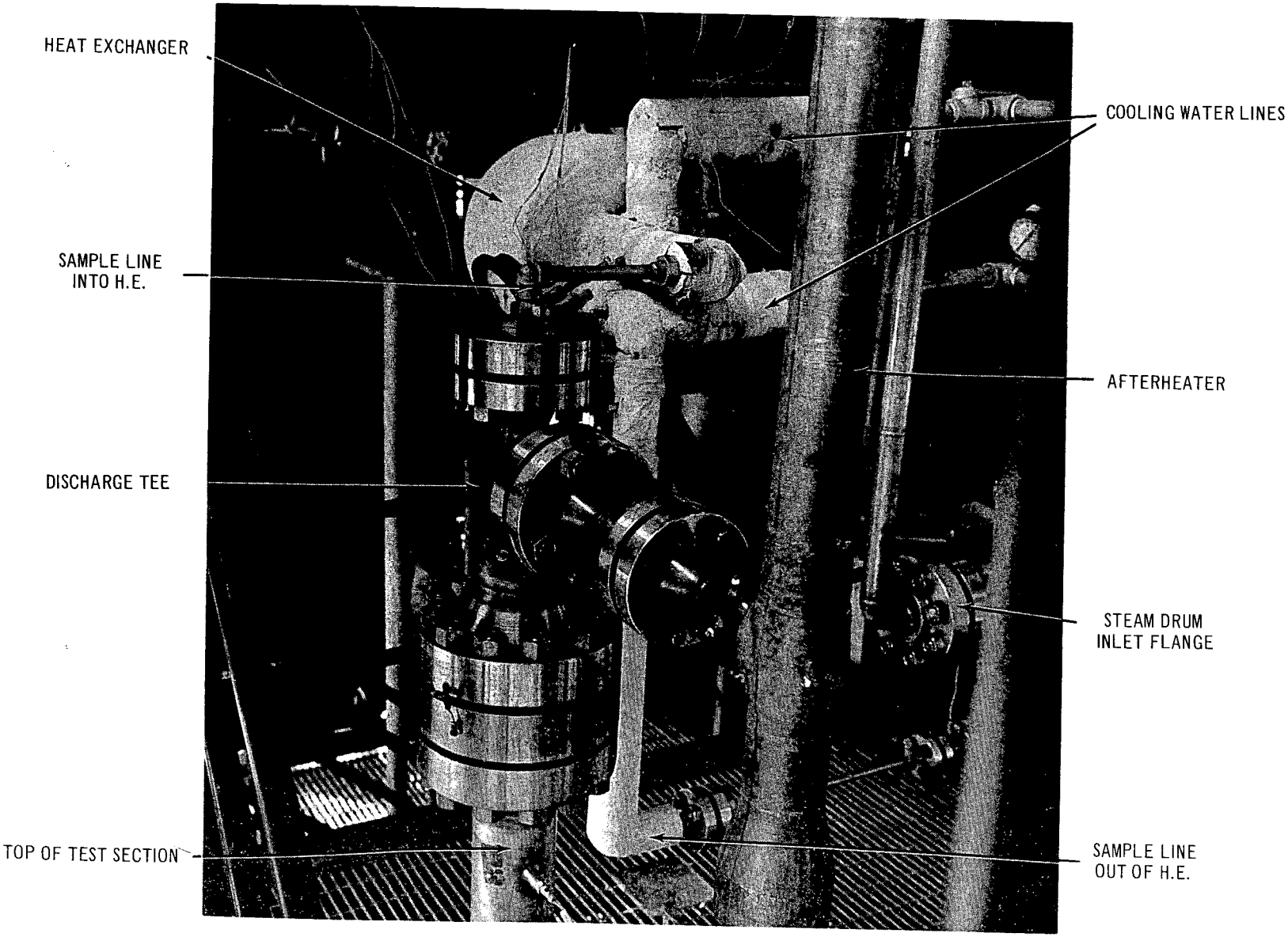

Figure 4. Top End of Nine-Rod Test Section Installed in Heat-Transfer Loop (Insulation was removed to show detail more clearly)

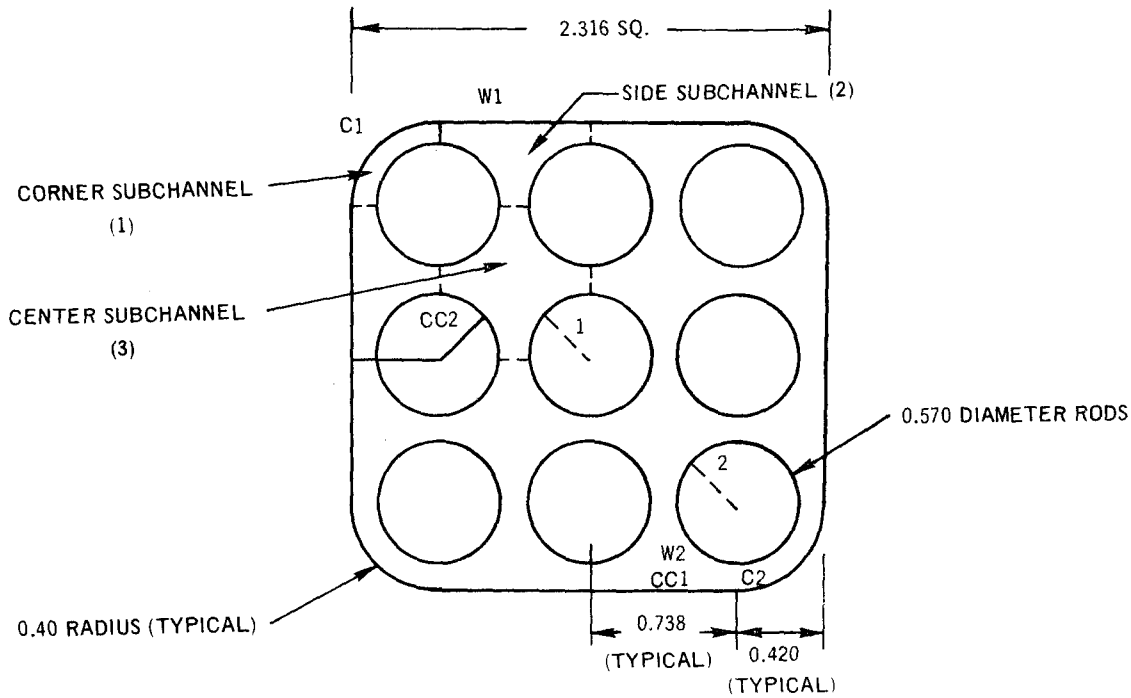

SECTION "A–A"
(NOTE SPLITTER POSITIONS FOR THE VARIOUS SUBCHANNELS)

Figure 5. Positions of Pressure Taps for Setting Isokinetic Conditions

3. DATA REDUCTION

Most of the data were obtained in the form of paper tape output from the DYMEC data acquisition system. The raw data consist of (1) the bundle flow rate and inlet temperature, (2) electrical power to the test section, (3) the system pressure and pressure differential between subchannels, (4) temperatures of the inlet and outlet flows from the heat exchanger, (5) pressure drop along the test section, and (6) temperatures along the vessel wall for calculation of the hydrostatic head corrections. A computer program was written to reduce the data to the engineering units of interest.

The flow rate of the system is obtained from the turbine meter in the main loop, as well as a 1-inch orifice used in conjunction with a 60-inch, high-pressure manometer. The bundle-average, exit, equilibrium quality is calculated from the first law of thermodynamics as:

$$\bar{x}_e = [(3413 \times P_t - Q_L)/\bar{W} - H_{sub}]/H_{fg}$$

where

P_t = Total power, kW,
Q_L = Heat loss, Btu/h
$= 0.13\ (Gr \times Pr)^{1/3} \cdot A_H \cdot (T_{avg} - T_{room})$,

where

Gr = Grashof number,
Pr = Prandtl number,
A_h = Test-vessel surface area, ft^2
T_{avg} = Average test vessel temperature, °F
T_{room} = Room temperature, °F.
$\bar{w}$ = System flow, lb/h,
H_{sub} = Inlet subcooling, Btu/lb and
H_{fg} = Latent heat of evaporation, Btu/lb

The sample or subchannel quality is calculated as:

$$x_{ch} = \left(\frac{F_{cw}}{w_{ch}} \cdot C_p \cdot \Delta T_{cw} - H_{sat} + H_{out} + \frac{Q'}{w_{ch}}\right)/H_{fg},$$

where

F_w = Cooling water flow, lb/h
W_{ch} = Sample flow lb/h
ΔT_{cw} = Temperature rise of cooling water, °F
H_{sat} = Enthalpy of saturated liquid, Btu/lb
H_{out} = Enthalpy of sample at heat exchanger outlet, Btu/lb
Q' = Sample heat loss (to be determined experimentally), Btu/h

All pressure drop measurements were corrected for the hydrostatic head in the pressure tap lines based on the average density of water between the relevant pressure taps.

Further details on the reduction of pressure drop data are given in the section in which the pressure drop results are presented.

A detailed error analysis of the data is made in Appendix A. Generally, it was estimated that the maximum error limits in the subchannel flow was of the order of ±2 % and in subchannel quality of ±0.020. The chief sources of error are those in the isokinetic setting and in the calorimetry. To minimize these errors preliminary tests were performed to determine the heat loss from the sample pipe and calorimeter, and the isokinetic setting of the pressure differential.

Heat balance tests were run with single-phase water between 400°F to 500°F at pressures of 1100 psi to 1200 psi to obtain higher accuracy in the estimation of the subchannel quality (i.e., to estimate Q' in the equation for x_{ch}). It was found that there was negligible heat loss in the sample piping between the test section exit and heat exchanger inlet. However, the heat balances were in error by as much as ±5 % of the total sample energy transfer. This was well above the upper limit indicated by an error analysis, but the reason for the discrepancy could not be determined. During the course of a day's run, the variation in the error was much smaller, of the order of ±1 %. For this reason, the following procedure was adopted during two-phase runs: during heat up, checks of heat loss were made with single-phase water, and then the descrepancy in heat balance was used as Q' for that particular series of tests.

The isokinetic setting for the corner subchannel was found experimentally to be a fraction of the average dynamic head at the exit, indicating probable static-pressure tap impacting. This was done by measuring the pressure differential with the sample tube removed from the top of the box forming the subchannel but with the splitters in place. Preliminary tests indicated that the effect of leaving in the splitters was small. The dynamic head p_{dyn} was evaluated as follows.

$$p_{dyn} = \frac{\overline{G}^2}{2g_c} (v_f + \overline{x}_e v_{fg})$$

where

v_f = Specific volume of liquid
v_{fg} = Difference in specific volumes between vapor and liquid

A plot of the pressure difference versus dynamic head is shown in Figure 6. At high flow rates and qualities, the pressure difference is seen to be appreciable. This plot was used in setting the isokinetic sampling settings for the corner subchannel.

Similar measurements were made for the side subchannel. In this case the isokinetic pressure differential was also correlated against the average dynamic head, as shown in Figure 7. Measurements could not be made with the center subchannel because of geometrical considerations, and it was assumed that zero was the isokinetic setting.

4. EXPERIMENTAL PROCEDURE

The following briefly outlines the procedure used in data acquisition.

1. The loop was filled with water and the pressure tap lines, sealpots, and pace cells were bled.

2. The loop was pressurized with a charging feed pump, and the Chem pumps were turned on to maintain flow through the loop.

3. Power was turned on. When the test section exit temperature was between 450°F and 500°F, heat-balance measurements were made. Care was taken to keep the cooling water temperature rise at about 40°F, in order to assure an accurate reading.

4. The desired two-phase conditions (i.e., the flow rate, heat flux and inlet subcooling) were set up.

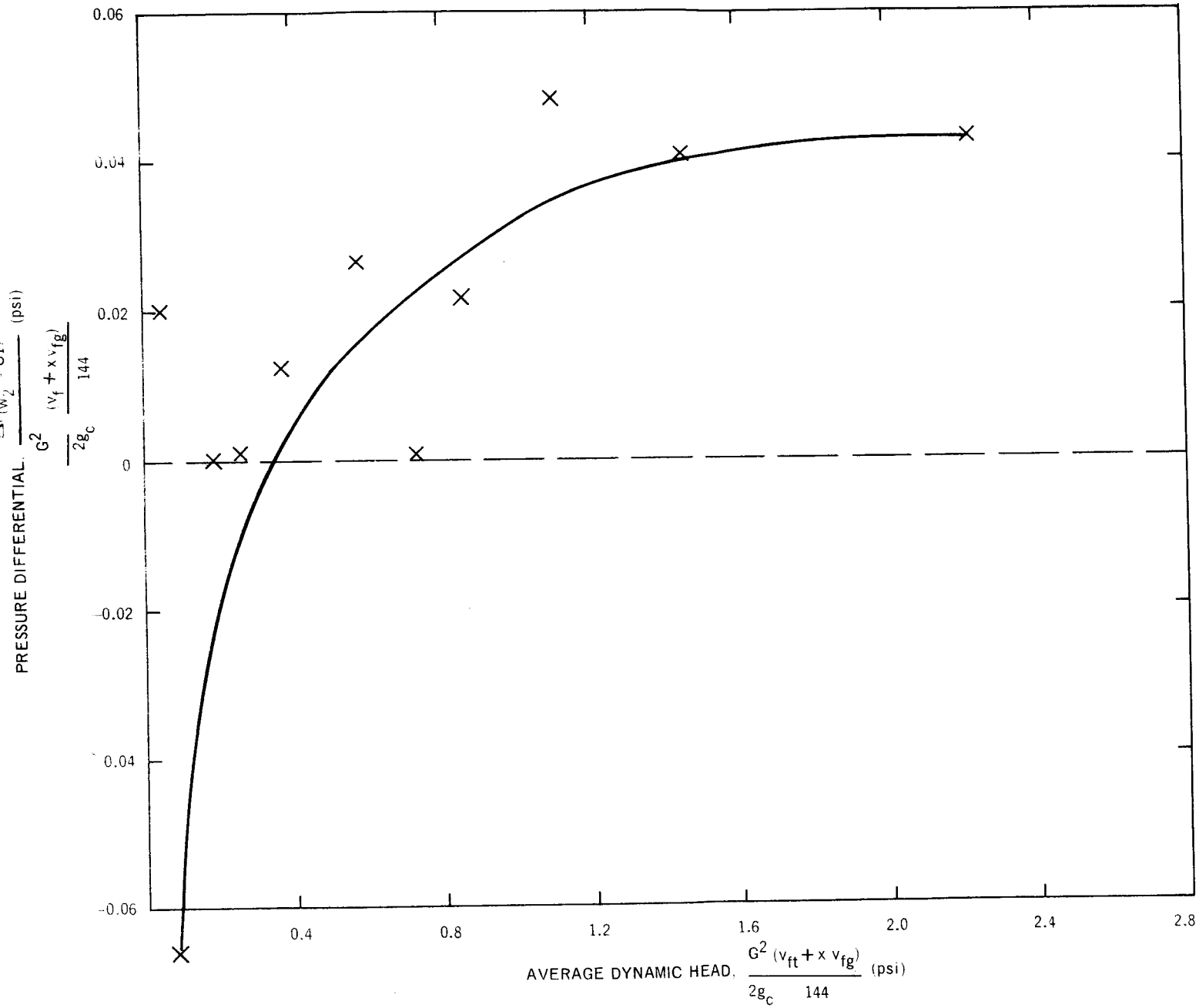

Figure 6. Calibration for Isokinetic Setting for Corner Subchannels

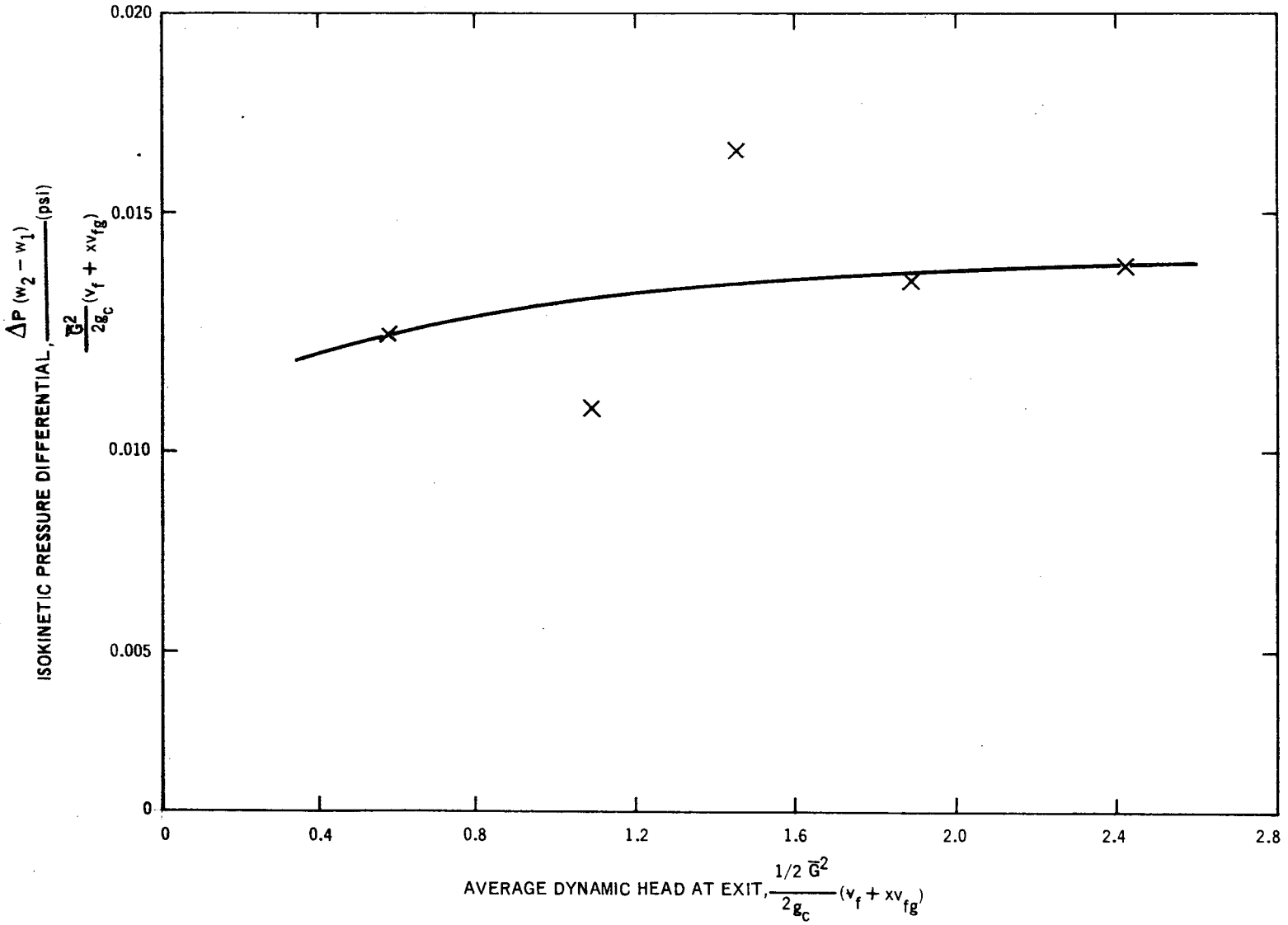

Figure 7. Calibration for Isokinetic Setting for Side Subchannel

5. The sample flow rate was adjusted using the sample valve until the desired pressure differential was obtained between the inside and outside of the subchannel being sampled. This was the isokinetic setting for isokinetic sampling, and some suitable value on either side of it was used for non-isokinetic sampling. For the center subchannel it was usually found necessary to throttle the Chem pump suction valve in the main loop in order to obtain sufficient sample flow. In some cases this caused unstable sample flows and the runs were aborted.

6. The data, including pressure drop readings, were sampled on the DYMEC data acquisition system. Manometer readings for the main flow orifice, the total pressure drop across the test section, and the ambient temperature were also recorded.

7. Steps 5 and 6 were repeated for the next non-isokinetic setting.

8. Steps 4 through 7 were repeated for the next test conditions.

5. TEST RESULTS

5.1 CORNER SUBCHANNEL TEST RESULTS

Tests were made at room temperature and at 1000 psi to obtain single-phase data. Non-isokinetic data were taken as well as isokinetic data. Isokinetic data will be discussed in Section 6. The non-isokinetic data will be discussed in Section 7.

The results obtained for single-phase sampling in the corner subchannel are shown in Figure 8. The pressure differential is plotted on the vertical coordinate with respect to the isokinetic setting, so that the intersection with the horizontal axis yields the natural flow split. As expected it can be seen that the high mass flux runs have the largest slope and hence are the least sensitive to the isokinetic setting.

Some typical trends in the two-phase data are shown in Figures 9 and 10. In this series of runs, all nine rods were equally heated, with a heated length of 6 feet. A comparison of these plots shows that as the subchannel flow is decreased below the isokinetic value the subchannel enthalpy generally decreases, indicating that the enthalpy of flow diversion is higher than the enthalpy of the donor subchannel. In Figure 11 is shown the variation in corner subchannel flow and enthalpy with average quality, for three runs (2E1, 2E2, 2E3) differing only in inlet subcooling. Hence, this plot also represents the change in subchannel flow and enthalpy along the heated length of the channel assuming there is a fully developed flow at the end of the subcooled region. The apparent trend of the subchannel mass flux to approach the bundle average mass flux in the quality region corresponding to the slug-annular flow regime transition is consistent with the steam-water data of other investigators.[1-2]

In general, the corner subchannel data show that the mass flux in the subchannel is lower than the bundle average mass flux and that the subchannel quality is lower than the average quality, except at the highest mass flux.

Some of the isokinetic data for single- and two-phase flow are shown in Table 1. The detailed test conditions for the different test points are shown in Table 2.

5.2 SIDE SUBCHANNEL TEST RESULTS

The nominal test conditions for the side subchannel are shown in Table 2. An attempt was made to maintain test conditions identical to those for the corner subchannel as far as possible. Generally, small discrepancies existed in the values of the average flow rate and the average exit quality. To compare the corner, side, and center subchannels on an identical basis, the following corrections were made to the data:

$$G_{ch} = G_{ch\ experimental} \times \frac{\overline{G}_{nominal}}{\overline{G}_{experimental}}$$

$$x_{ch} = x_{ch\ experimental} + \left(\overline{x}_{e\ nominal} - \overline{x}_{e\ experimental}\right)$$

These corrections are based on isokinetic sampling tests that were conducted for that purpose, involving small changes in the total flow rate and the average exit quality.

The changes in the subchannel quantities due to these small changes can be expressed as:

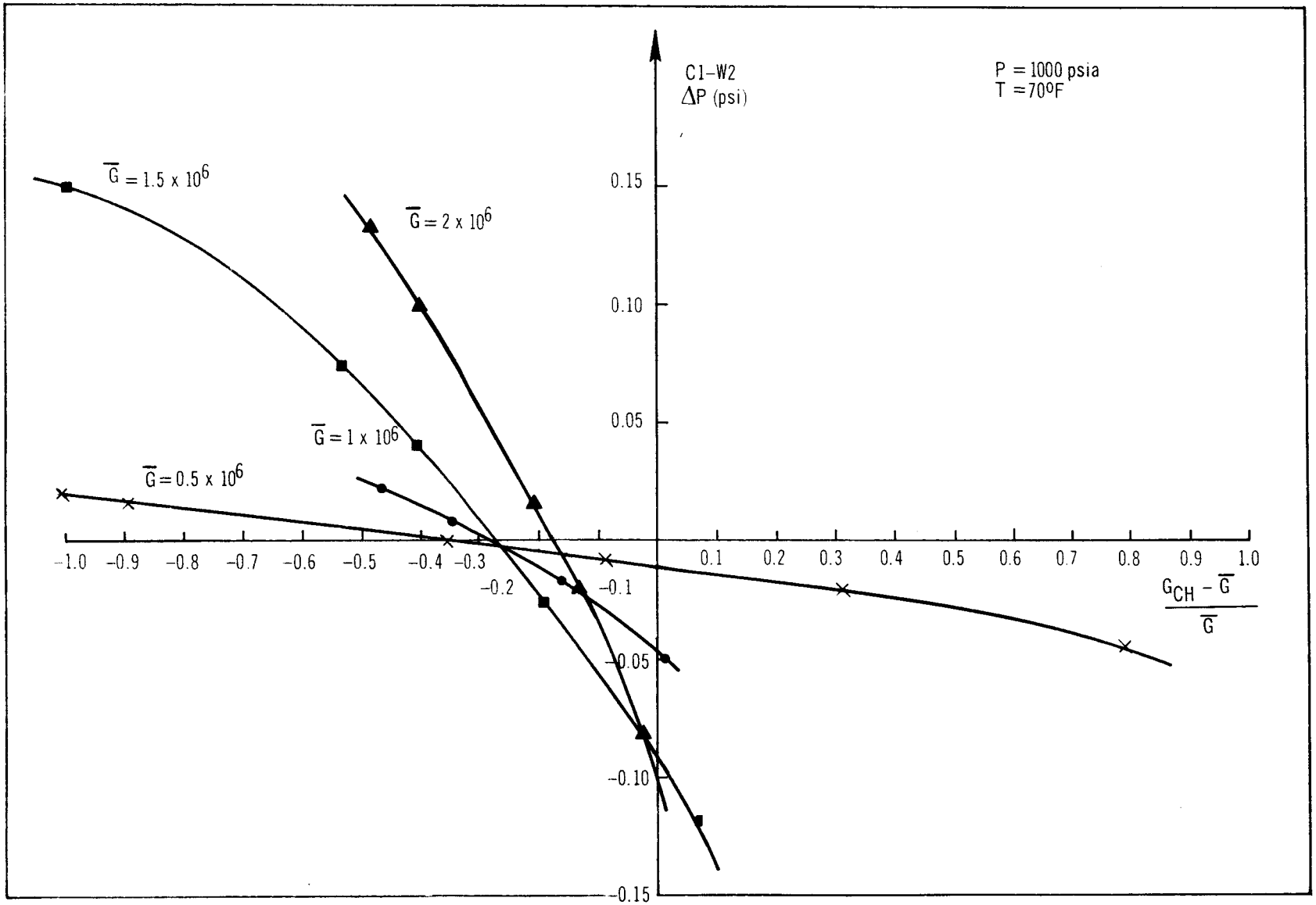

Figure 8. Corner Subchannel Cold Data

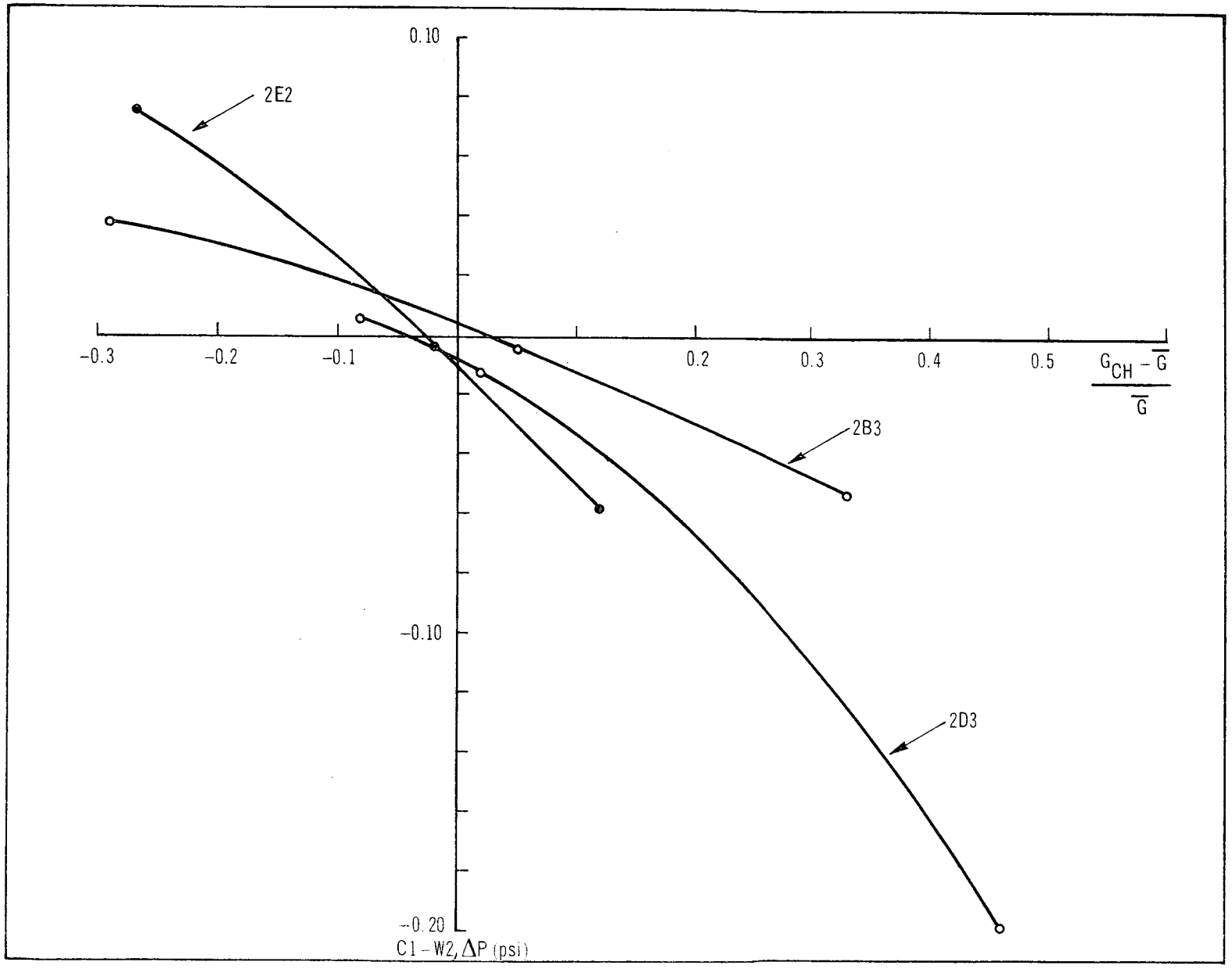

Figure 9. Variation of Channel Flow with Pressure Differential

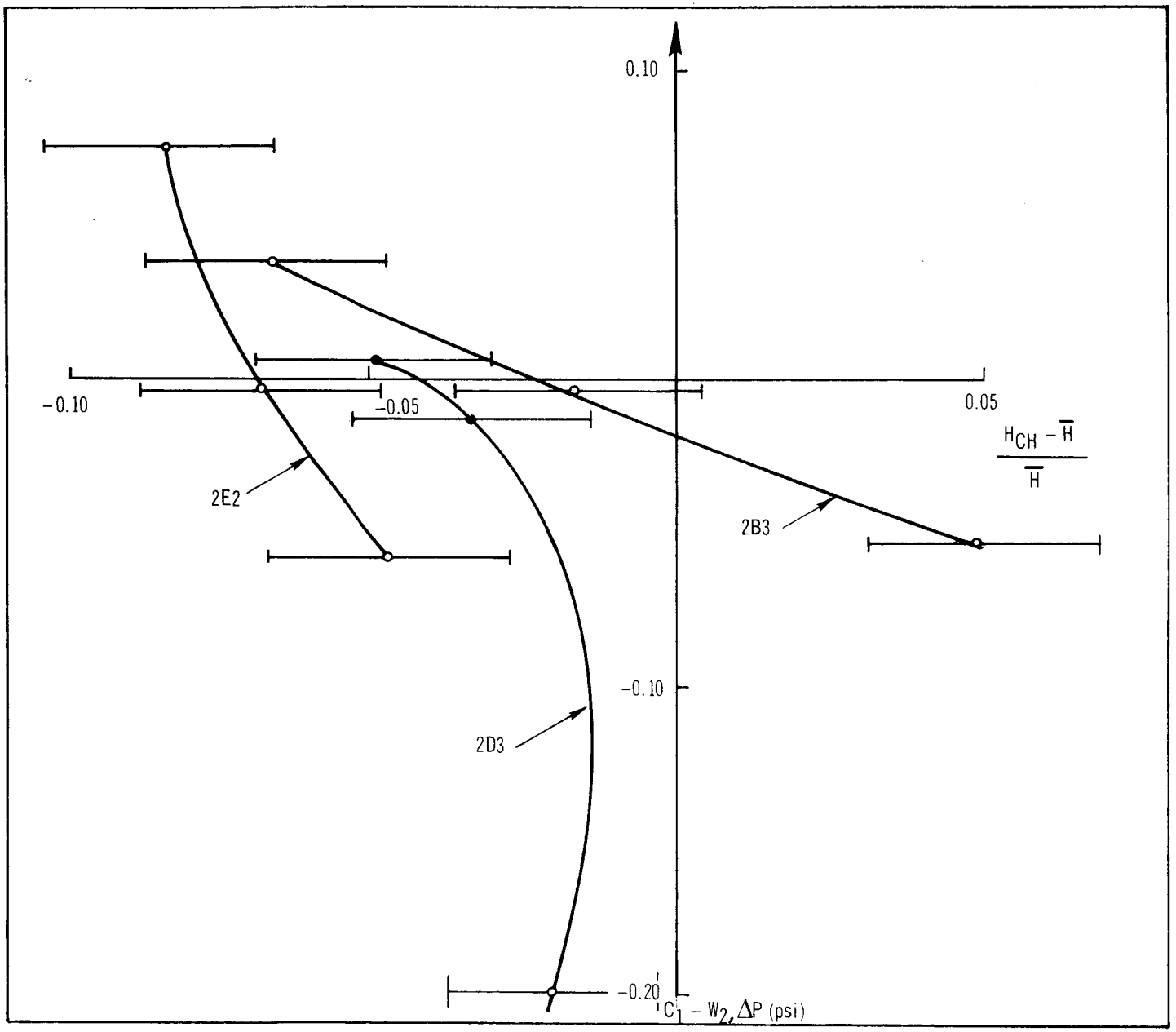

Figure 10. Variation of Channel Enthalpy with Differential Pressure

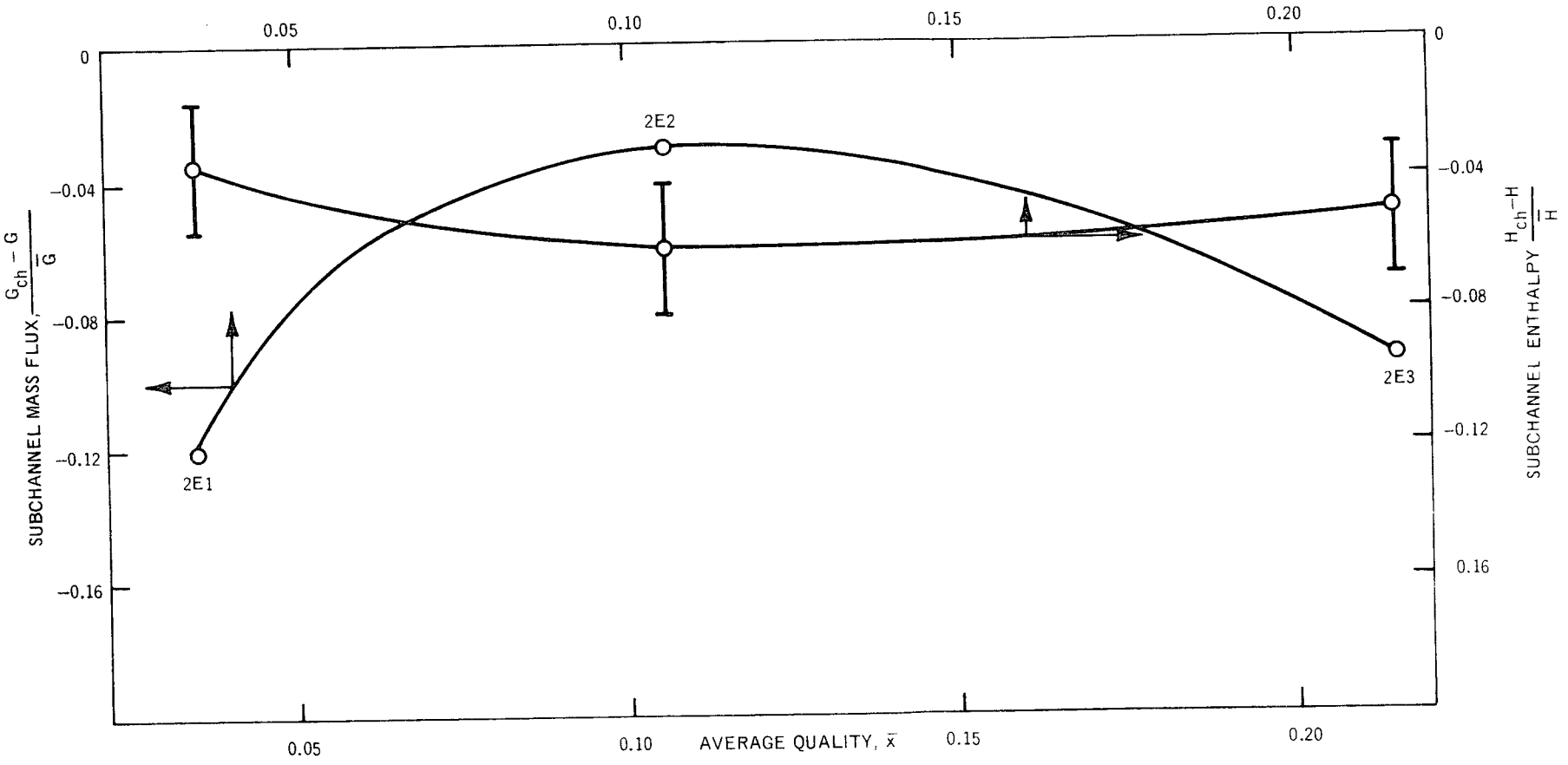

Figure 11. Variation of Channel Flow and Enthalpy with Average Quality

Table 1
CORNER SUBCHANNEL RESULTS
(p = 1000 psia)

Test Point	Bundle Average Mass Flux $\bar{G} \times 10^{-6}$ (lb/ft^2-h)	Bundle Average Exit Quality, $\bar{x}_e$	Subchannel Mass Flux, $G_{ch} \times 10^{-6}$ (lb/ft^2-h)	Subchannel Quality, x_{ch}	Normalized Subchannel Mass Flux, $\frac{G_{ch} - \bar{G}}{\bar{G}}$	Normalized Subchannel Enthalpy, $\frac{H_{ch} - \bar{H}}{\bar{H}}$
1B	0.480	–	0.311	–	–0.351	–
1C	0.990	–	0.701	–	–0.292	–
1D	1.510	–	1.095	–	–0.275	–
1E	1.97	–	1.62	–	–0.177	–
2B2	0.530	0.029	0.372	0.003	–0.298	–0.030
2B3	0.535	0.090	0.550	0.072	+0.028	–0.079
2B4	0.535	0.176	0.524	0.133	–0.021	–0.042
2C1	1.060	0.042	0.965	0.029	–0.089	–0.014
2C2	1.068	0.075	0.968	0.063	–0.093	–0.013
2D1	0.540	0.110	0.425	0.083	–0.212	–0.028
2D3	0.540	0.318	0.490	0.260	–0.093	–0.050
2E1	1.080	0.035	0.950	0.004	–0.121	–0.035
2E2	1.080	0.106	1.046	0.049	–0.032	–0.060
2E3	1.060	0.215	0.965	0.160	–0.095	–0.052
2F1	2.07	0.042	1.53	0.120	–0.261	+0.088
2F2	2.07	0.108	1.62	0.160	–0.218	+0.055
2G1	1.070	0.038	0.882	0.032	–0.175	–0.007
2G2	1.080	0.090	1.00	0.020	–0.074	–0.075
2G3	1.070	0.160	0.865	0.074	–0.192	–0.086
2H1	2.12	0.031	1.87	0.020	–0.119	–0.013
2H2	2.12	0.099	1.75	0.146	–0.175	+0.020
2I2	1.06	0.104	1.035	0.110	–0.024	+0.006

Table 2
TEST CONDITIONS
(p = 1000 psi)

Test Point	Bundle Average Mass Flux $\bar{G} \times 10^{-6}$ (lb/ft^2-h)	Power (kW)	Heat Flux (Btu/ft^2-h)	Subcooling (Btu/lb)	Bundle Average Exit Quality $\bar{x}_e$
1B	0.480	0	0	504.6	–
1C	0.990	0	0	504.6	–
1D	1.510	0	0	504.6	–
1E	1.97	0	0	504.6	–
2B2	0.530	532	225,000	149.9	0.029
2B3	0.535	532	225,000	108.7	0.090
2B4	0.535	532	225,000	52.8	0.176
2C1	1.060	532	225,000	57.2	0.042
2C2	1.068	532	225,000	35.1	0.075
2D1	0.540	1064	450,000	259.2	0.110
2D3	0.540	1064	450,000	124.4	0.318
2E1	1.080	1064	450,000	142.9	0.035
2E2	1.080	1064	450,000	96.7	0.106
2E3	1.060	1064	450,000	29.1	0.215
2F1	2.07	1064	450,000	59.6	0.040
2F2	2.07	1064	450,000	17.4	0.109
2G1	1.07	1596	675,000	225.9	0.038
2G2	1.080	1596	675,000	189.8	0.090
2G3	1.070	1596	675,000	146.7	0.160
2H1	2.12	1560	660,000	102.6	0.031
2H2	2.12	1596	675,000	59.2	0.099
2I2	1.06	1880	800,000	227.5	0.104

$$\Delta G_{ch} = \frac{\partial G_{ch}}{\partial \bar{G}} d\bar{G} + \frac{\partial G_{ch}}{\partial \bar{x}} d\bar{x}$$

$$\Delta x_{ch} = \frac{\partial x_{ch}}{\partial \bar{x}} d\bar{x} + \frac{\partial x_{ch}}{\partial \bar{G}} d\bar{G}$$

Where ΔG_{ch} and Δx_{ch} are changes in subchannel conditions due to $d\bar{G}$ and $d\bar{x}$.

The tests showed that the second term on the right hand side of both equations was of a smaller order of magnitude than the first team. Also, the derivatives $\partial G_{ch}/\partial \bar{G}$ and $\partial x_{ch}/\partial x$ were of the order $G_{ch}/\bar{G}$ and 1, respectively.

Therefore

$$\Delta G_{ch} \cong \frac{\partial G_{ch}}{\partial G} d\bar{G} = \frac{G_{ch}}{\bar{G}} d\bar{G}$$

or

$$G_{ch} - G_{ch\ experimental} \cong \frac{G_{ch\ experimental}}{\bar{G}_{experimental}} \left(\bar{G}_{nominal} - \bar{G}_{experimental}\right)$$

so that

$$\frac{G_{ch} - G_{ch\ experimental}}{G_{ch\ experimental}} = \frac{\bar{G}_{nominal} - \bar{G}_{experimental}}{\bar{G}_{experimental}}$$

or

$$\frac{G_{ch}}{G_{ch\ experimental}} = \frac{\bar{G}_{nominal}}{\bar{G}_{experimental}}$$

and similarly,

$$\Delta x_{ch} \cong \frac{\partial x_{ch}}{\partial \bar{x}} d\bar{x}$$

or,

$$\Delta x_{ch} \cong d\bar{x}$$

so that finally,

$$x_{ch} - x_{ch\ experimental} = \bar{x}_{nominal} - \bar{x}_{experimental}$$

The maximum variations in the test conditions between the different subchannels were of the order of 4 % in $\bar{G}$ and 0.03 in $\bar{x}$ (at high values of $\bar{x}$). The test results for the side subchannel, as corrected, using this procedure are shown in Table 3. The subchannel mass flux and exit quality are based on isokinetic conditions, set with the calibration in Figure 7.

Non-isokinetic data were also taken for the side subchannel for some of the test points. These are shown in Figures 12 and 13, where the differential pressure W1-W2, is plotted against the nondimensionalized, subchannel flow rate and enthalpy. The higher slope for Curve 2G1 in Figure 12 is caused by the higher mass velocity ($G = 1 \times 10^6$ lb/ft^2-h). A comparison between Figures 12 and 13 shows that as the amount of flow in the subchannel is decreased, the subchannel enthalpy also generally decreases, indicating again that the enthalpy of flow diversion is higher than the subchannel enthalpy.

Figures 12 and 15 represent the variation in isokinetic flow rate and subchannel enthalpy as a function of the average channel exit quality. Error bands for the flow rate are not shown, to avoid confusion. The error was estimated to be of the order of 1 % of the channel flow. The trends show that the side subchannel flow rate and enthalpy are very close to the average conditions. An examination of Table 3 reveals that generally the subchannel flow and enthalpy are slightly on the low side, compared with the mean flow rate and enthalpy.

5.3 CENTER SUBCHANNEL TEST RESULTS

Table 4 shows the results of isokinetic sampling for the center subchannel. These data have been corrected for nominal conditions using the method described in Section 5.2, above. The center subchannel flow rate was generally higher than the average flow rate, and the quality was also higher than average.

Non-isokinetic data were also taken, some of which are shown plotted in Figures 16 and 17. Figure 17 shows that as the subchannel flow rate is increased, its enthalpy increases slightly. The effect was generally smaller than in the corner and side subchannels because the center subchannel is bounded on two sides by similar center subchannels.

Figures 18 and 19 show the variation in the isokinetic center subchannel flow rate and enthalpy with channel quality. Most points lie above the zero of the ordinate, indicating higher than average conditions.

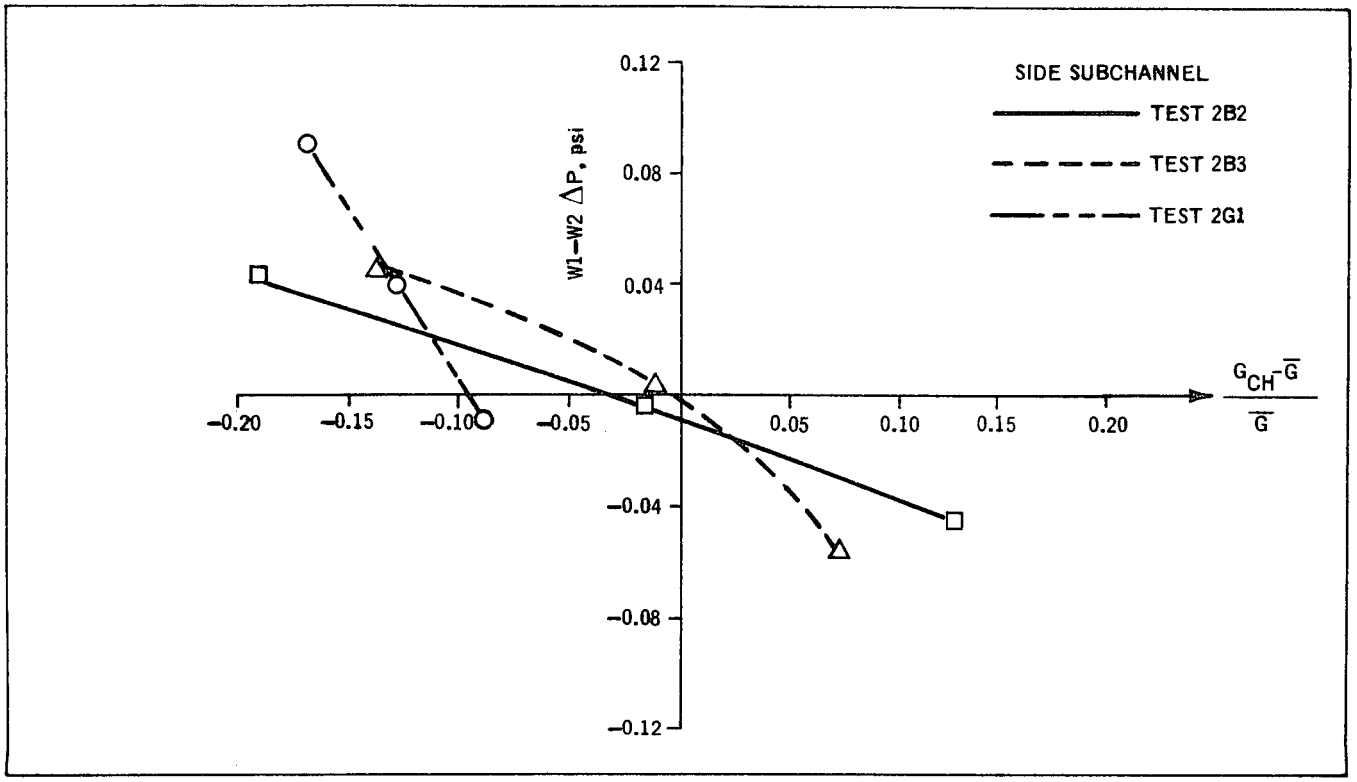

Figure 12. Non-Isokinetic Data: Variation of Differential Pressure with Subchannel Flow

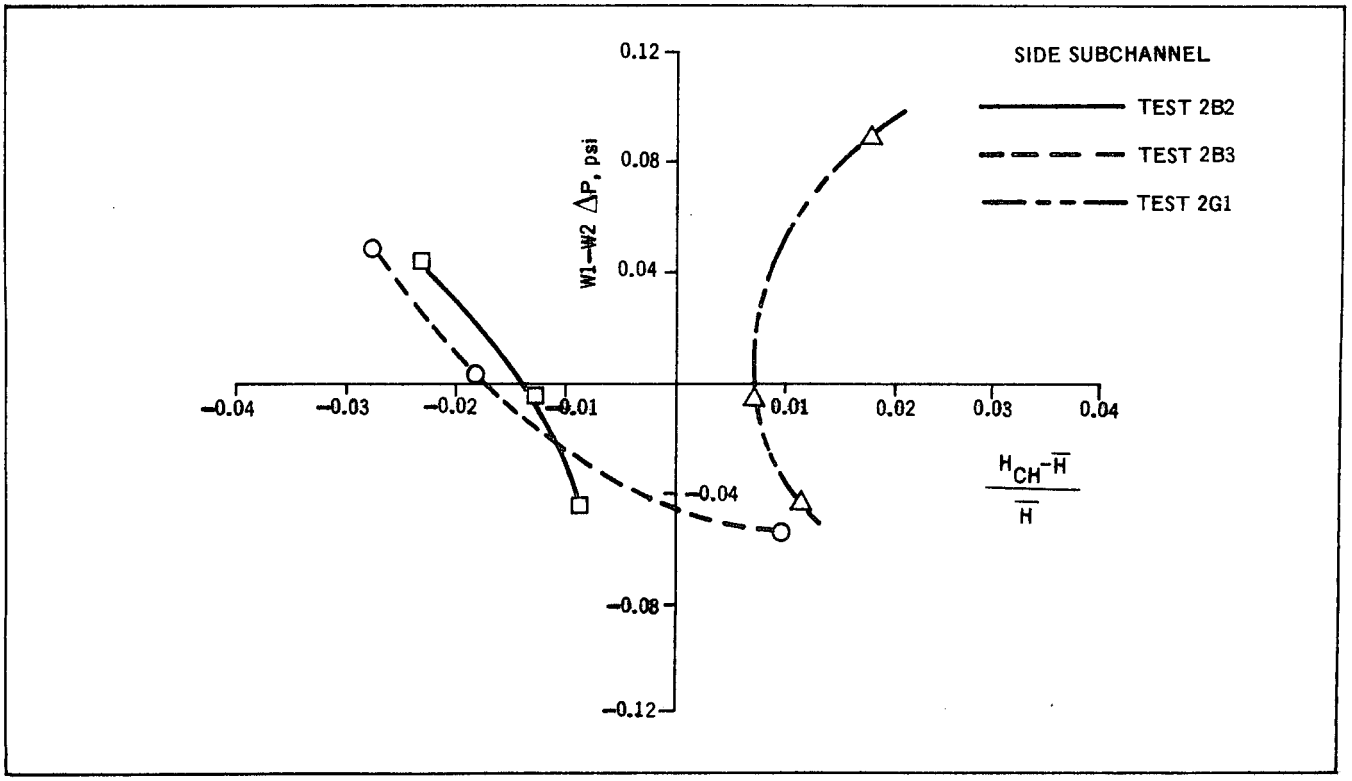

Figure 13. Non-Isokinetic Data: Variation of Differential Pressure with Subchannel Enthalpy

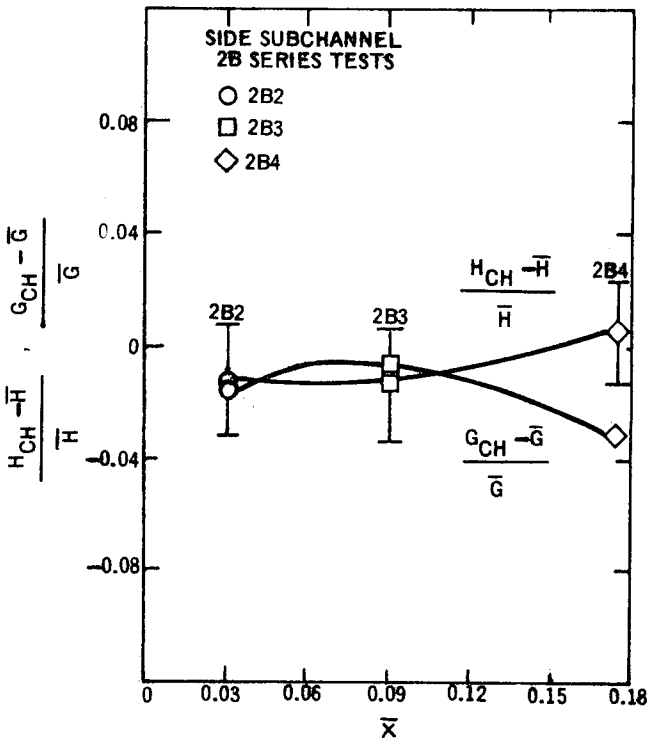

Figure 14. Variation in Subchannel Flow and Enthalpy with Average Quality

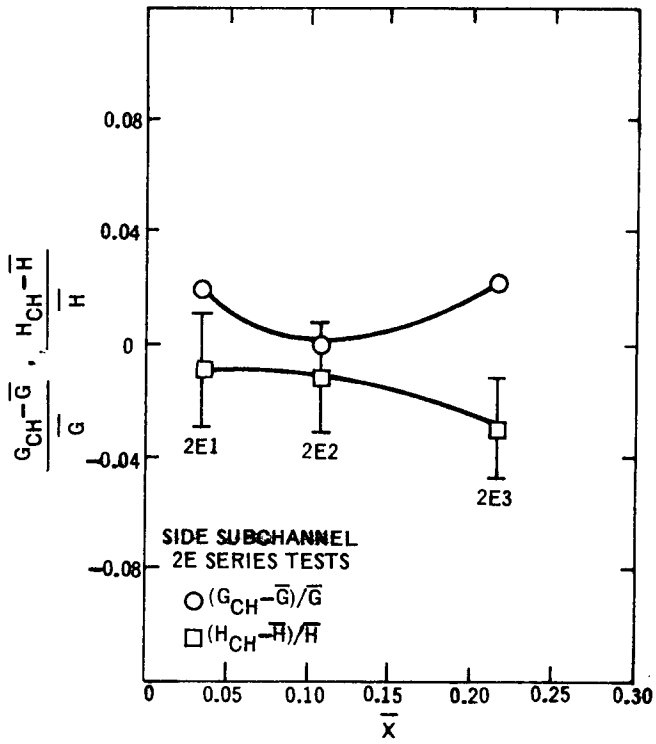

Figure 15. Variation in Subchannel Flow and Enthalpy with Average Quality

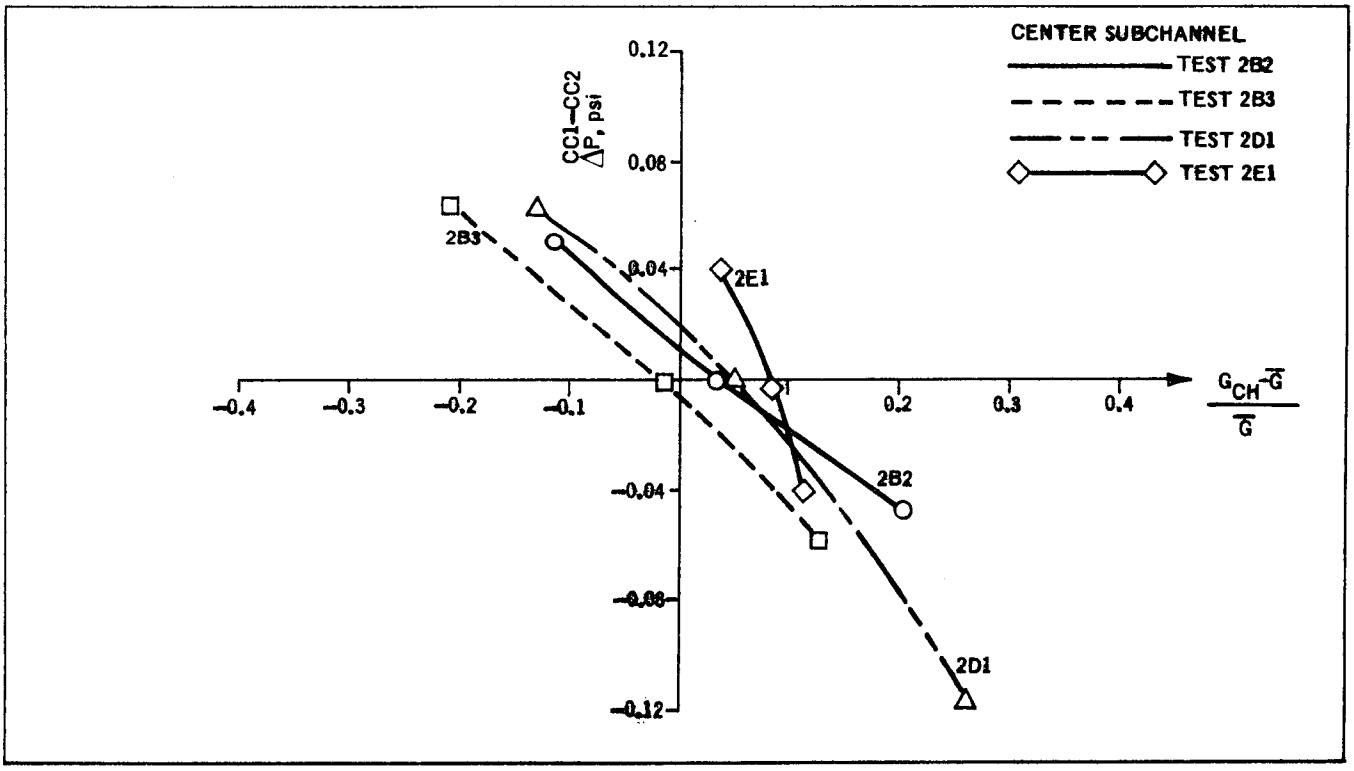

Figure 16. Non-Isokinetic Data: Variation of Differential Pressure with Subchannel Flow

Table 3
TEST RESULTS FOR SIDE SUBCHANNEL

Test Point	Bundle Average Mass Flux, $\bar{G} \times 10^{-6}$ (lb/ft^2-h)	Bundle Average Exit Quality $\bar{x}_e$	Subchannel Mass Flux, $G_{ch} \times 10^{-6}$ (lb/ft^2-h)	Subchannel Quality x_{ch}	Normalized Subchannel Mass Flux, $\frac{G_{ch} - \bar{G}}{\bar{G}}$	Normalized Subchannel Enthalpy, $\frac{H_{ch} - \bar{H}}{\bar{H}}$
1B	0.480	–	0.462	–	–0.037	–
1C	0.990	–	0.939	–	–0.0515	–
1D	1.510	–	1.441	–	–0.0458	–
1E	1.97	–	1.91	–	–0.0304	–
2B2	0.530	0.029	0.521	0.015	–0.017	–0.0144
2B3	0.535	0.090	0.530	0.076	–0.0093	–0.0175
2B4	0.535	0.176	0.517	0.180	–0.0336	0.0039
2C1	1.060	0.042	1.066	0.018	+0.0054	–0.0273
2C2	1.068	0.075	1.028	0.075	–0.0374	0
2D1	0.540	0.110	0.560	0.105	+0.037	–0.0053
2D3	0.540	0.318	0.532	0.330	–0.015	0.0103
2E1	1.080	0.035	1.102	0.026	+0.020	–0.0103
2E2	1.080	0.106	1.078	0.097	–0.002	–0.0095
2E3	1.060	0.215	1.081	0.185	+0.0197	–0.0286
2G1	1.070	0.038	0.968	0.044	–0.095	+0.0069
2G2	1.080	0.090	1.111	0.068	+0.0287	–0.0238
2G3	1.070	0.160	1.132	0.127	+0.0551	–0.0332

Table 4
CENTER SUBCHANNEL RESULTS

Test Point	Bundle Average Mass Flux, $\bar{G} \times 10^{-6}$ (lb/ft^2-h)	Bundle Average Exit Quality, $\bar{x}_e$	Subchannel Mass Flux, $G_{ch} \times 10^{-6}$ (lb/ft^2-h)	Subchannel Quality, x_{ch}	Normalized Subchannel Mass Flux, $\frac{G_{ch} - \bar{G}}{\bar{G}}$	Normalized Subchannel Enthalpy, $\frac{H_{ch} - \bar{H}}{\bar{H}}$
1B	0.480	–	0.526	–	0.096	–
1C	0.990	–	1.150	–	0.162	–
1D	1.510	–	1.690	–	0.119	–
1E	1.97	–	2.190	–	0.119	–
2B2	0.530	0.029	0.540	0.030	0.0188	0.0011
2B3	0.535	0.090	0.521	0.104	–0.0265	0.0151
2B4	0.535	0.176	0.560	0.220	0.0467	0.0435
2C1	1.060	0.042	1.077	0.059	0.0161	0.0195
2C2	1.068	0.075	1.144	0.100	0.0712	0.0275
2D1	0.540	0.110	0.556	0.117	0.0295	0.0074
2D3	0.540	0.318	0.563	0.364	0.0425	0.0399
2E1	1.080	0.035	1.162	0.051	0.0761	0.0184
2E2	1.080	0.106	1.180	0.105	0.0925	–0.001
2E3	1.060	0.215	1.126	0.249	0.0624	0.0324
2G1	1.070	0.038	1.142	0.043	0.0671	0.0057
2G2	1.080	0.090	1.130	0.110	0.0464	0.0216
2G3	1.070	0.160	1.160	0.176	0.0838	0.0161

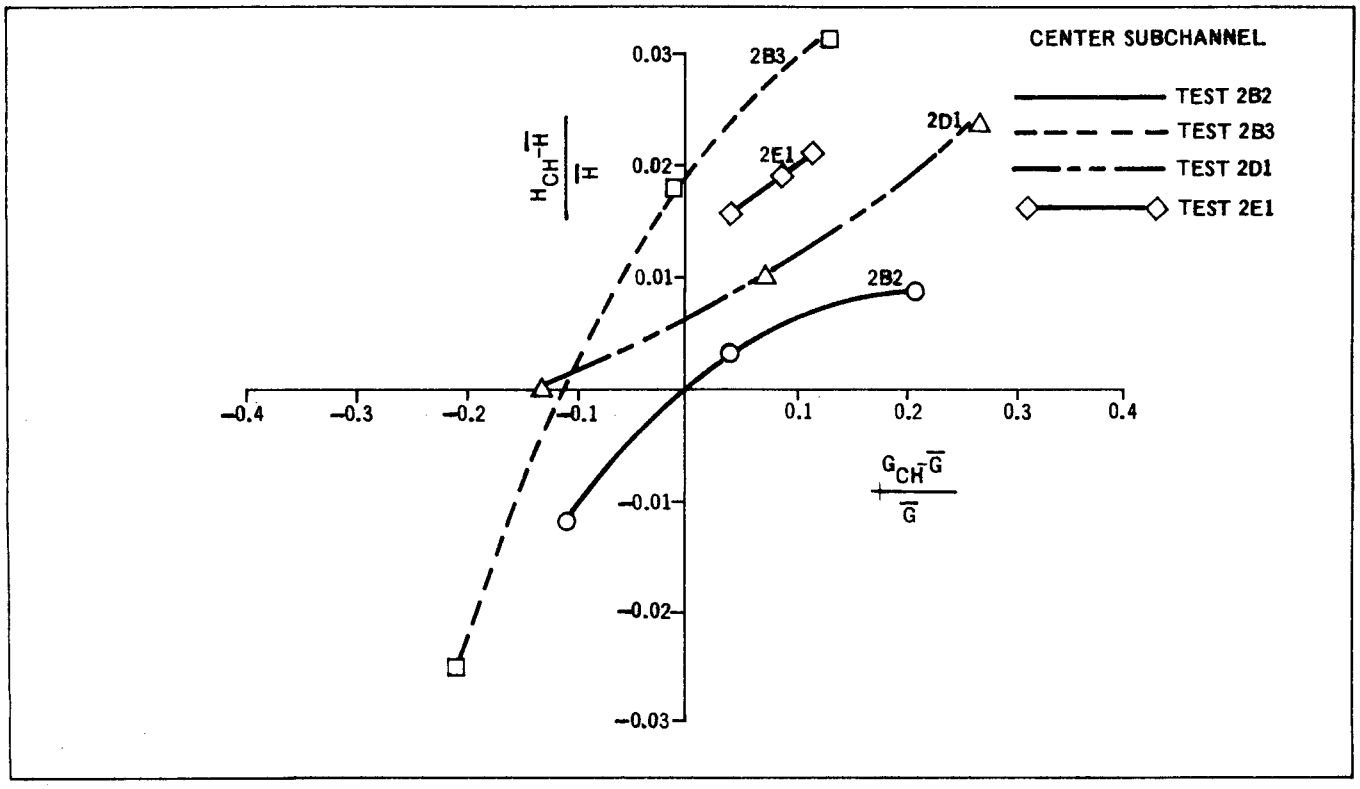

Figure 17. Non-Isokinetic Data: Variation of Subchannel Enthalpy with Subchannel Flow

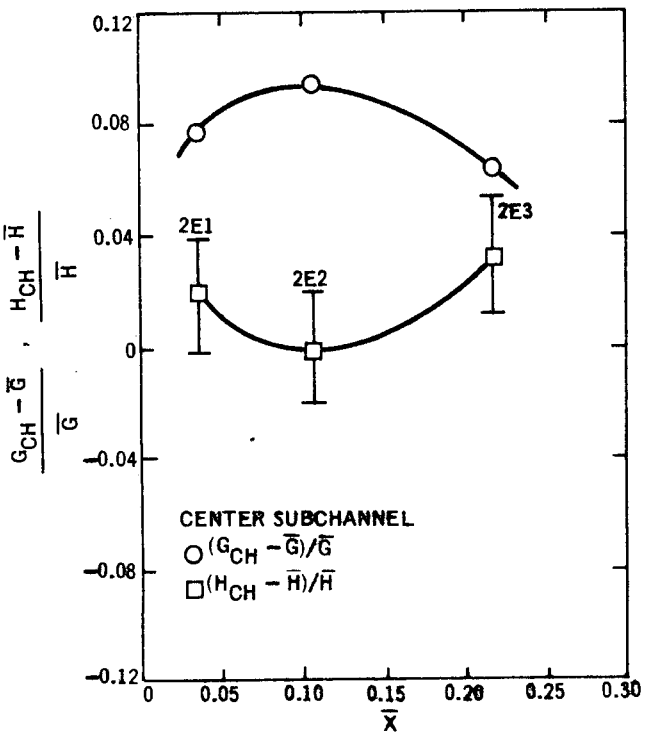

Figure 18. Variation of Subchannel Flow and Enthalpy with Average Quality

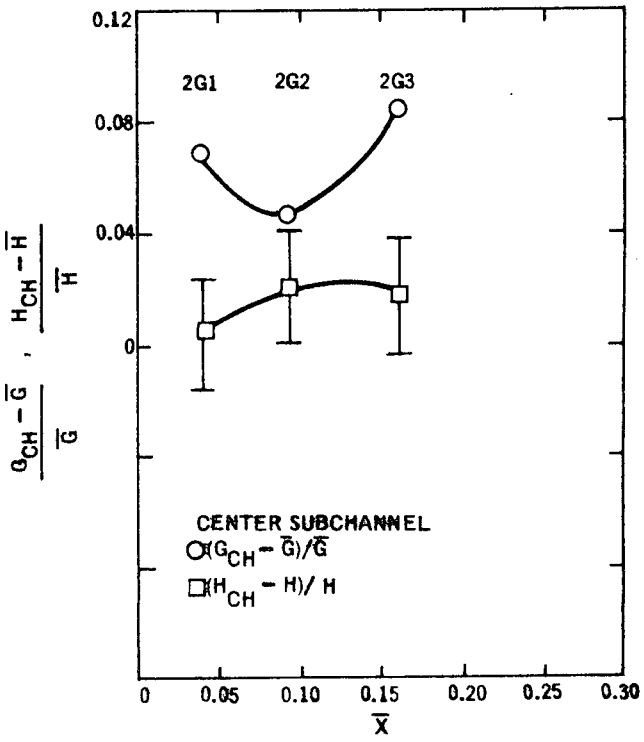

Figure 19. Variation of Subchannel Flow and Enthalpy with Average Quality

6. DISCUSSION OF ISOKINETIC SAMPLING DATA

Table 5 presents the overall results for the three subchannels. Assuming four identical corner subchannels (total flow area = 0.3128 in.^{2}), eight identical side subchannels (total flow area = 1.4592 in.^{2}), and four identical center subchannels (total flow area = 1.1576 in.^{2}), the total mass flux and enthalpy flux at the channel exit were calculated and compared with the average channel flow rate and average exit quality (as calculated on the basis of a heat balance). Table 5 shows that the results check within ±5 %, with only three runs deviating more than 3 %. This increases confidence in the isokinetic sampling procedure, since the energy and continuity equation must balance for valid data.

Figures 20, 21, and 22 illustrate the trends in the subchannel qualities with respect to the bundle average quality. The subchannel qualities increase monotonically with the average quality, the center subchannel (3) being the "hottest" and the corner subchannel (1) the "coolest". The center subchannel quality is seen to be consistently higher than the average, and the corner subchannel quality is lower than the average. The quality of the side subchannel (2) is near the average, sometimes higher and sometimes lower. Within the accuracy of the data there appears to be a trend for the subchannel qualities to converge to the average at approximately 5-10 % bundle average quality. This has been attributed to enhanced

Table 5
OVERALL RESULTS FOR ISOKINETIC SAMPLING

Test Point	Bundle Average Mass Flux, $\bar{G} \times 10^{-6}$	Bundle Average Exit Quality $\bar{x}$	Mass Flux: Corner Subchannel $G_1 \times 10^{-6}$	Quality: Corner Subchannel x_1	Mass Flux: Side Subchannel $G_2 \times 10^{-6}$	Quality: Side Subchannel x_2	Mass Flux: Center Subchannel $G_3 \times 10^{-6}$	Quality: Center Subchannel x_3	Bundle Average Mass Flux Error $\frac{\hat{G} - \bar{G}}{\bar{G}}$ (%)	Bundle Average Quality Error $\hat{x} - \bar{x}$
1B	0.480	–	0.311	–	0.462	–	0.526	–	−1.6	–
1C	0.990	–	0.701	–	0.939	–	1.150	–	+0.70	–
1D	1.510	–	1.095	–	1.441	–	1.690	–	+0.46	–
1E	1.97	–	1.62	–	1.91	–	2.190	–	+1.06	–
2B2	0.530	0.029	0.372	0.003	0.521	0.014	0.540	0.030	−1.51	−0.010
2B3	0.535	0.090	0.550	0.072	0.530	0.076	0.521	0.104	−1.12	−0.004
2B4	0.535	0.176	0.524	0.133	0.517	0.180	0.560	0.220	−0.0	+0.015
2C1	1.060	0.042	0.965	0.029	1.066	0.018	1.077	0.059	−0.05	−0.006
2C2	1.068	0.075	0.968	0.063	1.028	0.075	1.144	0.100	0.05	+0.009
2D1	0.540	0.110	0.425	0.083	0.560	0.105	0.556	0.117	0.74	−0.002
2D3	0.540	0.318	0.490	0.260	0.532	0.330	0.563	0.364	0.03	+0.019
2E1	1.080	0.035	0.950	0.004	1.102	0.026	1.162	0.051	2.77	0.000
2E2	1.080	0.106	1.046	0.049	1.078	0.097	1.180	0.105	3.24	−0.007
2E3	1.060	0.215	0.965	0.160	1.081	0.185	1.126	0.249	2.55	−0.007
2G1	1.070	0.038	0.882	0.032	0.968	0.044	1.142	0.043	−4.86	0.003
2G2	1.080	0.090	01.00	0.020	1.111	0.068	1.130	0.110	2.50	−0.008
2G3	1.070	0.160	0.865	0.074	1.132	0.127	1.160	0.176	4.11	−0.009

$$\hat{G} = \frac{\Sigma G_i A_i}{\Sigma A_i}, \quad \hat{H} = \frac{\Sigma G_i H_i A_i}{\Sigma G_i A_i}, \quad \hat{x} = \frac{\hat{H} - H_f}{H_{fg}}$$

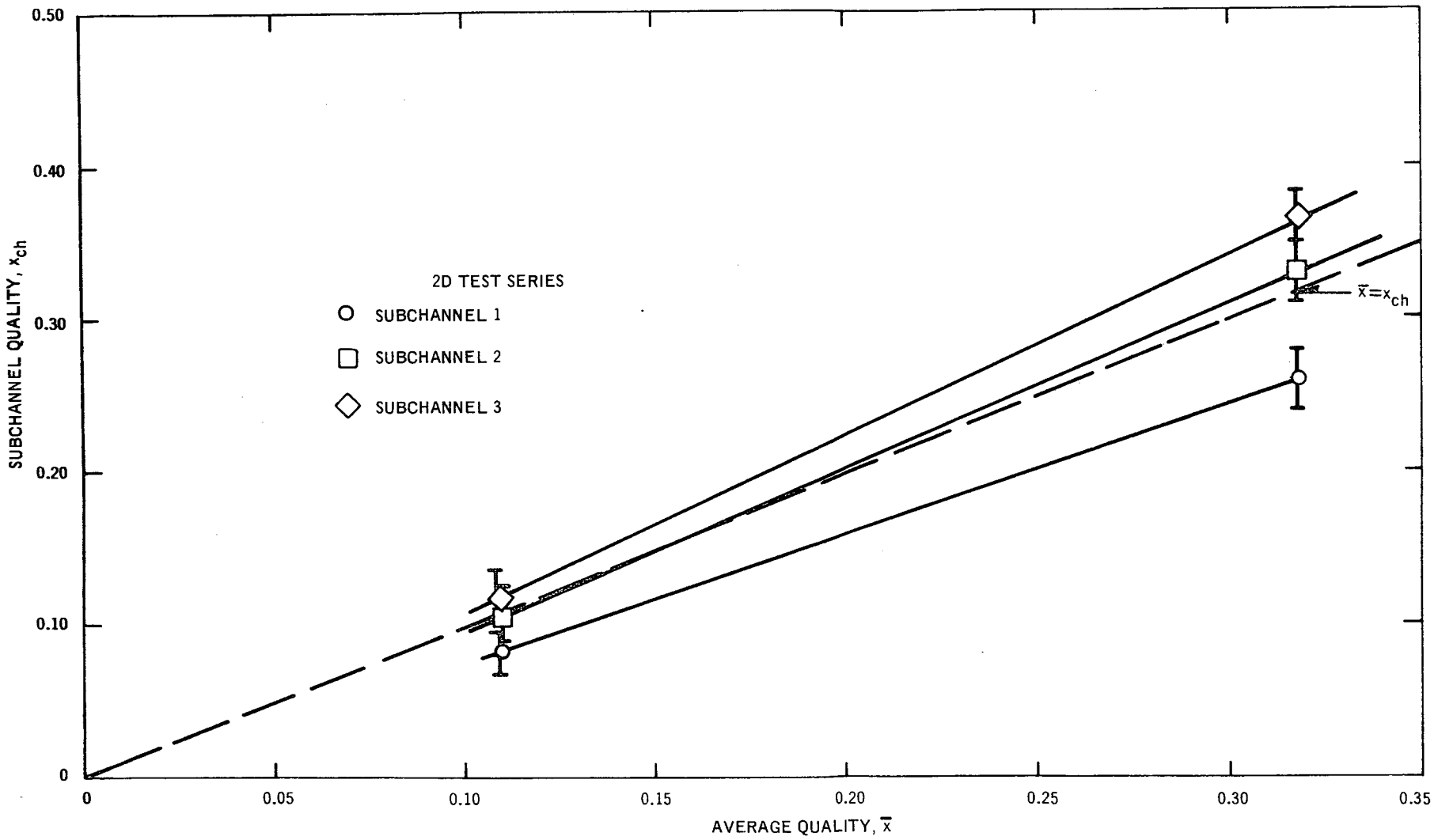

Figure 20. Variation of Subchannel Qualities with Average Quality: 2D Test Series

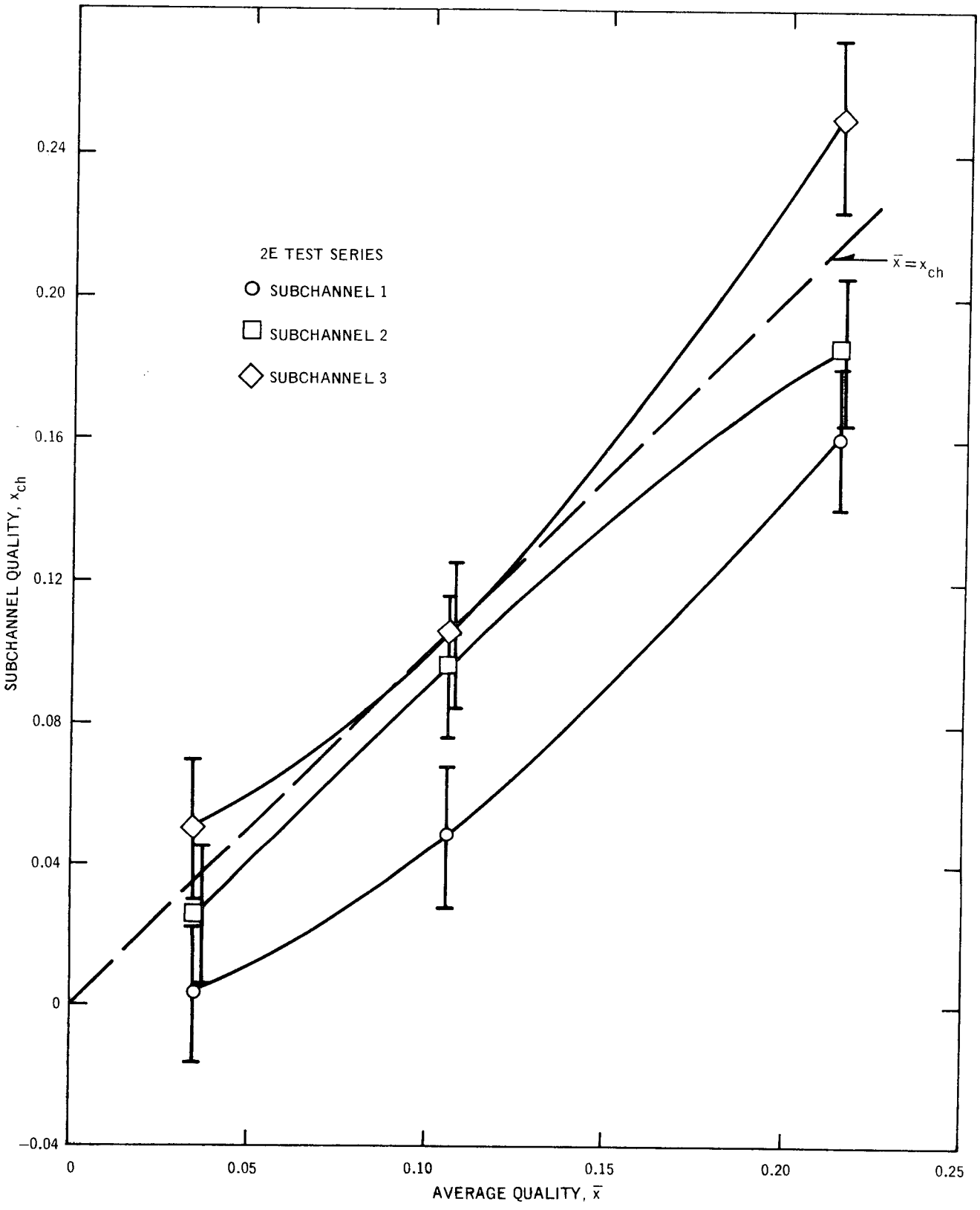

Figure 21. Variation of Subchannel Qualities with Average Quality: 2E Test Series

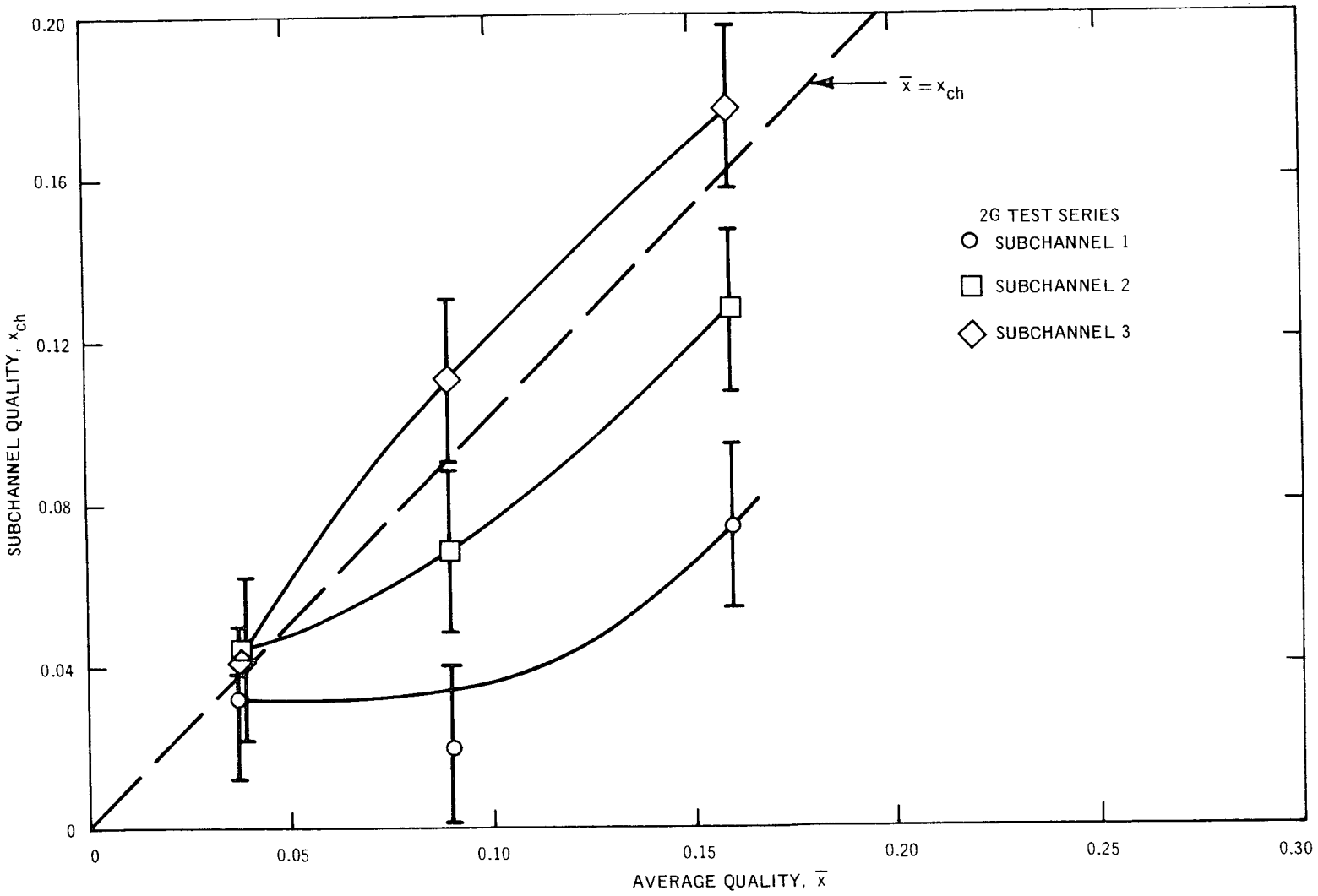

Figure 22. Variation of Subchannel Qualities with Average Quality: 2G Test Series

mixing in the slug-annular flow-transition regime. Since this transition may occur in different subchannels at different values of the average quality, the "pinching" effect may not occur simultaneously in all subchannels.

Figures 23 and 24 compare the mass fluxes in the three subchannels with the bundle average quality. The flows have been nondimensionalized with respect to the average mass flux. These figures show that the mass flux is highest in the center subchannel and lowest in the corner subchannel. Here also the subchannel mass fluxes approach each other in the neighborhood of 10 % average quality. It appears that this trend with flow regime is weaker in actual rod arrays than in two-subchannel test sections. In fact, within the scatter of the data, the trend is often not observed.

Figures 25, 26, 27, and 28 show the variation in subchannel enthalpies as a function of the average quality. These figures contain information similar to that in Figures 20, 21, and 22, except that nondimensionalized enthalpy, instead of subchannel quality has been used as the ordinate.

It is possible to derive information from the data by plotting certain parameters against bundle average quality while holding other parameters, except the subcooling, constant. It should be recognized at the outset that at a given $\bar{x}$ the boiling length and inlet conditions are quite different, and thus the effect of subcooled boiling is not constant. Figures 29 to 34 show the effect on the nondimensionalized subchannel enthalpies of changing the bundle average mass flux. Figures 29, 30, and 31 compare the results of two series of runs with the same nominal heat flux of 0.45×10^6 Btu/ft^2-h with mass fluxes of 0.5×10^6 lbs/ft^2-h and 1.0×10^6 lbs/ft^2-h, respectively, for the corner, side, and center subchannels. The effect on the subchannel enthalpy of changing the flow rate is seen to be very weak and is to be considered negligible within the uncertainty of the data. Figures 32, 33, and 34 show the effect of changing the mass flux at a lower value of the heat flux, 0.225×10^6 Btu/ft^2-h. Here also the effect of the mass flux is small. The only consistent trend that one can see in Figures 29 to 34 is that at the higher heat flux of 0.45×10^6 Btu/ft^2-h for each subchannel the data for $\bar{G} = 0.5 \times 10^6$ lb/ft^2-h tends to be above the data for $\bar{G} = 1.0 \times 10^6$ lb/ft^2-h, whereas at $q'' = 0.225 \times 10^6$ Btu/ft^2-h the trend is reversed. As will be shown this is due to a heat-flux trend. Figures 35 to 40 show the effect of the heat flux on the subchannel qualities. The effects are presumably different in the very low quality region, the region where subcooled boiling may exist in one or more subchannels, and the higher quality region. Unfortunately, no data were available for comparison in the very low quality region. At an average mass flux of 0.5×10^6 lbs/ft^2-h, no marked effects are seen on raising the heat flux from 0.225 Btu/ft^2-h to 0.45×10^6 Btu/ft^2-h. Since the boiling length is quite different in these cases, it is seen that the "memory effect" is apparently small at these lower flows. In Figures 38, 39, and 40, where plots for three different values of heat flux are shown for $\bar{G} = 1.0 \times 10^6$ lb/ft^2-h, there appears to be a reversal in trend at an average quality of 4-6 %. Above this value of quality, the corner and side subchannels run cooler as the heat flux is increased while the center subchannel increases in quality. At low qualities the opposite is true. Presumably, this trend can be attributed to the effect of subcooled boiling, which is more pronounced for cases of higher flow and subcooling. It would be expected that the corner subchannel would start boiling first, and then, as the bundle average quality increases, the effect of subcooled boiling would diminish, and so a reversal in the trend with heat flux could occur. Figures 41 to 43 show the variation in subchannel mass flux, as a function of the average mass flux, with average quality. There is a slight increase in the nondimensionalized mass flux in the center and corner subchannels as the bundle average mass flux is increased and there is a corresponding drop in the side subchannel flow. Presumably this trend is also due partially to the effect of subcooled boiling.

Similar plots (Figures 44, 45, and 46) were made to determine the effect of heat flux on the subchannel flow rates. As might be expected, the corner subchannel flow dropped as the heat flux was increased. The changes in the other two subchannels were slight. It should be noted that the energy balance was still maintained since a relatively large percentage change of flow in the corner subchannel produces only a small percentage change in the larger subchannels because most of the flow is already in these larger subchannels.

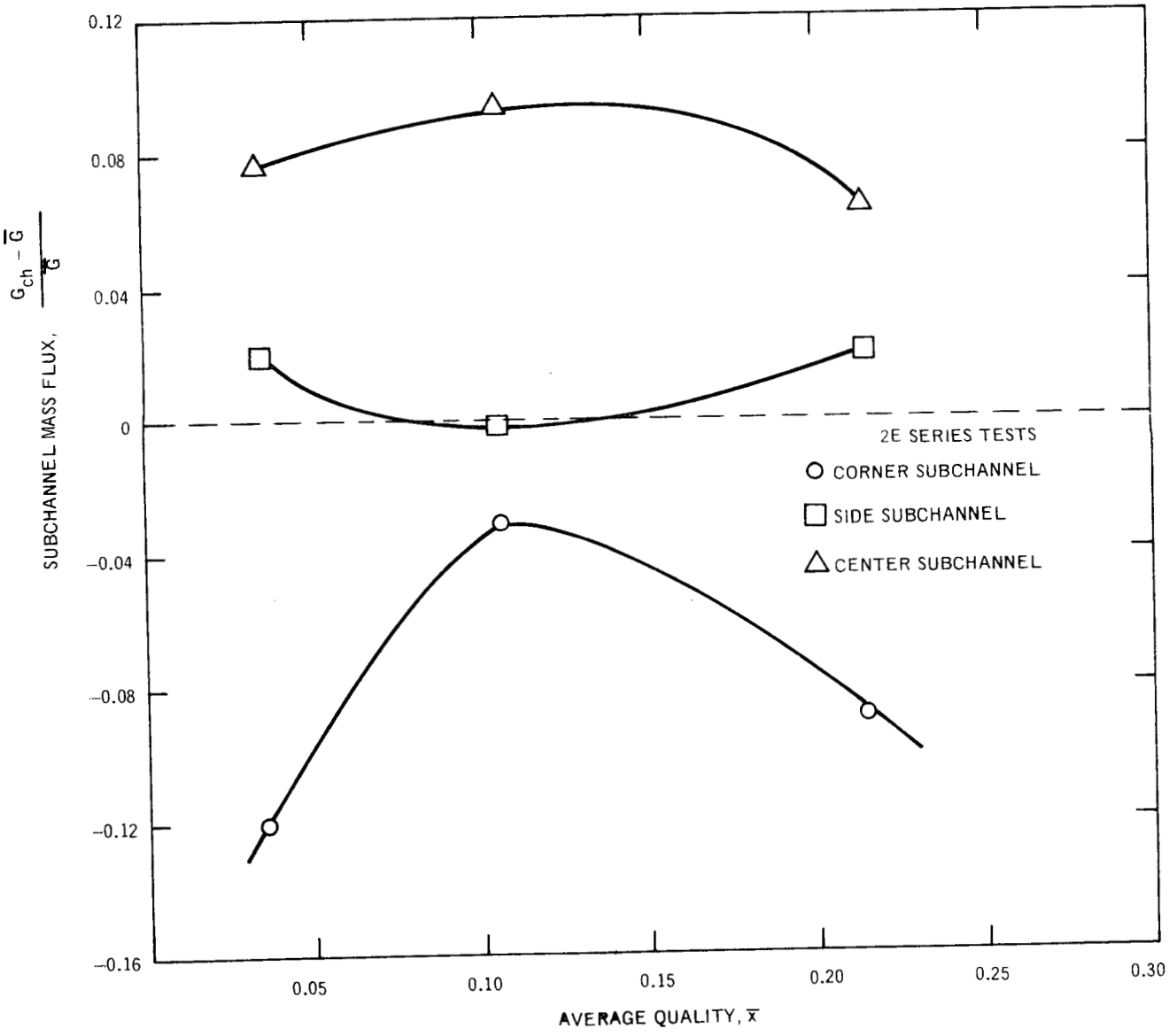

Figure 23. Comparison of Flows for Three Subchannels: 2E Test Series

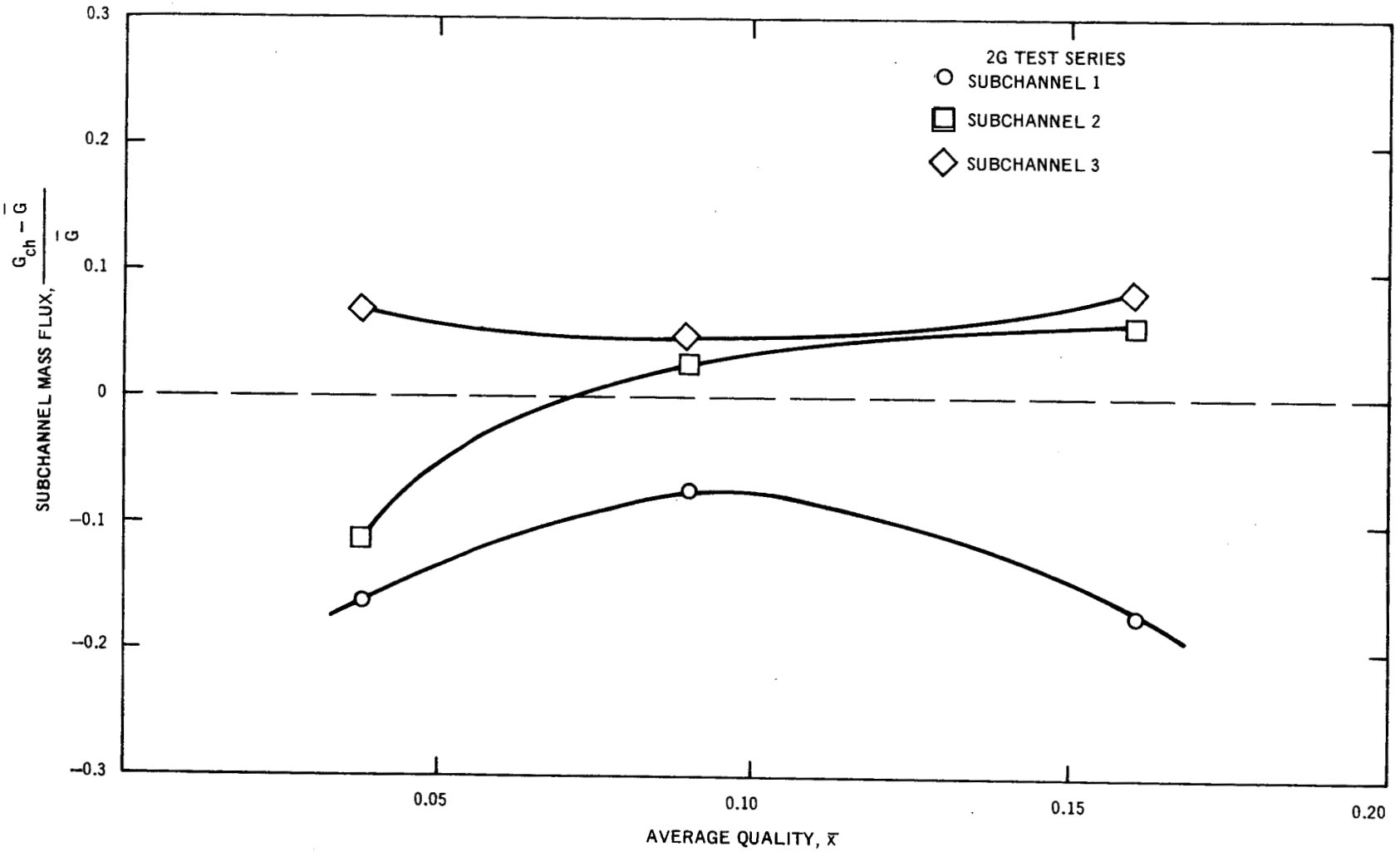

Figure 24. Comparison of Subchannel Flows for Three Subchannels: 2G Test Series

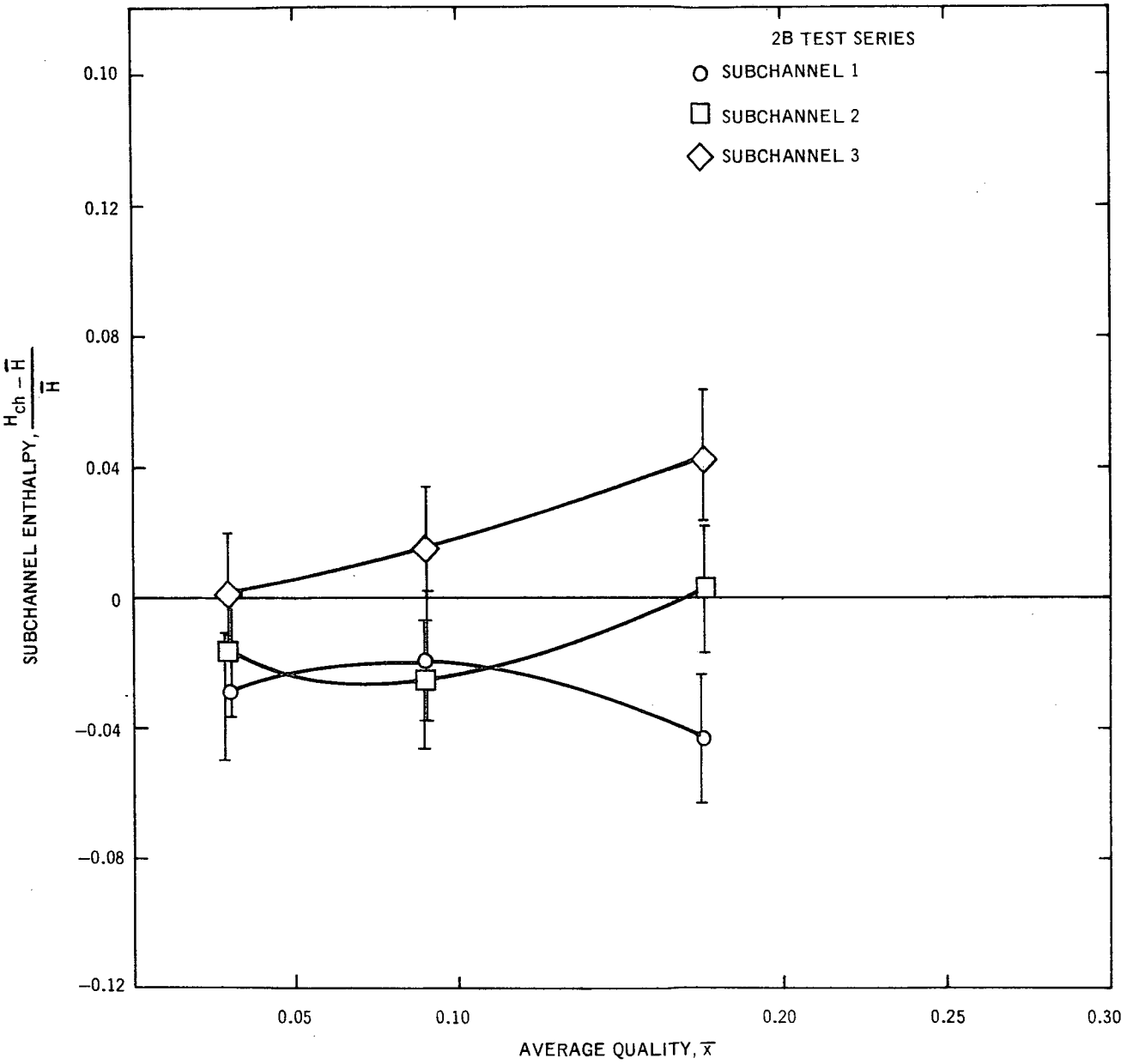

Figure 25. Comparison of Nondimensionalized Subchannel Enthalpies: 2B Test Series

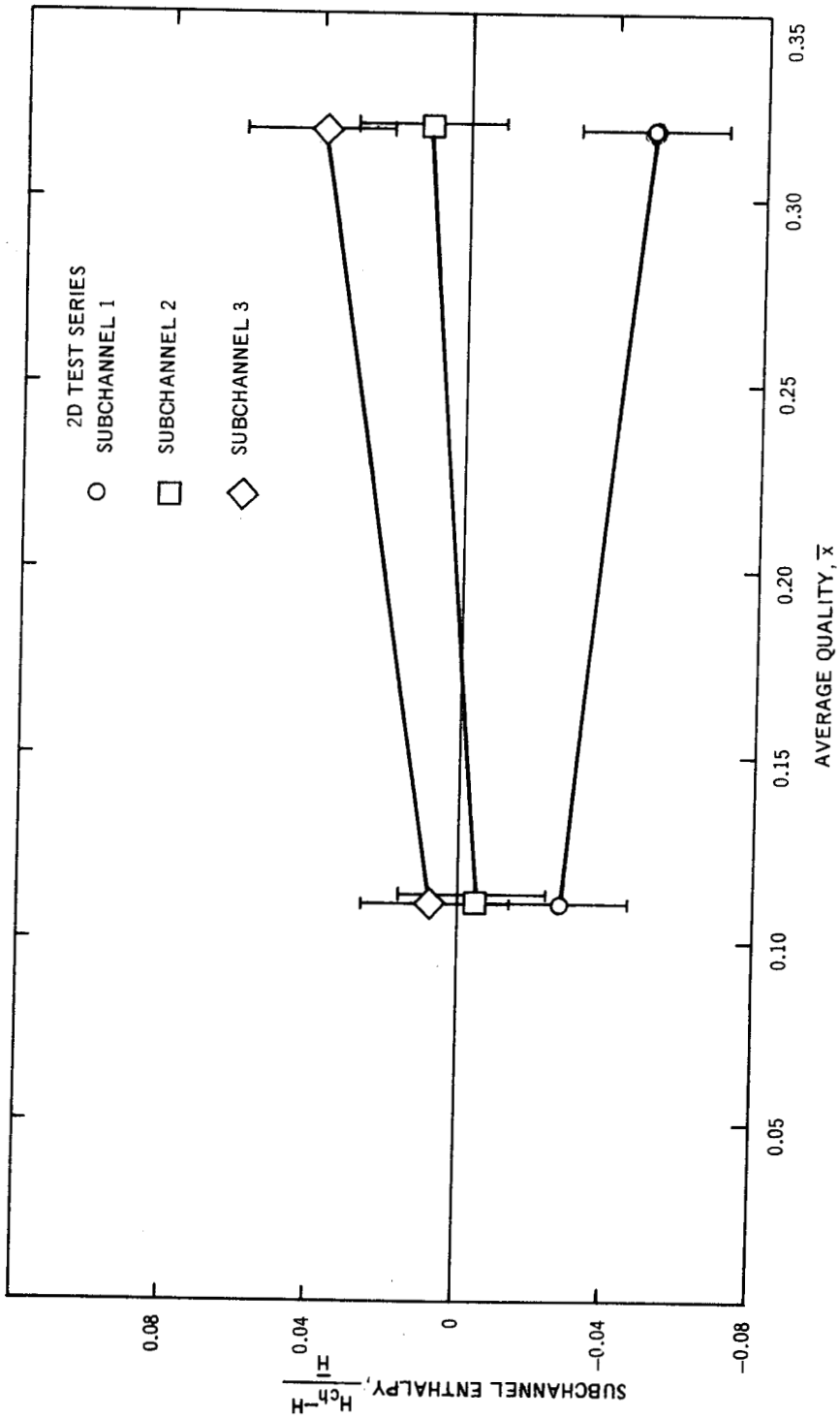

Figure 26. Comparison of Nondimensionalized Subchannel Enthalpies: 2D Test Series

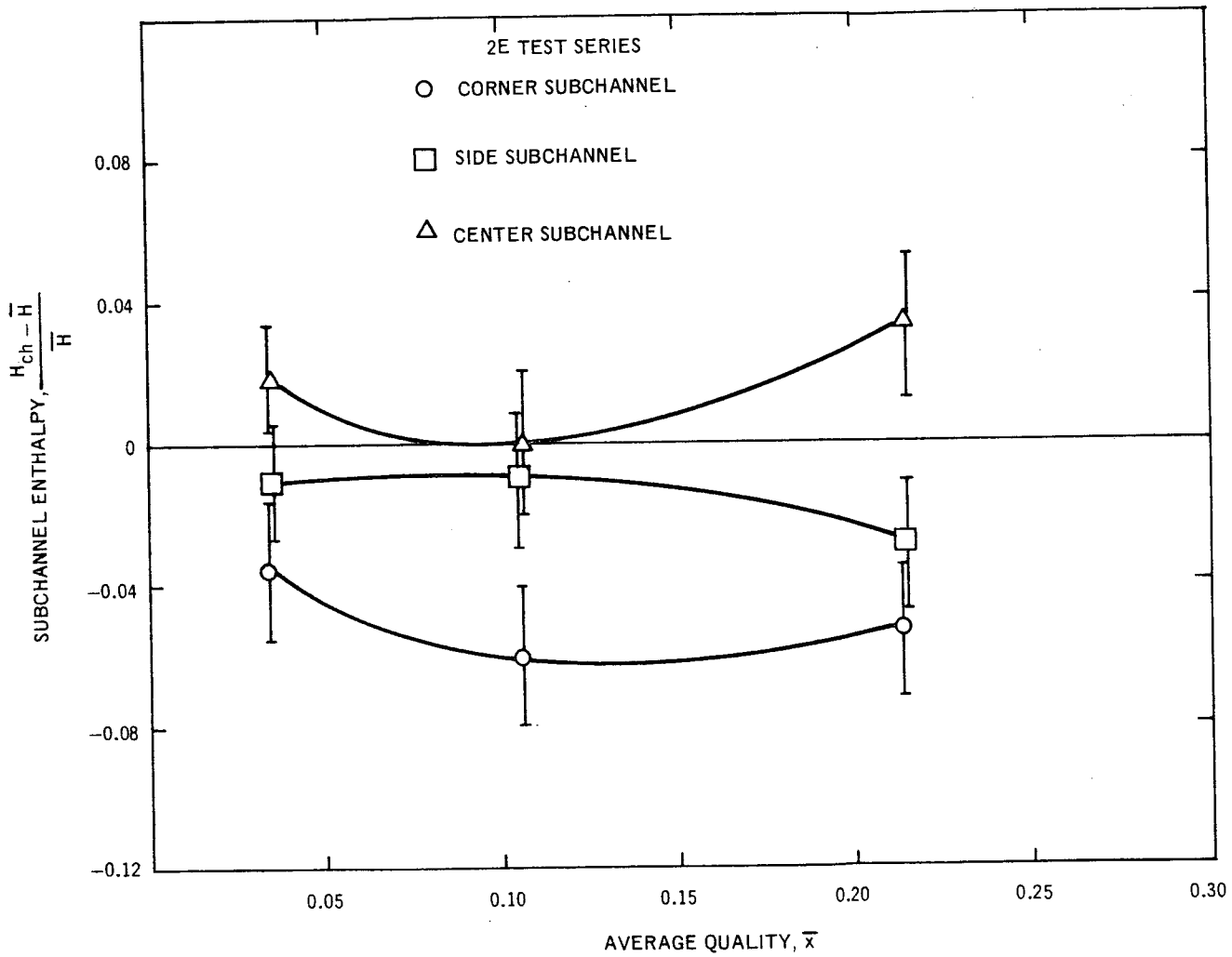

Figure 27. Comparison of Nondimensionalized Subchannel Enthalpies: 2E Test Series

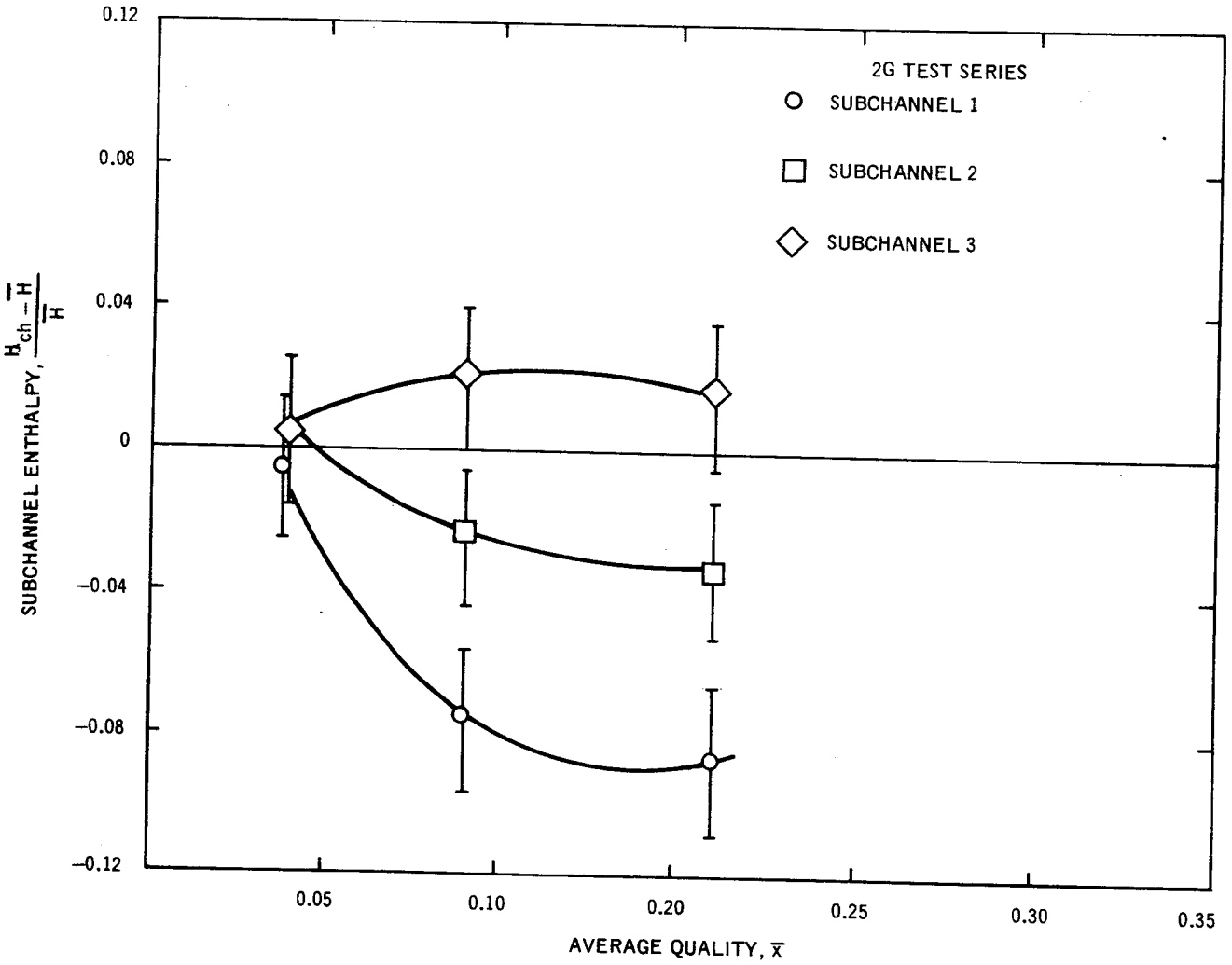

Figure 28. Comparison of Nondimensionalized Subchannel Enthalpies: 2G Test Series

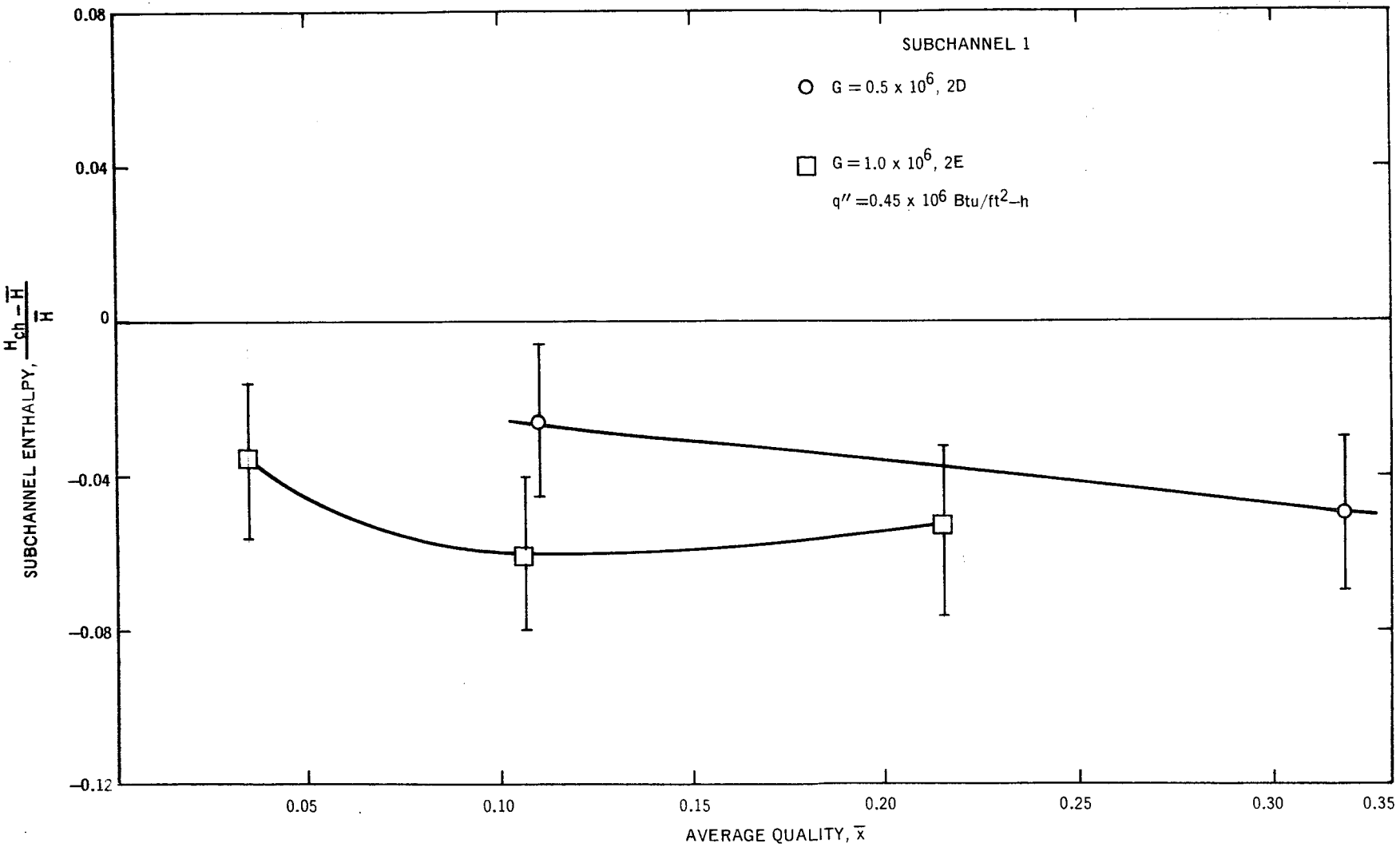

Figure 29. Effect of Average Mass Flux on Subchannel Enthalpy: Subchannel 1 at $q'' = 0.45 \times 10^6$ Btu/ft^2-h

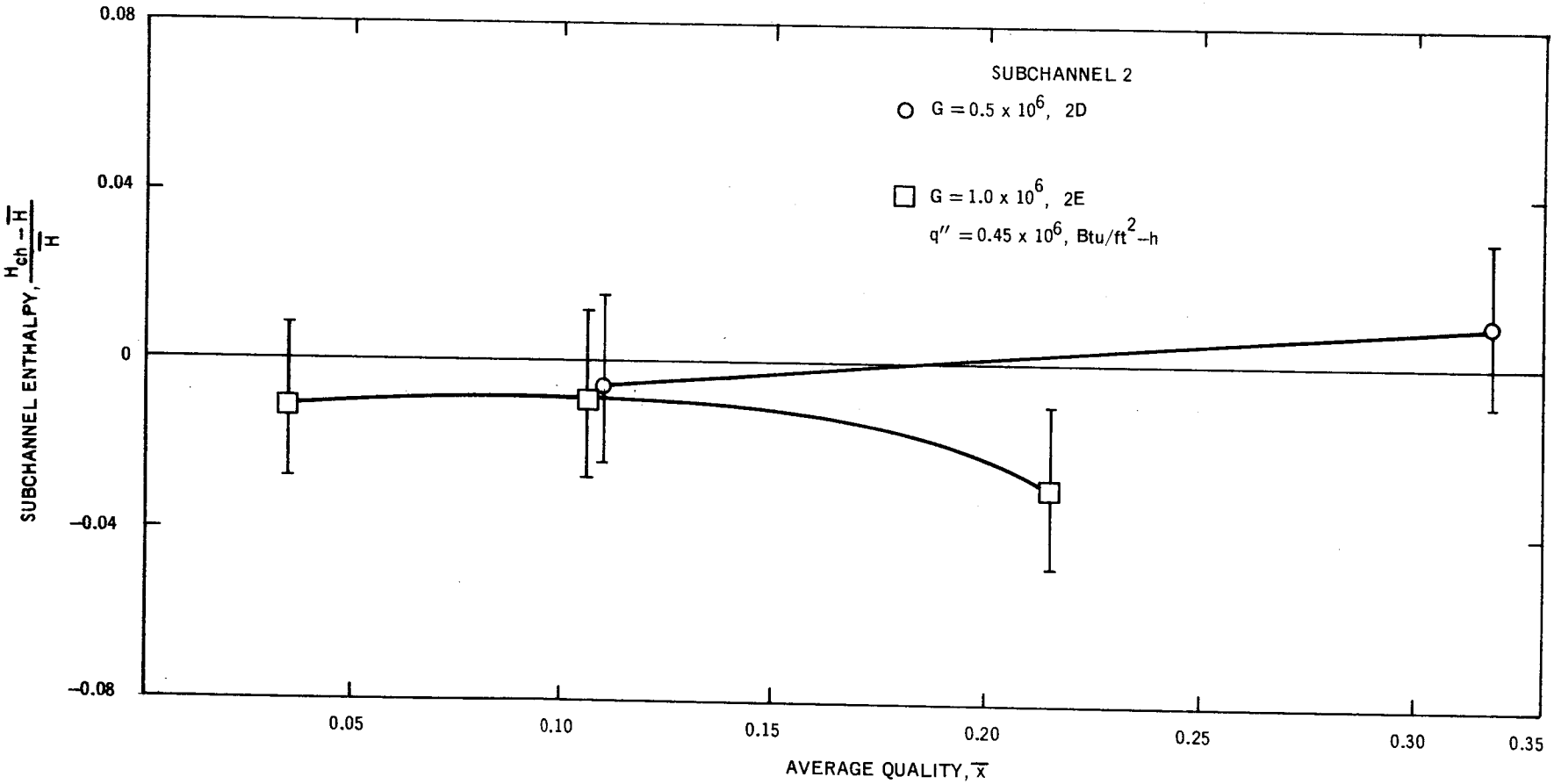

Figure 30. Effect of Average Mass Flux on Subchannel Enthalpy: Subchannel 2 at $q'' = 0.45 \times 10^6$ Btu/ft^2-h

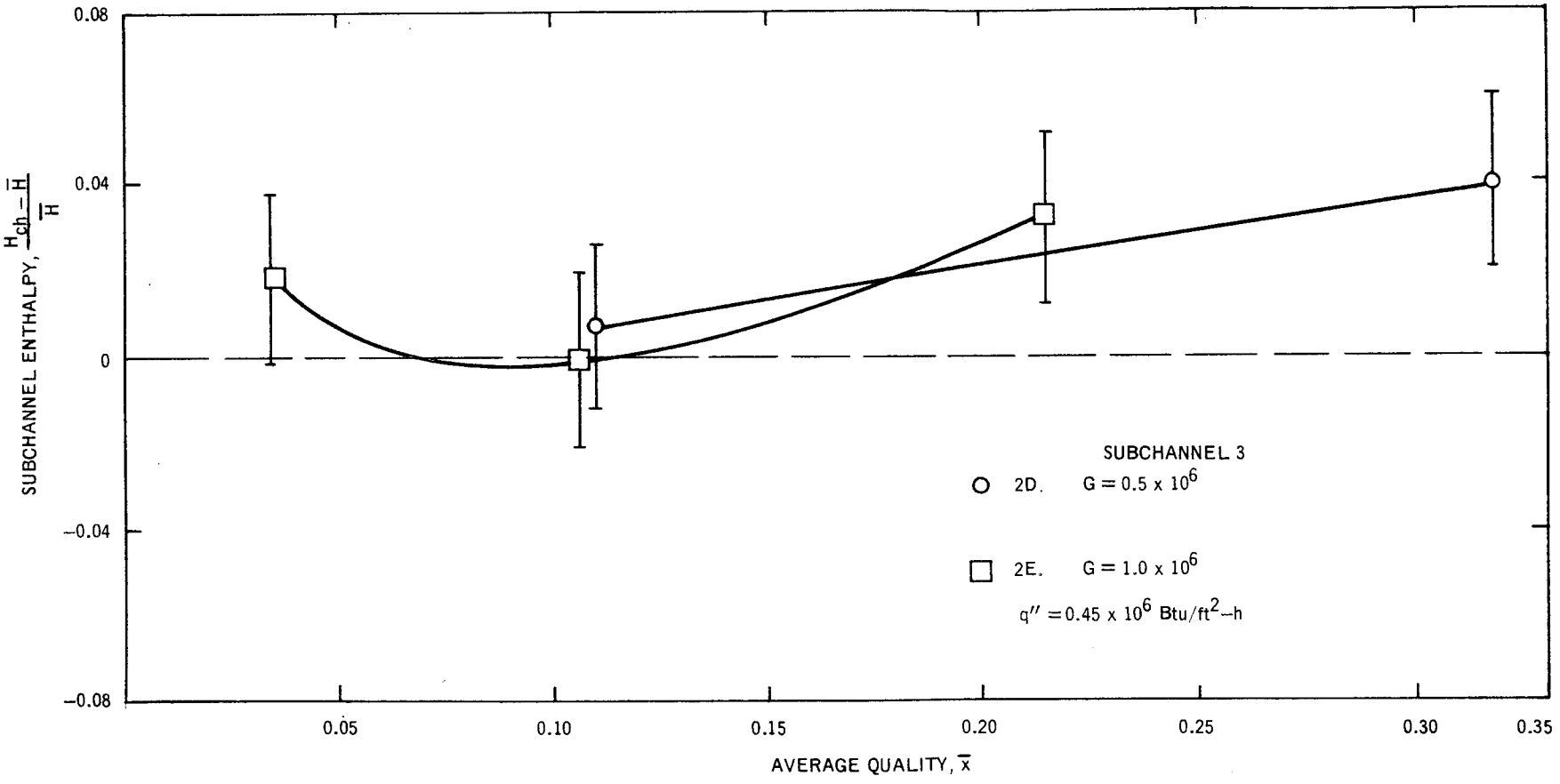

Figure 31. Effect of Average Mass Flux on Subchannel Enthalpy: Subchannel 3 at q″ = 0.45 × 10^6 Btu/ft^2-h

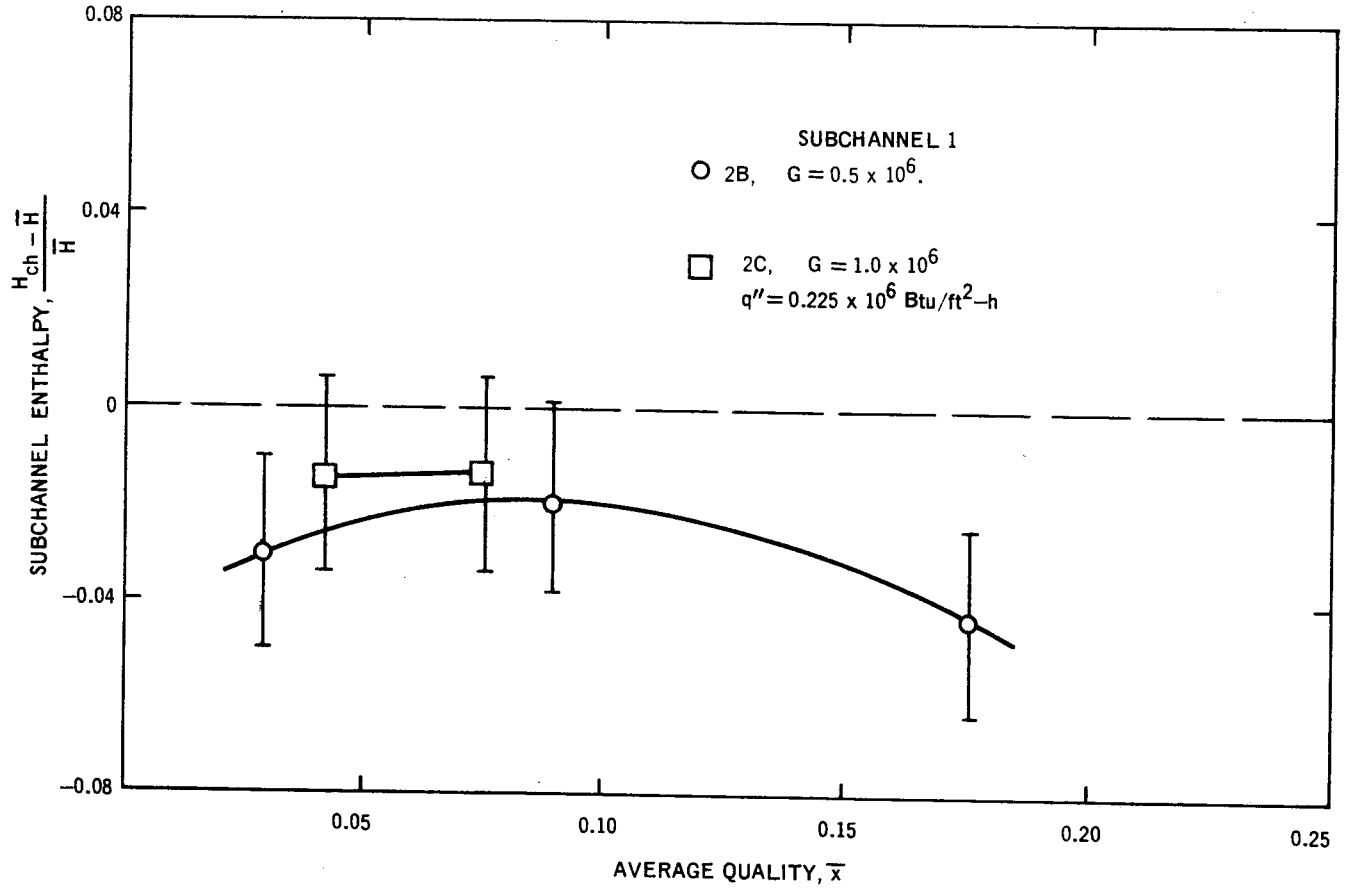

Figure 32. Effect of Average Mass Flux on Subchannel Enthalpy: Subchannel 1 at q'' = 0.225 X 10⁶ Btu/ft²-h

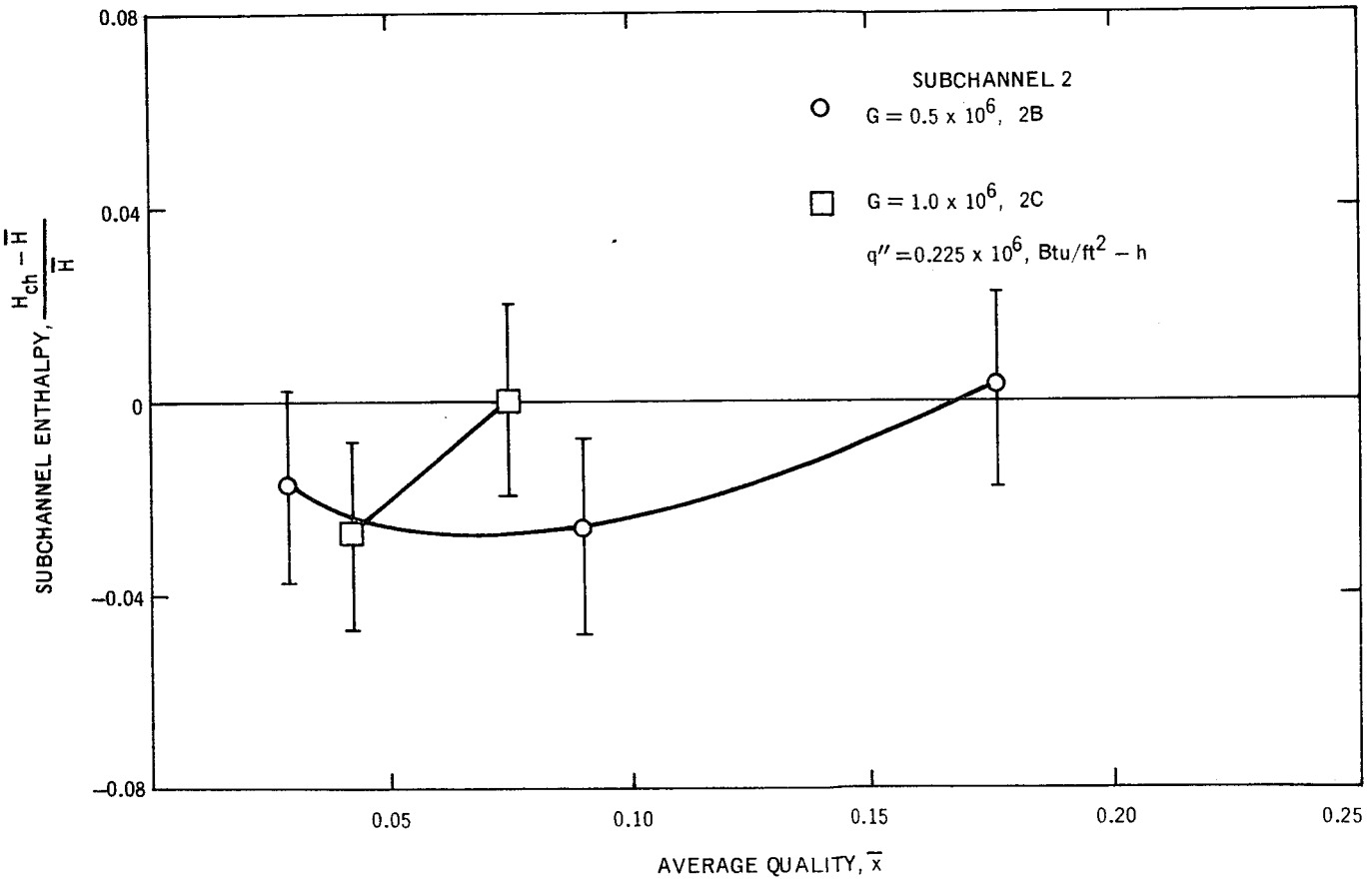

Figure 33. Effect of Average Mass Flux on Subchannel Enthalpy: Subchannel 2 at $q'' = 0.225 \times 10^6$ Btu/ft^2-h

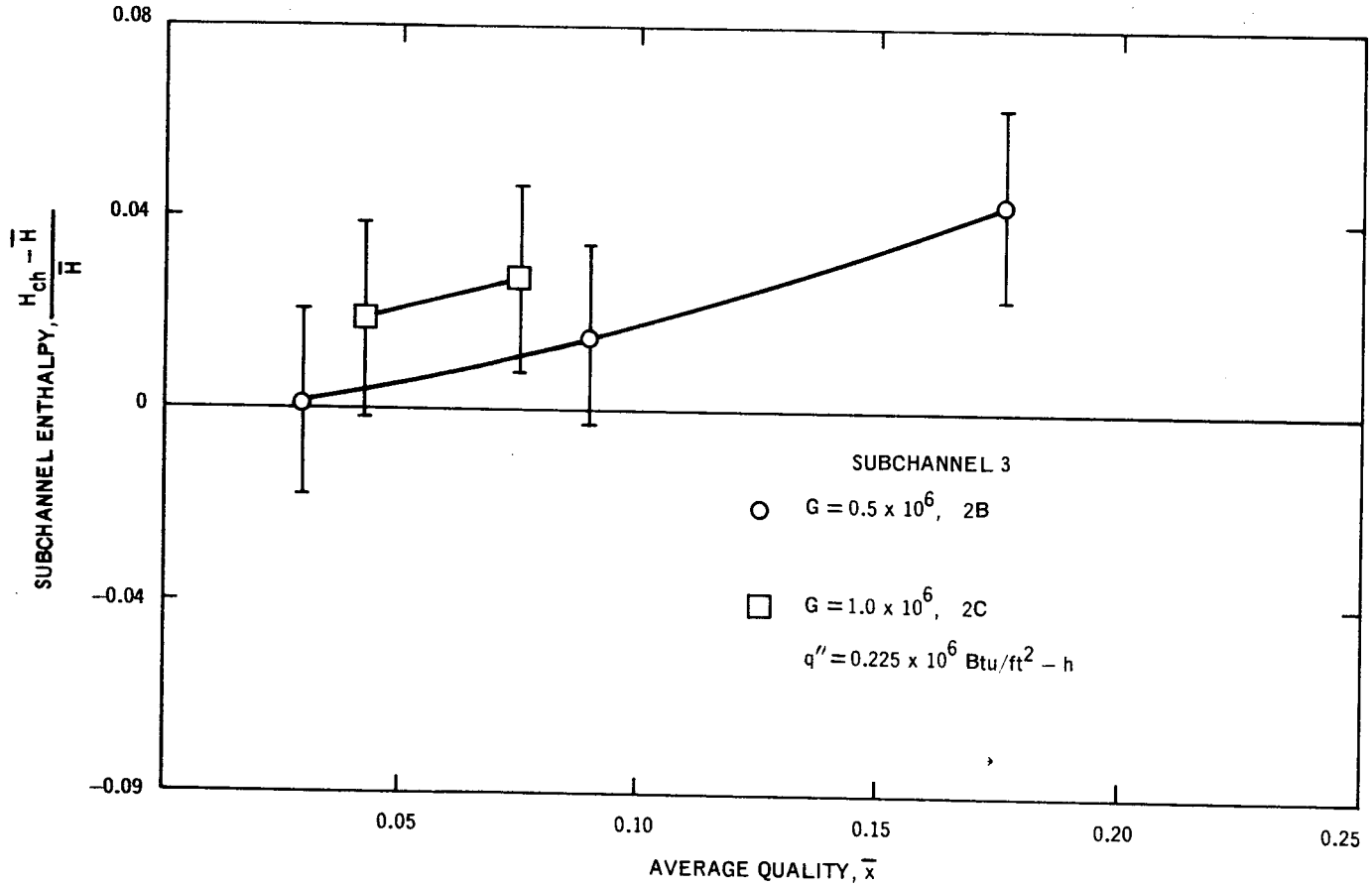

Figure 34. Effect of Average Mass Flux on Subchannel Enthalpy: Subchannel 3 at q″ = 0.225 × 10^6 Btu/ft^2-h

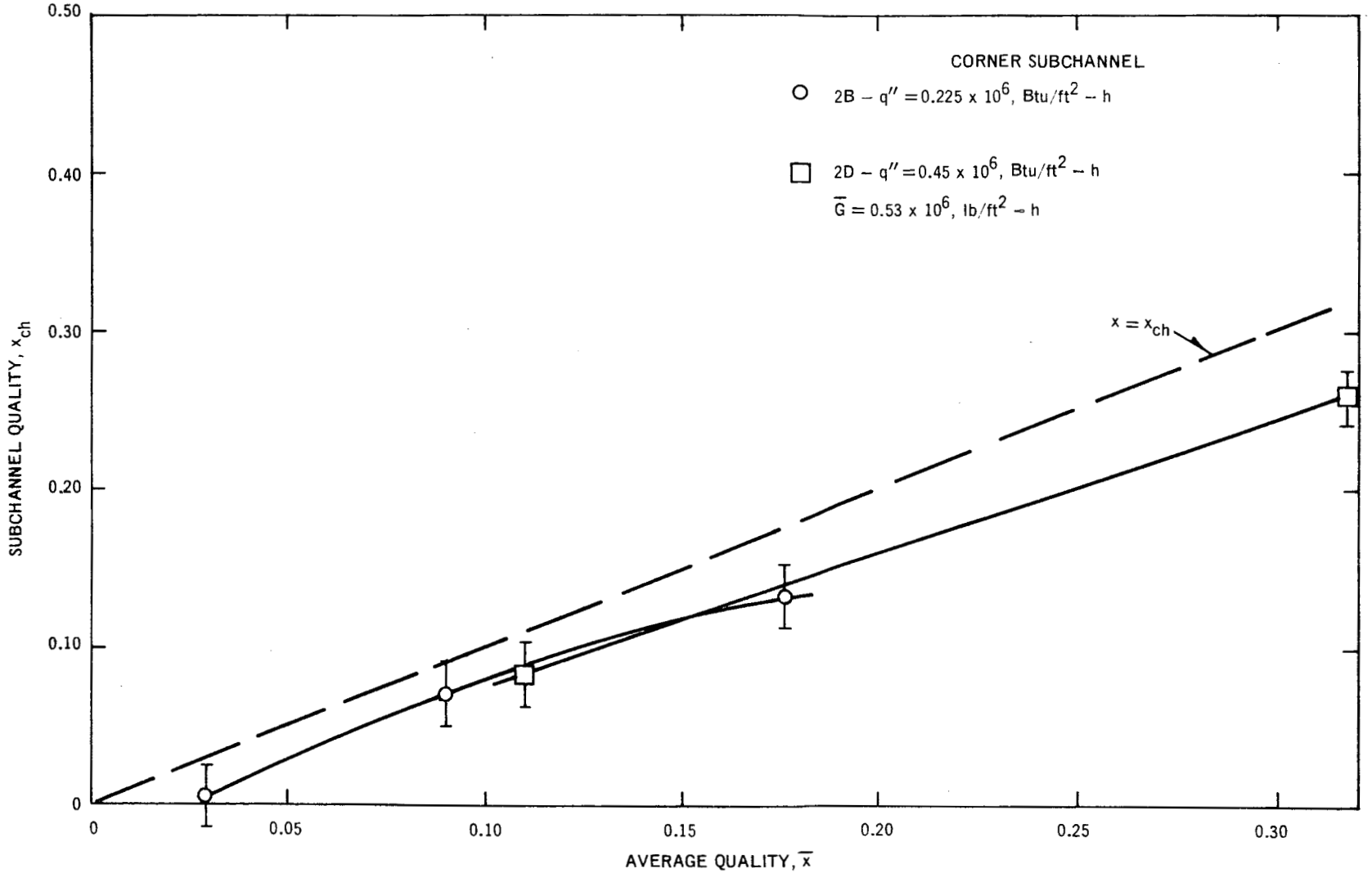

Figure 35. Effect of Heat Flux on Corner-Subchannel Quality: $\overline{G} = 0.5 \times 10^6$ lb/ft²-h

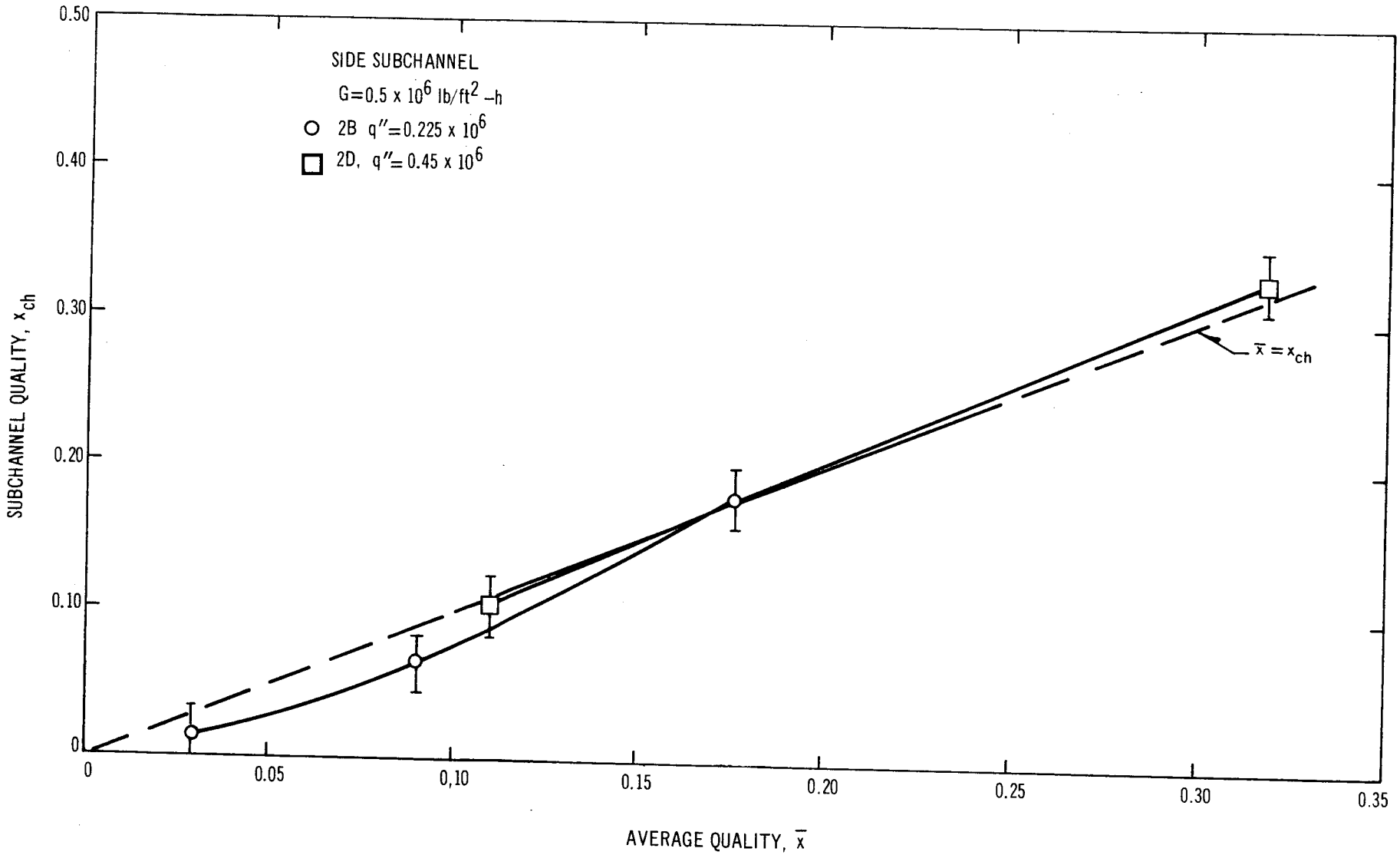

Figure 36. Effect of Heat Flux on Side-Subchannel Quality: $\bar{G} = 0.5 \times 10^6$ lb/ft^2-h

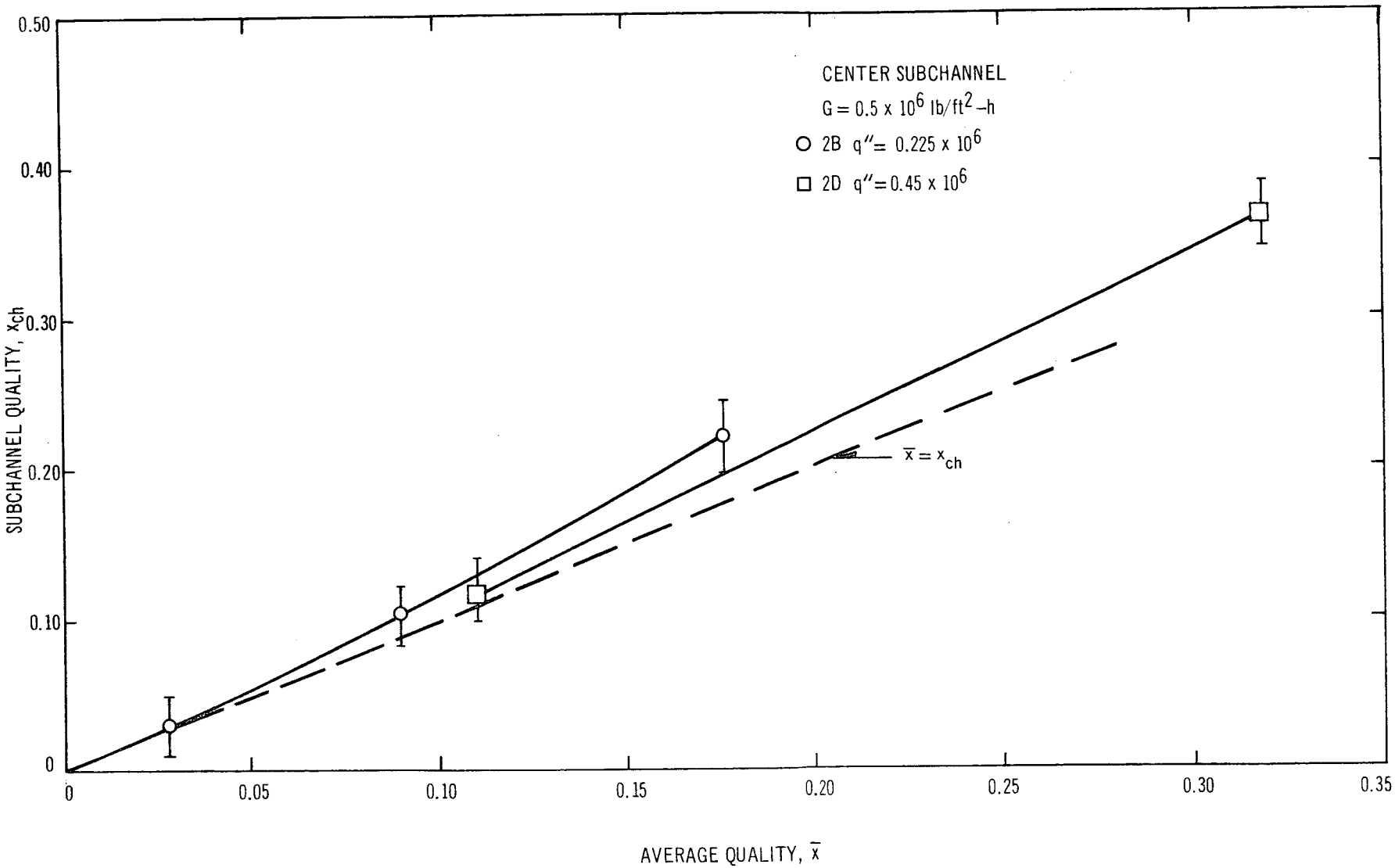

Figure 37. Effect of Heat Flux on Center-Subchannel Quality: $\bar{G} = 0.5 \times 10^6$ lb/ft^2-h

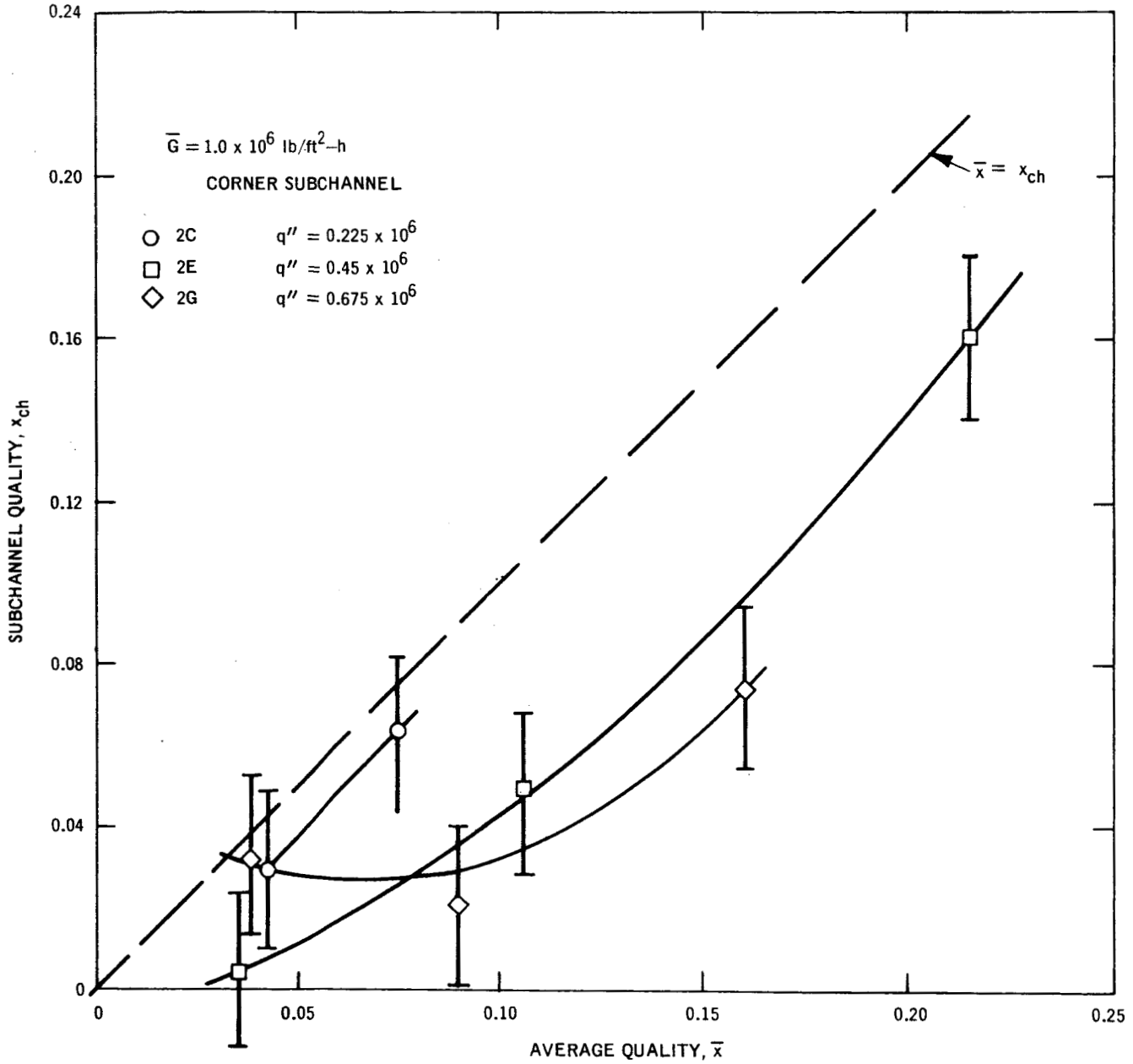

Figure 38. Effect of Heat Flux in Corner-Subchannel Quality: $\overline{G} = 1.0 \times 10^6$ lb/ft^2-h

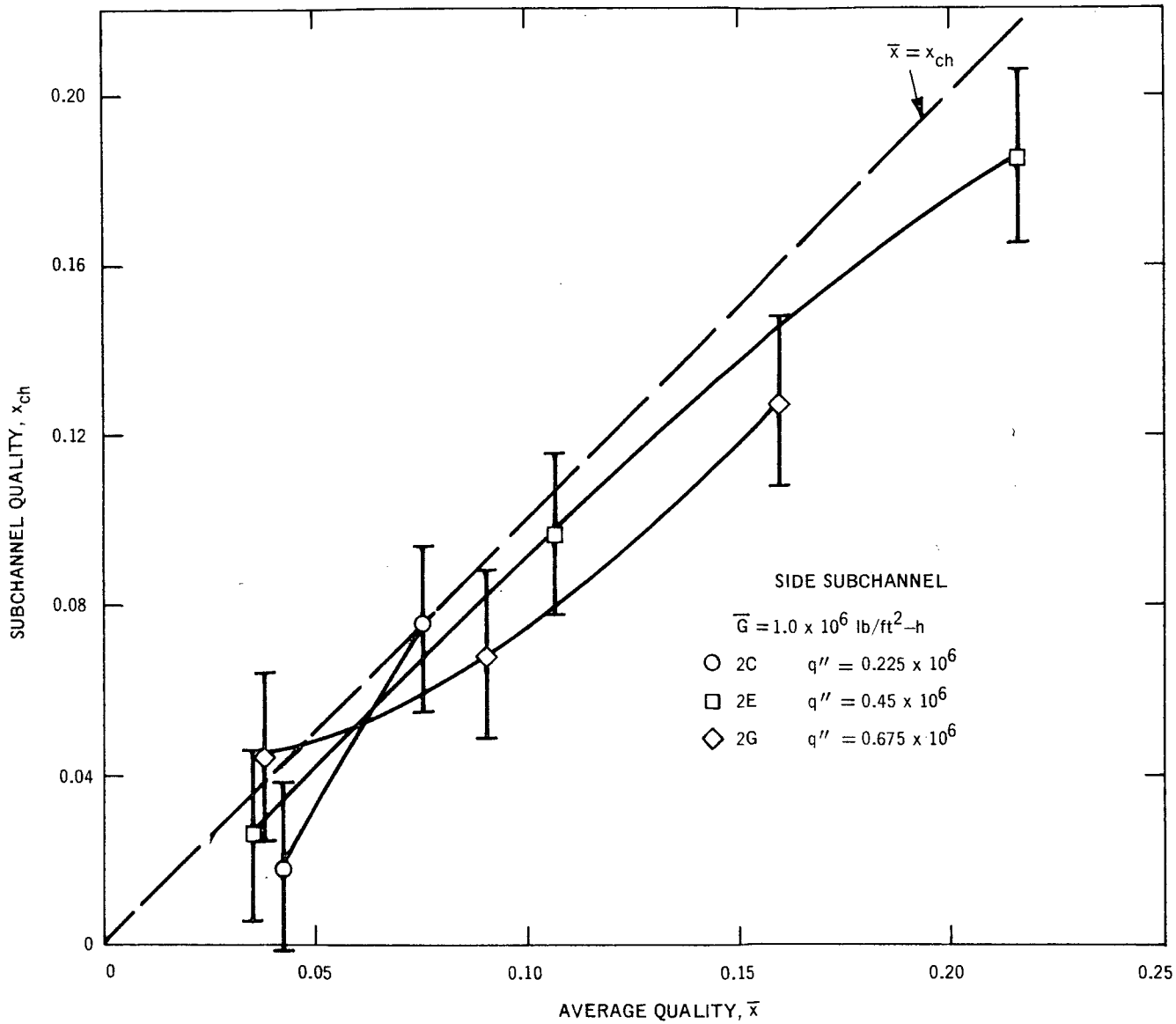

Figure 39. Effect of Heat Flux on Side-Subchannel Quality: $\overline{G} = 1.0 \times 10^6$ lb/ft^2-h

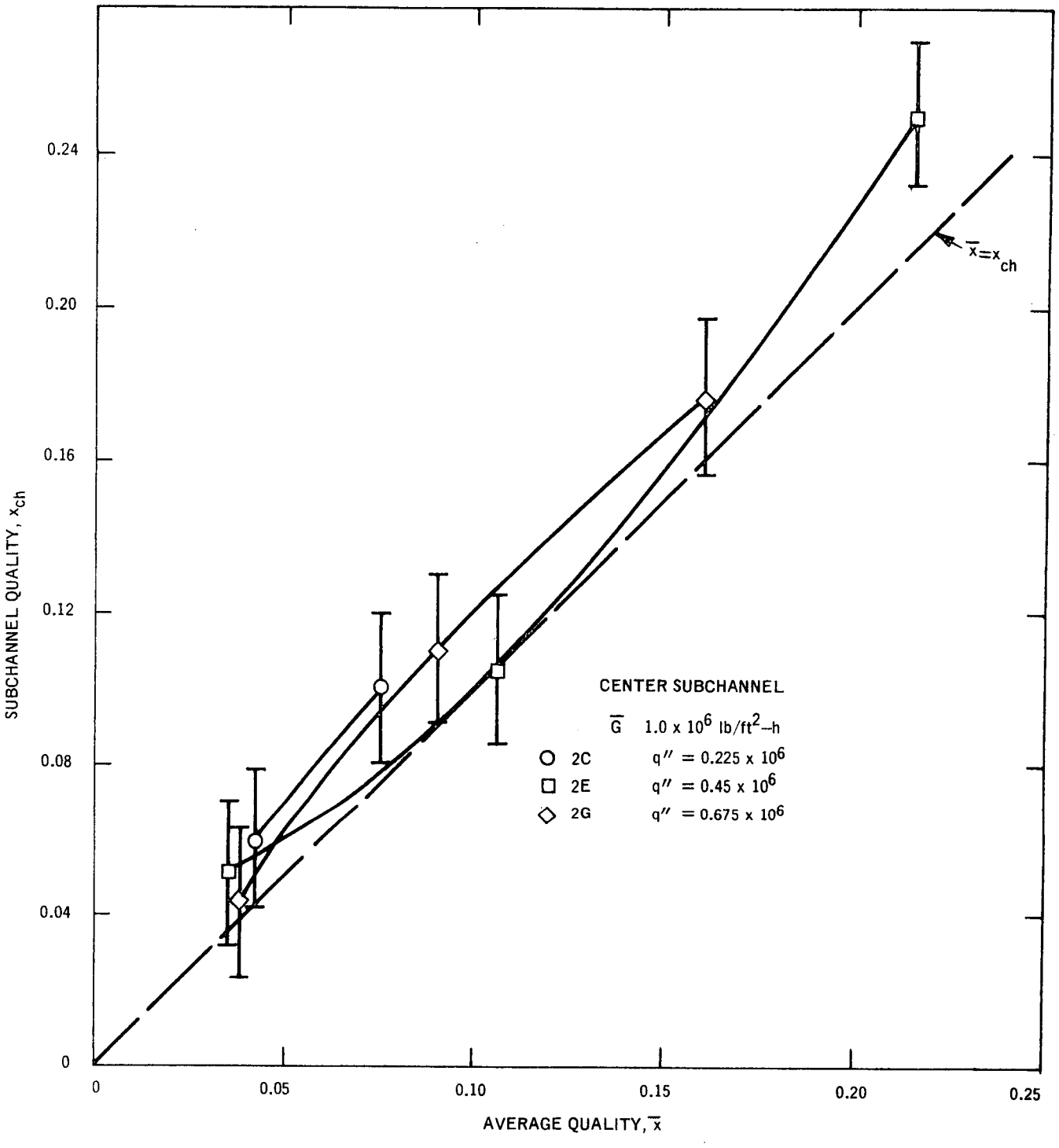

Figure 40. Effect of Heat Flux on Center-Subchannel Quality: $\bar{G}$ = 1.0 × 10^6 lb/ft^2-h

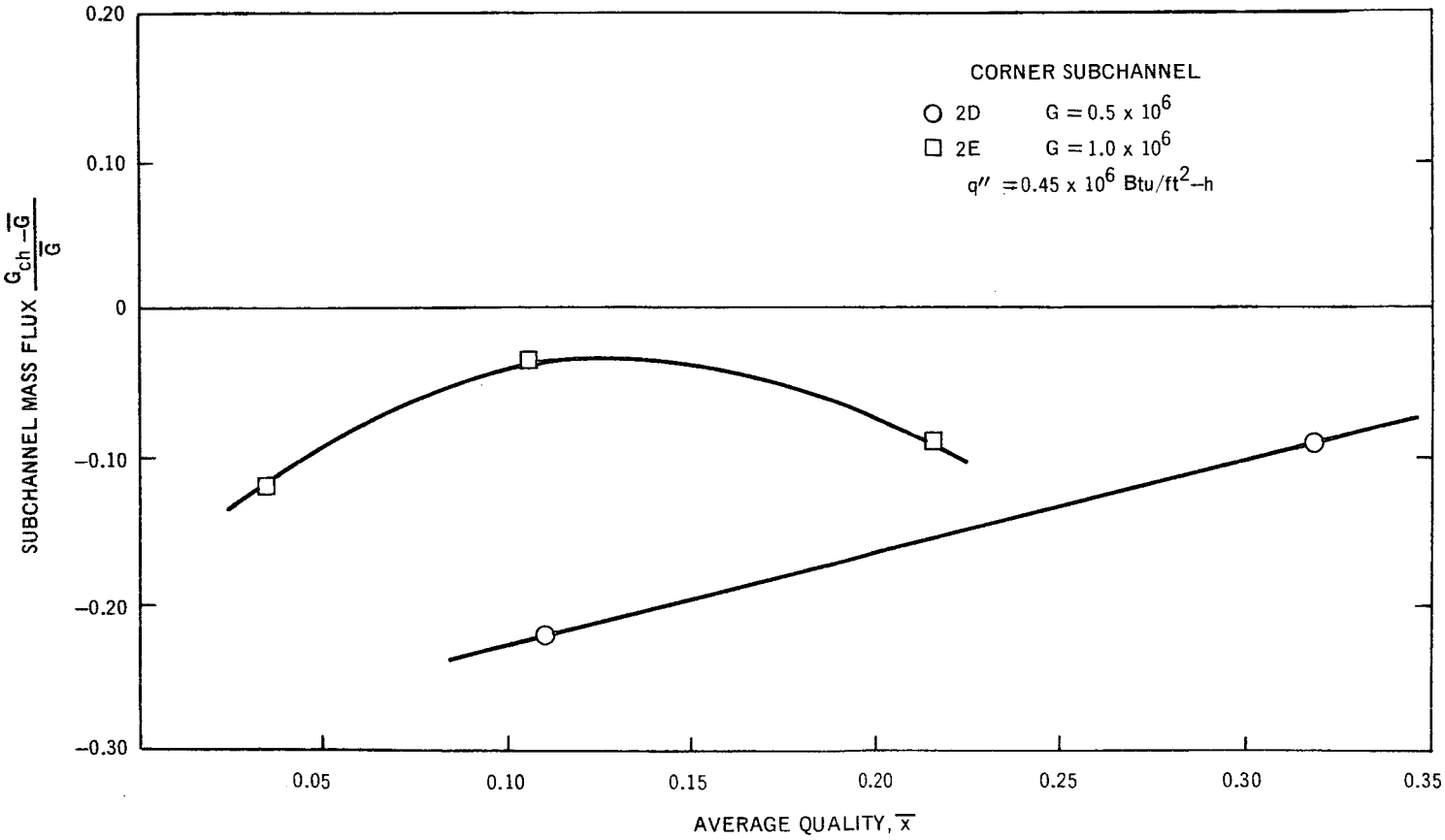

Figure 41. Effect of Average Mass Flux on Corner-Subchannel Mass Flux

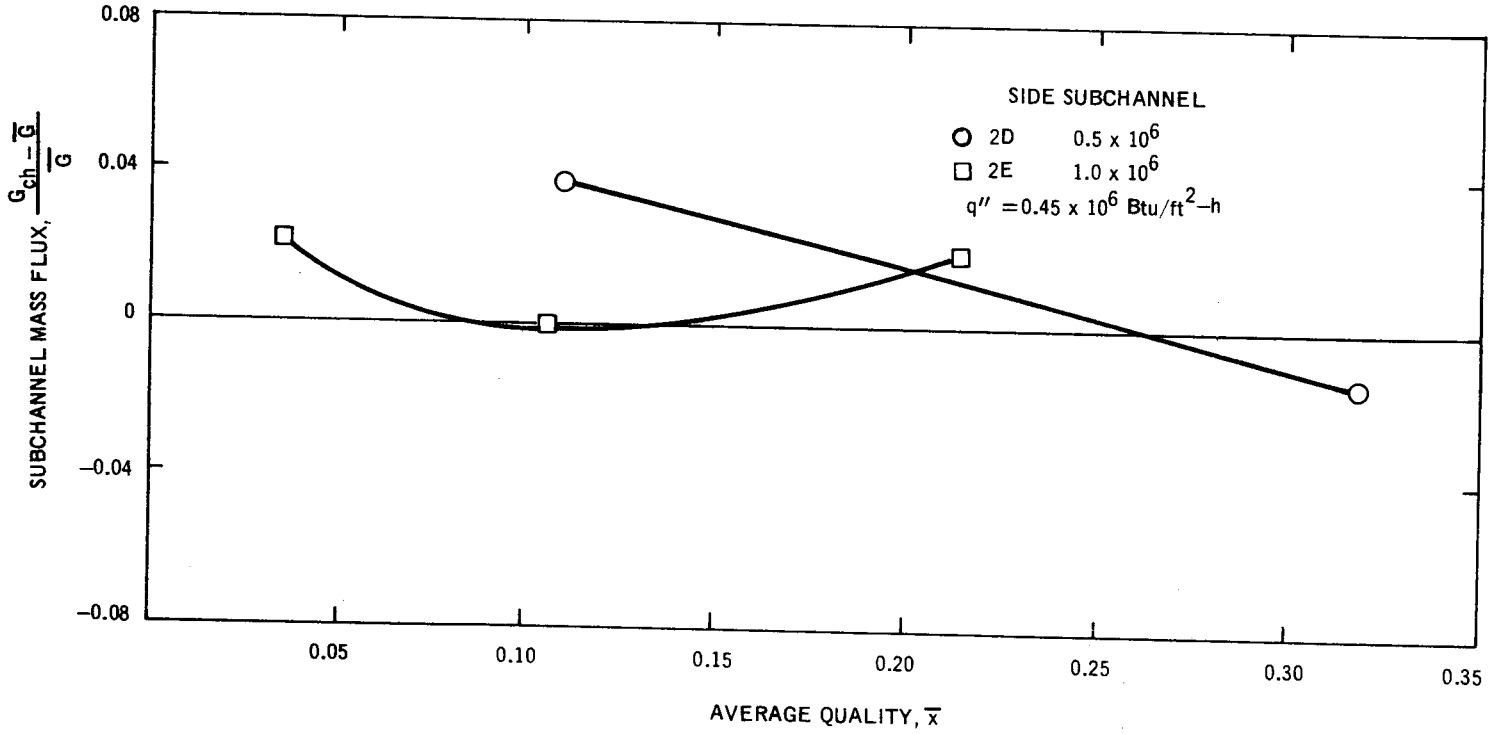

Figure 42. Effect of Average Mass Flux on Side-Subchannel Mass Flux

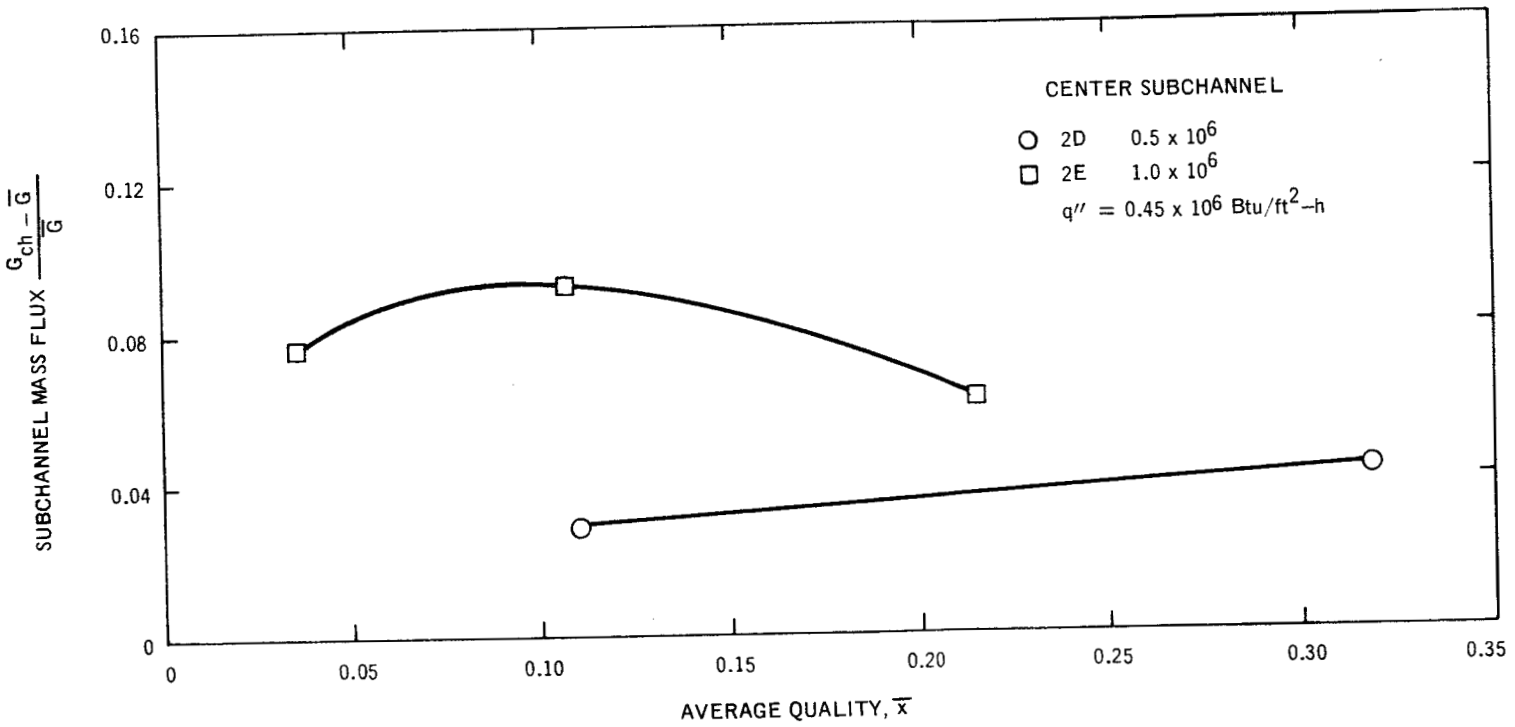

Figure 43. Effect of Average Mass Flux on Center-Subchannel Mass Flux

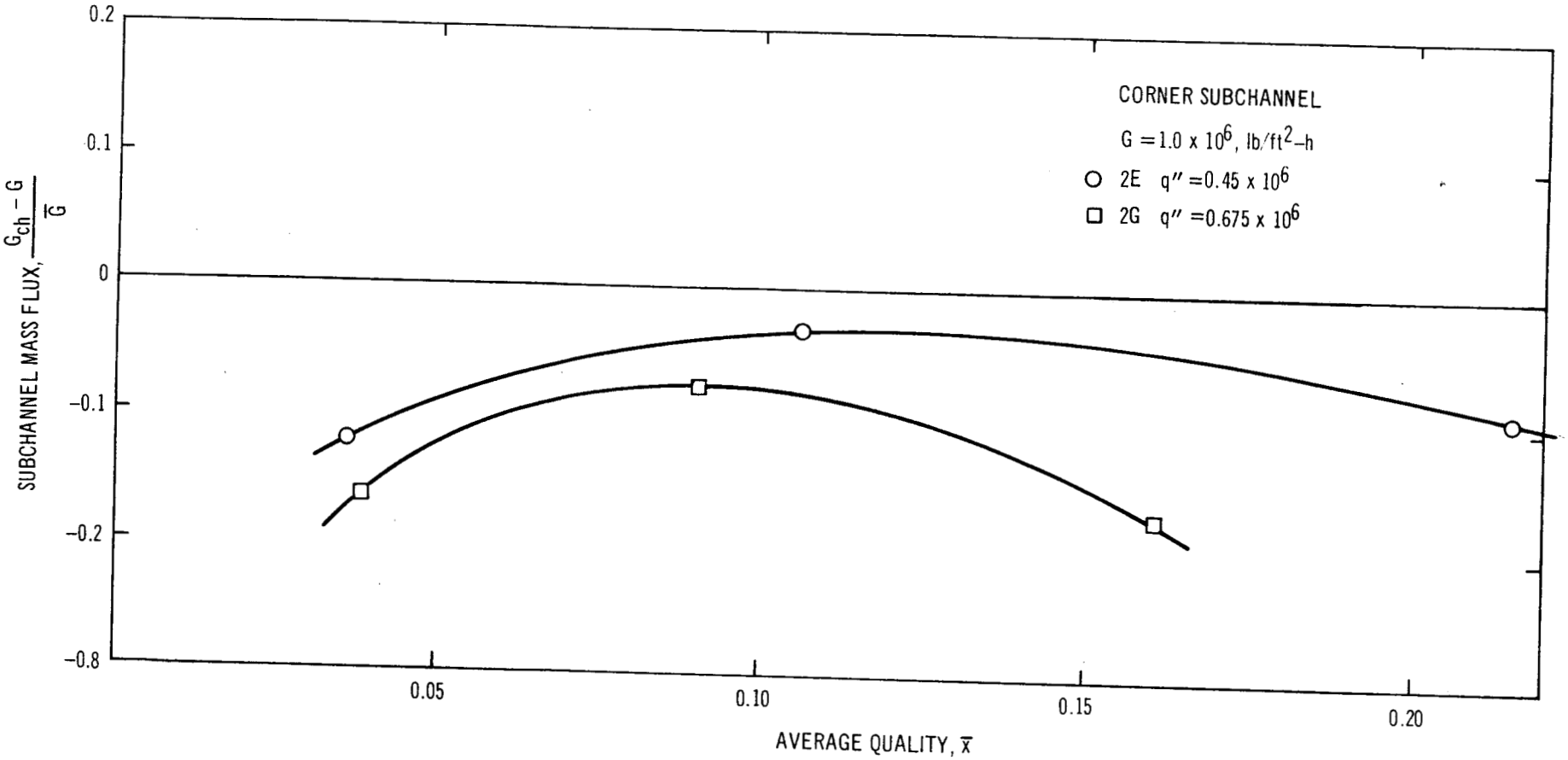

Figure 44. Effect of Heat Flux on Corner Subchannel Mass Flux

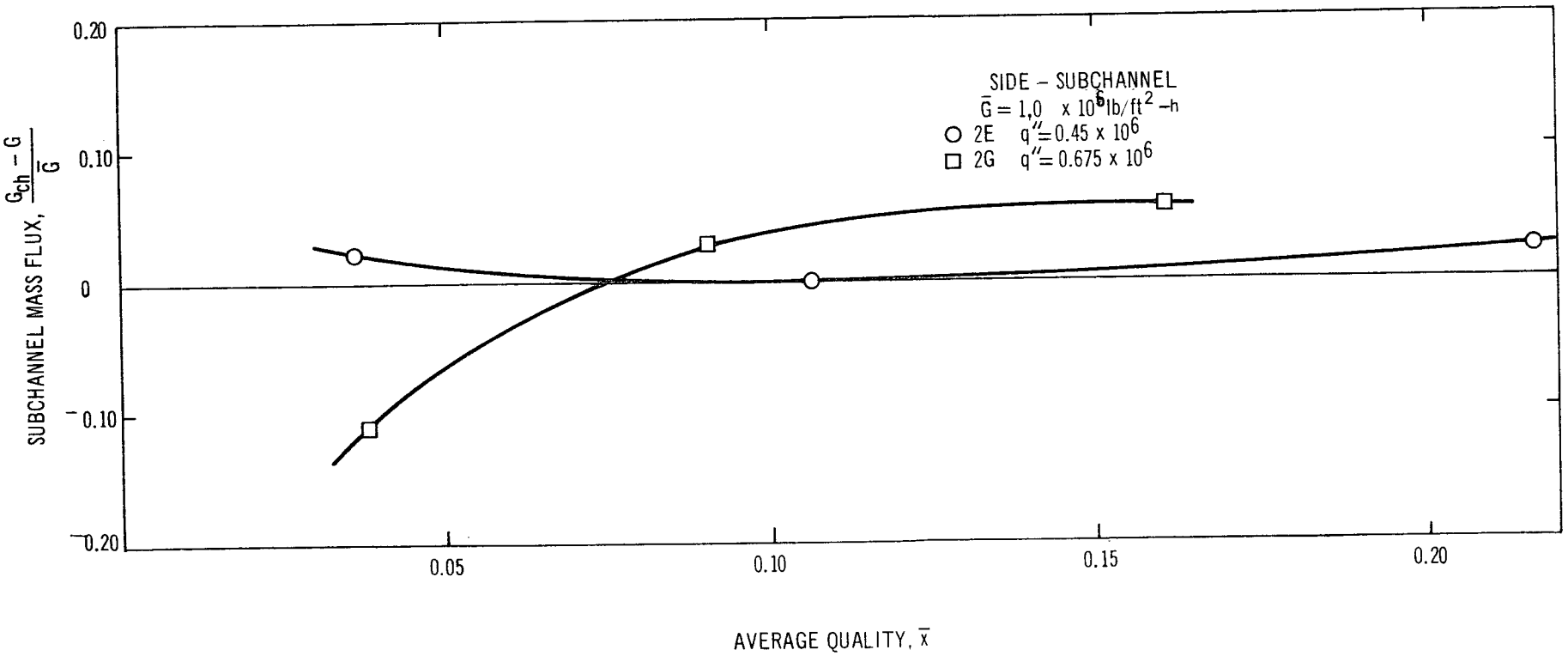

Figure 45. Effect of Heat Flux on Side-Subchannel Mass Flux

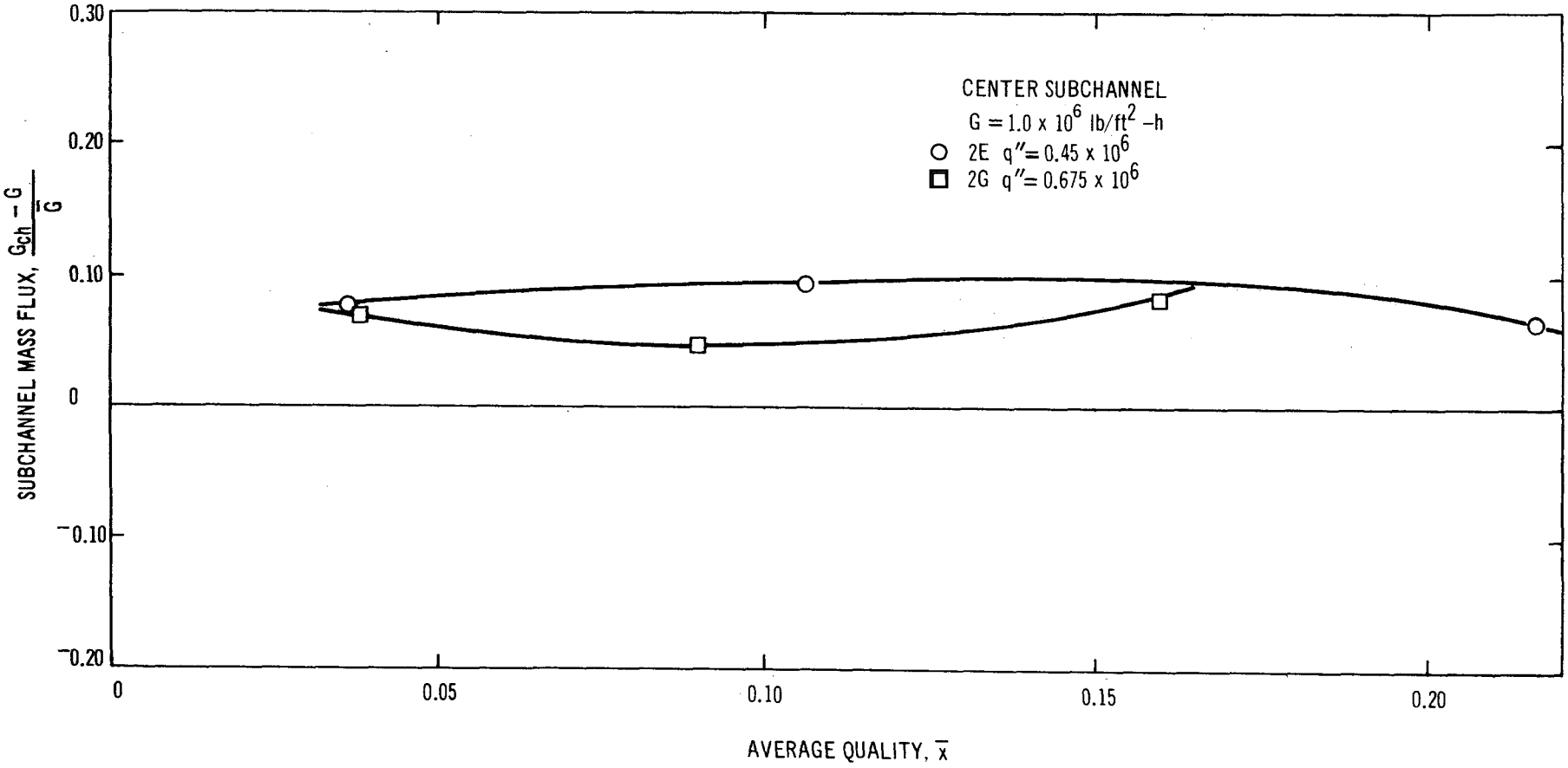

Figure 46. Effect of Heat Flux on Center-Subchannel Mass Flux

7. DISCUSSION OF NON-ISOKINETIC DATA

By taking non-isokinetic data (i.e., with a set pressure differential between the subchannel being sampled and the diametrically opposite subchannel), some deductions can be made about the flow diversion between subchannels and the enthalpy associated with this cross flow.

7.1 COLD RUNS

For the cold runs, the theoretical pressure differential versus the subchannel flow rate may be calculated, assuming that the pressure is constant across the cross section at a small distance upstream from the splitters. The pressure differential has components of acceleration and friction pressure drop. Under isokinetic conditions the pressure differential is almost zero, and there is very little redistribution of flow over a short length near the exit. For non-isokinetic conditions, there is a measurable change in the axial acceleration component of pressure drop due to a sizeable change in subchannel flow. Because of the change in flow rate there is also a change in the friction pressure drop over the axial length of flow diversion. This is expected to be small for small flow diversion lengths and small cross flow rates. The theoretical model used for these calculations is derived in Appendix A. Figure 47 shows the non-isokinetic data for the center subchannel for two mass fluxes, together with the theoretical acceleration pressure differential. For $\bar{G} = 1.0 \times 10^6$ lb/ft^2-h, the agreement with the data is good. At $\bar{G} = 2.0 \times 10^6$ lb/ft^2-h, the friction pressure-drop component, which has been neglected in the theoretical calculation, becomes appreciable, and so the theoretical model begins to deviate from the data. Bowring[3] analyzed his freon data in a similar way and came to the conclusion that the flow diversion occurs over a small length (about 1.8 inches), which independently supports our assumption of a small diversion length.

7.2 TWO PHASE RUNS

A similar procedure may be worked out for two-phase exit conditions, but it is sensitive to the accuracy of the measured exit conditions. Figure 48 shows some representative comparisons between the calculated values (using the Model in Appendix A) and experimented values for the center subchannel. It can be seen that the agreement is quite good for both values of mass flux considered.

7.3 CROSS-FLOW ENTHALPY

Assuming that the flow diversion length $d\ell$ is small and neglecting the flow diversion in this increment for the isokinetic case, the following energy balance equations may be formulated for the last node.

For the isokinetic case,

$$\left(w_{ch\ iso}\ H_{ch\ iso}\right)_{out} = \left(w_{ch\ iso}\ H_{ch\ iso}\right)_{in} + q''\ P_h d\ell$$

For the non-isokinetic case,

$$\left[\left(w_{ch\ iso} + dw\right)\quad\left(H_{ch\ iso} + dH\right)\right]_{out} = \left(w_{ch\ iso}\ H_{ch\ iso}\right)_{in} + dw\ H_x + q''\ P_h d\ell$$

Subtracting the isokinetic energy balance from the non-isokinetic one gives,

$$\left(w_{ch\ iso} + dw\right)\left(H_{ch\ iso} + dH\right)_{out} - \left(w_{ch\ iso}\ H_{ch\ iso}\right)_{out} = dw\ H_x$$

or, neglecting second order differentials,

$$d\left(w\ H_{ch}\right)_{iso} = dw\ H_x$$

where w_{iso} and H_{iso} are the flow rate and enthalpy for the subchannel under isokinetic condition, H_x is the crossflow enthalpy, and dw is the flow diversion.

Therefore, H_x is given by,

$$H_x = \left.\frac{d\left(w_{ch}\ H_x\right)}{dw_{ch}}\right|_{iso} = \left.\frac{d\left(G_{ch}\ H_{ch}\right)}{d\ G_{ch}}\right|_{iso}$$

This slope was measured from plots of $G_{ch}\ H_{ch}$ versus G_{ch} as shown in Figures 49 and 50 for the corner subchannel. Strictly speaking these plots are only applicable to the determination of cross flow enthalpy from the corner subchannel (i.e., when the flow is less then isokinetic). However, the figure shows that the plots are continuous lines above and below the isokinetic condition. Table 6

Table 6
CROSSFLOW ENTHALPY FOR A CORNER SUBCHANNEL

Test Point	Subchannel Mass Flux (lb/ft^2-h) $G_{ch} \times 10^{-6}$	Subchannel Quality, x_{ch}	Crossflow Enthalpy, (Btu/lb) H_x	Crossflow Quality, x_x	Flow Regime
2B3	0.550	0.072	680	0.212	Bubbly
2B4	0.524	0.133	675	0.205	Bubbly
2C1	0.925	0.042	680	0.212	Bubbly
2D1	0.425	0.083	685	0.217	Bubbly
2D3	0.490	0.260	752	0.323	Annular
2E1	0.950	0.004	565	0.037	Bubbly
2E2	1.046	0.049	615	0.112	Bubbly
2E3	0.965	0.170	660	0.182	Annular
2F1	1.51	0.120	618	0.117	Transition
2F2	1.58	0.161	645	0.158	Annular
2G1	0.926	0.067	705	0.250	Bubbly
2G2	1.00	0.020	605	0.097	Bubbly
2G3	0.870	0.077	670	0.197	Bubbly
2H1	1.75	0.023	620	0.117	Bubbly

shows the results for some of the test conditions for the corner subchannel. These results have been plotted against the average channel quality in Figure 51. The plot shows that the crossflow enthalpy is generally higher than the average enthalpy of the donor subchannel. If the data are grouped by flow regime as determined by the Steen-Wallis[4] criterion $j_g^* = 0.4 + 0.6 j_f^*$, it is found that there is a drop in the cross-flow enthalpy near the slug-annular transition, probably due to the liquid slugs in this regime. Above this region the cross flow enthalpy increases monotonically, and remains well above the average subchannel enthalpy. In the bubbly- and annular-flow regimes, the crossflow enthalpy can be correlated by two straight lines. The heat-balance errors associated with these values of crossflow enthalpy are considerably less than those associated with the subchannel enthalpies, since the crossflow enthalpies are determined from differences in readings (readings taken within a few minutes of each other) which have the same heat balance error. Unfortunately, as shown in Appendix D the possible error associated with reading the slope of curves, such as in Figure 50, is about ± 35 Btu/lb, which makes the crossflow-quality error about ±5 %. In a similar manner, the crossflow enthalpy from the center subchannel was also calculated. Figures 52 and 53 show representative $G_{ch}H_{ch}$ versus G_{ch} plots at average mass fluxes of 1.0×10^6 lb/ft^2-h and 0.5×10^6 lb/ft^2-h, respectively. The results are given in Table 7, and plots versus the subchannel quality are shown in Figure 54. Again the data fall into two groups, representative of the different flow regimes. The crossflow enthalpy is generally greater than the subchannel enthalpy, though near the slug-annular transition it is below the average value.

Unfortunately not enough non-isokinetic data was taken on the side subchannel to prepare plots of crossflow enthalpy. However, it would be expected to agree with the trends of the other subchannels. In summary, it appears that the cross flow enthalpy is strongly dependent upon flow regime and is, in general, higher than the average enthalpy of the donor subchannel.

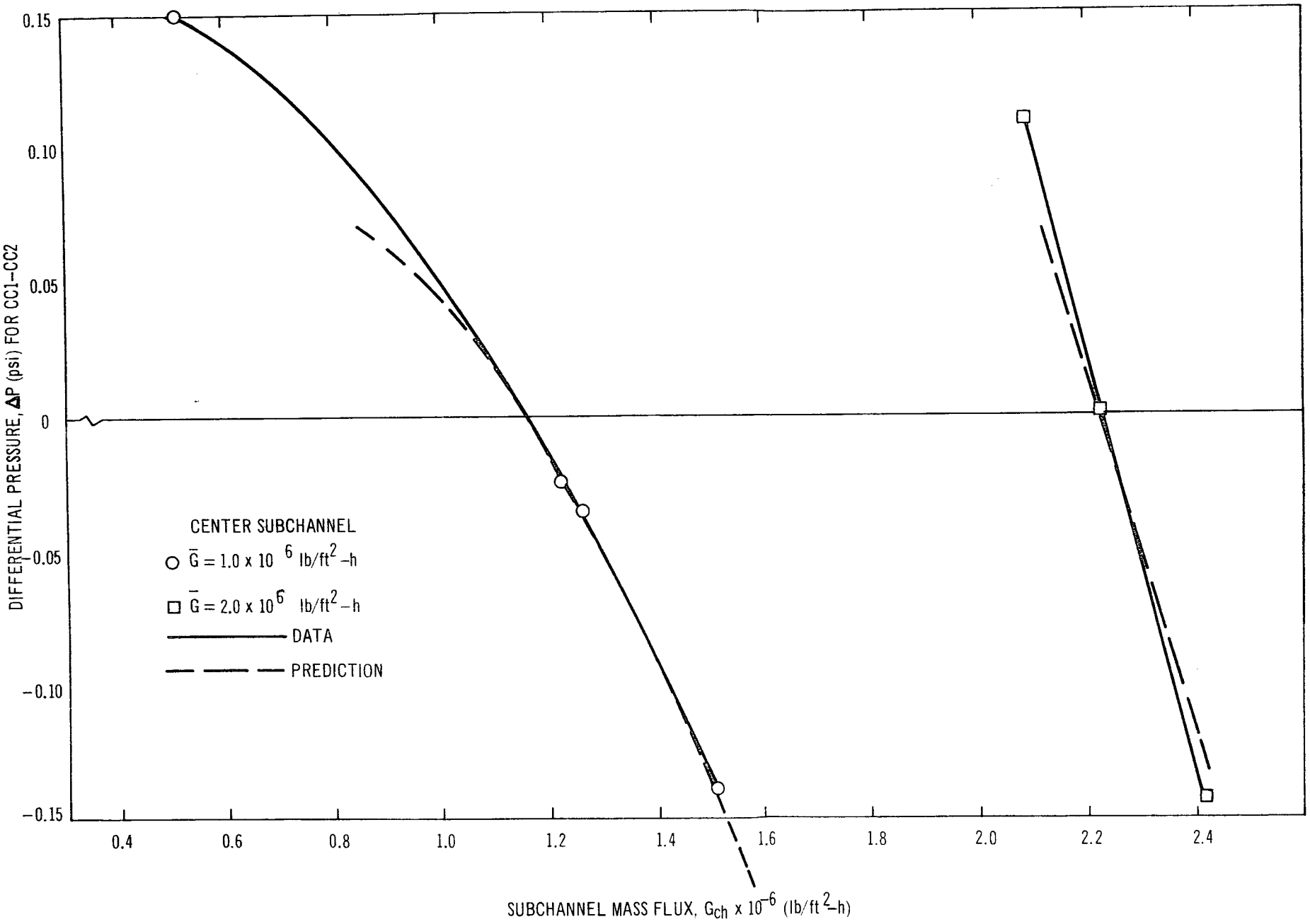

Figure 47. Non-Isokinetic Cold Data and Predictions for a Center-Subchannel

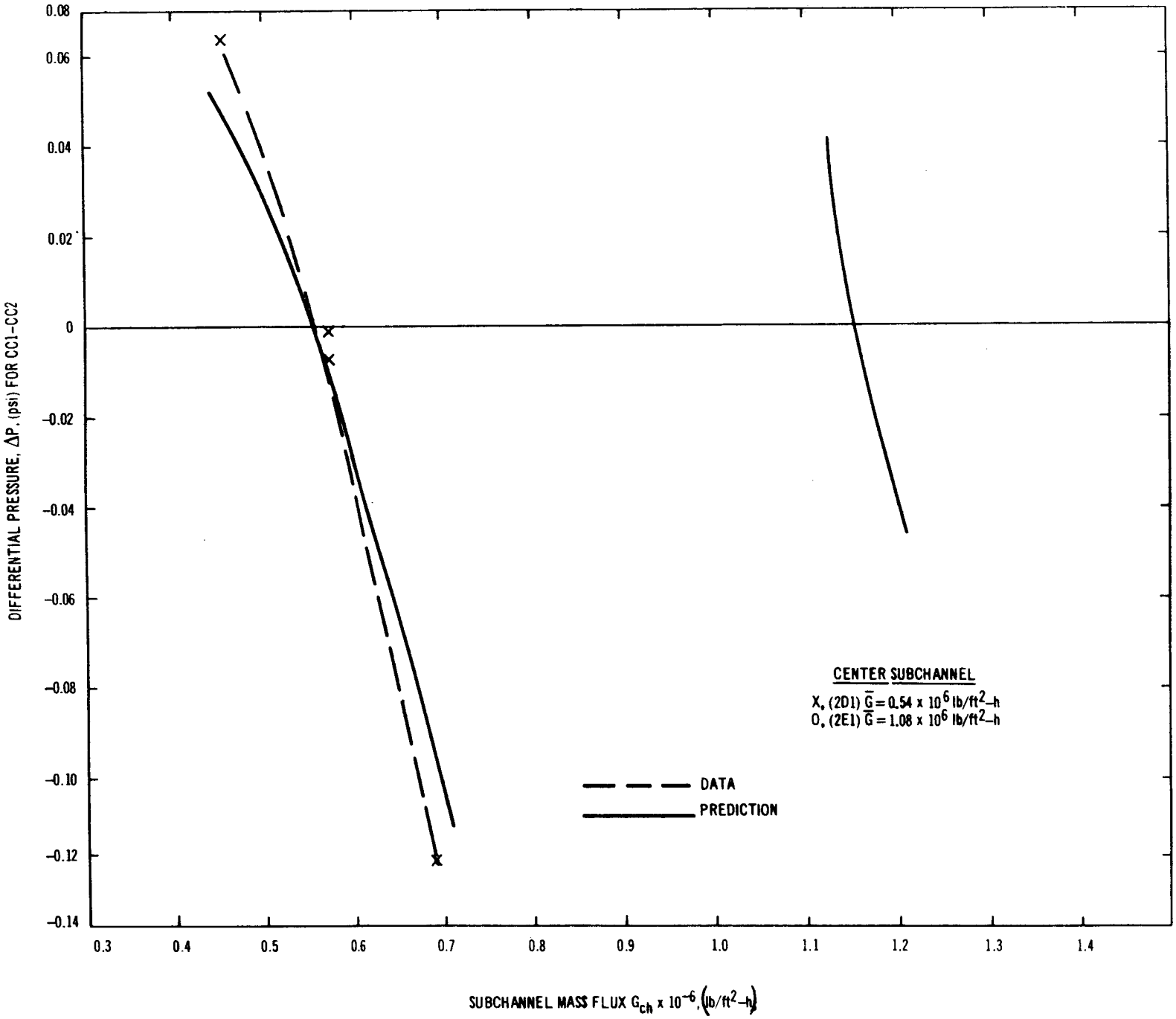

Figure 48. Non-Isokinetic Two-Phase Predictions for a Center Subchannel

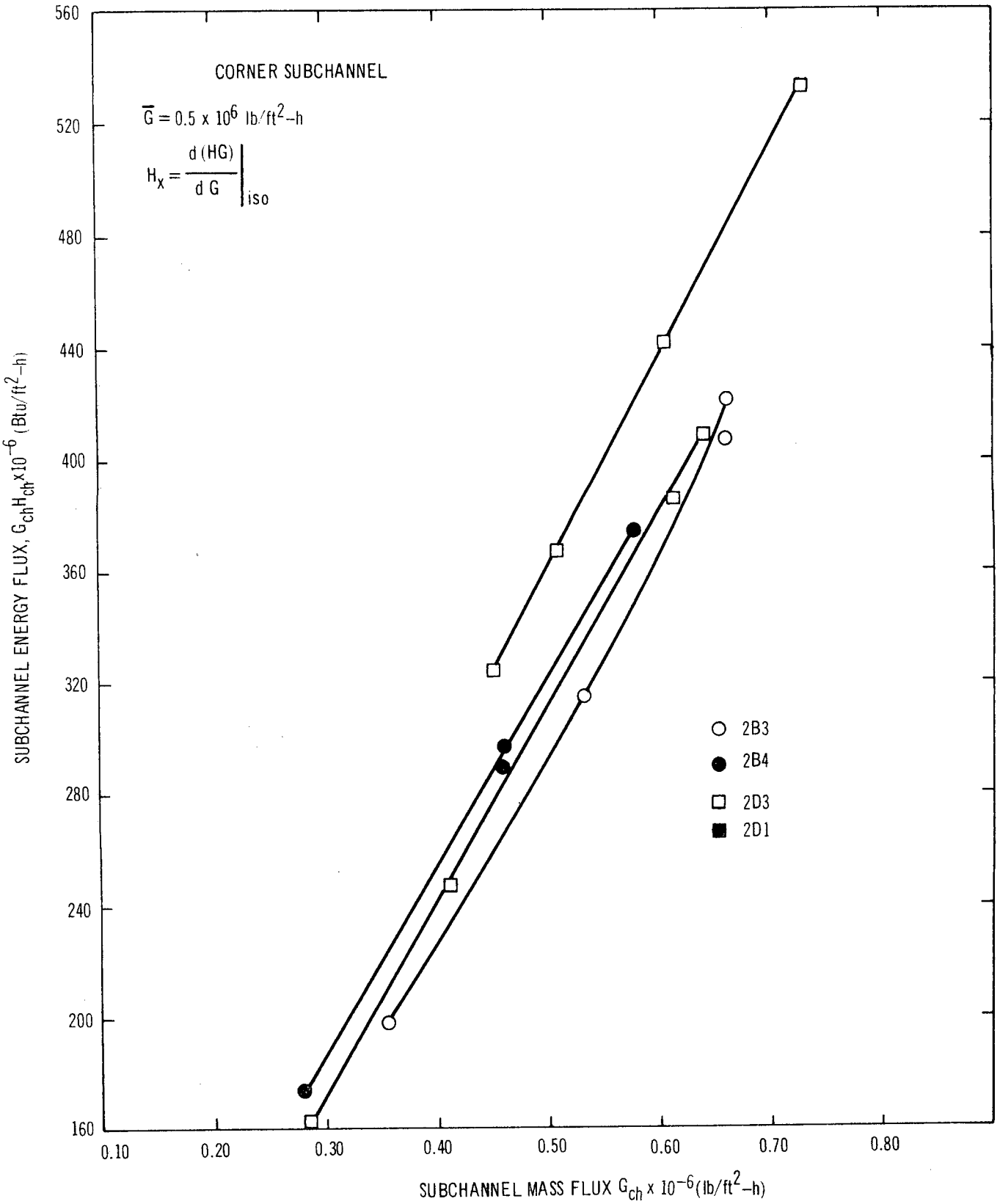

Figure 49. Crossflow Enthalpy Determination for Corner Subchannels: $\overline{G} = 0.5 \times 10^6$ lb/ft^2-h

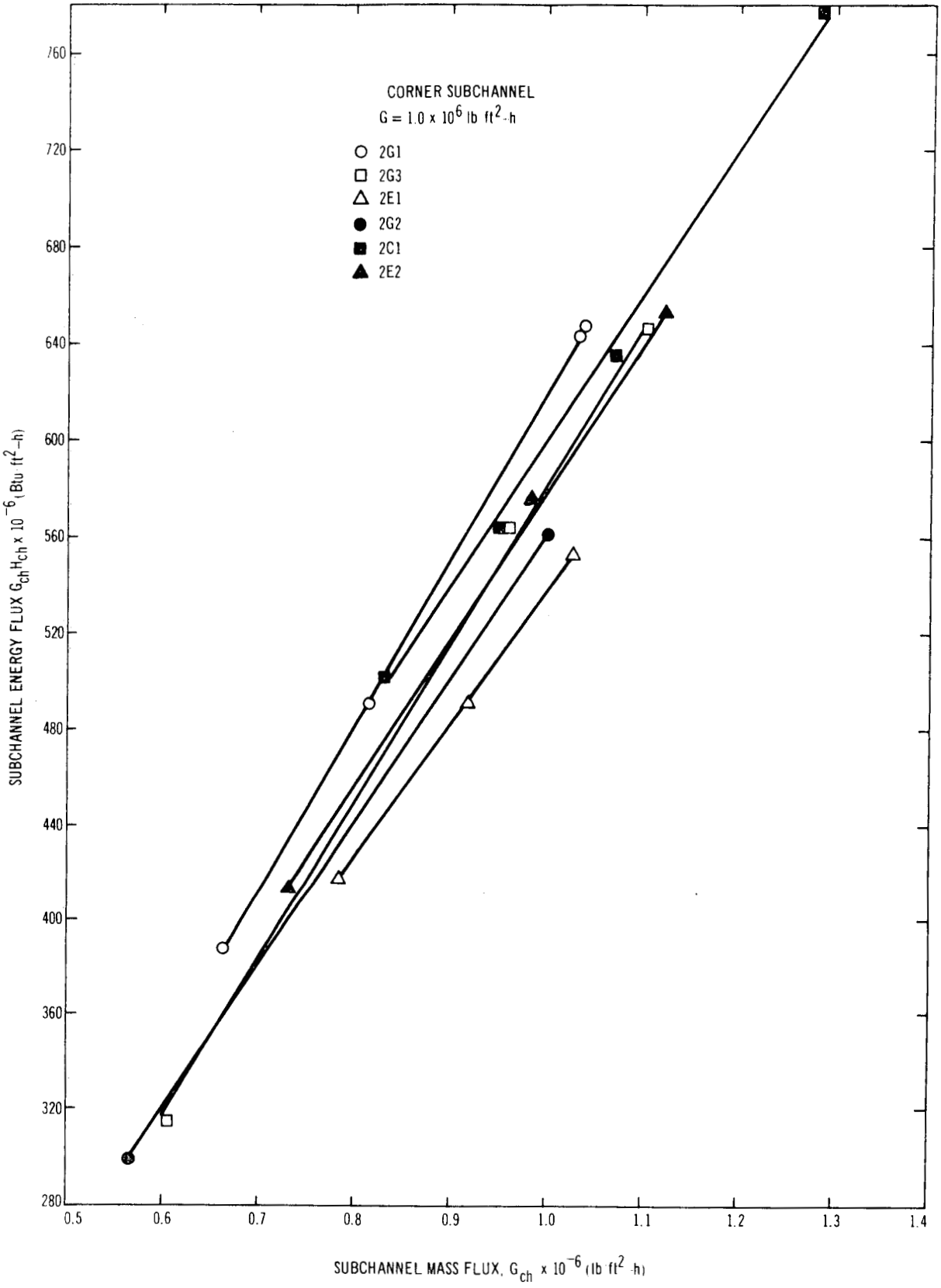

Figure 50. Crossflow Enthalpy Determination for Corner Subchannels: $\bar{G}$ = 1.0 × 10^6 lb/ft^2-h

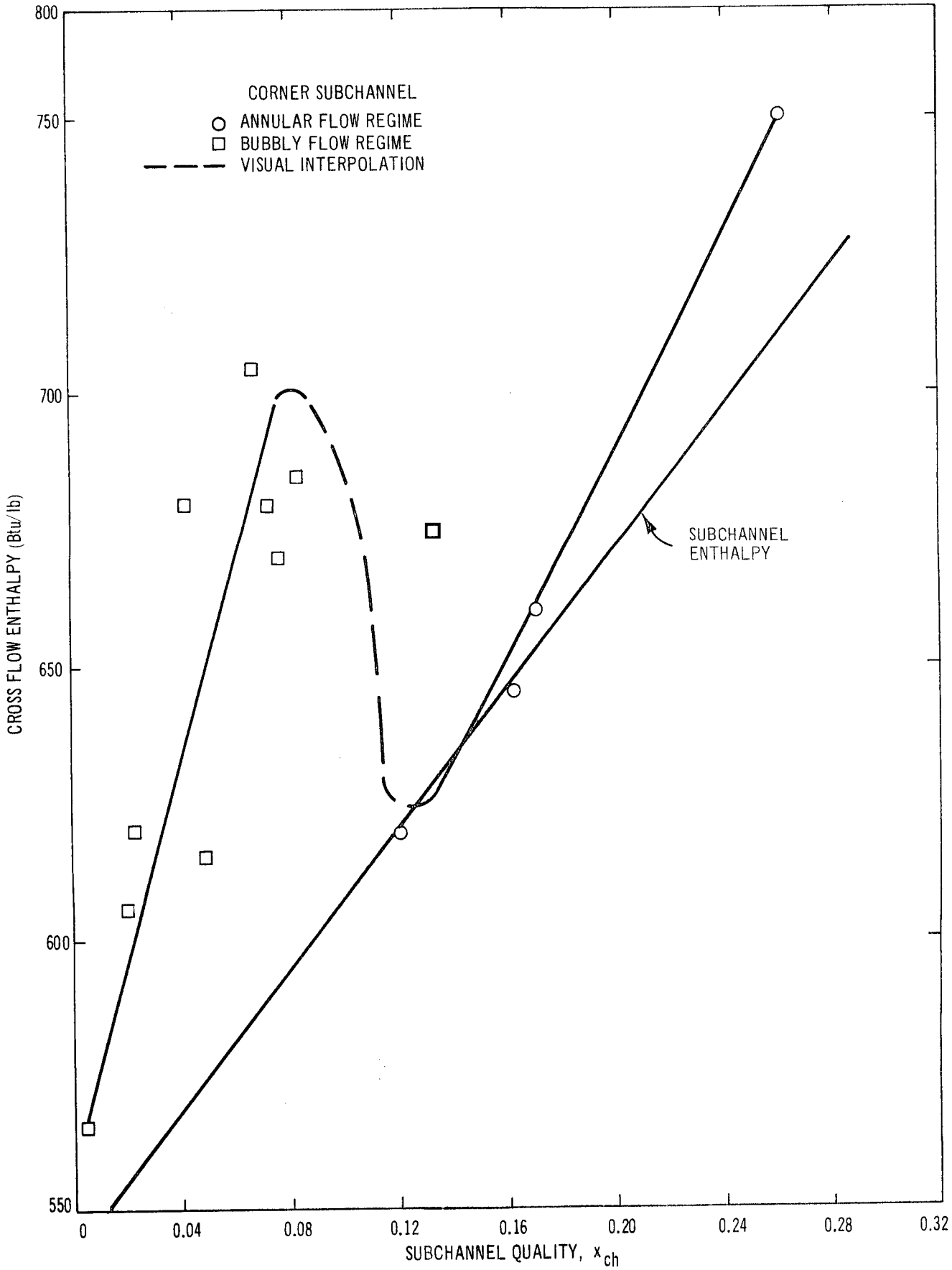

Figure 51. Crossflow Enthalpy from a Corner Subchannel

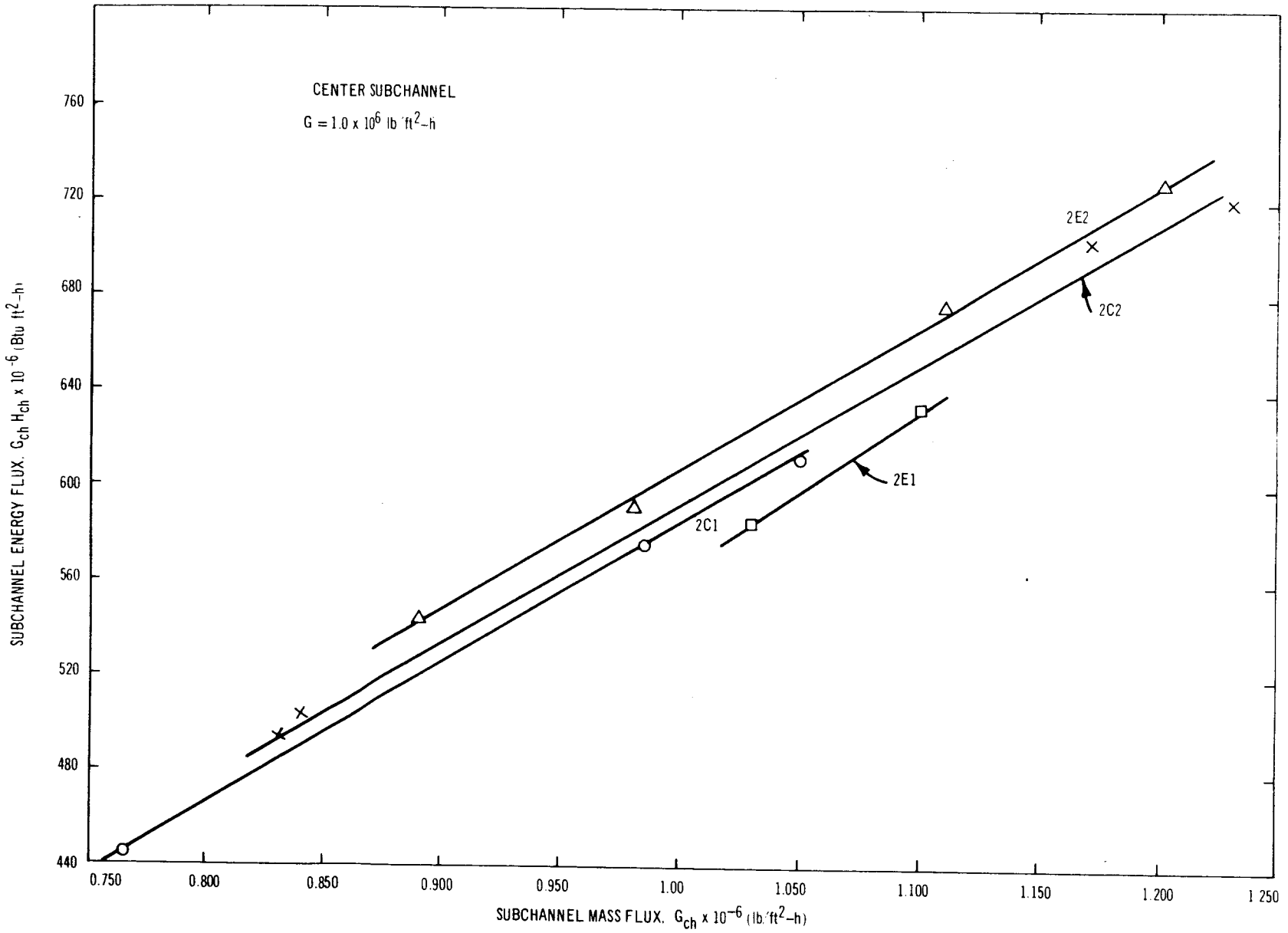

Figure 52. Crossflow Enthalpy for a Center Subchannel: $\bar{G} = 1.0 \times 10^6$ lb/ft²-h

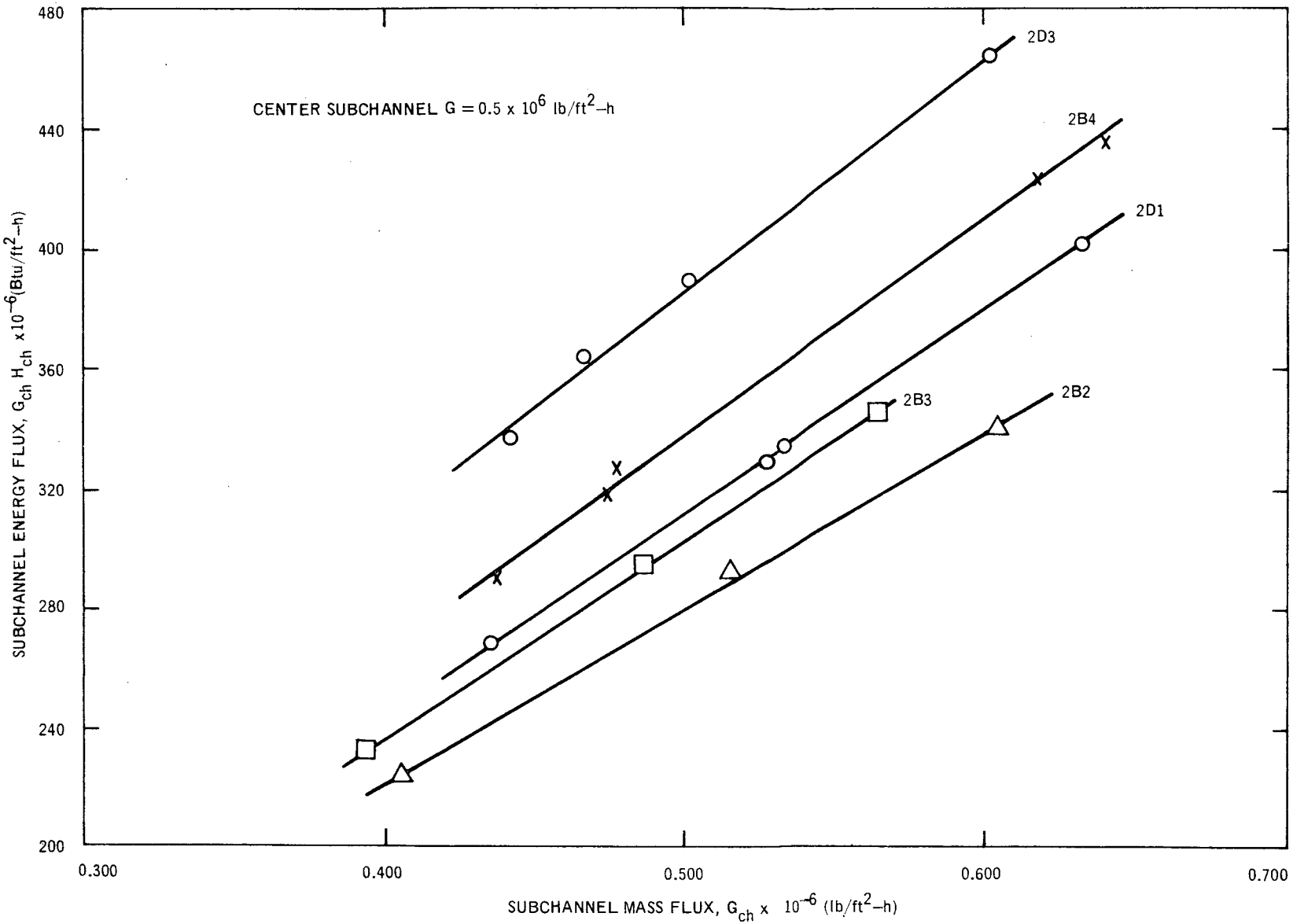

Figure 53. Crossflow Enthalpy for a Center Subchannel: $\overline{G} = 0.5 \times 10^6$ lb/ft^2-h

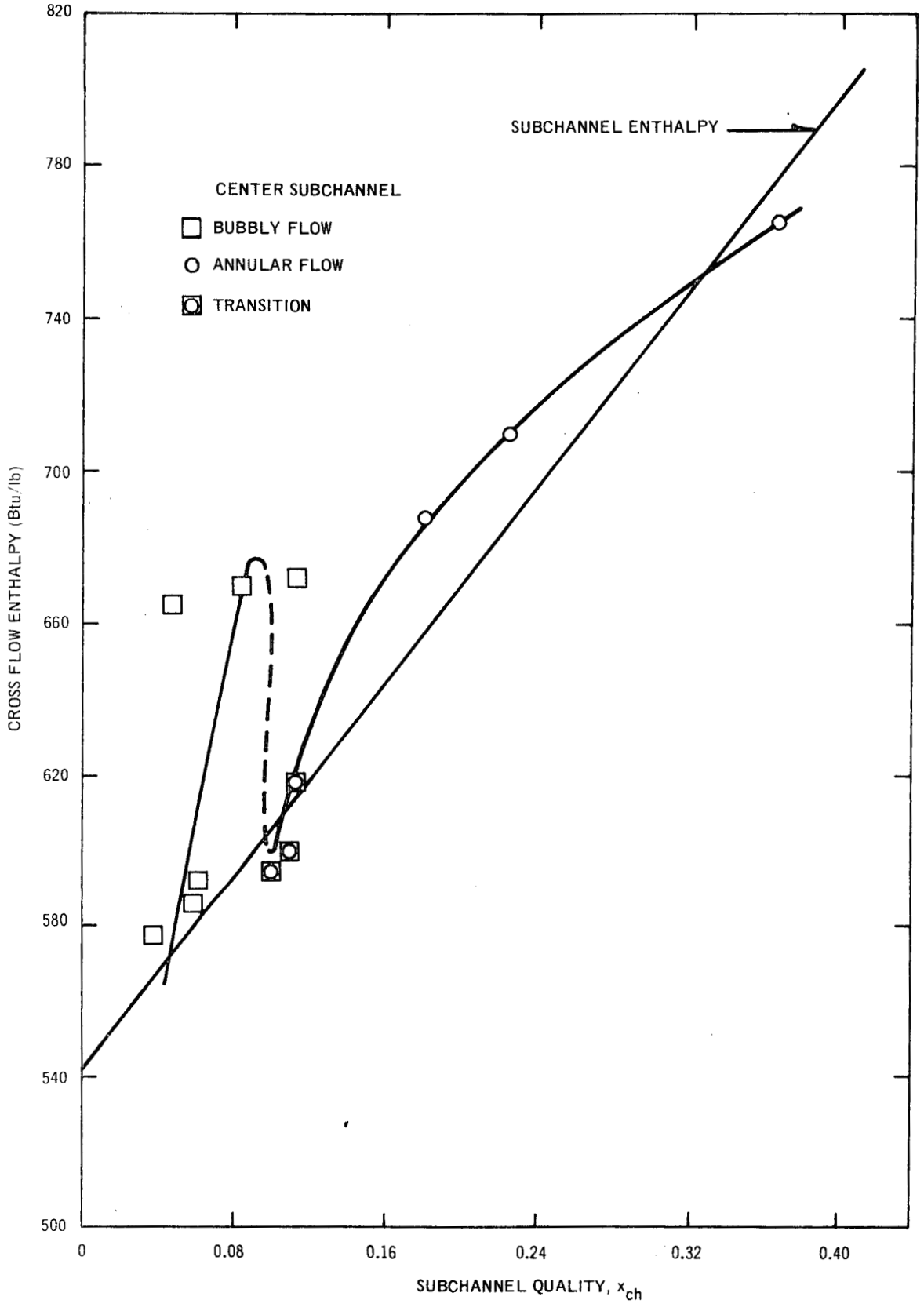

Figure 54. Crossflow Enthalpy from the Center Subchannel

Table 7
CROSSFLOW ENTHALPY FOR A CENTER SUBCHANNEL

Test Point	Subchannel Mass Flux (lb/ft^2-h) $G_{ch} \times 10^{-6}$	Subchannel Quality x_{ch}	Crossflow Enthalpy (Btu/lb) H_x	Crossflow Quality, x_x	Flow Regime
2B2	0.561	0.038	577	0.053	Bubbly
2B3	0.537	0.084	670	0.196	Bubbly
2B4	0.584	0.224	710	0.258	Annular
2D1	0.500	0.113	672	0.199	Bubbly
2D3	0.563	0.364	765	0.343	Annular
2C1	1.077	0.059	585	0.066	Bubbly
2C2	1.144	0.100	595	0.081	Transition
2E1	1.086	0.047	665	0.189	Bubbly
2E2	1.091	0.109	600	0.088	Transition
2G1	1.287	0.060	592	0.076	Bubbly
2G2	1.001	0.111	618	0.116	Transition
2G3	0.954	0.178	688	0.224	Annular

8. COMPARISON WITH PREVIOUS SUBCHANNEL DATA

Subchannel sampling data, to determine the enthalpy and flow distribution, have been taken previously in rod bundles by investigators at Columbia University[5 6] and at Winfrith, England.[3] Indirect approaches to estimating the quality and flow rate in various regions of a bundle have also been used by Bergles[7 8] and Schraub, et al.[9] In addition, work has been done to determine the nature of turbulent mixing and the cross-flow between adjoining subchannels. A comprehensive review of all these investigations may be found in Reference 10.

Most of the data from Columbia are for subcooled exit quality typical of conditions in pressurized water reactors, hence direct comparison with the present data is difficult. Sampling was done in two geometries, as shown in Figures 55 and 56. The unpublished data taken for the 19-rod, triangular array are sketchy, and in most cases they are inconsistent, so they will not be discussed here. In the 16-rod, square array, two of the center subchannels, one hotter than average and one colder than average were sampled. The dimensions of the array are shown in Figure 56. Large redistribution of flow was found to occur in both subchannels in the subcooled boiling region.

It was found that the center subchannels ran "hotter" than average under all conditions, similar to the present data. The trends in the Columbia data may be summarized as follows.

1. Both "cold" and "hot" center subchannels are higher in quality than the bundle average quality.

2. The mass flux in both subchannels drops from above average during single phase flow to below average at zero bundle-average thermodynamic equilibrium quality with the flow in the cold subchannel being higher than in the hot subchannel.

3. At higher heat fluxes, the drop in flow rate was greater and occurred at lower bundle average quality because of earlier subcooled boiling in the hot subchannel. The effect of heat flux was smaller under conditions of bulk boiling.

4. Under subcooled conditions the quality in the hot-center subchannel increased at a given value of bundle average quality as the heat flux was increased.

5. As the bundle average flow rate was increased, the hot subchannel quality approached the bundle average quality.

In contrast, the present data show little effect of heat flux on the center-subchannel flow-rate or of bundle average flow rate on the subchannel quality. However, the

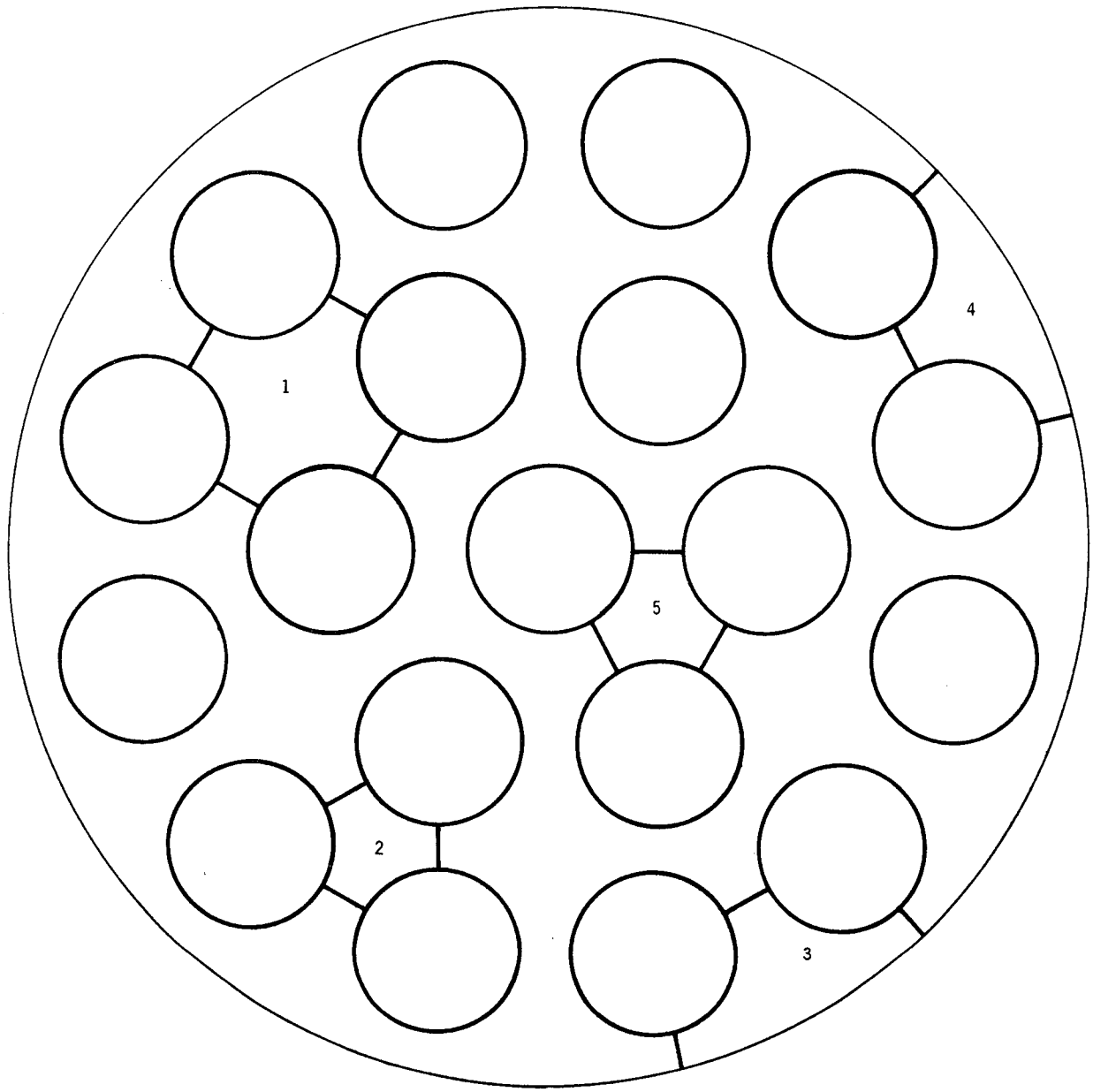

FLOW TUBE I.D. = 4.068 in.; HEATED LENGTH = 6 ft
INNER PITCH CIRCLE = 1.640 in. DIA.
OUTER PITCH CIRCLE = 3.168 in. DIA.
HEATER O.D. = 0.780 in.
ROD TO ROD SPACING = 0.040 in.
ROD TO WALL SPACING = 0.060 in.
POWER DISTRIBUTION:
OUTER ROD = 100%
INNER ROD = 79.9%
CENTER ROD = 69.7%

Figure 55. Columbia University 19-Rod Test Geometry

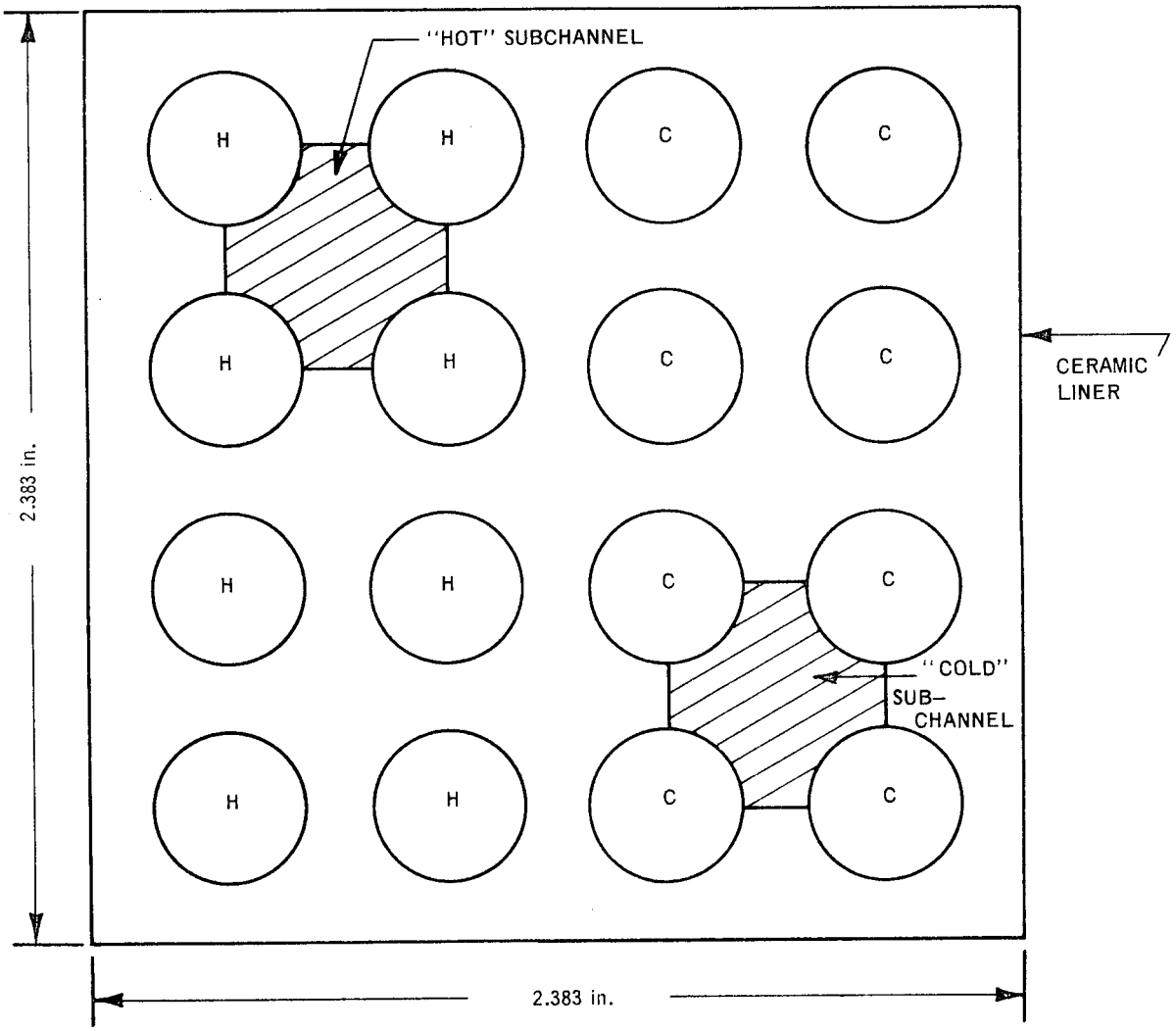

ROD OUTSIDE DIAMETER	0.422 in.
ROD PITCH	0.555 in.
ROD TO WALL SPACING	0.148 in.
ROD TO ROD SPACING	0.133 in.
TOTAL FLOW AREA	0.02389 ft^2
SUBCHANNEL AREA	0.001168 ft^2
RADIAL HEAT FLUX	
HOT RODS [H]	100%
COLD RODS [C]	80%
HEATED LENGTH	60 in.

Figure 56. Columbia University 16-Rod Test Geometry

center-subchannel quality was found to increase when the heat flux was raised. It must be remembered, however, that the Columbia tests were performed mainly with subcooled exit conditions and radially-non-uniform heating, whereas the tests discussed so far in this report were done under conditions of bulk boiling at the exit and uniform heat flux in both the axial and radial directions. Unfortunately, the Columbia test data was not taken in all the subchannels, so it is impossible to check the validity of the data by trying to balance the mass flow and energy inventory. Nevertheless, the basic trends in that center-subchannel data agree quite well with the present data and so provide valuable information about the region of subcooled boiling.

Bowring and Levy[3] discuss tests performed in a 7-rod cluster using Freon-12. The test section was divided into two subchannels, an outer subchannel and an inner subchannel as shown in Figure 57. The flow rate in the inner subchannel was found to be of the order of 1/6 of the total flow rate under single-phase conditions, and it decreased for two-phase exit conditions. The heat balance errors were on the order of ±7 %, which due to the small latent heat of Freon-12, gives rather large errors in quality. However, as expected, it was found that the enthalpy rise in the inner subchannel was higher than in the outer subchannel.

Non-isokinetic data were taken, and within the accuracy of the data, the crossflow enthalpy was found to be higher than for that of the donor subchannel. The flow-diversion length in the axial direction was calculated to be small, of the order of 2 inches, which is in agreement with other investigators.[24]

Bergles[7] has made an investigation of flow regimes in a four-rod bundle with water pressure of 1000 psia. On the basis of the observed fact that the slug-annular transition takes place in the center of the bundle at higher mass flux and lower average quality than in the corner, it may be concluded that the central portion of the bundle was a higher quality region.

Schraub et al.,[9] have made detailed measurement for air-water mixtures in a nine-rod array of dimensions similar to the one used in the present series of tests. Quality and mass-flux maps for the test section were made from samplings with isokinetic probes traversed across the bundle cross section. For bundle average qualities up to about 28 %, their results indicate a lower than average quality and a slightly greater than average mass flux in the corner subchannel of the bundle but above this quality a sharp reversal in both quantities occurred. It is not known how much effect the method of introduction of the air (in this case, axial) has on the eventual distribution of air over the cross section, but the basic trends in this data are similar to that in the data of the present investigation.

An extensive gamma-scran program was completed in Sweden,[11] to determine the radial void distribution in a rod bundle. These tests were performed in a six-rod array in a 2.5 MW out-of-pile test loop. It was found that the void fraction, and therefore the quality, was the highest in the interior of the bundle and lowest in the outer region, which had an unheated cannister wall. Similar tests have been made more recently[12] in a 36-rod bundle in the 8 MW, electrically heated, FRIGG loop. The results were qualitatively the same as for the six-rod test section. Both of these sets of data agree with the trends in quality distribution observed in the present data. Although the trends in the Swedish data can be interpreted on the basis of power-to-flow ratio, that argument fails to explain other data;[10] including the present data.

Two subchannel mixing tests have been performed by Rowe and Angle[1-2] from which the enthalpy and flow distributions were obtained. These show the expected trends, with the subchannel having the smaller hydraulic diameter at the smaller flow rate and the higher enthalpy. The enhanced eddy-diffusivity mixing, which was observed in the neighborhood of the slug-annular transition[1,2,10] and had such a strong effect in the two-subchannel tests just mentioned, apparently plays lesser role in the present rod-bundle geometry.

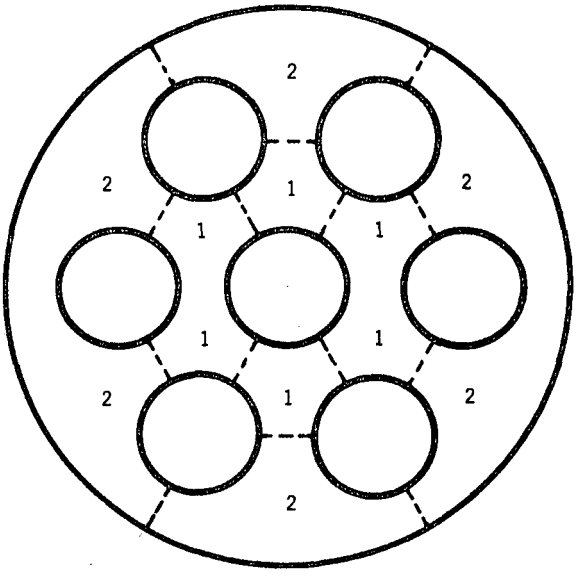

ROD DIAMETER : 0.625 in.
ROD P.C.D. : 1.370 in.
SHROUD I.D. : 2.153 in.
GAP (INNER) : 0.060 in.
(OUTER) : 0.079 in.

ENTRY LENGTH (UNHEATED) : 3 in.
HEATED LENGTH : 36 in.
CHIMNEY (UNHEATED) : 24 in.

Figure 57. Subchannel Division of a Seven-Rod-Cluster Cross Section

9. COMPARISON OF DATA WITH THE ANALYTICAL PREDICTIONS

There are several subchannel computer programs in the open literature that predict the enthalpy and flow distributions in multi-rod bundles. Examples are HAMBO,[13] SASS,[14] and COBRA.[15] The programs are all similar in principle; the rod bundle is divided into multiple flow tubes or ventilated subchannels. Each subchannel is then divided into axial nodes. Finite-difference forms of the conservation equations are then solved for this system numerically using a high speed digital computer. For purposes of comparison with data, the COBRA program has been chosen.

One of the variables that has to be specified in the computer solution is the amount of "mixing" between adjoining subchannels. For this purpose, COBRA uses a parameter β defined by:

$$w' = \beta s \tilde{G}$$

where

w' = fluctuating mass flow rate per unit length in the axial direction
β = dimensionless mixing parameter (Mixing Stanton Number)
s = gap spacing (rod-rod or rod-wall spacing)
$\tilde{G}$ — average mass flux of adjacent subchannels

β may be redefined in terms of the eddy diffusivity as,

$$\beta = \frac{\epsilon \rho_f}{\tilde{G} \ell}$$

where

ℓ = the mixing length, or the "effective mixing distance" between subchannels

Rowe[1] recommends a value for β given by

$$\beta = (0.0062) \frac{D_h}{s} (Re)^{-0.1}$$

for single phase mixing, which for the present geometry is of the order of 0.005.

For zero mixing the flow distribution may be calculated analytically as follows. For the single-phase adiabatic runs, the total static pressure drop is approximately the same in all the parallel subchannels.

$$\Delta p_l = f_i \frac{G_i^2 \, 4L}{2\rho_i g_c D_{h_l}} + \rho_i \frac{gL}{g_c} = \Delta p_{Total}$$

Hence, for each subchannel,

$$f_i \frac{G_i^2}{D_{h_i}} \triangleq C_1 \text{ (a constant)}$$

where the subscript i, refers to the i^{th} subchannel.

$$\text{If} \quad f_i \sim Re_i^{-0.2} \triangleq \left(\frac{G_i D_{h_i}}{\mu} \right)^{-0.2}$$

Then, by substitution one obtains

$$\frac{G_i^{1.8}}{D_h^{1.2}} \simeq C_2$$

where

$$C_2 \triangleq C_1 \mu^{-0.2}$$

or

$$G_i = C_2^{0.55} \cdot D_{h_i}^{2/3} = C_3 \cdot D_{h_i}^{2/3}$$

Table 8 shows the single phase data, the $D_h^{2/3}$-prediction with no mixing, and COBRA predictions with β equal to 0.005 and 0.01. At low flows the best overall agreement is obtained with the mixing parameter $\beta = 0.005$. However at $\bar{G} = 1.97 \times 10^6$ lbs/ft^2-h it appears that $\beta > 0.01$ would produce better agreement with data.

The latest indications[2, 10, 16, 17] are that two-phase mixing is a function of the subchannel geometry, quality and flow regime. Values of β between 0.01 and 0.04 are probably appropriate for the present range of test conditions. Actually the mixing should depend on local conditions and should thus vary in the axial direction. Nevertheless a constant value of β was used, as described above, since the exact dependence of β on flow regime and local conditions was not known. In any event this is compatible with previous practice and thus produces a consistent comparison. Table 9 shows a comparison between some of the data and the predictions with COBRA for β equal to 0.01 and 0.04. Somewhat better agreement is obtained with data for $\beta = 0.04$. However, the trends in subchannel qualities are not predicted by the computer code. Even with the high mixing, COBRA cannot predict the substantially lower-than-average qualities in the corner subchannel, and higher-than-average qualities in the center

subchannel. In fact, if mixing were made infinitely large the three subchannels would all be at average conditions and thus the data cannot be explained in terms of mixing. COBRA has an inherent defect in that it does not take subcooled voids into account; however, the disparity between the trends in the data and the predictions cannot be attributed to this.

The most probable explantions for this behavior are the tendency for the steam to move preferentially to the center of the rod bundle and/or the presence of a thick liquid film on the unheated channel wall. This latter hypothesis is consistent with the trends in the void fraction and flow regime measurements of the air-water test described in the previous section and further discussed in Reference 10. Although the reasons for the failure of the subchannel approach for a typical present generation computer code (COBRA) are not completely clear, it is evident that without modification of the thermal-hydraulic physics in these codes, agreement with actual multirod data can not be achieved.

Table 8
SINGLE-PHASE (COLD): MEASURED AND PREDICTED MASS FLUXES

Test Point		$\bar{G} \times 10^{-6}$ (lb/ft^2-h)	$G_1 \times 10^{-6}$ (lb/ft^2-h)	$G_2 \times 10^{-6}$ (lb/ft^2-h)	$G_3 \times 10^{-6}$ (lb/ft^2-h)
1B	Data	0.480	0.311	0.462	0.526
	$D_h^{2/3}$-Prediction*	0.480	0.322	0.447	0.562
	COBRA $\beta = 0.01$	0.480	0.352	0.451	0.551
	COBRA $\beta = 0.005$	0.480	0.336	0.447	0.560
1C	Data	0.990	0.701	0.939	1.150
	$D_h^{2/3}$-Prediction	0.990	0.664	0.922	1.159
	COBRA $\beta = 0.01$	0.990	0.740	0.934	1.128
	COBRA $\beta = 0.005$	0.990	0.704	0.925	1.149
1D	Data	1.510	1.095	1.441	1.690
	$D_h^{2/3}$-Prediction	1.510	1.013	1.406	1.768
	COBRA $\beta = 0.01$	1.510	1.143	1.427	1.713
	COBRA $\beta = 0.005$	1.510	1.085	1.414	1.746
1E	Data	1.97	1.62	1.91	2.19
	$D_h^{2/3}$-Prediction	1.97	1.321	1.834	2.306
	COBRA $\beta = 0.01$	1.97	1.502	1.865	2.229
	COBRA $\beta = 0.005$	1.97	1.424	1.847	2.273

* Assuming no mixing.

Table 9
TWO-PHASE: MEASURED AND PREDICTED FLOW AND ENTHALPY DISTRIBUTION

Test Point	$\bar{G} \times 10^{-6}$ (lb/ft^2-h)	$\bar{x}_e$		$G_1 \times 10^{-6}$ (lb/ft^2-h)	$\bar{x}_1$	$G_2 \times 10^{-6}$ (lb/ft^2-h)	x_2	$G_3 \times 10^{-6}$ (lb/ft^2-h)	x_3
2B2	0.530	0.029	Data	0.372	0.003	0.521	0.014	0.540	0.030
			COBRA $\beta = 0.04$	0.482	0.030	0.523	0.026	0.552	0.031
			COBRA $\beta = 0.01$	0.491	0.046	0.516	0.025	0.558	0.029
2B3	0.535	0.090	Data	0.550	0.072	0.530	0.076	0.521	0.104
			COBRA $\beta = 0.04$	0.478	0.090	0.528	0.086	0.560	0.092
			COBRA $\beta = 0.01$	0.454	0.104	0.524	0.084	0.571	0.092
2B4	0.535	0.176	Data	0.524	0.133	0.517	0.180	0.560	0.220
			COBRA $\beta = 0.04$	0.469	0.177	0.526	0.172	0.565	0.178
			COBRA $\beta = 0.01$	0.417	0.194	0.524	0.169	0.581	0.179
2E1	1.080	0.035	Data	0.950	0.004	1.102	0.026	1.162	0.051
			COBRA $\beta = 0.04$	0.990	0.035	1.082	0.031	1.102	0.038
			COBRA $\beta = 0.01$	0.874	0.057	1.068	0.030	1.151	0.034
2E2	1.080	0.106	Data	1.046	0.049	1.078	0.097	1.180	0.105
			COBRA $\beta = 0.04$	0.979	0.106	1.073	0.102	1.117	0.109
			COBRA $\beta = 0.01$	0.878	0.125	1.073	0.099	1.143	0.109
2E3	1.060	0.215	Data	0.965	0.160	1.081	0.185	1.126	0.249
			COBRA $\beta = 0.04$	0.938	0.215	1.044	0.211	1.113	0.217
			COBRA $\beta = 0.01$	0.826	0.234	1.046	0.206	1.140	0.220

10. DATA WITH A RADIALLY NON-UNIFORM HEAT FLUX DISTRIBUTION

Subchannel sampling tests were run with different power on the nine rods in order to obtain a radial peaking distribution. Axially, the heat flux was uniform.

The radial peaking pattern was achieved by using three peaking transformers one for each phase, as shown in Figure 58. Each phase supplies power for three rods. In this way, a peaking pattern approximately symmetrical (but not exactly symmetrical due to variations in the individual transformers) about the diagonal was achieved as shown in Figure 59. For this configuration, there are approximately ten different types of subchannels. Due to the shortage of test loop time, only subchannels 1 through 5 were sampled. Subchannels 1, 3, and 5 were sampled with the peaking pattern in Figure 59 in the usual manner. In order to sample subchannels 2 and 4 without changing the splitter locations the peaking pattern was reversed as in Figure 60, and the same side and corner subchannels were sampled. These peaking factors are defined with respect to the average heat flux and were determined from actual measurements. In addition to the total power, the power to each rod was measured separately and recorded on the DYMEC paper tape. The test conditions are shown in Table 10. These test conditions are nominally the same as 2B2, 2D1, 2E1, and 2E2. A slightly lower total power was used for Test 3E2 because of the possibility of critical heat flux (CHF) in the presence of 1.3 peaking on the corner rod.

Table 11 shows results obtained for the peaking runs. These cover the hot (No. 1) and cold (No. 2) corner subchannels, hot (No. 3) and cold (No. 4) side subchannels, and the hot (No. 5) center subchannel. The hot center subchannel ran at the highest quality in all cases. Unfortunately not much data is available for the hot side subchannel. It was found that the cold side subchannel was the lowest in quality and generally had the highest mass

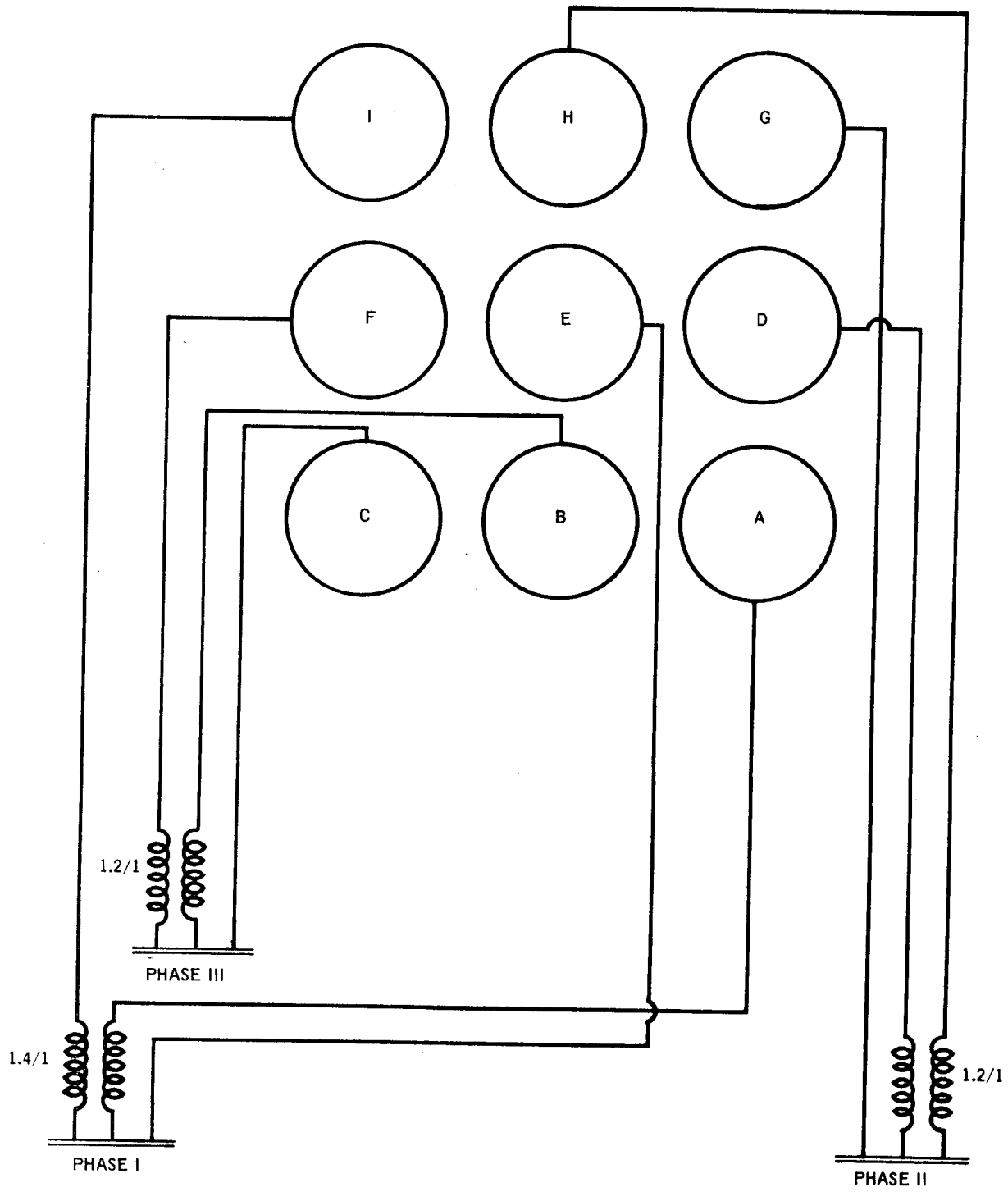

Figure 58. Typical Power Hook-Up for Radial Peaking Runs

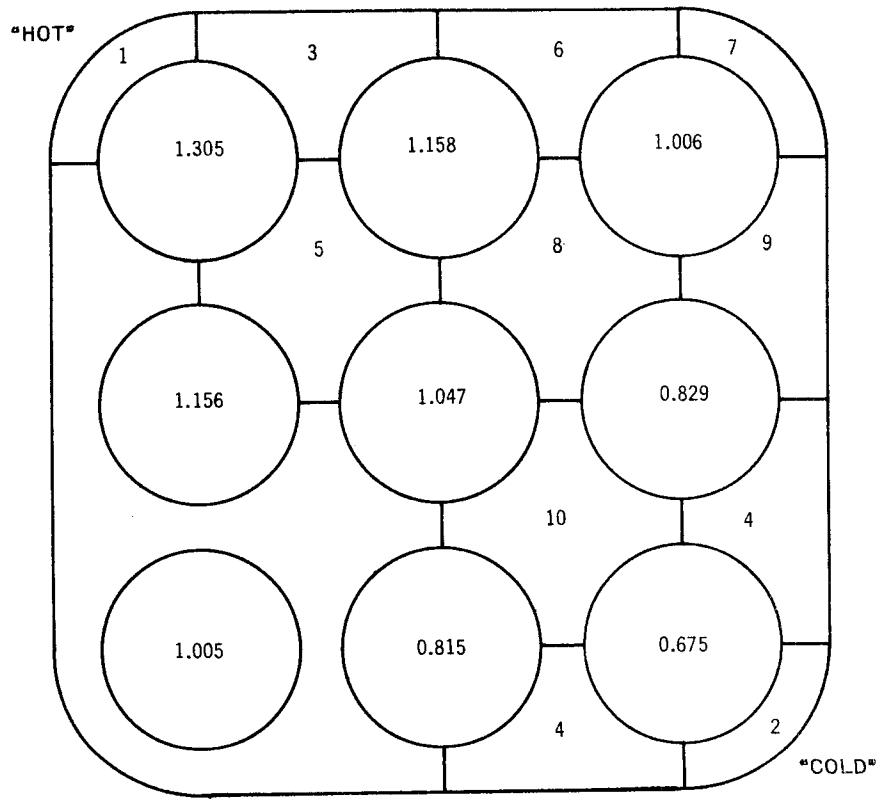

Figure 59. Subchannels and Peaking Pattern

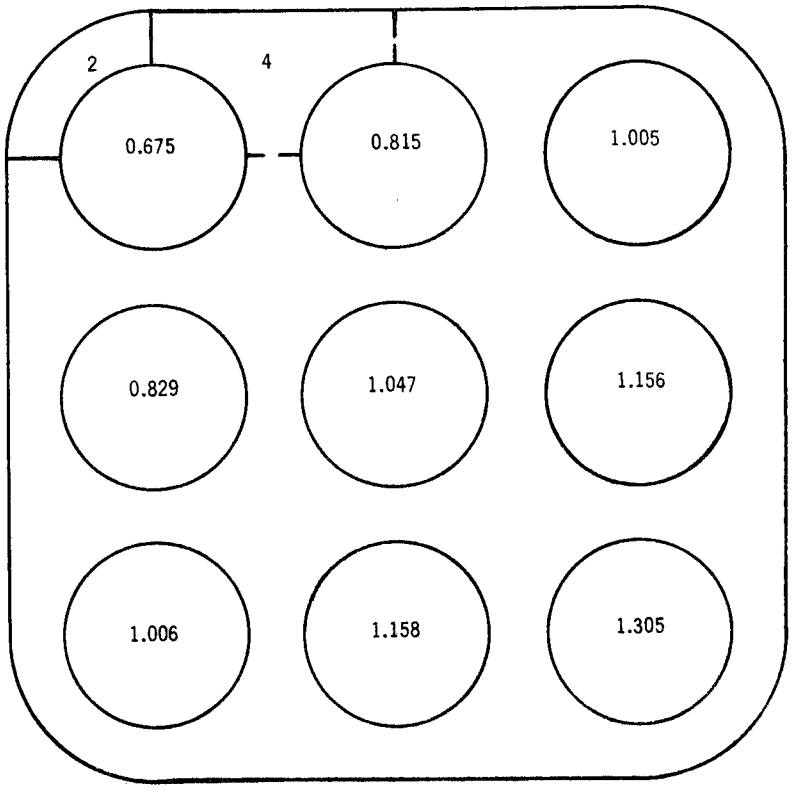

Figure 60. Peaking Pattern Used for Subchannels 2 and 4

Table 10
TEST CONDITIONS FOR PEAKING RUNS

Test Point	Average Mass Flux (lb/ft^2-h) $\overline{G} \times 10^{-6}$	Power (kW)	Average Heat Flux (Btu/ft^2-h) q''	Subcooling (Btu/lb)	Average Exit Quality $\overline{x}_e$
3B2	0.535	532	225,000	146.1	0.032
3D1	0.545	1064	450,000	273.0	0.084
3E1	1.080	1064	450,000	142.9	0.035
3E2	1.060	994	420,000	92.4	0.100

flux. In fact, in three of the four runs the cold subchannel was substantially subcooled at the exit, so that the exit enthalpy could be accurately determined by measurement of the temperature of the sample at the inlet to the heat exchanger. The hot corner subchannel ran at higher than average quality and was the lowest in mass flux for all the runs considered.

Since not all ten subchannels were sampled, errors in the continuity and energy balance could not be evaluated. Comparisons with uniform data are made in Figures 61 to 82. Figures 61 to 64 show that the quality of the hot corner subchannel runs much higher than that of the corner subchannel for uniform local peaking conditions and that it also runs higher than the average bundle quality. The quality of the cold corner subchannel is not affected as much, and runs close to the corner subchannel under conditions of uniform heat flux. Sometimes the cold corner subchannel quality appears to be a little higher than that in the uniform case. This trend is closely related to the subchannel mass flux as will be seen when Figures 72 to 75 are discussed. The probable error in these quality measurements is of the order of ±2% (see Appendix B). Since this is true, the uniform and cold subchannel qualities can be considered the same in most cases. Figures 65 to 68 show the qualities in the hot and cold side subchannels, and the side subchannel for uniform heat flux (referred to hereafter as "uniform" side subchannel). Here the cold subchannel is seen to be at a much lower quality and subcooled for three out of the four test runs. The quality of the hot side subchannel is higher than in the uniform side subchannel and higher than the bundle average quality. Figures 69 to 71 show the quality in the hot center subchannel together with previously obtained results for the center subchannel in the absence of local peaking. The hot subchannel is seen to run at a substantially higher quality. This is the hottest subchannel in the bundle.

Figures 72 to 82 show the trends in the normalized mass flux. These trends are not as clearly defined as the trends in quality. With the exception of Figure 72, the hot corner subchannel has the least flow when compared to the uniform and cold corner subchannel flows. The cold corner subchannel flow appears generally to be below the uniform corner subchannel flow, but greater than the hot subchannel flow. At first thought, one might expect the cold corner subchannel to be higher in mass flux than the uniform case, with the hot corner subchannel being the lowest. With the exception of Figure 72, which is for a run of low flow and quality, the trend between the hot and cold cases is about as expected. However, in every case, the uniform corner subchannel has higher flow than the corresponding cold case. Since not all subchannels were sampled, it is not possible to check the validity of this trend. It may be possible that the subchannel size was different in this particular assembly due to the tolerances on the rod/wall spacing or that the relatively unrestricted cold center subchannel (Subchannel 10 in Figure 59) had very high flow rates for these peaking runs and thus the cold corner subchannel (Subchannel-2) was "flow starved."

Figures 76 to 79 indicate that the cold side subchannel (see Figure 59) had a greater mass flux than the uniform side subchannel except at low flow and quality. The hot side subchannel flow is lower than the uniform side subchannel flow in every case tabulated. As indicated in Figures 80 to 82, the trends are reversed for the hot center subchannel, which has lower flow rate than the uniform case except at low values of average flow rate and quality.

Table 11
MASS FLUX AND ENTHALPY DATA
FOR RADIAL PEAKING PATTERNS

Test Point	Average Mass Flux (lb/ft^2-h) $\bar{G} \times 10^{-6}$	Average Exit Quality $\bar{x}$	Average Heat Flux (Btu/ft^2-h) $\bar{q}''$	$G_1 \times 10^{-6}$	x_1	$G_2 \times 10^{-6}$	x_2	$G_3 \times 10^{-6}$	x_3	$G_4 \times 10^{-6}$	x_4	$G_5 \times 10^{-6}$	x_5
3B2	0.535	0.032	225,000	0.400	0.080	0.320	0.009	0.507	0.042	0.505	−0.043	0.555	0.108
3D1	0.545	0.084	450,000	0.322	0.123	0.335	0.024	–	–	0.628	−0.037	–	–
3E1	1.080	0.035	450,000	0.794	0.105	0.925	0.002	–	–	1.430	−0.036	0.852	0.163
3E2	1.060	0.100	420,000	0.800	0.160	0.940	0.075	0.755	0.167	1.475	0.034	0.890	0.227

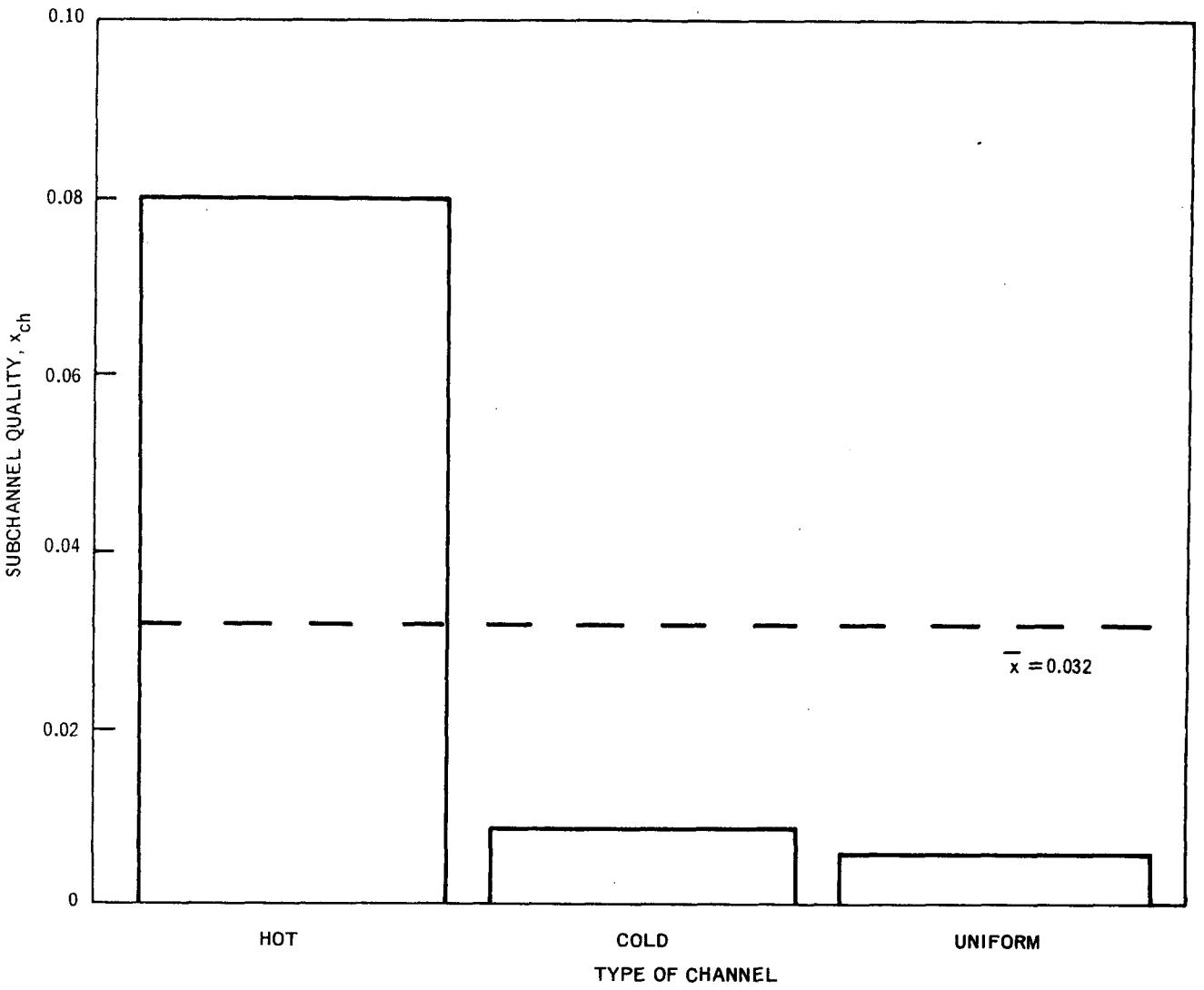

Figure 61. Comparison of Non-Uniform and Uniform Data: Corner Subchannel Qualities 3B2

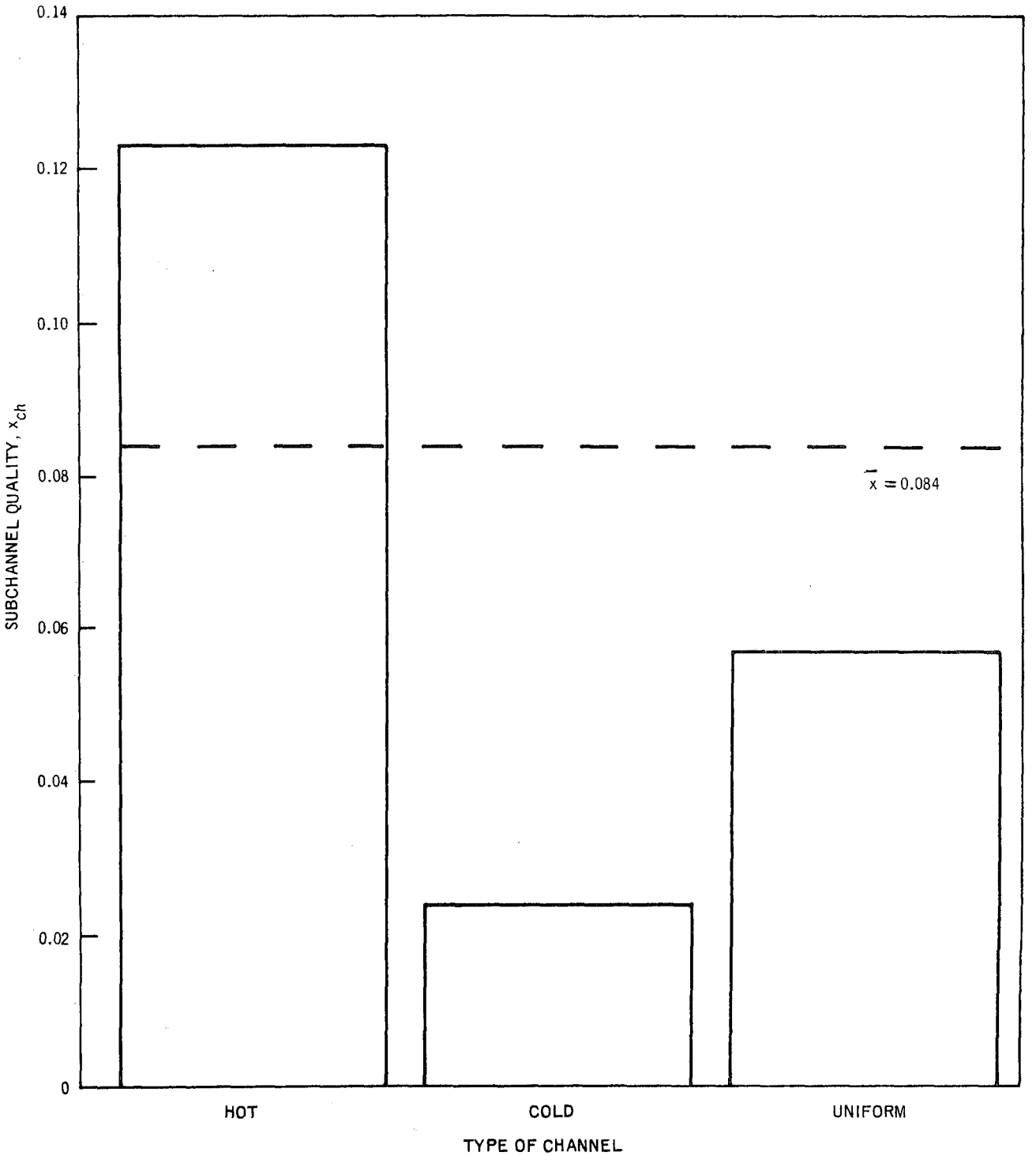

Figure 62. Comparison of Non-Uniform and Uniform Data: Corner Subchannel Qualities 3D1

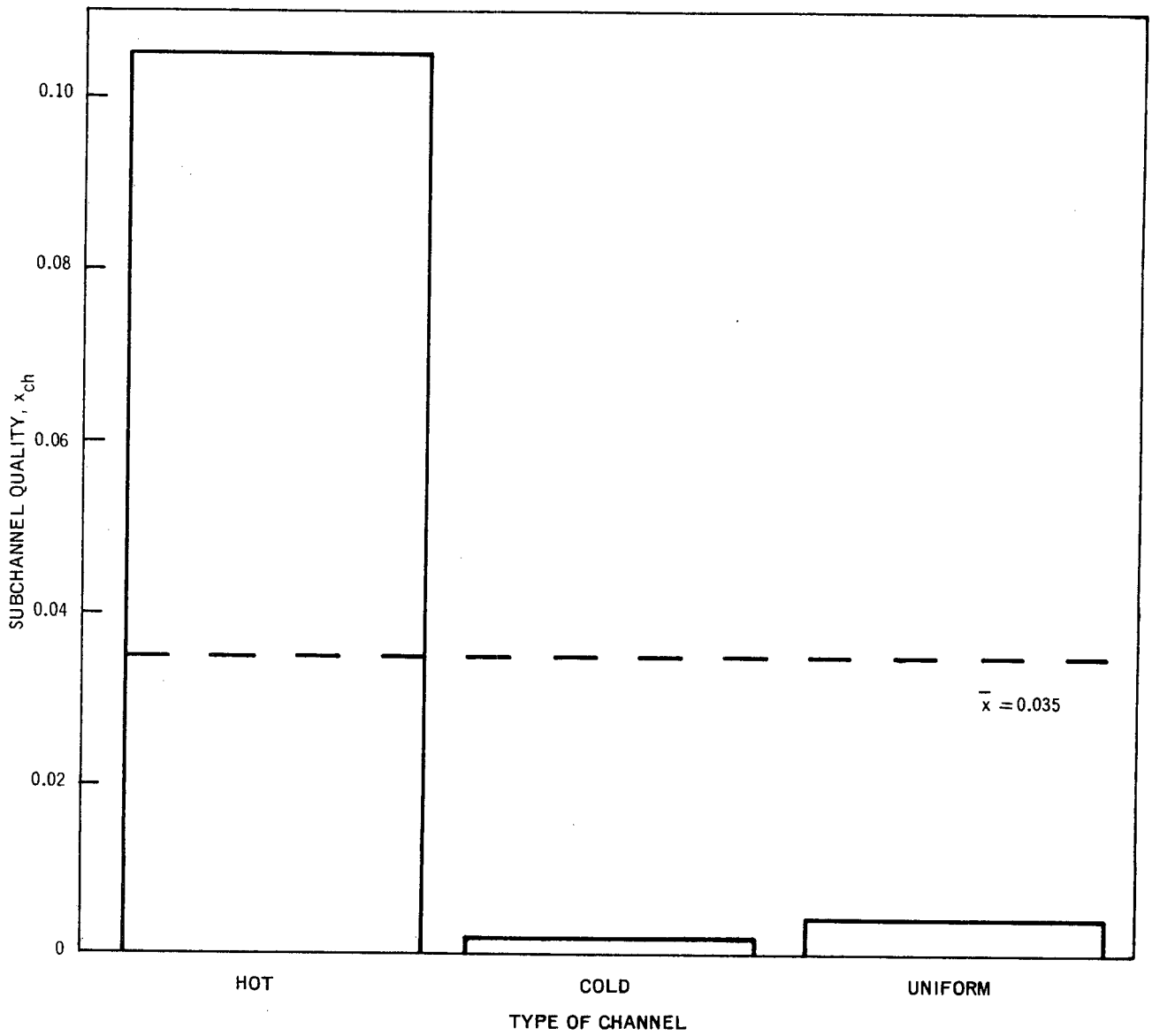

Figure 63. Comparison of Non-Uniform and Uniform Data: Corner Subchannel Qualities 3E1

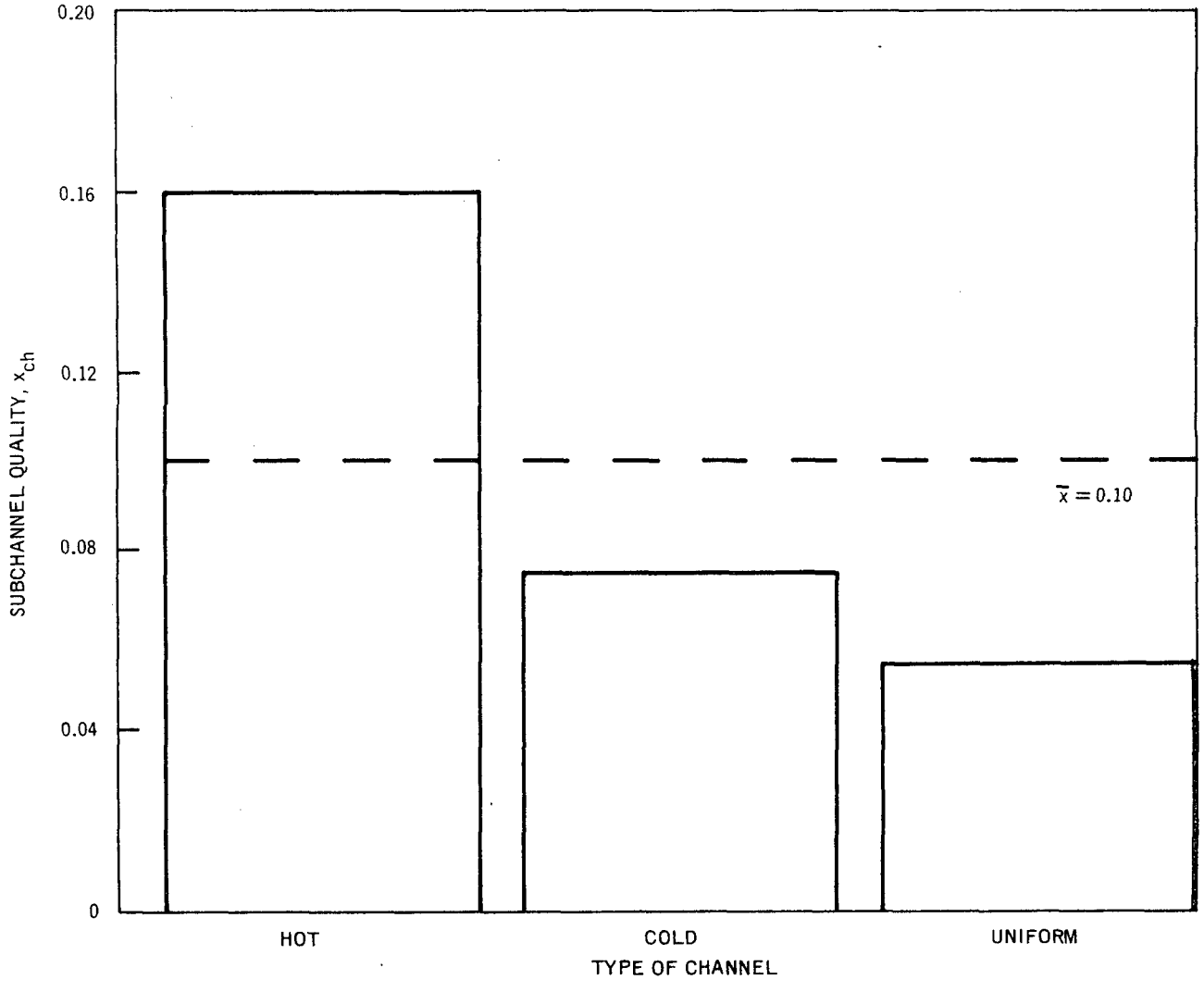

Figure 64. Comparison of Non-Uniform and Uniform Data: Corner Subchannel Qualities 3E2

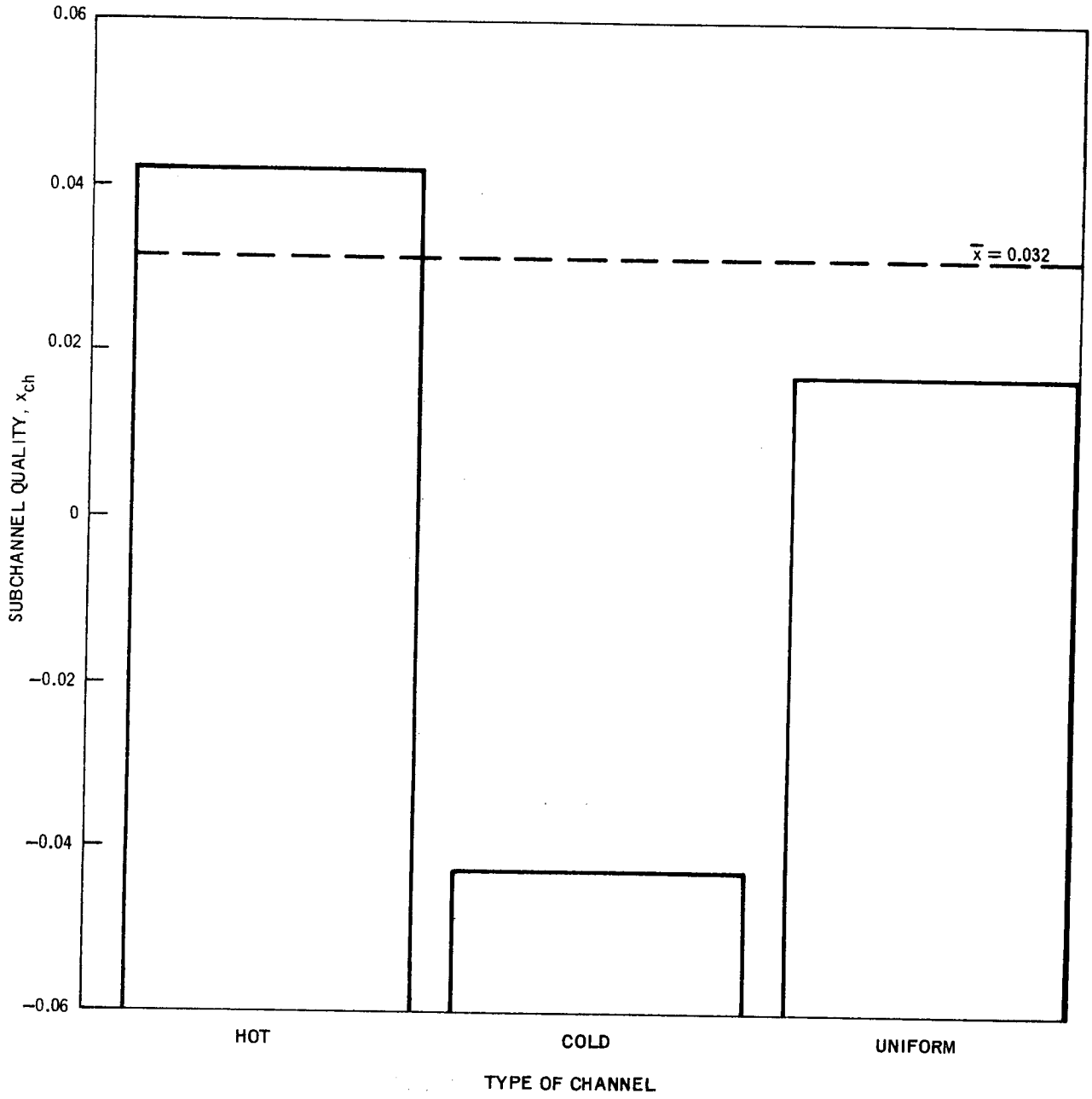

Figure 65. Comparison of Non-Uniform and Uniform Data: Side Subchannel Qualities 3B2

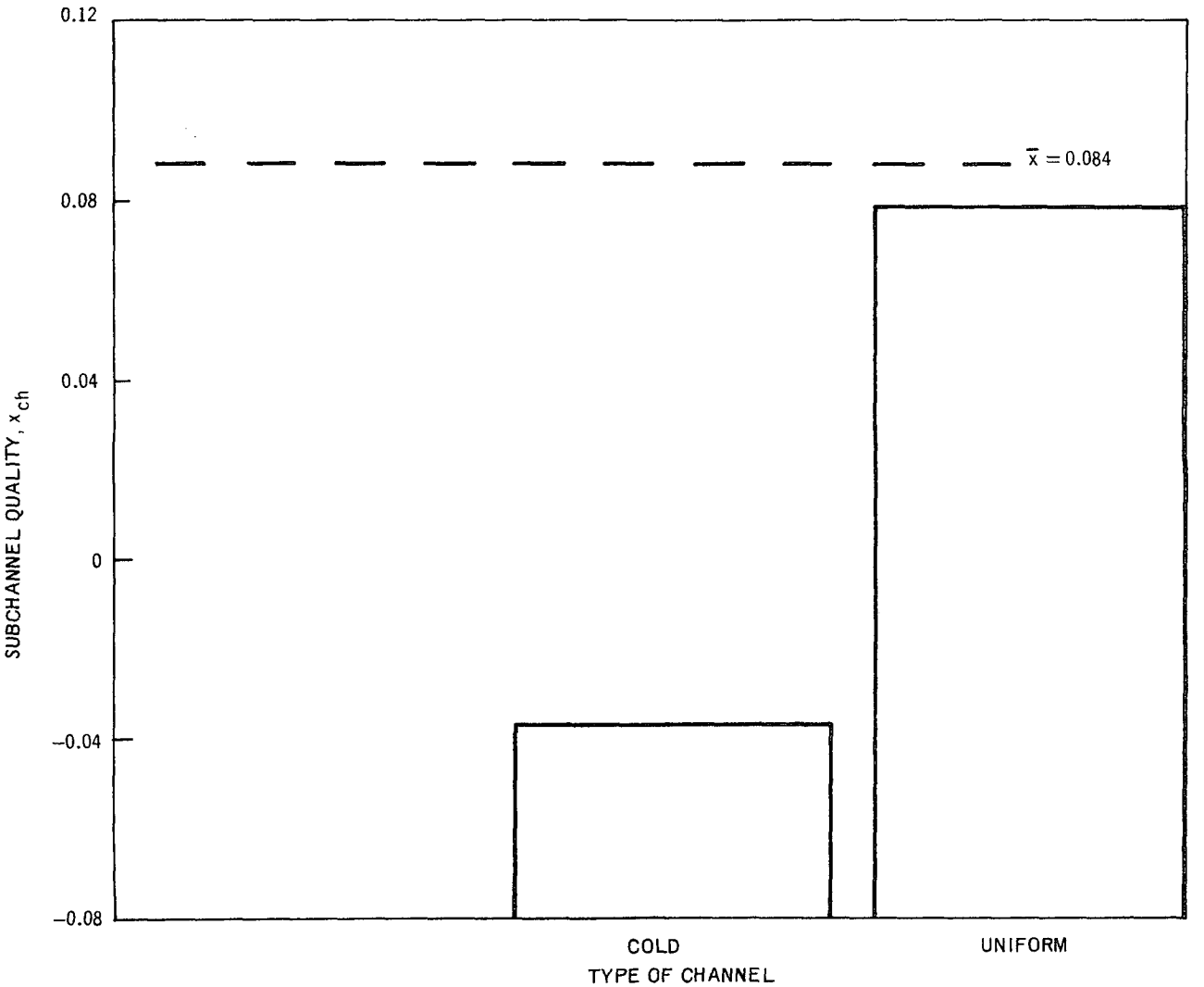

Figure 66. Comparison of Non-Uniform and Uniform Data: Side Subchannel Qualities 3D1

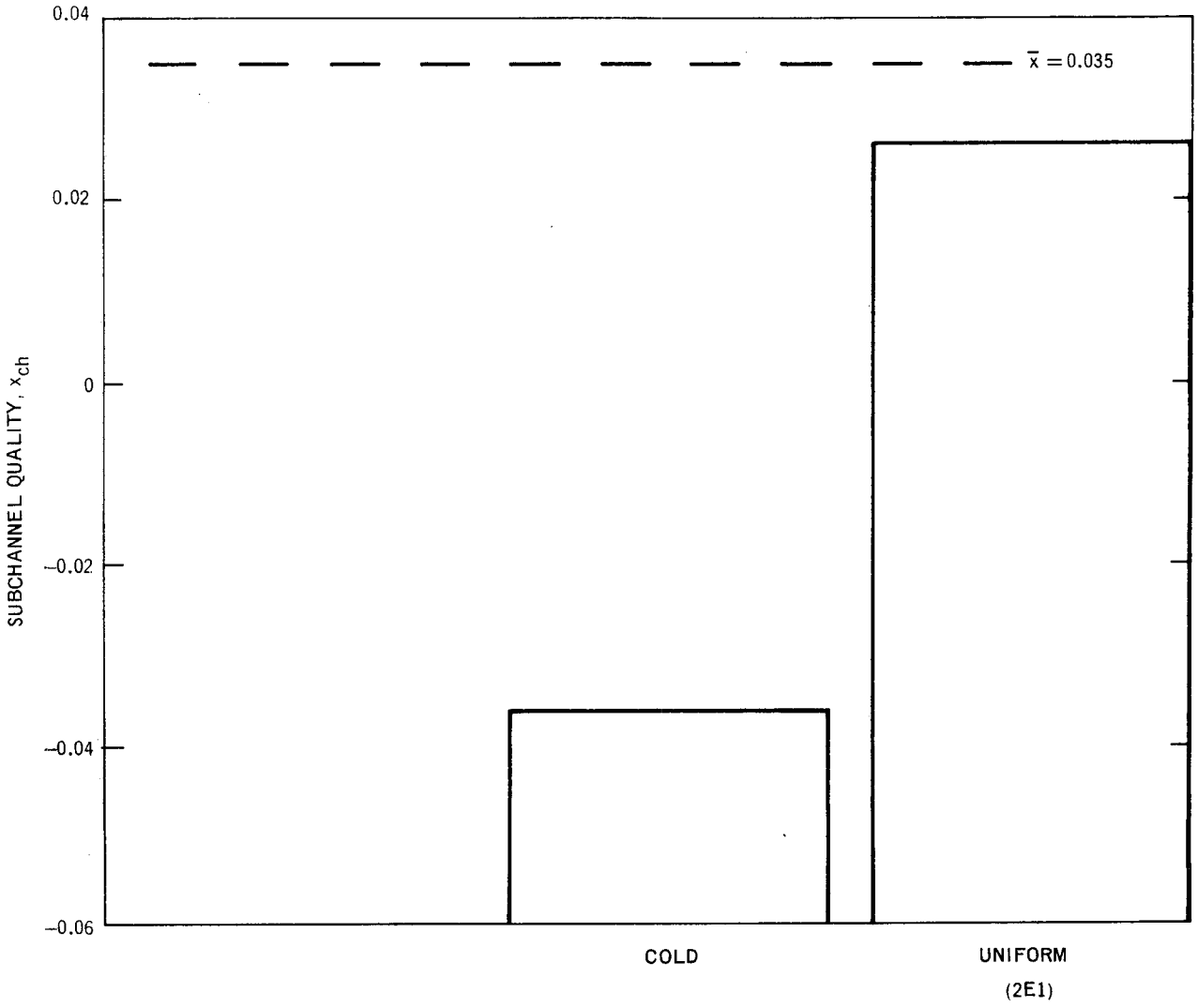

Figure 67. Comparison of Non-Uniform and Uniform Data: Side Subchannel Qualities 3E1

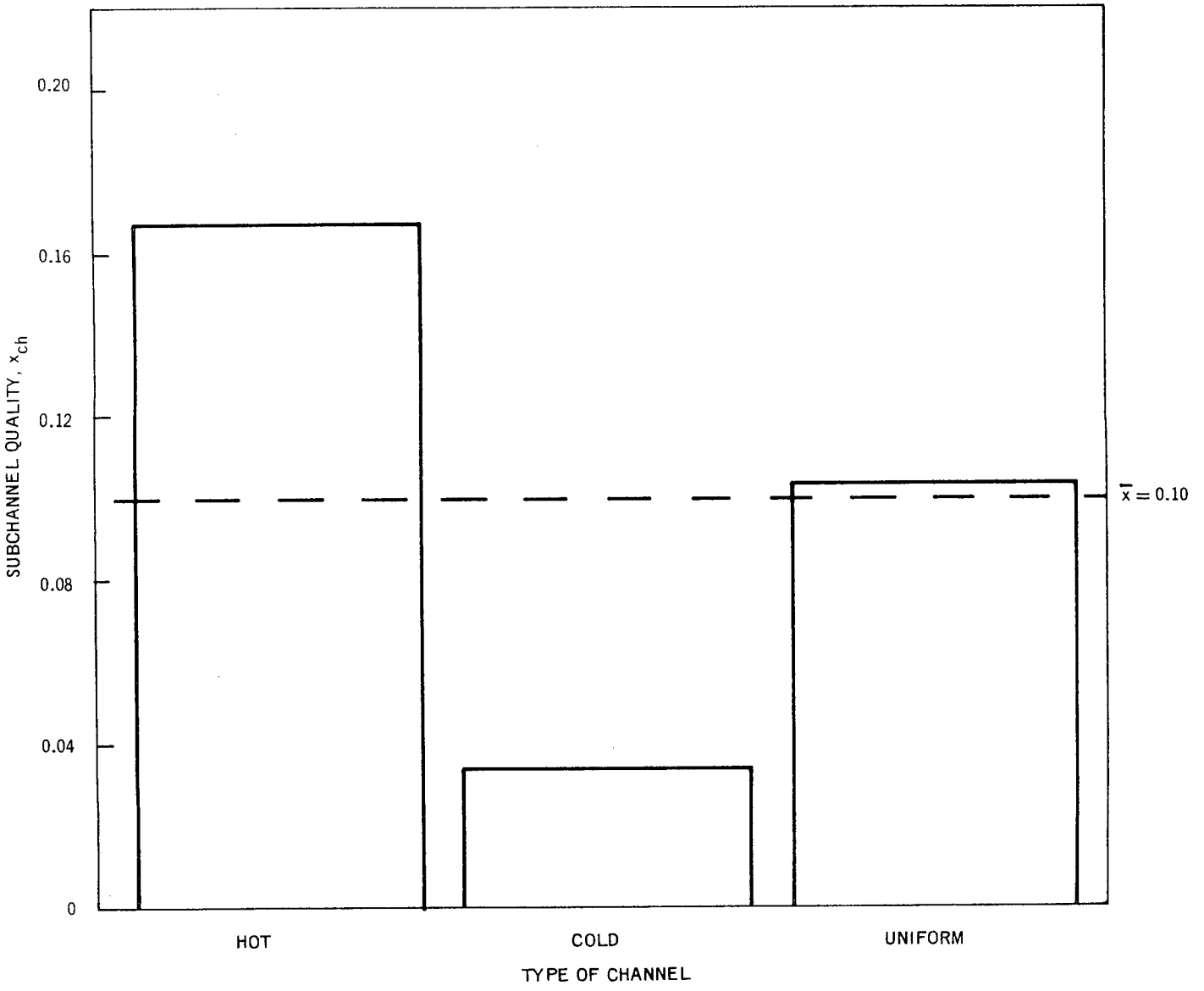

Figure 68. Comparison of Non-Uniform and Uniform Data: Side Subchannel Qualities 3E2

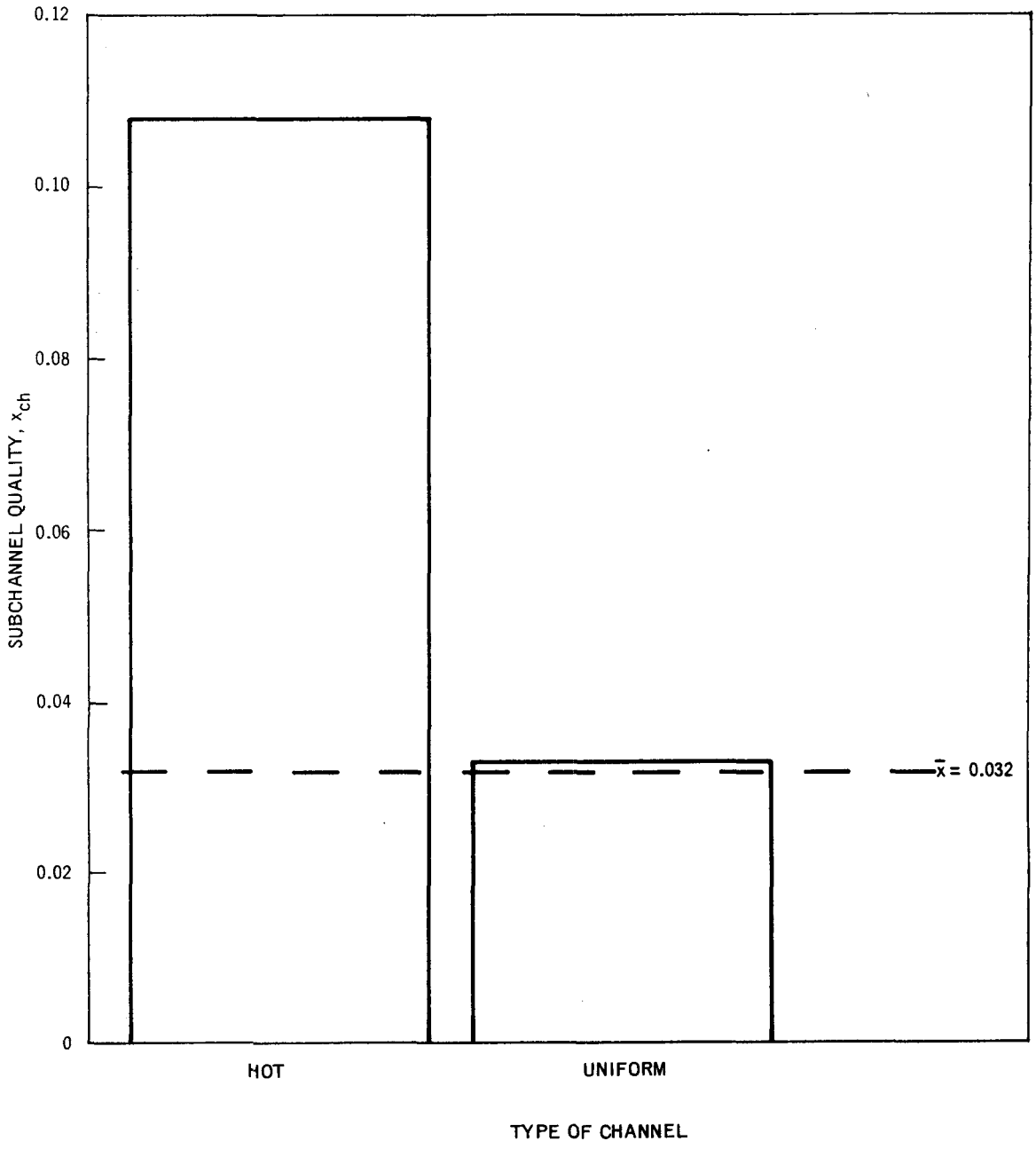

Figure 69. Comparison of Non-Uniform and Uniform Data: Center Subchannel Qualities 3B2

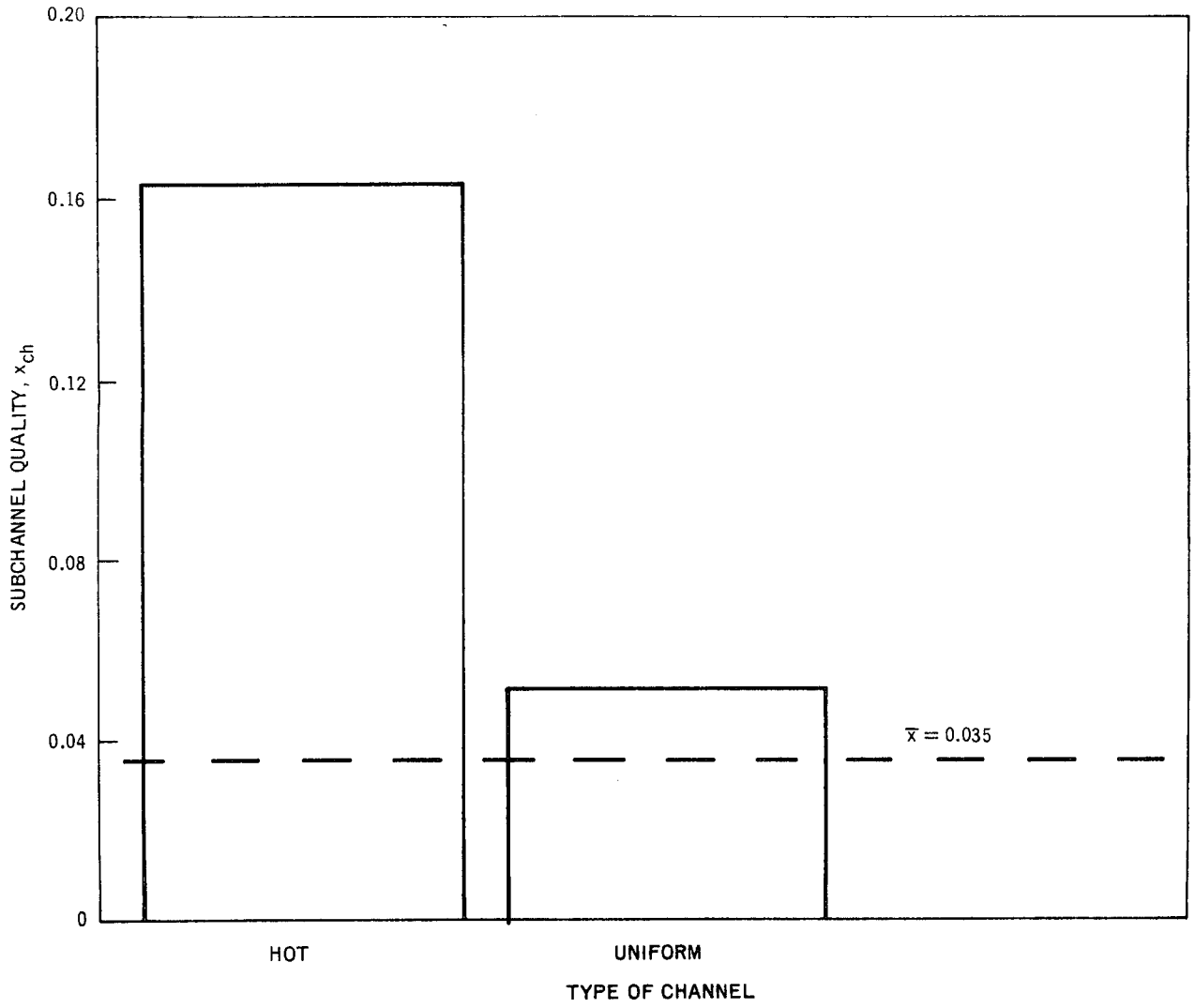

Figure 70. Comparison of Non-Uniform and Uniform Data: Center Subchannel Qualities 3E1

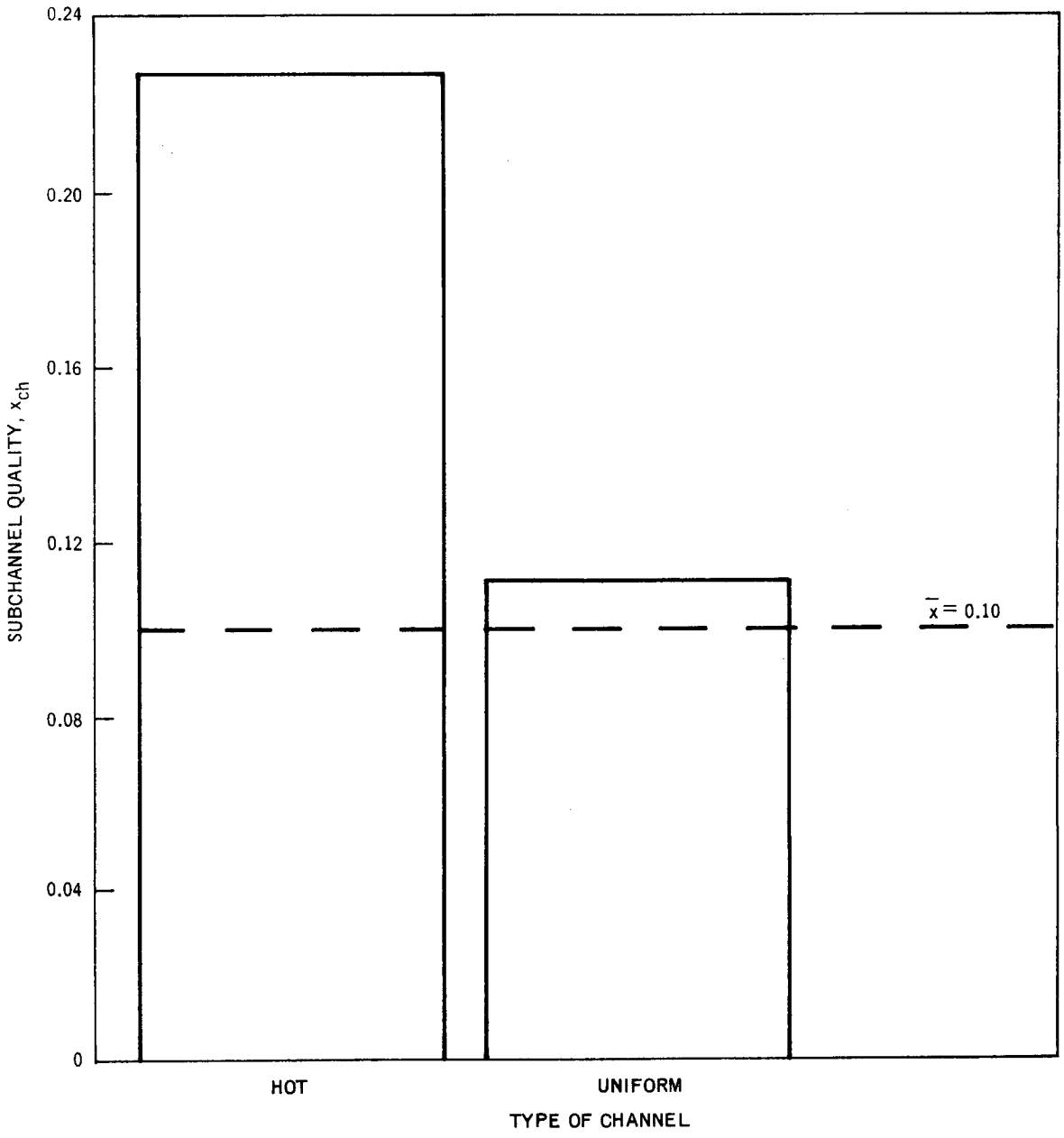

Figure 71. Comparison of Non-Uniform and Uniform Data: Center Subchannel Qualities 3E2

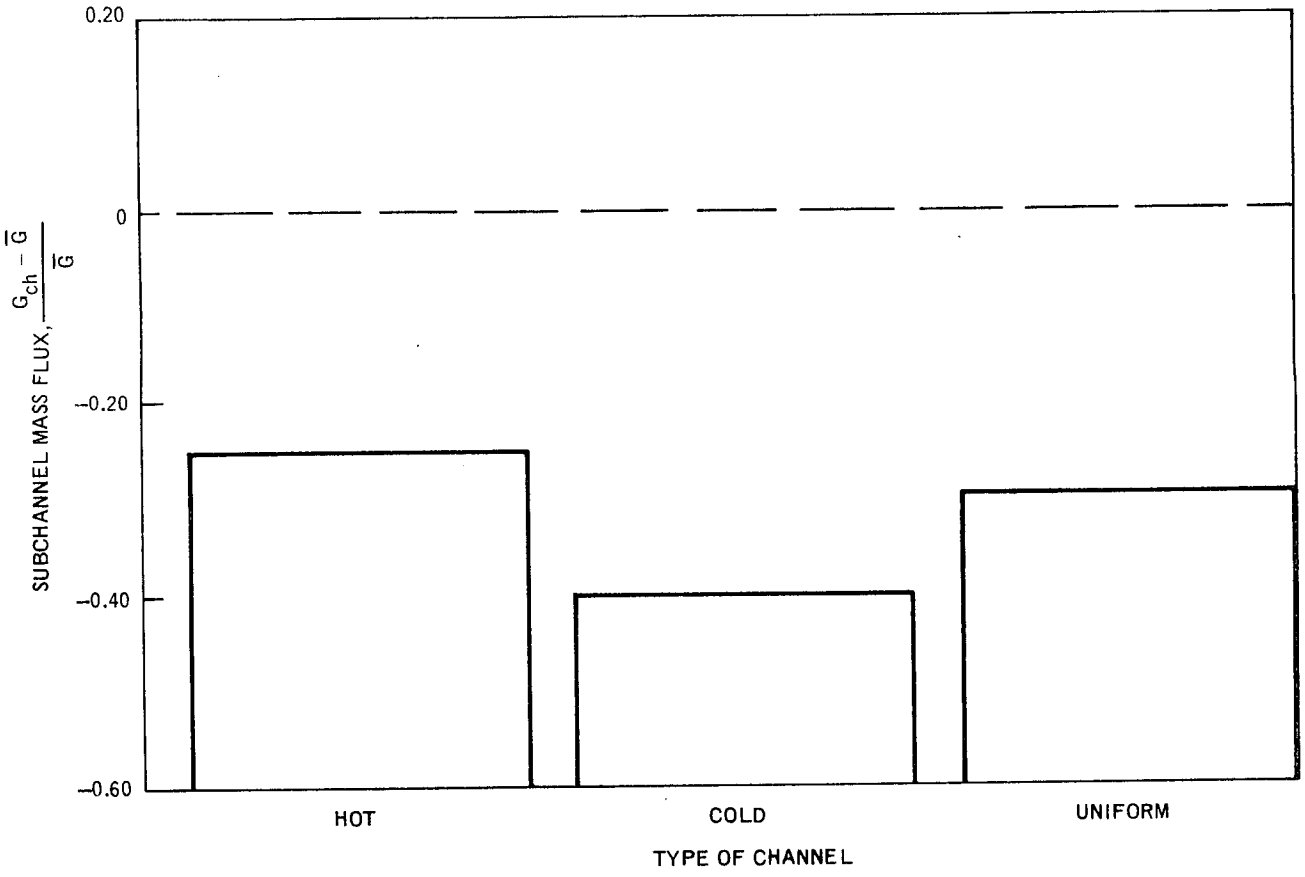

Figure 72. Comparison of Non-Uniform and Uniform Data: Corner Subchannel Mass Fluxes 3B2

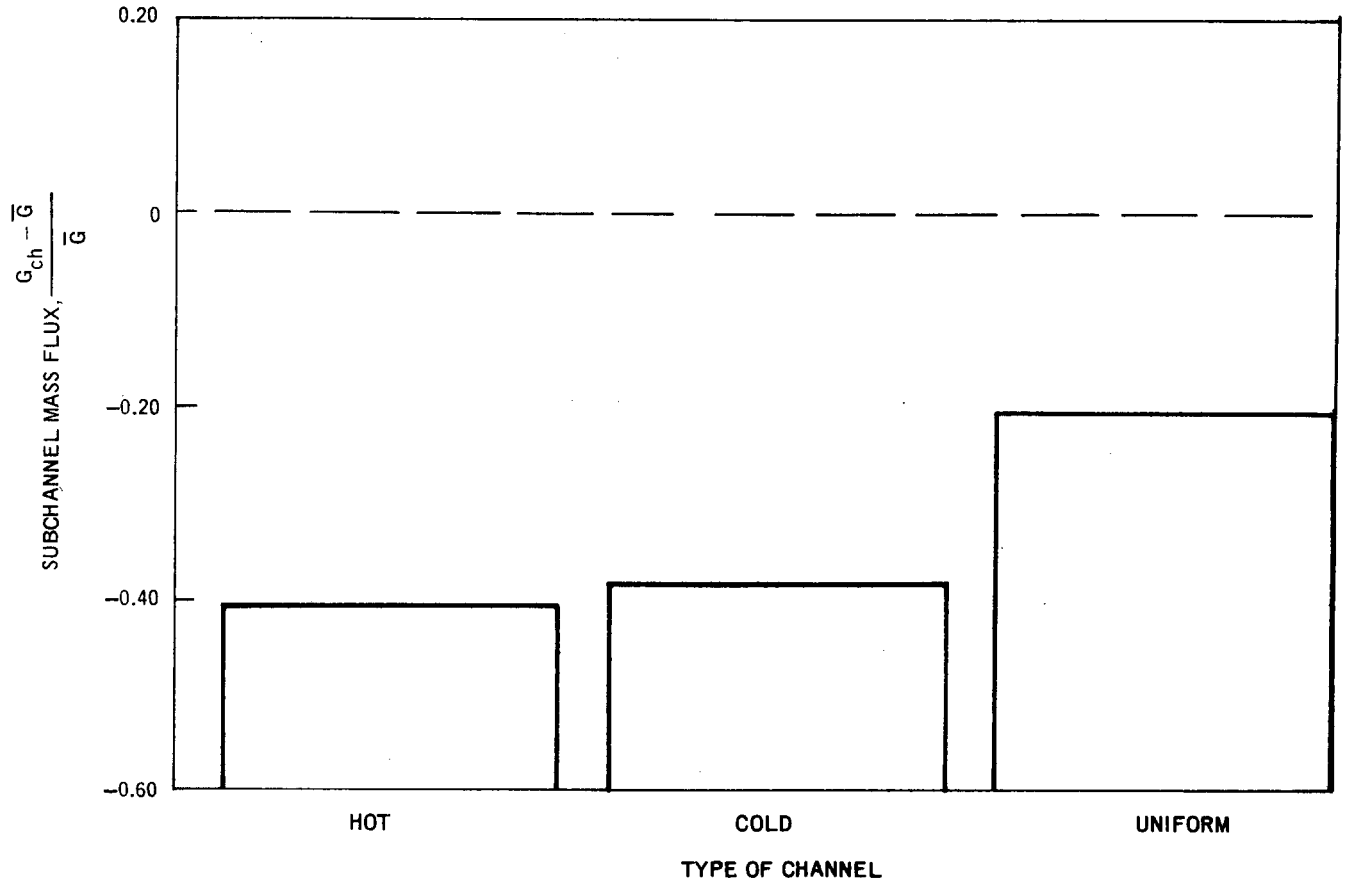

Figure 73. Comparison of Non-Uniform and Uniform Data: Corner Subchannel Mass Fluxes 3D1

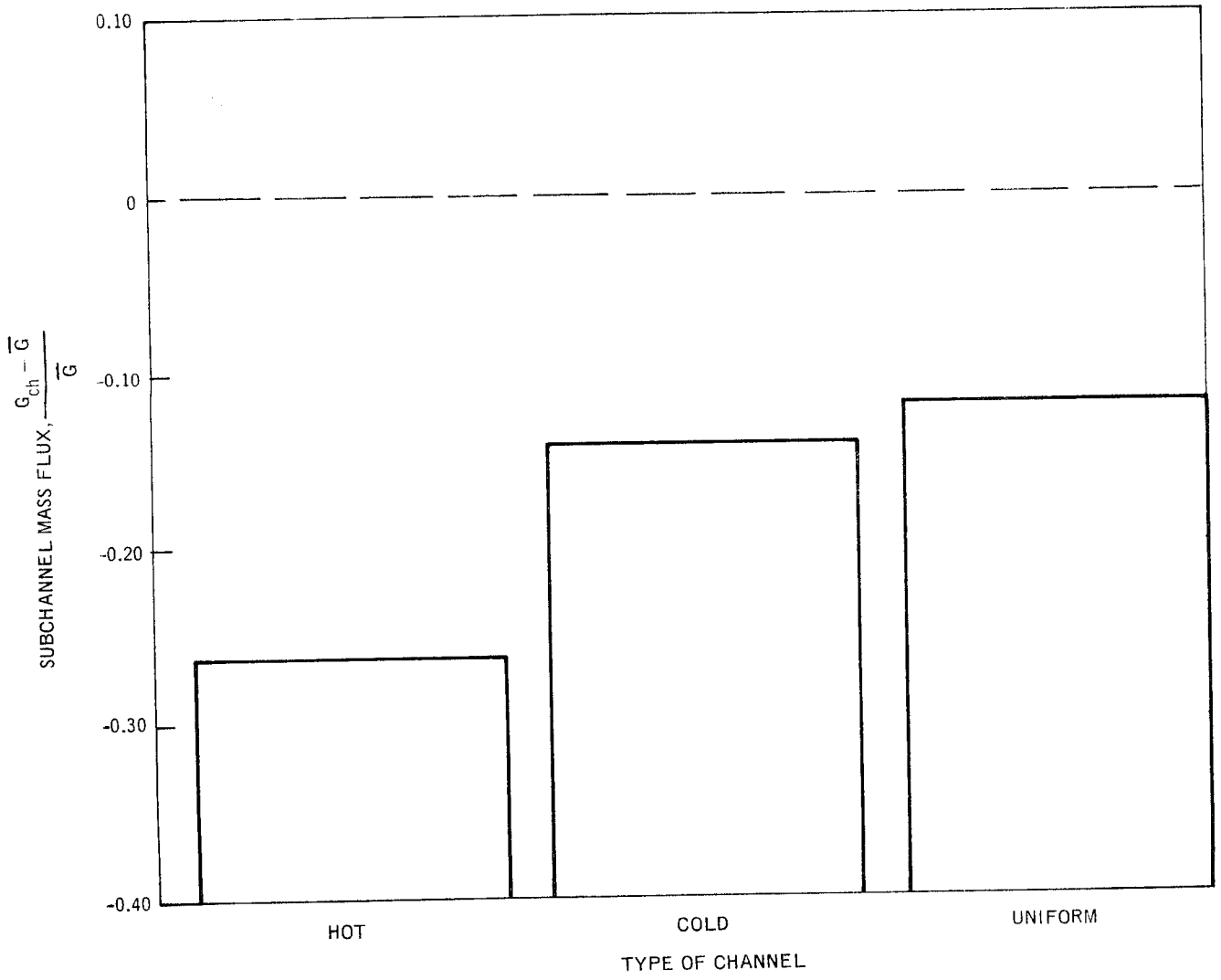

Figure 74. Comparison of Non-Uniform and Uniform Data: Corner Subchannel Mass Fluxes 3E1

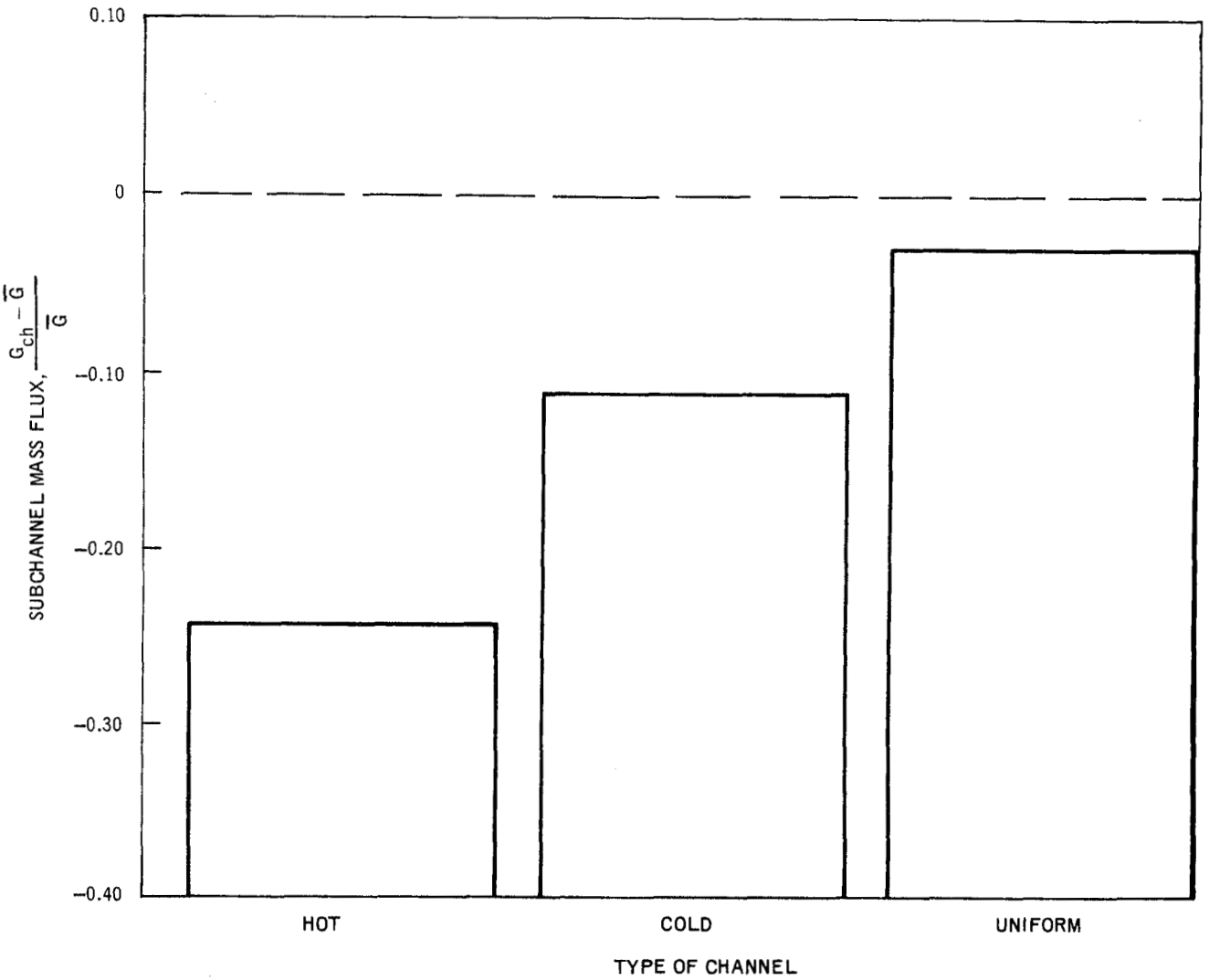

Figure 75. Comparison of Non-Uniform and Uniform Data: Corner Subchannel Mass Fluxes 3E2

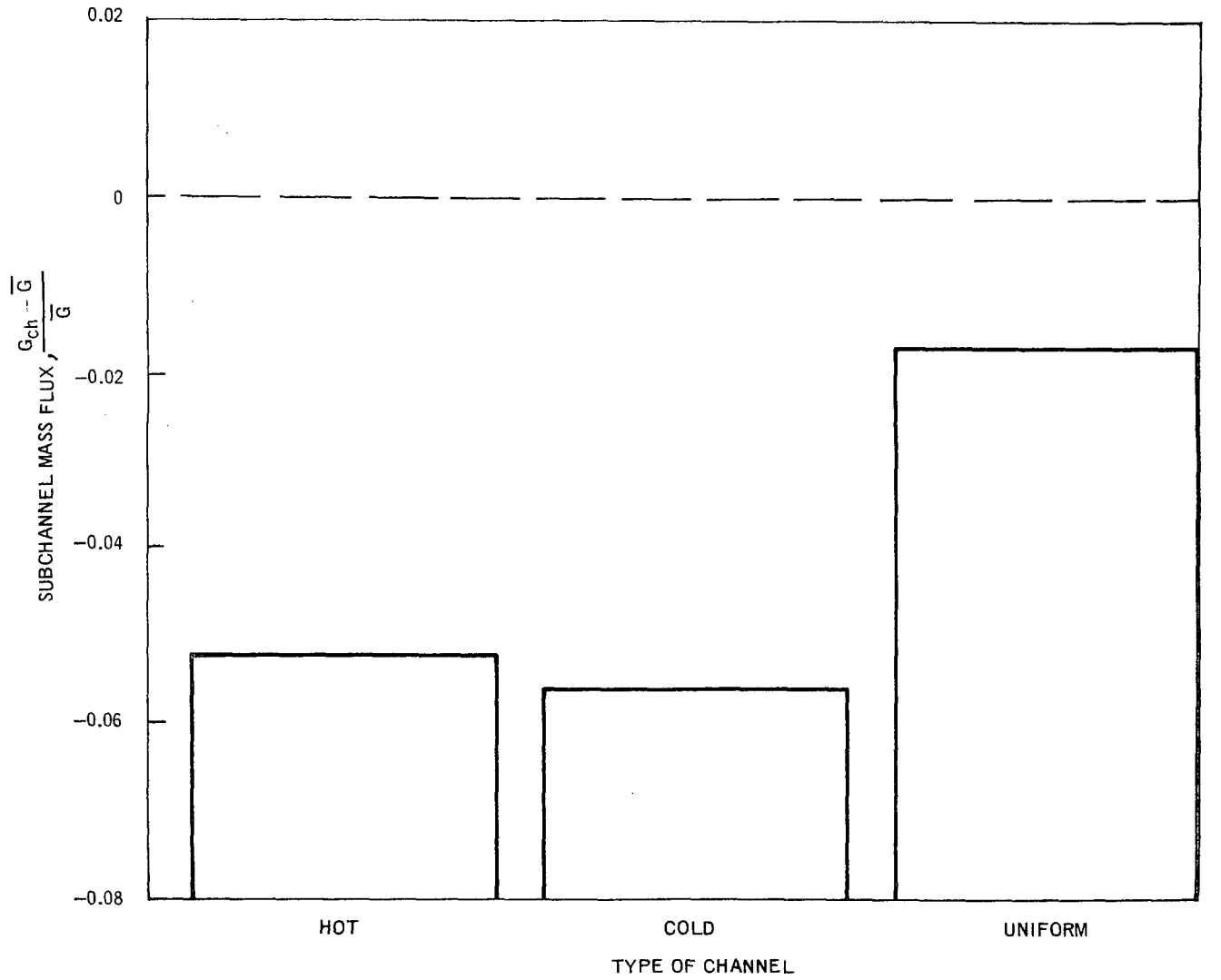

Figure 76. Comparison of Non-Uniform and Uniform Data: Side Subchannel Mass Fluxes 3B2

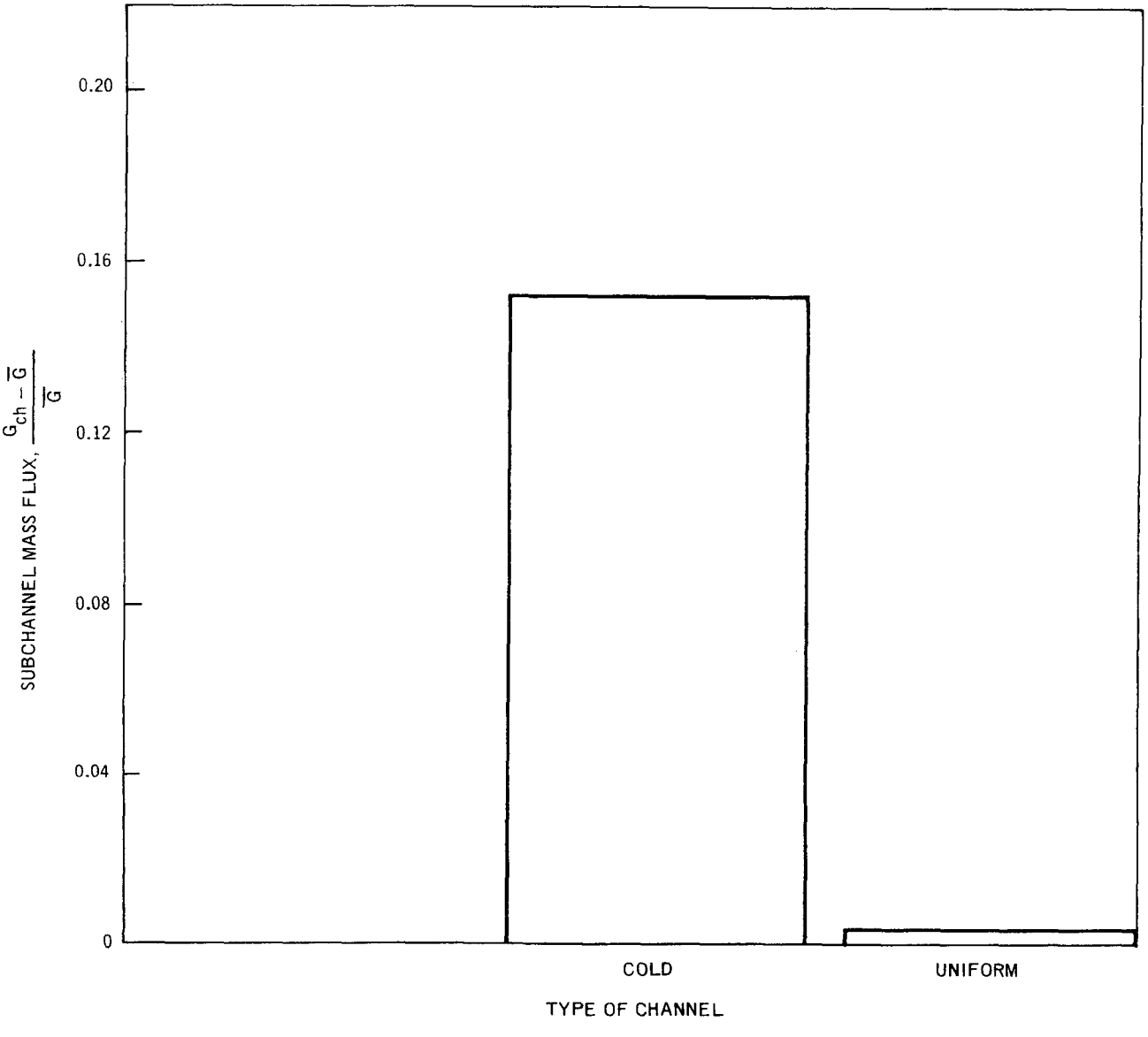

Figure 77. Comparison of Non-Uniform and Uniform Data: Side Subchannel Mass Fluxes 3D1

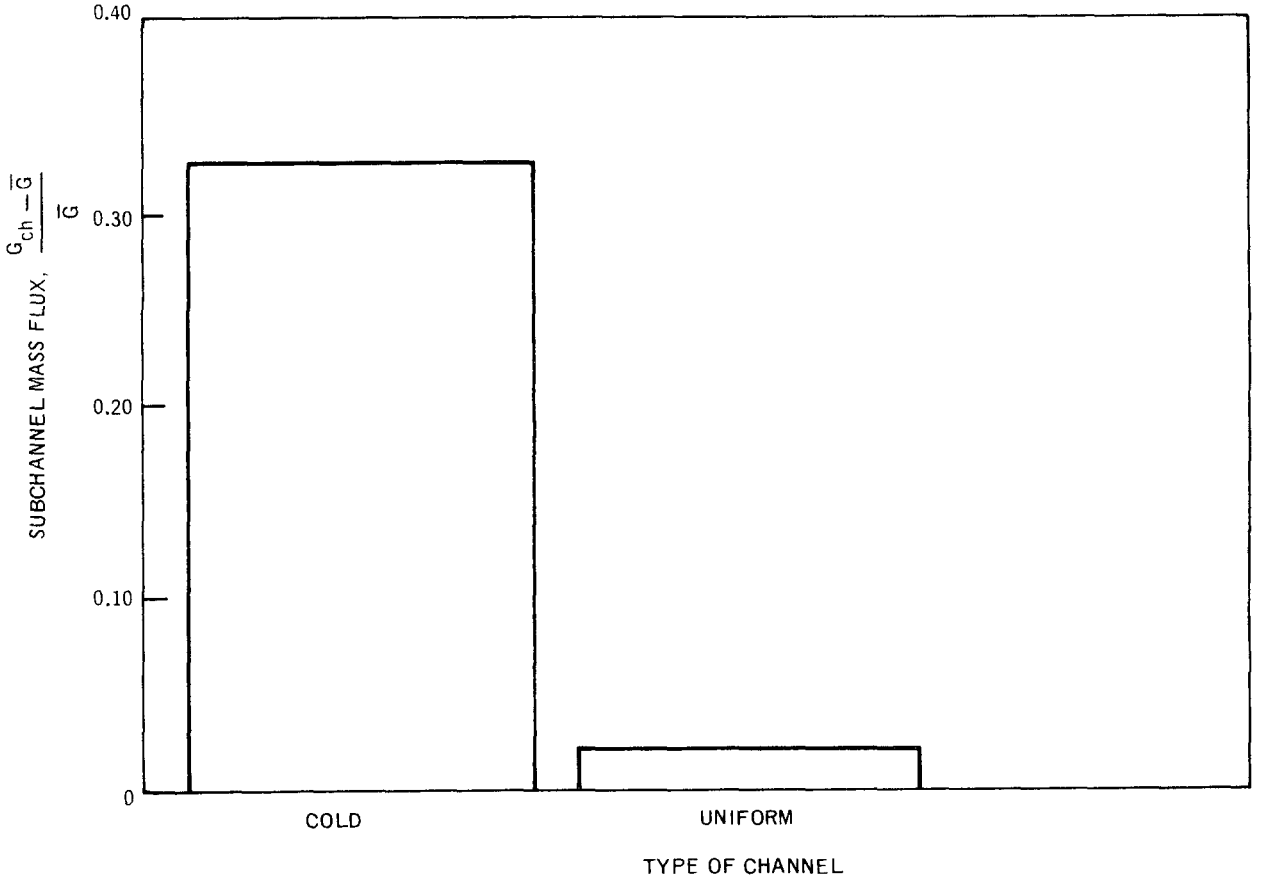

Figure 78. Comparison of Non-Uniform and Uniform Data: Side Subchannel Mass Fluxes 3E1

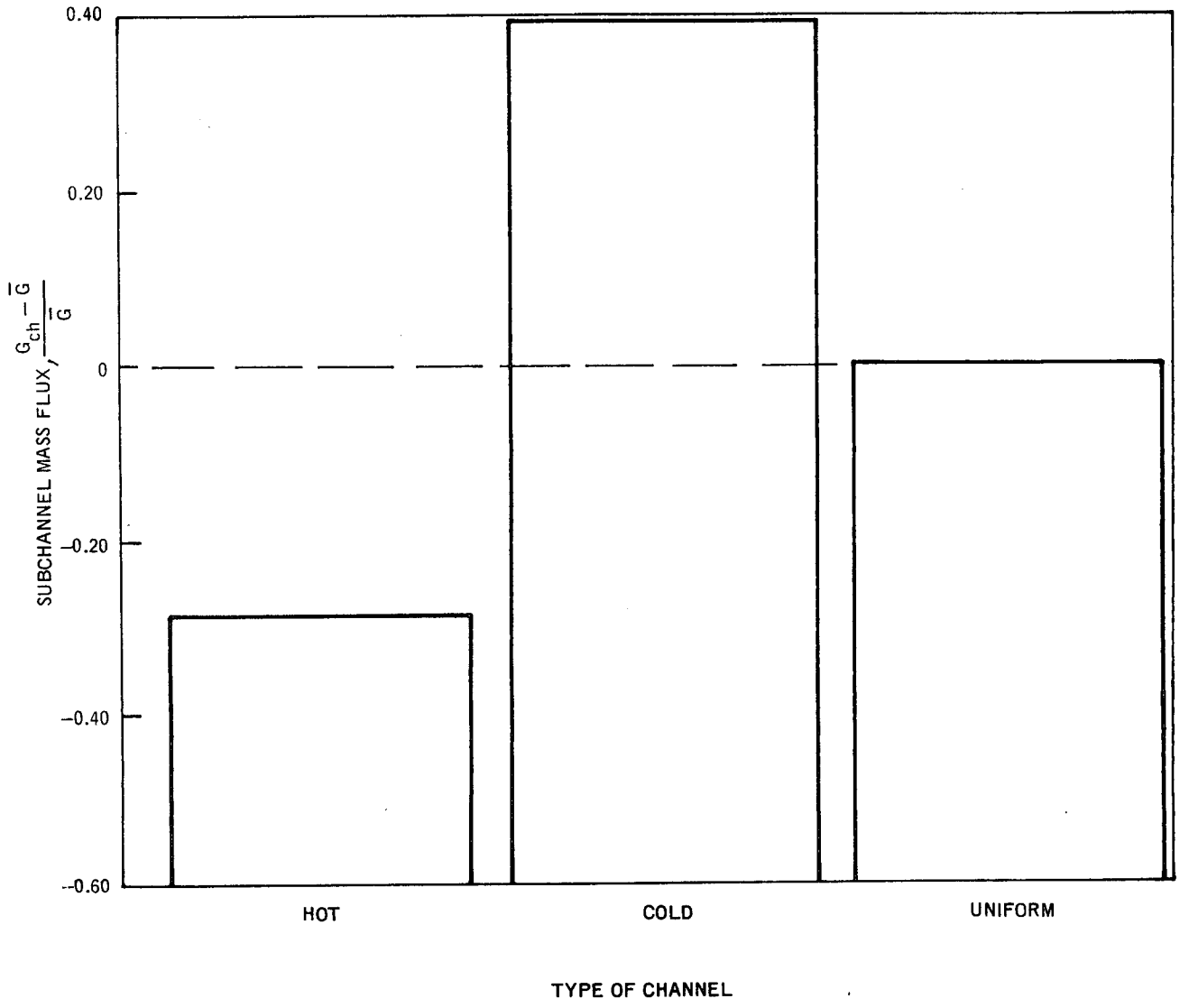

Figure 79. Comparison of Non-Uniform and Uniform Data: Side Subchannel Mass Fluxes 3E2

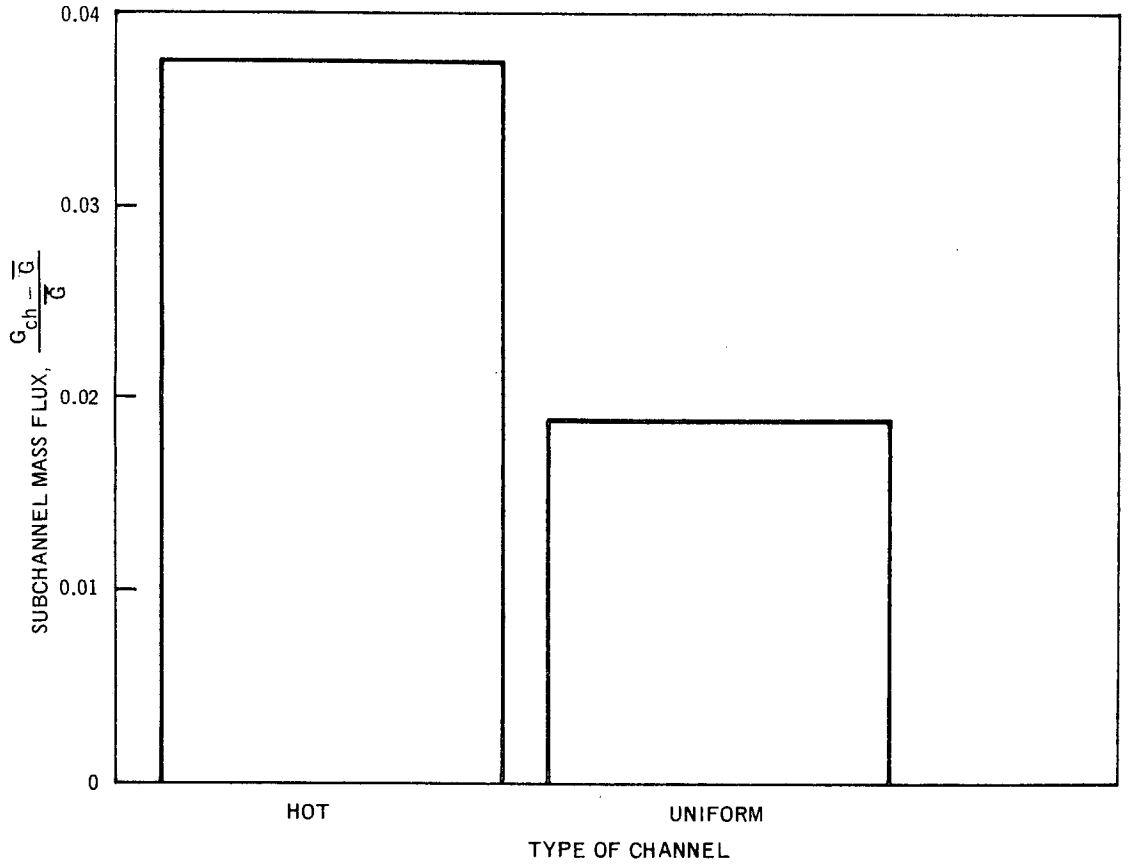

Figure 80. Comparison of Non-Uniform and Uniform Data: Center Subchannel Mass Fluxes 3B2

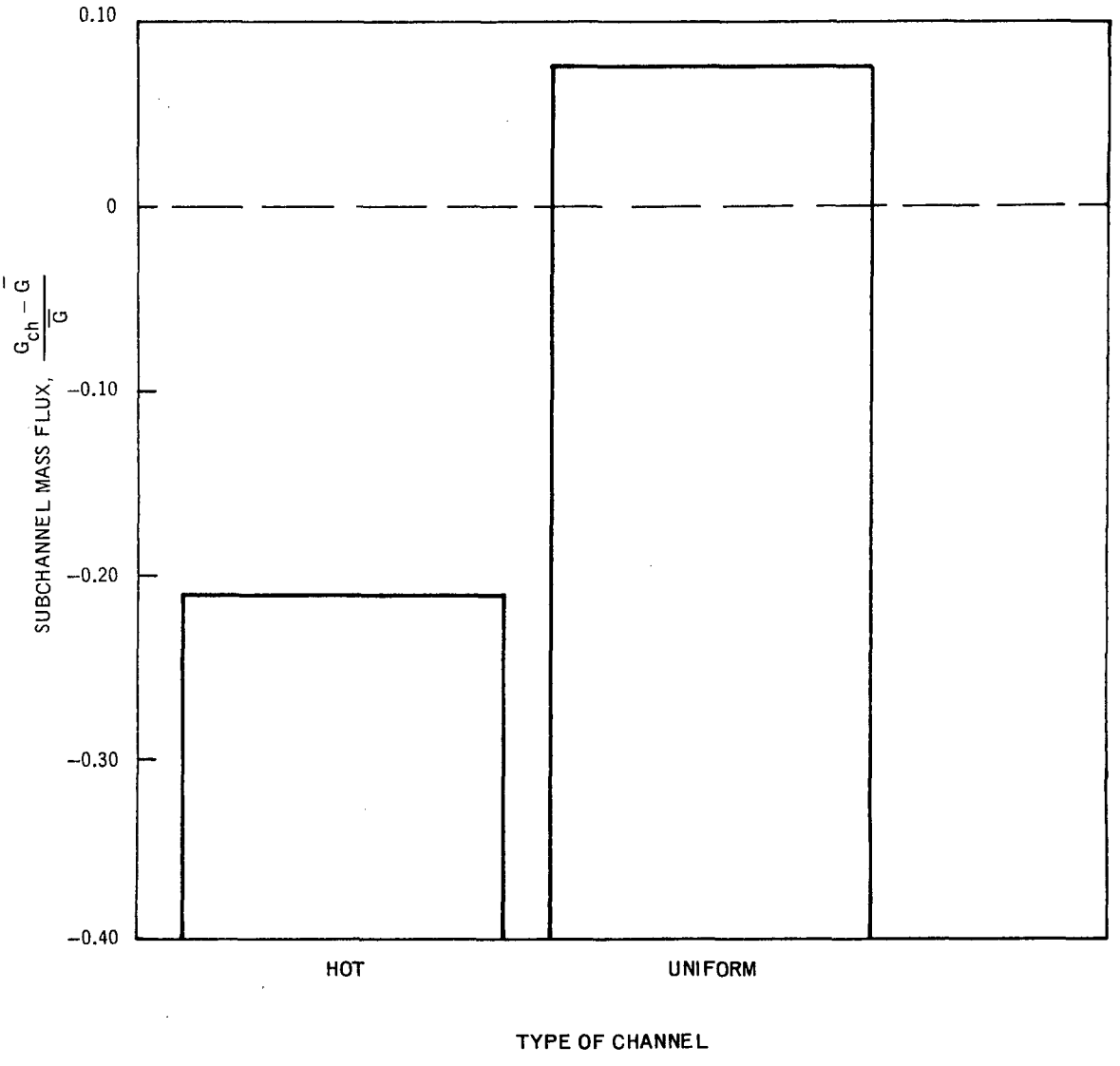

Figure 81. Comparison of Non-Uniform and Uniform Data: Center Subchannel Mass Fluxes 3E1

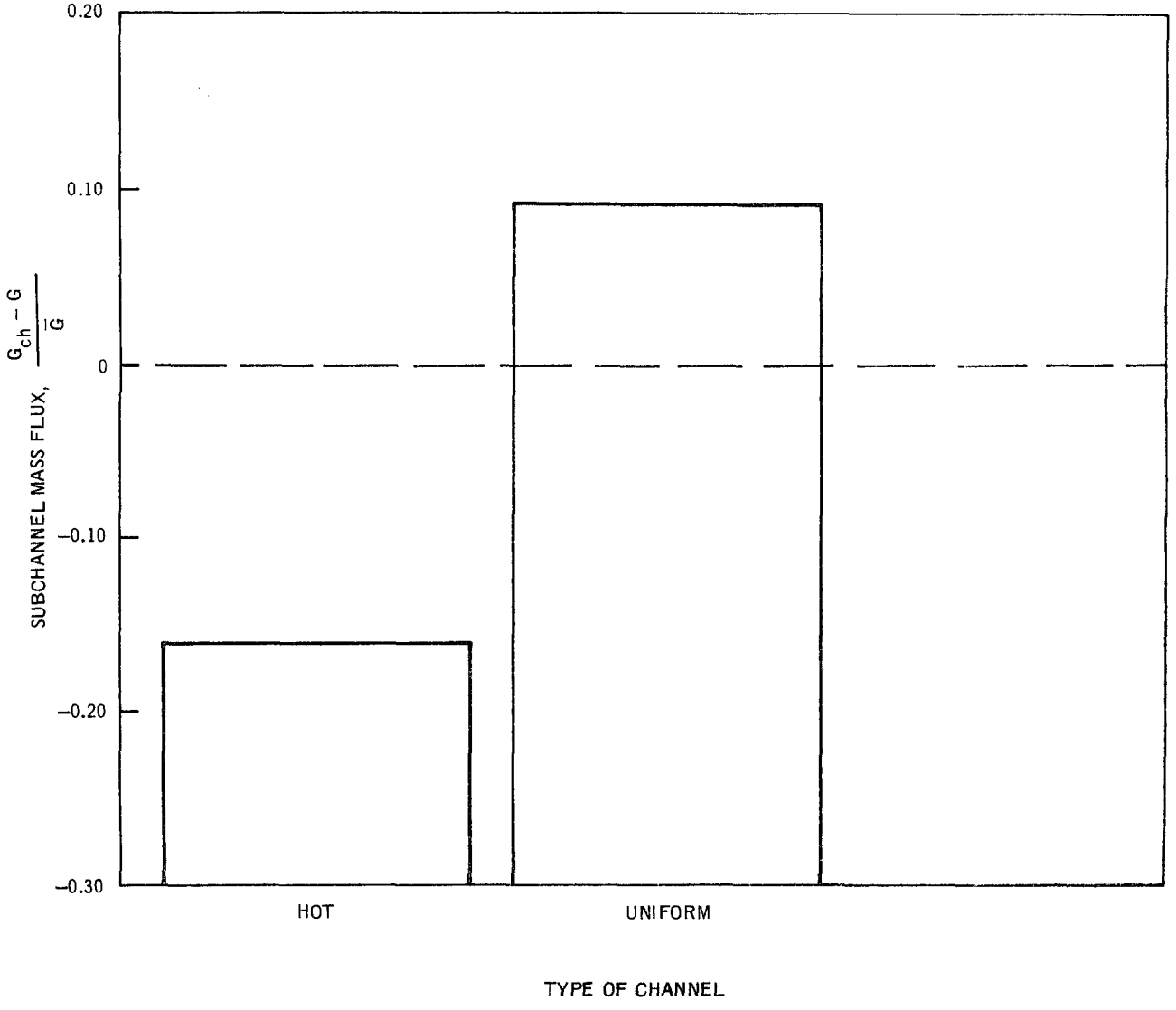

Figure 82. Comparison of Non-Unif[illegible] and Uniform Data: Center Subchannel Mass Flow 3E2

11. PRESSURE DROP DATA

Single-phase and two-phase pressure drop data have been taken in the nine-rod assembly. The single-phase data were taken both for adiabatic and diabatic conditions while the two-phase data were only taken for diabatic conditions. The single-phase friction factor (Moody) was obtained from adiabatic runs. The relative positions of the heater rods were maintained by 1/8 inch spacer pins, and so a pressure drop due to these pins must be subtracted in order to get the "clean" friction factor. The method used to obtain the portion of the pressure drop associated with the spacer pins is described in Appendix C. Table 12 gives a tabulation of the single-phase pressure drop data. Figure 83 shows the adiabatic friction factor for the "clean" channel, the equivalent friction factor for the channel including spacer pins, and the classical smooth tube friction factor. It is seen that the friction factor for the "clean" multirod assembly is slightly higher than for the smooth tube. Some multirod data in the literature indicate a friction factor below that for the smooth tube[19 20] while other pressure drop tests[25 26] indicate a friction factor that is higher than that for the smooth tube. The present data, which lie in the latter category, are self consistent and considered valid for the present nine-rod test section.

The same model for the spacer pins is used for determining the spacer-pin pressure drop for two-phase conditions. In this case the two-phase pressure drop multiplier is taken as the homogeneous multiplier.

The pressure drop data were taken for one-foot intervals along the heated length, and a total reading was made across the entire six-foot heated length. These readings were made with Pace Δp cells connected to the pressure taps via a seal-pot system as described in Section 2. The pressure-tap lines were routed to the instrumentation flange in the annular space between the test section and the pressure vessel wall inside the pressure vessel. The temperature gradient was measured along the water gap in the pressure vessel allowing corrections in the normal elevation head for the pressure tap lines to be made accurately. It has been found that the main problem in taking data with Pace cells is that any entrapped air must be bled off quite well or an erroneous signal will result and that, in addition, damage to the diaphragms is not unusual during the bleeding process. As a consequence, although much data was easily accumulated (in this case on a Hewlett-Packard DYMEC system), many data runs were found to be invalid. The criterion that was used to determine whether a set of pressure-drop measurements was valid or not, was to add up all the individual one-foot pressure drops and compare them with the overall heated-length pressure drop measured both with a Pace cell and a manometer. If these three agreed within a few percent, the data was considered valid. Otherwise, it was suspect and discarded.

The method used for reduction of the pressure drop data follows.

(1) The static pressure drop was plotted against axial length for the entire heated length. A smooth curve was fitted to this data, and in most cases the scatter was not excessive.

(2) The start of subcooled boiling was determined using the method described by Levy.[21] The density-head pressure drop and the axial-acceleration pressure drop were subtracted from the two-phase static pressure gradient. The void-quality relation due to Zuber-Findlay as described by Levy[21] was used. The density head p_ρ, for the two-phase region was integrated numerically as:

$$p_\rho = \frac{g}{g_c} \int_o^{L_b} \left\{ \rho_f \left[1 - \alpha(z)\right] + \rho_g \alpha(z) \right\} dz$$

The appropriate acceleration head p_{acc} was taken to be that of a separated flow model:

$$p_{acc} = \frac{1}{g_c} \left(\frac{G^2}{\rho'} \right) \Bigg|_{z=L_b} - \left(\frac{G^2}{\rho_f} \right) \Bigg|_{z=O}$$

where

G = Axial Mass Flux lb/ft^2-h

L_b = Boiling Length,

ρ' = Momentum Density, lb/ft^3

$$\frac{1}{\rho'} \triangleq \left[\frac{(1-x)^2}{\rho_f (1-\alpha)} + \frac{x^2}{\rho_g \alpha} \right]$$

z = A variable of integration having an origin at the start of subcooled boiling, ft.

(3) The number of 1/8-inch spacer pins in the boiling length were determined, and the local pressure drop associated with these pins was computed by

Table 12
SINGLE PHASE PRESSURE DROP DATA
(Nine-Rod Subchannel 6 Foot Length at 1000 psig)

Run	G × 10 $^{-6}$ (lb/ft^2-h)	Δp_t (psi)	Δp_h (psi)	Δp_f (psi)	T (°F)	μ (lb/ft-h)	Re × 10^{-3}	f_t	f_p	f
1A	0.25	–	–	0.0709	67	2.23	4.34	0.0584	0.0059	0.0526
1B	0.50	–	–	0.2128	67	2.23	8.77	0.0430	0.0055	0.0375
1C	1.0	–	–	0.7130	67	2.23	17.54	0.0360	0.0056	0.0305
1D	1.5	–	–	1.596	67	2.23	27.12	0.0337	0.0061	0.0277
1E	2.0	–	–	2.540	67	2.23	35.08	0.0321	0.0067	0.0254
1D (repeated)	1.5	–	–	1.610	75	2.23	27.11	0.0341	0.0061	0.0280
No. 1	1.378				248	0.579	94.3			
Pace Total		3.711	2.461	1.250				0.0308	0.0076	0.0232
Overall		3.695	2.461	1.233				0.0304	0.0076	0.0228
No. 2	1.302				348	0.381	135.3			
Pace Total		3.458	2.332	1.126				0.0295	0.0077	0.0219
Overall		3.412	2.332	1.080				0.0283	0.0077	0.0207
No. 3	2.489				326	0.411	240.0			
Pace Total		5.944	2.363	3.580				0.0260	0.0077	0.0184
Overall		5.912	2.363	3.585				0.0261	0.0077	0.0184
No. 4	1.150				449	0.290	157.0			
Pace Total		3.041	2.158	0.8830				0.0274	0.0077	0.0198
Overall		3.021	2.158	0.8628				0.0268	0.0077	0.0192
No. 5	1.110				494	0.260	170.0			
Pace Total		2.909	2.062	0.8464				0.0270	0.0077	0.0193
Overall		2.886	2.062	0.8231				0.0263	0.0077	0.0186
No. 6	1.389				490	0.262	210.1			
Pace Total		3.346	2.072	1.274				0.0261	0.0077	0.0184
Overall		3.353	2.072	1.281				0.0262	0.0077	0.0185
No. 7	1.548				206	0.72	85.2			
Pace Total		4.063	2.509	1.555				0.0310	0.0076	0.0234
Overall		4.007	2.509	1.499				0.0299	0.0076	0.0223
No. 8	1.545				204	0.722	84.8			
Pace Total		4.141	2.510	1.631				0.0326	0.0076	0.0251
Overall		4.135	2.510	1.625				0.0325	0.0076	0.0249
No. 9	2.067				208	0.710	115.3			
Pace Total		5.237	2.507	2.730				0.0305	0.0077	0.0228
Overall		5.266	2.507	2.759				0.0308	0.0077	0.0232
No. 10	1.536				249	0.521	116.7			
Pace Total		4.058	2.460	1.597				0.0317	0.0077	0.0241
Overall		4.045	2.460	1.585				0.0315	0.0077	0.0238
No. 11	2.005				251	0.568	139.8			
Pace Total		5.038	2.458	2.580				0.0300	0.0077	0.0224
Overall		5.045	2.458	2.587				0.0301	0.0077	0.0225
No. 12	0.662				250	0.570	46.0			
Pace Total		2.787	2.459	0.3285				0.0351	0.0071	0.0280
Overall		2.763	2.459	0.3042				0.0325	0.0071	0.0254

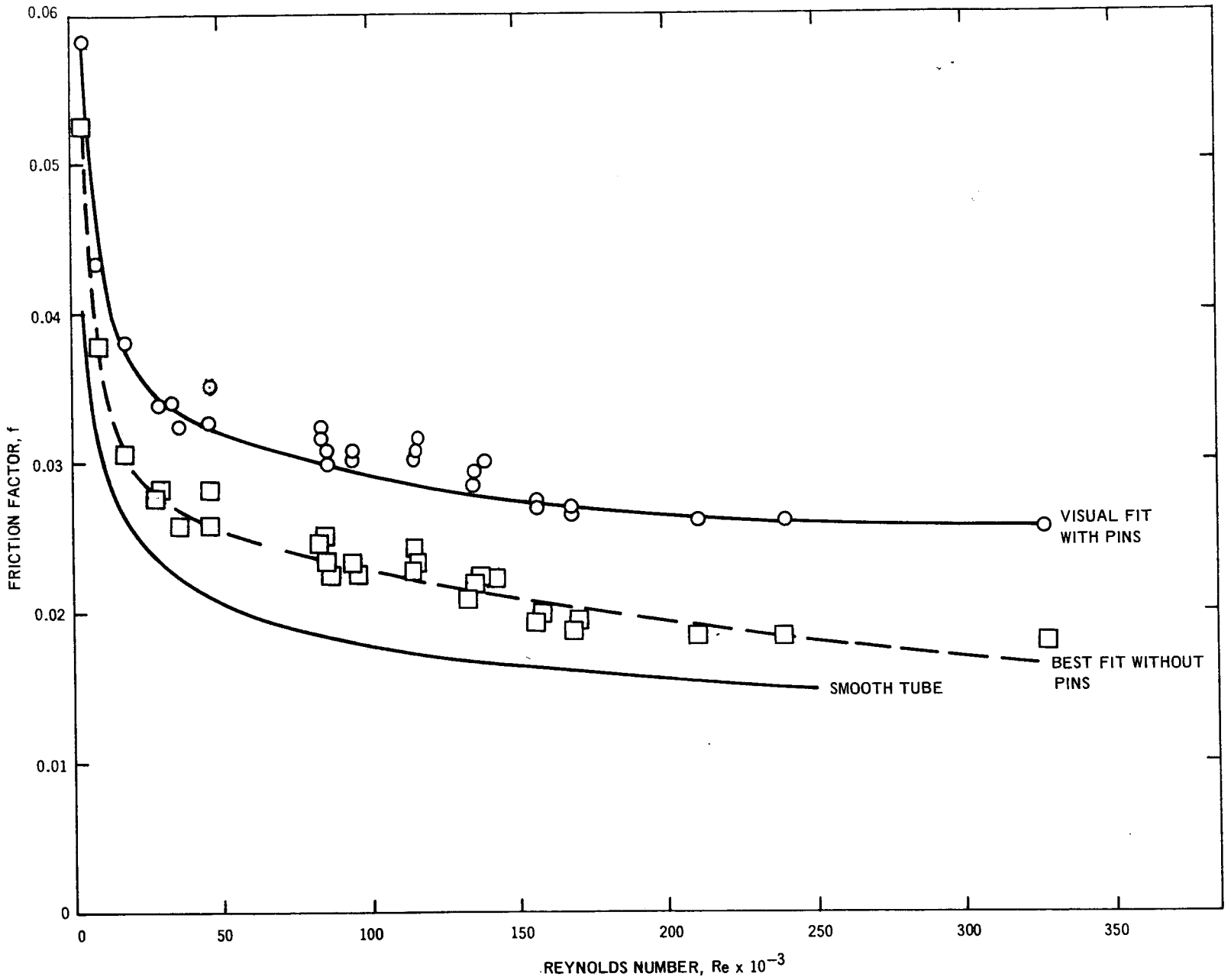

Figure 83. Single Phase Adiabatic Friction Factor for Nine-Rod Test Section

multiplying the single-phase pressure drop due to spacer pins by the homogeneous multiplier at each pin location. The sum of these local drops was subtracted from the reading to yield the two-phase friction pressure drop.

(4) The two-phase friction pressure-drop data was plotted against axial length in the boiling region. This data was fitted by the method of "least squares" with a fourth degree polynomial which was constrained to agree with the single-phase pressure-drop gradient at zero flow quality.

(5) The derivative of the above fit was formed to obtain $(dp/dz)_{2\phi}$. This was normalized by the single phase pressure gradient $(dp/dz)_0$ to form the classical ϕ_{Lo}^2 multiplier (Martinelli-Nelson notation) at each quality of interest.

Table 13 gives a detailed tabulation of the data and the intermediate steps as described in items (1) to (5) above.

This reduced data has been plotted in Figures 84, 85, and 86. It can be seen, within the scatter of the data introduced by the differentiation process, that the classical Martinelli-Nelson curve for 1000 psia, does a good job of correlating the data based on flow quality. It is very interesting to note that there appears to be only a very mild flow effect in the two-phase multiplier, which is contrary to the simple-geometry results of other investigators.[23] It is consistent, however, with previous heated rod-bundle results.[11,12] Presumably the differences are due not only to geometry but to the void-quality model used, since the calculation of ϕ_{Lo}^2 is quite sensitive to calculation of the density head. In this regard, it is felt that the flow-dependent void-quality relation given by Levy[21] is more accurate than the flow-independent table look-up values used by other investigators. For the sake of completeness, Table 14 gives a tabulation of some unreduced static pressure-drop data. These data were not processed since it was felt that enough reduced data at these flows were already available. However, it has been documented here for the reader.

12. SUMMARY AND CONCLUSIONS

The present study of subchannel and pressure drop measurements was conducted in an electrically-heated nine-rod assembly that was constructed specifically for this test series. At the start of the program, exploratory calibration runs indicated that great care was needed in data aquisition and reduction. A technique was developed in which daily calibration runs were made to establish the isokinetic setting and to determine the "heat loss" to be used in data reduction. In order to simplify the test rig and operations, only a single subchannel was sampled at a time. This proved to be a reliable method of data aquisition but had the undesirable feature that the same test conditions had to be established each time a new subchannel was sampled. Nevertheless, subsequent checks of the conservation of mass and energy have indicated that the data taken in this manner are valid.

Subchannel test data were taken for both isokinetic (natural flow split) and non-isokinetic conditions. The isokinetic data gave the normal local conditions that occured in the test bundle. The non-isokinetic data were used to determine the flow diversion enthalpy and the sensitivity of the isokinetic setting. At the same subchannel measurements were being made, detailed pressure drop data were taken for both adiabatic and diabatic conditions. It was found that these pressure drop readings were quite insensitive to the sample flow, indicating that the axial length for flow-diversion was small.

The main conclusions that can be drawn for the data have been tabulated below:

A. Conclusions From Isokinetic Data (Uniform Radial)

1. The corner subchannel runs at a mass flux below the bundle average mass flux and at a quality below the bundle average quality.
2. The side subchannel has mass flux and quality approximately equal to or slightly below the bundle average.
3. The center subchannel has both mass flux and quality above the bundle average values.
4. There is an observable, though somewhat inconsistent, tendency for the subchannels to approach bundle average conditions in the regions of slug-annular flow-regime transition. This effect is less pronounced than that observed in two-subchannel tests.[2,17]

TABLE 13. REDUCTION OF PRESSURE DROP DATA

	(1)	(2)	(3)		(4)	(5)	(6)	(7)	(8)	(9)	(10)	(11)	(12)	(13)	(14)	(15)	(16)	(17)*	(18)	(19)	(20)
Run No.	$G \times 10^{-6}$	$R_e \times 10^{-3}$	x_e	x_{flow}	Δh_{sub} (Btu/lb)	$q'' \times 10^{-6}$ (Btu/ft^2-h)	L (ft)	L_b (ft)	Pin Location (ft)	x_p	v_{hp} (ft^3/lb)	Δp_t (6 ft) (psi)	$\Sigma\delta\ p_t$ (psi)	$\Sigma\delta\ p_{acc}$ (psi)	$\Sigma\delta\ p_{el}$ (psi)	f_p (1-)	$\Sigma\delta\ p_{pins}$ (psi)	$\Sigma\delta\ p_f$ (2-) (psi)	$\Sigma\delta\ p_f$ (2-) (fit) (psi)	x_{flow} (%)	LO
2A2-1	0.263	43.3	9.8	10	290	0.229	4.13	0	–	–	–	2.12	1.590	0	0	0.007	–	–			
							4.5	0.37	4.15	0.0010	0.0220		1.715	0.002	0.120		0.0022	0.0008	0.0038	0.4	1.895
							5.0	0.87	4.15	0.0010	0		1.873	0.009	0.259		0.0022	0.0128	0.0111	2.5	2.067
							5.5	1.37	5.15	0.0515	0.0434		2.005	0.017	0.372		0.0066	0.0194	0.0205	5.9	2.528
							6.0	1.87	5.15	0.0515	0		2.120	0.027	0.464		0.0066	0.0324	0.0315	10	2.878
2A2-2	0.281	46.1	6.9	7.3	293	0.229	4.32	0	–	–	–	2.18	1.650	0	0	0.0071	–				
							4.70	0.38	–	–	–		1.790	0.0022	0.1254		0	0.0024	0.0049	0.3	1.844
							5.00	0.68	–	–	–		1.880	0.0060	0.215		0	0.0170	0.0111	1.1	2.714
							5.50	1.18	5.15	0.0315	0.0350		2.035	0.0140	0.341		0.0041	0.0259	0.0276	3.7	4.567
							6.00	1.68	5.15	0.0315	0		2.180	0.0230	0.444		0.0041	0.0589	0.0537	7.3	6.923
2A3-1	0.235	38.7	44.4	44.4	463	0.229	0.8	0	–	–	–	1.632	0.279	0	0	0.0068	–	–	–	–	
							2.0	1.2	1.15	0.3000	0.0343		0.665	0.012	0.331		0.0027	0.0403	0.0494	5.5	10.634
									2.15	0.1150	0.07036						0.0083				
							3.3	2.5	3.15	0.2000	0.1064		1.250	0.0372	0.5454		0.0167	0.1717	0.1663	17.8	15.566
							4.6	3.8	4.15	0.2860	0.1429		1.370	0.070	0.690		0.0280	0.3030	0.3010	30.8	14.776
							6.0	5.2	5.15	0.3724	0.1795		1.632	0.114	0.806		0.0422	0.3909	0.4094	44.4	7.523
2A3-3	0.242	40.0	41.6	41.6	460	0.227	0.942	0	–	–	–	1.63	0.323	0	0	0.0069	–	–	–	–	–
									1.15	0.0185	0.0294						0.0025				
							2.2	1.258	2.15	0.1000	0.0640		0.735	0.0144	0.3406		0.0081	0.0490	0.0464	6.0	9.0
							3.4	2.458	3.15	0.1820	0.0988		1.075	0.0376	0.5372		0.0166	0.1606	0.1456	16.9	14.06
							4.7	3.758	4.15	0.2640	0.1335		1.387	0.070	0.6852		0.0281	0.2807	0.2886	29.2	16.689
							6.0	5.058	5.15	0.346	0.1683		1.630	0.111	0.796		0.0426	0.3574	0.4422	41.6	16.368
2B2-1	0.525	86.4	3.3	3.8	417	0.224	3.98	0	–	–	–	2.31	1.555	0	0	0.0076	–	–			
							4.5	0.52	4.15	0.003	0.0229		1.760	0.006	0.170		0.0101	0.0189	0.0164	0.2	1.212
							5.0	1.02	4.15	0.003	0		1.940	0.019	0.318		0.0101	0.0379	0.0375	0.9	1.735
							5.5	1.52	5.15	0.021	0.0305		2.130	0.036	0.448		0.0235	0.0675	0.0686	2.1	2.571
							6.0	2.02	5.15	0.021	0		2.31	0.054	0.562		0.0235	0.1155	0.1142	3.8	3.720
2B4-1	0.536	88.2	21.4	21.4	514	0.227	0.133	0	–	–	–	2.395	0.050	0	0	0.0076	–	–	–		
							1.5	1.367	1.15	0.034	0.0360		0.530	0	0.342		0.0165	0.1215	0.0926	2.5	3.402
							3	2.867	2.15	0.0675	0.0502		1.090	0.057	0.635		0.0395	0.3085	0.2997	8.6	5.621
									3.15	0.101	0.0644						0.0691				
							4.5	4.367	4.15	0.134	0.0784		1.720	0.128	0.852		0.1051	0.5850	0.5979	15.0	7.403
							6	5.867	5.15	0.1677	0.0927		2.395	0.205	1.027		0.1476	0.9654	0.9673	21.4	8.749
2B4-2	0.537	88.3	19.7	19.7	517	0.219	0.14	0	–	–	–	2.46	0.05	0	0	0.0076	–	–	–	–	
							1.5	1.36	1.15	0.033	0.0356		0.620	0.034	0.353		0.0164	0.1166	0.0994	1.9	3.662
							3.0	2.86	2.15	0.066	0.0496		1.255	0.045	0.663		0.0392	0.3578	0.3151	7.3	5.638
									3.15	0.0984	0.0633						0.0684				
							4.5	4.36	4.15	0.1310	0.0771		1.860	0.112	0.893		0.1039	0.6011	0.5993	13.5	6.607
2C2-1	1.047	173.2	11.0	11.0	533	0.221	0.13	0	–	–	–	3.725	0.05	0	0	0.0077	–	–	–	–	
							1.5	1.37	1.15	0.0185	0.0294		0.77	0.061	0.351		0.0524	0.2556	0.1909	1.4	1.763
							3	2.87	2.15	0.0368	0.0372		1.61	0.211	0.684		0.1187	0.5463	0.5232	4.5	2.629
									3.15	0.0549	0.0449						0.1987				
							4.5	4.37	4.15	0.0730	0.0526		2.61	0.351	0.953		0.2925	0.9635	0.9890	7.7	3.526
							6.0	5.87	5.15	0.0913	0.0603		3.725	0.491	1.181		0.3999	1.603	1.593	11.0	4.453
2C2-2	1.053	173.2	9.4	9.4	527	0.222	0.14	0	–	–	–	3.773	0.0650	0	0	0.0077	–	–	–	–	
							1.5	1.36	1.15	0.0170	0.0288		0.8100	0.009	0.353		0.0513	0.3317	0.2105	0.7	2.03
							3.0	2.86	2.15	0.0340	0.0360		1.700	0.140	0.720		0.1155	0.6595	0.5884	3.1	2.915
									3.15	0.0510	0.0432						0.1925				
							4.5	4.36	4.15	0.0680	0.0504		2.660	0.276	1.012		0.2823	1.025	1.081	6.2	3.538
							6.0	5.86	5.15	0.0852	0.0577		3.773	0.414	1.258		0.3851	1.651	1.647	9.4	3.899

* (17) = (12)$|_{L_b}$ − (12)$|_0$ − (13) − (14) − (16)

TABLE 13.–(Continued)

Run No.	① G × 10^{-6}	② R_e × 10^{-5}	③ x_e	③ x_{flow}	④ Δh_{sub} (Btu/lb)	⑤ q″ × 10^{-6} (Btu/ft²-h)	⑥ L (ft)	⑦ L_b (ft)	⑧ Pin Location (ft)	⑨ x_p	⑩ v_{hp} (ft³/lb)	⑪ Δp_t (6 ft) (psi)	⑫ $\Sigma\delta p_t$ (psi)	⑬ $\Sigma\delta p_{acc}$ (psi)	⑭ $\Sigma\delta p_{el}$ (psi)	⑮ f_p (1.5)	⑯ $\Sigma\delta p_{pins}$ (psi)	⑰* $\Sigma\delta p_f$ (2.5) (psi)	⑱ $\Sigma\delta p_f$ (2.5) (ft) (psi)	⑲ x_{flow} (%)	⑳ LO
2C2-4	1.057	173.9	8.5	8.5	520	0.229	0.3	0	–	–	–	3.744	0.1300	0	0	0.0077	–	–			
							1.5	1.2	1.15	0.0132	0.0272		0.8150	0.049	0.383		0.0488	0.2042	0.1649	0.4	1.697
							3.0	2.7	2.15	0.0275	0.0333		1.710	0.170	0.774		0.1086	0.5274	0.4867	2.3	2.512
									3.15	0.044	0.0403						0.1808				
							4.5	4.2	4.15	0.0595	0.0468		2.670	0.305	1.086		0.2650	0.8840	0.9278	5.3	3.263
							6.0	5.7	5.15	0.0749	0.0534		3.744	0.444	1.343		0.3608	1.4662	1.479	8.5	3.950
2C2-7	1.068	175.7	9.1	9.1	524	0.227	0.13	0	–	–	–	3.84	0.055	0	0	0.00765	–	–	–		
							1.5	1.37	1.15	0.0160	0.0284		0.785	0.014	0.370		0.0521	0.2939	0.1783	0.5	1.562
							3.0	2.87	2.15	0.0320	0.0352		1.635	0.145	0.743		0.1166	0.5754	0.4890	2.9	2.497
									3.15	0.0479	0.0419						0.1934				
							4.5	4.37	4.15	0.0639	0.0487		2.610	0.285	1.041		0.2827	0.9463	0.9707	5.9	3.766
							6.0	5.87	5.15	0.0799	0.0555		3.840	0.425	1.290		0.3844	1.686	1.675	9.1	5.369
2D1-1	0.525	86.4	11.6	12.0	302	0.456	3.46	0	–	–	–	2.47	1.44	0	0	0.0076	–	–	–	–	
							4.17	0.71	4.15	0.0310	0.0347		1.73	0.018	0.226		0.0153	0.0307	0.0298	0.8	1.963
							4.83	1.37	4.15	0.0310	0		1.99	0.055	0.393		0.0153	0.0867	0.0802	3.6	3.362
							5.33	1.87	5.15	0.0760	0.0538		2.19	0.089	0.492		0.0389	0.1301	0.1385	6.9	4.683
							6.00	2.54	5.15	0.0760	0		2.470	0.142	0.598		0.0389	0.2511	0.2512	12.0	6.903
2D3-4	0.535	88.01	32.9	32.9	436	0.461	0.98	0	–		–	2.83	0.380	0	0	0.0076	–	–	–	–	
							1.5	0.52	1.15	0.0100	0.0258		0.580	0.011	0.174		0.0118	0.0032	0.0204	0.3	1.626
							3.0	2.02	2.15	0.0755	0.0536		1.189	0.101	0.526		0.0363	0.1457	0.1521	7.6	4.422
									3.15	0.1398	0.0809										
							4.5	3.52	4.15	0.2045	0.1083		1.885	0.239	0.732		0.1228	0.4112	0.4441	19.9	8.693
							6.0	5.02	5.15	0.2700	0.1361		2.830	0.417	0.872		0.1850	0.9760	0.9634	32.9	14.44
2D3-5	0.532	87.5	32.7	32.7	436	0.458	0.98	0	–	–	–	2.82	0.370	0	0	0.0076	–	–	–	–	–
							2.0	1.02	1.15	0.0120	0.0267		0.765	0.032	0.315		0.0121	0.0360	0.0563	1.6	2.75
							3.0	2.02	2.15	0.076	0.0538		1.185	0.098	0.527		0.0363	0.1537	0.1691	7.4	4.85
									3.15	0.140	0.0810						0.0729				
							4.5	3.52	4.15	0.205	0.1085		1.803	0.234	0.735		0.1219	0.4421	0.4700	19.6	8.705
							6.0	5.02	5.15	0.270	0.1361		2.820	0.408	0.876		0.1833	0.9827	0.9629	32.7	13.4
2C1-1	1.046	172.1	5.4	5.5	503	0.225	1.67	0	–	–	–	3.17	0.775	0	0	0.0077	–	–	–	–	
							3.0	1.33	2.15	0.0059	0.0241		1.469	0.057	0.419		0.0424	0.1756	0.1580	0.5	1.393
							4.0	2.33	3.15	0.0176	0.0290		2.006	0.134	0.685		0.0934	0.3186	0.3140	1.7	1.741
							5.0	3.33	4.15	0.0291	0.0339		2.570	0.220	0.913		0.1531	0.5089	0.5071	3.5	2.134
							6.0	4.33	5.15	0.0410	0.0390		3.170	0.309	1.110		0.2216	0.7544	0.7416	5.5	2.572
2C2-8	1.071	176.2	10.1	10.1	530	0.227	0.13	0	–	–	–	3.86	0.055	0	0	0.00765	–	–	–	–	
							1.5	1.37	1.15	0.0180	0.0224		0.770	0.035	0.359		0.0413	0.2797	0.1875	0.9	1.662
							3.0	2.87	2.15	0.0359	0.0368		1.629	0.180	0.712		0.1091	0.5729	0.5160	3.7	2.585
									3.15	0.0534	0.0442						0.1906				
							4.5	4.37	4.15	0.0510	0.0432		2.610	0.324	0.994		0.2703	0.9667	1.005	6.8	3.717
							6.0	5.87	5.15	0.0889	0.0593		3.860	0.467	1.232		0.3796	1.726	1.687	10.1	5.057
2E1-1	1.053	173.2	4.2	5.0	422	0.451	3.165	0	–	–	–	3.37	1.56	0	0	0.00765	–	–	–	–	–
							3.83	0.66	–	–	–		1.91	0.029	0.220		–	0.1010	0.0655	0.2	1.061
							4.5	1.33	4.15	0.0140	0.0275		2.29	0.092	0.417		0.0490	0.1720	0.1557	0.9	1.703
							5.17	2.00	5.15	0.0284	0.0336		2.72	0.179	0.585		0.1089	0.2871	0.3092	2.3	2.932
							6.0	2.83	5.15	0.0284	0		3.37	0.300	0.760		0.1089	0.6411	0.6465	5.0	5.267
2G1-1	1.07	175.9	3.4	5.2	346	0.666	3.61	0	–	–	–	3.59	1.860	0	0	0.00765	–	–	–	–	
							4.16	0.55	4.15	0.0076	0.0248		2.210	0.0305	0.1868		0.0456	0.0871	0.0745	0.2	1.635
							4.83	1.22	4.15	0.0076	0		2.660	0.1375	0.3851		0.0456	0.2318	0.2197	1.1	2.579
							5.51	1.90	5.15	0.0219	0.0309		3.170	0.2319	0.5491		0.1023	0.4267	0.4409	3.1	3.729
							6.00	2.39	5.15	0.0219	0		3.590	0.328	0.648		0.1023	0.6517	0.6539	5.2	4.677

* ⑰ = ⑫ $|_{L_b}$ − ⑫ $|_0$ − ⑬ − ⑭ − ⑯.

TABLE 13.–(Continued)

	①	②	③		④	⑤	⑥	⑦	⑧	⑨	⑩	⑪	⑫	⑬	⑭	⑮	⑯	⑰	⑱	⑲	⑳
Run No.	$G \times 10^{-6}$	$R_e \times 10^{-3}$	x_e	x_{flow}	Δh_{sub} (Btu/lb)	$q'' \times 10^{-6}$ (Btu/ft²-h)	L (ft)	L_b (ft)	Pin Location (ft)	x_p	v_{hp} (ft³/lb)	Δp_t (6 ft) (psi)	$\Sigma\delta\ p_t$ (psi)	$\Sigma\delta\ p_{acc}$ (psi)	$\Sigma\delta\ p_{el}$ (psi)	f_p (1-ϕ)	$\Sigma\delta\ p_{pins}$ (psi)	$\Sigma\delta\ p_f$ (2-ϕ) (psi)	$\Sigma\delta\ p_f$ (2-ϕ) [fit] (psi)	x_{flow} (%)	LO
2G1-3	1.06	174.2	4.1	5.7	348	0.667	3.48	0	–	–	–	3.575	1.765	0	0	0.00765	–	–			
							4.00	0.52	–	–	–		2.110	0.026	0.177		–	0.1420	0.0777	0.1	1.697
							4.67	1.19	4.15	0.0110	0.0263		2.600	0.101	0.377		0.0474	0.3096	0.2387	1.0	2.762
							5.33	1.85	5.15	0.0275	0.0333		3.075	0.217	0.542		0.1074	0.4436	0.4444	2.9	3.295
							6.00	2.52	5.15	0.0275	0		3.575	0.346	0.675		0.1074	0.6816	0.6788	5.7	3.513
2G3-2	1.073	176.5	15.5	15.7	420	0.670	1.638	0	–	–	–	4.35	0.83	0	0	0.00765	–	–			
							3.00	1.362	2.15	0.0180	0.0292		1.722	0.124	0.427		0.0540	0.2870	0.2599	1.3	2.570
							4.00	2.362	3.15	0.0520	0.0436		2.506	0.311	0.652		0.1347	0.5783	0.5731	4.7	3.387
							5.00	3.362	4.15	0.0860	0.0581		3.360	0.540	0.821		0.2422	0.9269	0.9568	9.9	3.92
2H1-3	2.118	348.4	3.2	4.3	459	0.660	2.29	0	–	–	–	6.56	1.89	0	0	0.00765	–	–			
							3.17	0.88	3.15	0.0070	0.0246		2.75	0.113	0.290		0.1774	0.2796	0.2999	0.1	1.169
							4.16	1.87	4.15	0.0155	0.0282		3.90	0.395	0.585		0.3807	0.6493	0.7189	0.8	1.524
							5.00	2.71	4.15	0.0155	0		5.06	0.725	0.794		0.3807	1.270	1.181	2.1	1.963
							6.00	3.71	5.15	0.0241	0.0318		6.56	1.149	1.006		0.6100	1.905	1.909	4.3	2.648
2H1-4	2.192	360.6	3.1	4.2	461	0.662	2.29	0	–	–	–	6.77	1.96	0	0	0.00765	–	–	–		
							3.17	0.88	3.15	0.0067	0.0244		2.84	0.124	0.286		0.1884	0.2816	0.3163	0.1	1.163
							4.16	1.87	4.15	0.0146	0.0278		4.04	0.422	0.581		0.4031	0.6739	0.7486	0.8	1.465
							5.00	2.71	4.15	0.0146	0		5.23	0.767	0.789		0.4031	1.311	1.209	2.1	1.820
							6.00	3.71	5.15	0.0226	0.0312		6.77	1.209	1.002		0.6441	1.955	1.905	4.2	2.362
2H2-1	2.114	347.8	7.3	7.6	498	0.550	0.60	0	–	–	–	9.75	0.60	0	0	0.00765	–	–	–	–	–
							1.5	0.90	1.15	0.0070	0.0246		1.53	0.114	0.295		0.1767	0.3443	0.3233	0.1	1.299
							3.0	2.40	2.15	0.0200	0.0301		3.332	0.543	0.719		0.3929	1.077	1.138	1.4	2.215
									3.15	0.0330	0.0356						0.6486				
							4.5	3.90	4.15	0.0460	0.0411		6.20	1.098	1.051		0.9438	2.507	2.511	4.1	3.652
							6.0	5.40	5.15	0.0590	0.0466		9.75	1.722	1.317		1.279	4.832	4.691	7.6	5.609
2I2-1	1.067	175.5	10.4	11.3	342	0.797	2.77	0	–	–	–	4.19	1.390	0	0	0.00765	–	–	–	–	
							3.50	0.730	3.15	0.0120	0.0267		1.855	0.052	0.242		0.0489	0.1221	0.1001	0.4	1.736
							4.33	1.563	4.15	0.0441	0.0403		2.50	0.187	0.468		0.1226	0.3324	0.3068	2.3	3.176
							5.167	2.397	5.15	0.0767	0.0541		3.32	0.374	0.638		0.2216	0.6964	0.6656	6.2	5.258
							6.00	3.230	5.15	0.0767	0		4.19	0.600	0.770		0.2216	1.208	1.231	11.3	7.979
2I2-3	1.062	174.7	10.1	11.1	340	0.792	2.8	0	–	–	–	4.06	1.42	0	0	0.00765	–	–	–		
							3.5	0.700	3.15	0.0110	0.0263		1.86	0.048	0.234		0.0477	0.1103	0.0904	0.3	1.59
							4.33	1.533	4.15	0.0421	0.0395		2.49	0.178	0.463		0.1193	0.3097	0.2751	2.2	2.835
							5.167	2.367	5.15	0.074	0.0530		3.25	0.362	0.635		0.2154	0.6176	0.5918	6.0	4.673
							6.00	3.20	5.15	0.074	0		4.06	0.584	0.768		0.2154	1.073	1.090	11.1	7.099
2F2-1	2.119	348.6	10.4	10.4	531	0.456	0.13	0	–	–	–	9.8	0.05	0	0	0.00765	–	–	–	–	
							1.5	1.37	1.15	0.0175	0.0290		1.78	0.362	0.358		0.2093	0.8007	0.6406	1.0	1.912
							3.0	2.87	2.15	0.0345	0.0362		4.064	0.969	0.698		0.4705	1.877	1.751	3.9	2.707
									3.15	0.0515	0.0434						0.7838				
							4.5	4.37	4.15	0.0687	0.0507		6.82	1.555	0.969		1.150	3.076	3.189	7.2	3.290
							6.0	5.87	5.15	0.858	0.0580		9.80	2.132	1.197		1.568	4.853	4.855	10.4	3.660
2F1-3	2.097	344.8	5.0	5.3	501	0.453	1.167	0	–	–	–	7.3	0.925	0	0	0.00765	–	–	–	–	
							2.335	1.168	2.15	0.0103	0.0260		2.05	0.162	0.374		0.1834	0.4056	0.3612	0.2	1.05
							3.66	2.493	3.15	0.0204	0.0303		3.52	0.523	0.742		0.3973	0.9327	0.8967	1.4	1.628
							4.83	3.663	4.15	0.0305	0.0345		5.07	0.887	1.009		0.6409	1.608	1.656	3.1	2.598
							6.00	4.883	5.15	0.0408	0.0389		7.30	1.285	1.238		0.9158	2.936	2.913	5.3	4.070

* ⑰ = ⑫ $|_{L_b}$ − ⑫ $|_0$ − ⑬ − ⑭ − ⑯

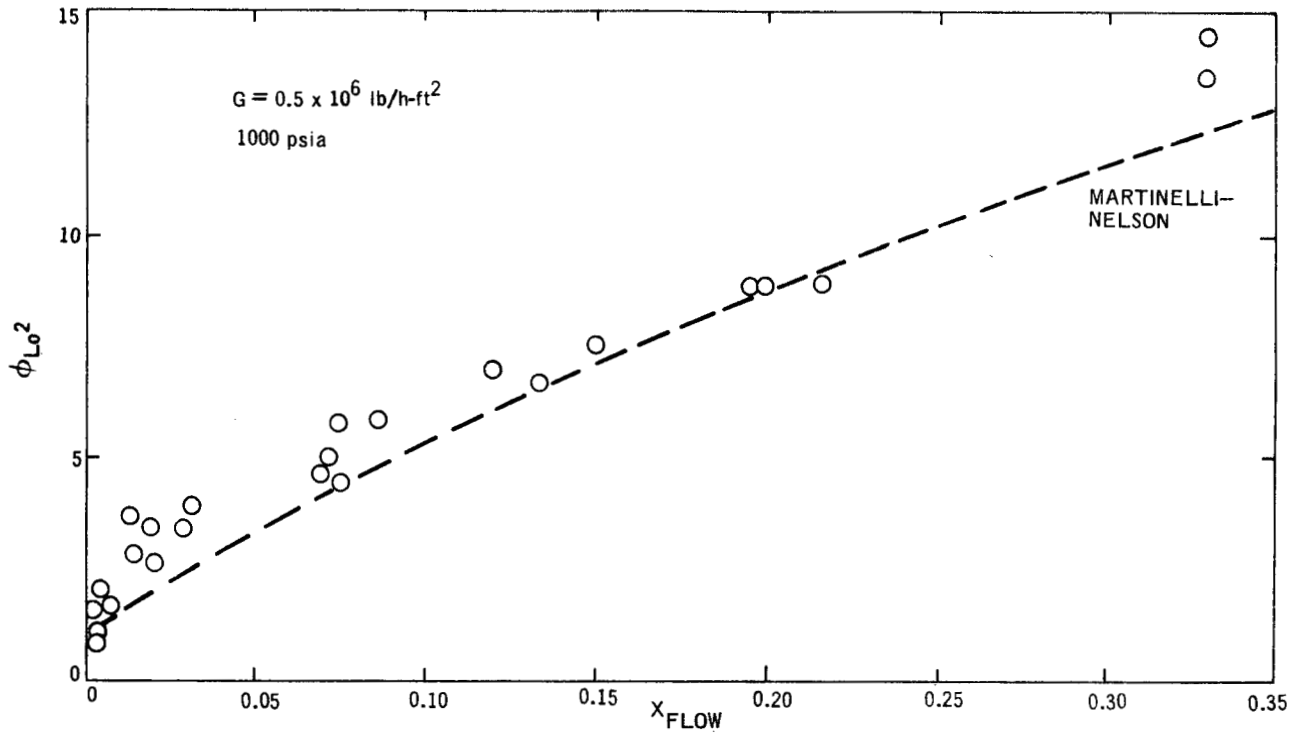

Figure 84. Two-Phase Friction Multiplier versus Bundle Average Flow Quality: $\overline{G} = 0.5 \times 10^6$ lb/ft^2-h

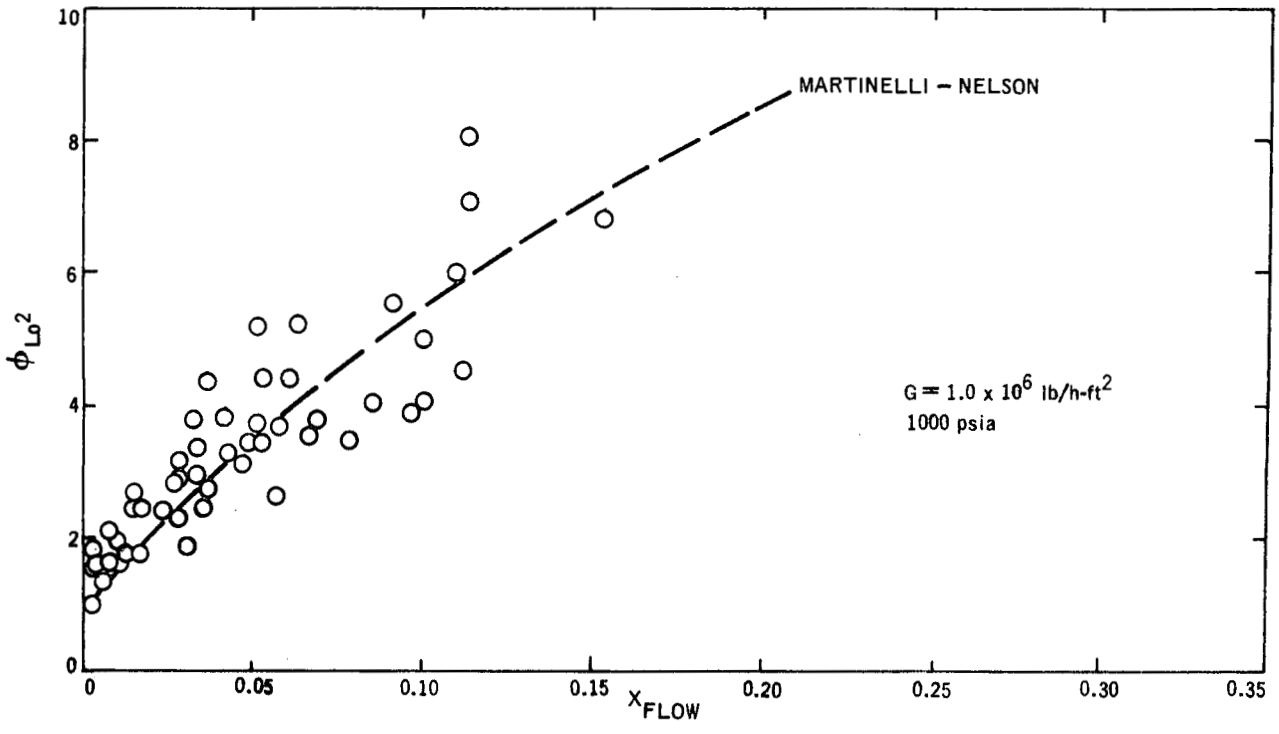

Figure 85. Two-Phase Friction Multiplier versus Bundle Average Flow Quality: $\overline{G} = 1.0 \times 10^6$ lb/ft^2-h

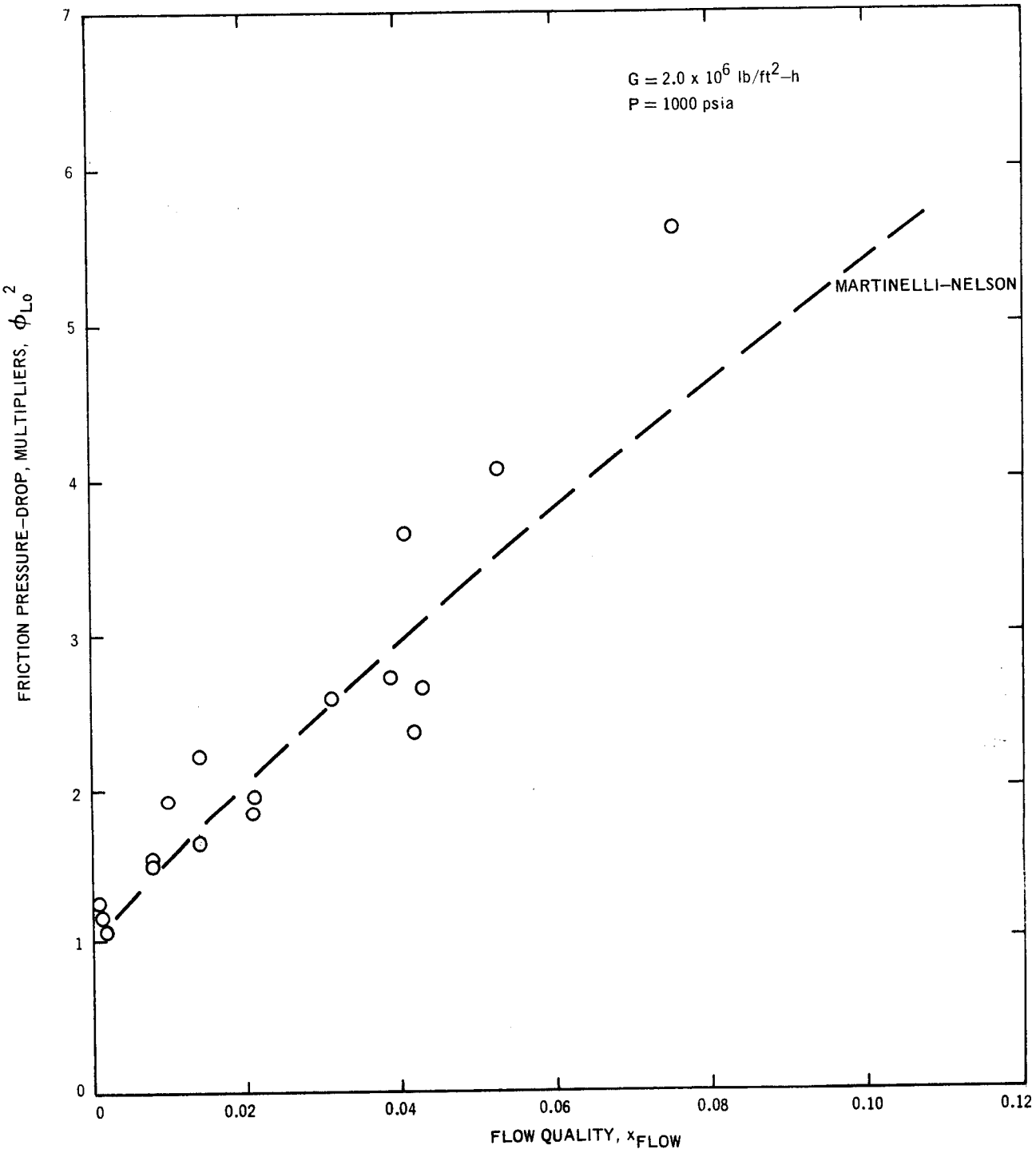

Figure 86. Two-Phase Friction Multiplier versus Bundle Average Flow Quality: $\overline{G} = 2.0 \times 10^6$ lb/ft^2-h

Table 14
TOTAL TWO-PHASE PRESSURE DROP
(Nine-Rod Subchannel - 1000 psig)

Run No.	Average Mass Flux (lb/ft^2-h) $G \times 10^{-6}$	Average Heat Flux (Btu/ft^2-h) $q'' \times 10^{-6}$	Inlet Temperature (°F)	Sub-Cooling	Quality at Exit (%)	Differential Pressure, Δp_t (psi) Heated Length, 1 ft	Heated Length, 2 ft	Heated Length, 3 ft	Heated Length, 4 ft	Heated Length, 5 ft	Heated Length, 6 ft
2B3-3	0.533	0.228	454	108	9.30	0.384	0.760	1.14	1.52	1.90	2.28
2B3-4	0.537	0.227	456	106	9.33	0.384	0.760	1.15	1.53	1.92	2.30
2B3-2	0.534	0.226	459	102	9.93	0.383	0.770	1.162	1.54	1.92	2.30
2B4-3	0.526	0.216	524	31.7	20.2	0.395	0.778	1.165	1.555	1.942	2.33
2F1-2	2.123	0.459	496	65.07	3.16	0.74	1.64	2.73	3.91	5.22	6.60
2F1-3	2.098	0.453	501	59.02	4.08	0.800	1.70	2.74	4.03	5.21	6.55
2F2-2	2.094	0.458	531	24.4	9.63	1.15	2.49	4.08	5.85	7.86	10.05
2F2-3	2.064	0.460	531	22.9	10.12	1.21	2.50	4.09	5.88	7.84	10.12
2H2-2	2.162	0.678	496	64.7	9.23	0.810	2.03	3.51	5.29	7.26	9.55

Note: Comparable total unreduced static pressure drop data can be found in columns 1, 3, 4, 5, 6, 11, and 12 of Table 13.

5. The effect of bundle average mass flux on the normalized enthalpy distribution is small.
6. The effect of heat flux on subchannel enthalpy distribution was small for low flow cases but showed a strong effect at the higher flows. There appeared to be a reversal of the trend at a bundle average quality of ~6 %.
7. The effect of the bundle average mass flux on subchannel mass flux distribution was to increase the mass flux in the corner and center subchannels, and decrease the mass flux in the side subchannel as the bundle average mass flux was increased.
8. The effect of heat flux on subchannel mass-flux distribution was to decrease the mass flux in the corner subchannel but leave the mass fluxes in the other subchannels relatively unchanged (i.e., the total flow change was small since the corner subchannel has a small flow area, thus its flow perturbation is not strongly felt by the other subchannels.)

B. Conclusions From Non-Isokinetic Data (Uniform Radial)

1. The agreement between theoretical results and data indicate that the assumptions made in the analytical model are valid: the length for flow diversion is small, and the separated flow model is appropriate for two-phase conditions.
2. The cross-flow enthalpy which is transported from one subchannel to the other during flow diversion is generally higher than the subchannel enthalpy of the donor subchannel and appears to be a strong function of flow regime.

C. Comparison of Data and Subchannel Code (COBRA) Predictions

Single-phase predictions of COBRA agree quite well with the data. The two-phase predictions do not agree with the trends in data since classical subchannel analysis predicts that the corner subchannel runs at a

lower mass flux and a higher quality and that the center subchannel runs at a lower quality than actually exists in the subchannels.

D. **Conclusion From Isokinetic Data With Radial Peaking Pattern**

Although insufficient funds and loop time prevented the acquisition of complete subchannel data the trends in the data taken for the peaking runs agreed with the uniform data (i.e., the "hottest" regions were found to be in the interior of the bundle).

E. **Conclusions From Pressure Drop Data**

1. The adiabatic single-phase friction factor for the clean nine-rod bundle under consideration was slightly higher than the smooth-tube friction factor, at all Reynolds numbers.

2. The two-phase friction pressure-drop multiplier ϕ_{Lo}^2, showed only a very minor flow effect, and the data was well correlated by the classical Martinelli-Nelson curve.

Although it was not possible to take all the data of interest, the overall scope of the subchannel test program was completed. It is felt that the overall program was quite successful because it identified various trends which occur in true multirod geometries, which were not known previously.

It is recommended that future work in this area include more extensive data with radial peaking and also data with axial heat flux profiles. In addition, subchannel data taken for off design conditions of rod swell and rod bowing would be of great interest. Finally, data taken with grid type spacers could be used to establish quantitatively the effect of local disturbances on the flow and enthalpy distribution in a rod bundle.

REFERENCES

1. Rowe, D. S. and Angle, C. W., *Crossflow Mixing Between Parallel Flow Channels During Boiling,* Part II, *Measurement of Flow Enthalpy in Two Parallel Channels,* AEC December 1967, (BNWL-371 Pt 2).
2. Rowe, D. S. and Angle, C. W., *Crossflow Mixing Between Parallel Flow Channels During Boiling,* Part III, AEC January 1969, (BNWL-371 Pt 3).
3. Bowring, R. W. and Levy, J., *Freon 7-Rod Cluster Subchannel Mixing Experiments,* May 1969, (AEEW-M906).
4. Collier, J. G. and Wallis, G. B., *Two-Phase Flow and Heat Transfer,* Stanford University Press, Palo Alto, August 1967, Vol. II.
5. Casterline, J. E., Personal Communication, 1968.
6. Casterline, J. E. Castellana, F. A., *Flow and Enthalpy Measurements in a Simulated Nuclear Fuel Assembly,* Columbia University, February 1969, (CU-187-2).
7. Bergles, A. E., *Two-Phase Flow Structure Observation for High Pressure Water in a Rod Bundle,* Paper presented to A.S.M.E., December 1969 (ASME-MS-69-1).
8. Bergles, A. E., Roos, J. P., and Bourne, J. G., *Investigation of Boiling Flow Regimes and Critical Heat Flux,* Dynatech Final Summary, Report (No. 797) July 1968, (NYO-3304-13).
9. Schraub, F. A., Simpson, R. L., Janssen E., *Two-Phase Flow and Heat Transfer in Multirod Geometries: Air-Water Flow Structure Data for a Round Tube, Concentric and Eccentric Annulus, and Nine-Rod Bundle,* January 1969, (GEAP-5739).
10. Lahey, R. T., and Schruab, F. A., *"Mixing, Flow Regimes, and Void Fraction for Two-Phase Flow in Rod Bundles,"* in *Two-Phase Flow and Heat Transfer, in Rod Bundles,* ASME, November 1969.
11. Nylund, O., Becker, K. M., et al., *Measurements of Hydrodynamic Characteristics, Instability Thresholds, and Burnout Limits for 6-Rod Clusters in Natural and Forced Circulation,* FRIGG-I (R4-422/RTL-914) Sweden, 1967.
12. Nylund, O, Baker, K. M., et al., *Hydrodynamic and Heat Transfer Measurements on a Full-Scale Simulated 36-Rod Marviken Fuel Element with Uniform Heat Flux Distribution,* FRIGG-II (R4-447/RTL-1007) Sweden, 1968.
13. Bowring, R. W., *HAMBO, A Computer Programme for the Subchannel Analysis of the Hydraulic and Burnout Characteristics of Rod Clusters-Pt 2, The Equations,* January 1968, (AEEW-R-582).
14. St. Pierre, C. C., *SASS Code-I, Subchannel Analysis for the Steady State,* September 1966, (APPE-41).
15. Rowe, D. S., *Crossflow Mixing Between Parallel Flow Channels During Boiling,* March 1967, BNWL-371 Pt 1).
16. Petrunik, K. J., *Turbulent Mixing Measurements for Single-Phase Water, and Two-Phase Air-Water Flows in Adjacent Rectangular Subchannels,* MS Thesis, Chemical Engineering, University of Windsor, 1968.
17. Walton, F. B., Petrunik, K. M., St. Pierre, C. C., *Two-Phase Air-Water Turbulent Mixing Between Parallel Flow Channels,* Paper presented to AIChE, Portland, Oregon, August 1969.
18. Kline, S. J., and Mc Clintock, F. A., *Describing Uncertainties in Single Sample Experiments,* **Mechanical Engineering** Magazine, January 1953.
19. Gunn, D. J., and Darling, C. W. W., *Fluid Flow and Energy Losses in Non-Circular Conduits* **Trans. Instn. Chem. Engrs, 41** (1963).
20. Waggener, J. P., *Friction Factors for Pressure-Drop Calculations,* **Nucleonics, 19**, 11, November 1961.
21. Levy, S., *Forced Convection Subcooled Boiling – Prediction of Vapor Volumetric Fraction,* April 1966, GEAP-5157.
22. Idelchik, I. E., *Handbook of Hydraulic Resistance Coefficients of Local Resistance and of Friction,* AEC 1960, (TR-6630).
23. Tong, L. S., *Boiling Heat Transfer and Two-Phase Flow,* John Wiley and Sons, New York, 1965.
24. Rowe, D. S., Personal Communication, August 1969.
25. Edwards, P. A., Obertelli, J. D., *6 MW Rig-Burnout and Pressure Drop Data on 37-Rod Clusters in High Pressure Water,* Paper presented at the meeting of the European Two-Phase Flow Group, at Ispra, June 14, 1966.
26. Polomik, E. E., *N. S. Savannah Fuel Development Program – Pressure-Drop through 25-Rod Partial Prototype at 520°F and 1000 psi, May 22, 1959,* (GEAP-3174).

APPENDIX A

CALCULATION OF NON-ISOKINETIC PRESSURE DIFFERENTIAL

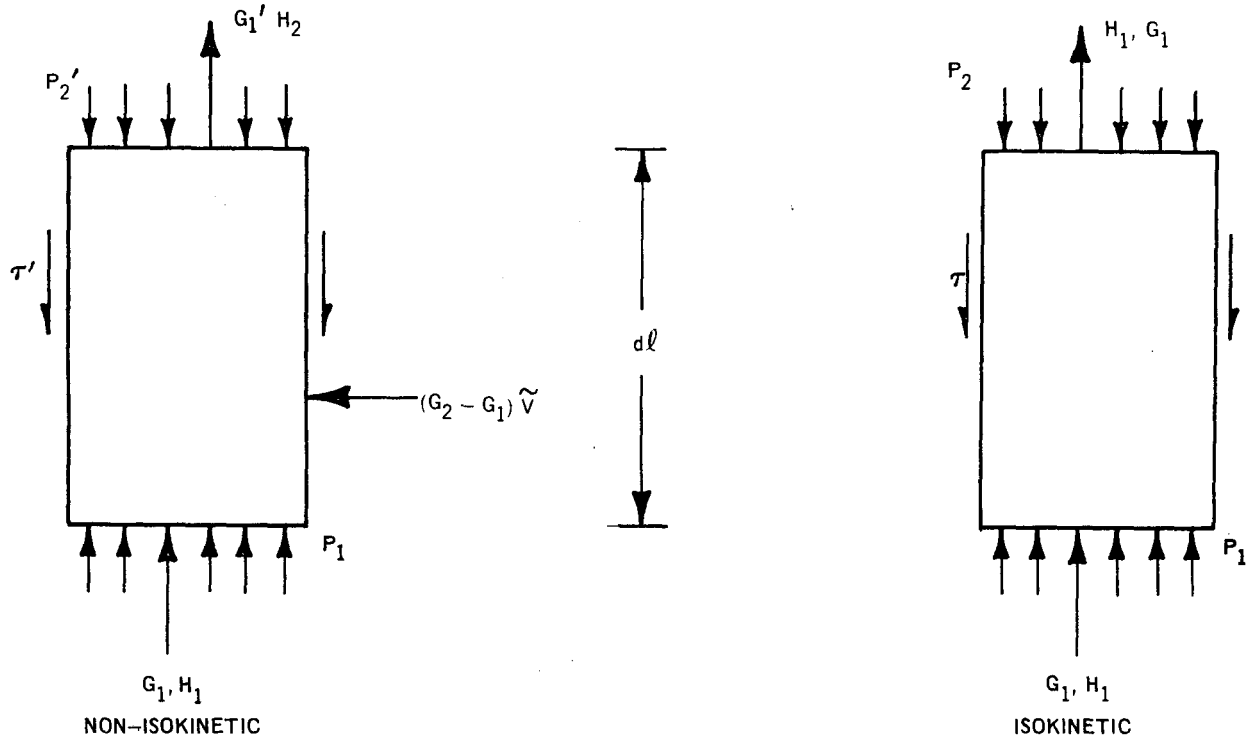

Figure A-1. Model for Calculation of Non-Isokinetic Pressure Differential

In order to estimate the non-isokinetic pressure differential due to acceleration drop, the simple model above (Figure A-1) may be used. It is assumed that for non-isokinetic conditions, the flow diversion occurs over a small length $d\ell$, and upstream of this point there is no difference between the two cases. It is also assumed that the length $d\ell$, is small enough so that there is negligible flow diversion over this length under isokinetic conditions. If p_1 is the static pressure at the upstream end of this section, and p_2 is the pressure at the downstream end, for isokinetic conditions, and p_2', for non-isokinetic condition, the momentum equations may be written as follows:

A. Cold Runs

$$(p_1 - p_2')\,A_{ch} - \tau' p_{ch}\,d\ell - \frac{\rho\, g\, d\ell\, A_{ch}}{g_c} = \frac{G_2^{\,2}}{\rho g_c} A_{ch} - \frac{G_1^{\,2}}{\rho g_c} A_{ch} - (G_2 - G_1)\frac{\tilde{V}}{g_c} A_{ch} \qquad (1)$$

$$(p_1 - p_2)\,A_{ch} - \tau\, p_{ch}\,d\ell - \frac{\rho\, g\, d\ell\, A_{ch}}{g_c} = 0 \qquad (2)$$

where

$\tilde{V}$ = Average Axial Velocity of the Cross Flow

Subtracting Equation (2) from (1), and dividing by A_{ch},

$$p_2 - p_2' = \frac{G_2^2}{\rho g_c} - \frac{G_1^2}{\rho g_c} - (G_2 - G_1)\frac{\tilde{V}}{g_c} + (\tau' - \tau)\frac{p_{ch}\, d\ell}{A_{ch}} \tag{3}$$

where

G_2 = Non-Isokinetic Mass Flux
G_1 = Isokinetic Mass Flux

$\tilde{V}$ was taken to be $(G_1 + G_2)/2\rho$, or the mean linear velocity in the two adjacent subchannels.

B. Two Phase Runs

The same method can be used for the two phase runs but the equations are more complicated and involve the void fractions in the adjacent subchannels.

$$(p_1 - p_2')\, A_{ch} - \tau' p_{ch}\, d\ell - \bar{\rho}'\frac{g}{g_c}\, d\ell\, A_{ch} = \frac{G_2^2}{g_c}\left[\frac{(x_2')^2}{\alpha_2'\rho_g} + \frac{(1 - x_2')^2}{(1 - \alpha_2')\rho_\ell}\right] A_{ch} - \frac{G_1^2}{g_c}\left[\frac{x_1^2}{\alpha_1 \rho_g} + \frac{(1 - x_1)^2}{(1 - \alpha_1)\rho_\ell}\right] A_{ch} - (G_2 - G_1)\frac{\tilde{V}}{g_c} A_{ch} \tag{4}$$

$$(p_1 - p_2)\, A_{ch} - \tau p_{ch}\, d\ell - \bar{\rho}\frac{g\, d\ell}{g_c} A_{ch} = \frac{G_1^2}{g_c}\left[\frac{x_2^2}{\alpha_2 \rho_g} + \frac{(1 - x_2)^2}{(1 - \alpha_2)\rho_\ell}\right] A_{ch} - \frac{G_1^2}{g_c}\left[\frac{x_1^2}{\alpha_1 \rho_g} + \frac{(1 - x_1)^2}{(1 - \alpha_1)\rho_\ell}\right] A_{ch} \tag{5}$$

Subtracting Equation (5) from (4),

$$p_2 - p_2' = \frac{G_2^2}{g_c}\left[\frac{(x_2')^2}{\alpha_2'\rho_g} + \frac{(1 - x_2')^2}{(1 - \alpha_2')\rho_\ell}\right] - \frac{G_1^2}{g_c}\left[\frac{x_2^2}{\alpha_2 \rho_g} + \frac{(1 - x_2)^2}{(1 - \alpha_2)\rho_\ell}\right] - (G_2 - G_1)\frac{\tilde{V}}{g_c} + (\tau' - \tau)\frac{p_{ch}\, d\ell}{A_{ch}} + (\bar{\rho}' - \bar{\rho})\frac{g\, d\ell}{g_c} \tag{6}$$

Here, $\tilde{V}$ was taken to be the average of the linear velocities in the adacent subchannels, calculated as $\frac{1}{2}(G_1/\rho_1' + G_2/\rho_2')$ where ρ_1' and ρ_2' are the momentum densities in the two subchannels. For fairly small crossflow diversions, over a short length, the last two terms on the right hand side of Equation 6 can be neglected.
Therefore,

$$(p_2 - p_2') \cong \frac{G_2^2}{g_c \rho_\ell}\left[\frac{(x_2')^2}{\alpha_2'}\left(\frac{\rho_\ell}{\rho_g}\right) + \frac{(1 - x_2')^2}{(1 - \alpha_2')}\right] - \frac{G_1^2}{g_c \rho_\ell}\left[\frac{x_2^2}{\alpha_2}\left(\frac{\rho_\ell}{\rho_g}\right) + \frac{(1 - x_2)^2}{(1 - \alpha_2)}\right] - (G_2 - G_1)\frac{\tilde{V}}{g_c} \tag{7}$$

APPENDIX B

ERROR ANALYSIS OF SUBCHANNEL FLOW AND ENTHALPY

A Kline and Mc Clintock type analysis was performed[18] for the systematic error in the experiments in subchannel quantities.

A. Error in Subchannel Flow

Due to error in isokinetic setting and turbine flow measurement the error in subchannel mass flux is given as,

$$\Delta G_{ch}^2 = \left[\frac{\partial G_{ch}}{\partial(\Delta p)}\, d\,\Delta p\right]^2 + \left[\frac{\partial G_{ch}}{\partial w_{ch}}\, dw_{ch}\right]^2 \qquad (1)$$

Δp = Pressure Differential
W_{ch} = Turbine Meter Flow

Typical values follow for corner subchannel flow, taken from calibration runs made during tests.

For $G_{ch} \sim 1.0 \times 10^6$ lb/ft^2-h, and $d(\Delta p) = 0.004$ lb/in.^{2}

$$\frac{\partial G_{ch}}{\partial(\Delta p)} = 3.25 \times 10^6 \ \frac{\text{lb/ft}^2\text{-h}}{\text{lb/in.}^2}$$

$$dw_{ch} = 16 \text{ lb/h},$$

$$\frac{\partial G_{ch}}{\partial w_{ch}} = \frac{1}{A_{ch}} = \frac{1}{0.000544 \text{ ft}^2}$$

Plugging these values into Equation (1):

$$\Delta G_{ch}^2 = \left[0.013 \times 10^6\right]^2 + \left[\frac{16}{544} \times 10^6\right]^2$$

$$\left|\Delta G_{ch}\right| \sim 0.032 \times 10^6 \quad \text{lb/ft}^2\text{-h}$$

B. Error in Subchannel Quality

Referring to Section 3,

$$x_{ch} = \left(\frac{F_{cw}}{w_{ch}} C_p\, \Delta T_{cw} - H_{sat} + H_{out} + \frac{Q'}{w_{ch}}\right) \Big/ H_{fg}$$

or,

$$H_{ch} = \frac{F_{cw}}{w_{ch}} C_p\, \Delta T_{cw} + H_{out} + \frac{Q'}{w_{ch}} \qquad (2)$$

The Error in subchannel enthalpy due to measurement error is given as:

$$\Delta H_{ch}^2 = \left[\frac{\partial H_{ch}}{\partial F_{cw}} \; dF_{cw}\right]^2 + \left[\frac{\partial H_{ch}}{\partial w_{ch}} \; dw_{ch}\right]^2 + \left[\frac{\partial H_{ch}}{\partial \Delta T_{cw}} \; d\left(\Delta T_{cw}\right)\right]^2$$

$$+ \left[\frac{\partial H_{ch}}{\partial H_{out}} \; dH_{out}\right]^2 + \left[\frac{\partial H_{ch}}{\partial Q'} \; dQ'\right]^2$$

Performing the indicated differentiation using the relation for H_{ch} Equation (2),

$$\Delta H_{ch}^2 = \left[\frac{C_p \, \Delta T_{cw}}{w_{ch}} \; dF_{cw}\right]^2 + \left[\left(\frac{F_{cw} \, C_p \, \Delta T_{cw}}{w_{ch}^2} + \frac{Q'}{w_{ch}^2}\right) dw_{ch}\right]^2$$

$$+ \left[\frac{F_{cw}}{w_{ch}} \; C_p \; d\left(\Delta T_{cw}\right)\right]^2 + \left[dH_{out}\right]^2 + \left[\frac{dQ'}{w_{ch}}\right]^2 \qquad (3)$$

Typical values for Corner subchannel* (Test 2B2)

$\Delta T_{cw} = 40^\circ F$, $d\Delta T_{cw} = \pm 1^\circ F$

$w_{ch} = 270$ lb/h, $dw_{ch} = \pm 5.4$ lb/h

$F_{cw} = 2600$ lb/h, $df_{cw} = \pm 26$ lb/h

$Q' = 2700$ Btu/h, $dH_{out} = \pm 1$ Btu/lb

$dQ' = \pm 1000$ Btu/h

Plugging these values into Equation (3):

$$\Delta H_{ch}^2 = \left[\frac{40}{270} \times 26\right]^2 + \left[\left(\frac{2600 \times 40}{(270)^2} + \frac{2700}{(270)^2}\right) 5.4\right]^2 + \left[\frac{2600}{270} \times 1\right]^2 + [1]^2 + \left[\frac{1000}{270}\right]^2$$

$$\left|\Delta H_{ch}\right| = 14.6 \text{ Btu/lb}$$

$$\left|\Delta x_{ch}\right| = 0.022$$

In addition there can be an error in the "isokinetic" enthalpy due to an error in the measurement of the pressure differential

$$\Delta H_{iso} = \frac{\partial H_{ch}}{\partial \Delta p} \; \Delta p$$

* These numeral values were taken from a typical corner subchannel run (2B2), since the corner subchannel case has the most potential error due to the fact that the sample flow w_{ch} is small and appears in the denominator of $(\Delta H_{ch})^2$.

For independent errors,

$$\left(\Delta H_{ch_{Total}}\right)^2 = \left(\Delta H_{ch}\right)^2 + \left(\Delta H_{iso}\right)^2$$

For a corner subchannel (Test 2B2),

$$\Delta H_{iso} = 125 \frac{\text{Btu/lb}}{\text{lb/in.}^2} \times 0.004 \text{ lb/in.}^2$$

$$\Delta H_{iso} = 0.5 \text{ Btu/lb}$$

consequently,

$$\Delta H_{ch_{Total}} \cong \Delta H_{ch}$$

Thus the systematic error in mass flux determination is on the order of ±3 %, while the corresponding error in subchannel quality determination is approximately ±2 % in quality.

APPENDIX C

PRESSURE DROP CORRECTION FOR SPACER PINS

At each of eight elevations along the channel, 24-1/8 in. o.d. stainless steel pins were used to maintain the spacing of the calrods, as shown schematically in Figure C-1. These consisted of 12 exterior pins, 1/8 in. o.d. X 0.135 in. long, and 12 longer interior pins, 1/8 in. o.d. X 0.168 in. long.

The pressure drop due to each cylindrical pin is dependent on the projected transverse area and the local velocity, which in turn determines the local drag coefficient. The methods used for evaluation of the pressure drop due to the pins, in both single- and two-phase flow, are described below.

1. Single-Phase Flow.

The single-phase pressure drop for a set of N pins, in a length L, of the channel, is readily obtained when the local velocities and drag coefficients are available. The pressure drop over a cylinder due to drag may be derived as follows.

The basic conservation of energy relation for a control volume enclosing N_i pins in the i-th flow tube.

$$\begin{matrix}\text{Rate of Creation} \\ \text{of Energy}\end{matrix} \triangleq \begin{matrix}\text{Outflow Rate} \\ \text{of Energy}\end{matrix} - \begin{matrix}\text{Inflow Rate} \\ \text{of Energy}\end{matrix} + \begin{matrix}\text{Storage Rate} \\ \text{of Energy}\end{matrix} = 0$$

For the adiabatic control volume under consideration:

$$w_i \left[\left(u_2 + \frac{p_2}{\rho}\right) + \frac{\bar{v}_2^{\,2}}{2g_c} + \frac{g}{g_c} z_1\right]_i + F_i v_{p_i} = w_i \left[\left(u_1 + \frac{p_1}{\rho}\right) + \frac{\bar{v}_1^2}{2g_c} + \frac{g}{g_c} z_2\right]_i$$

where

F_i = Force on the i-th spacer pin group
V_{p_i} = Local velocity upstream of the i-th pin

Now, assuming that the internal, potential and kinetic energy are constant on the control volume boundaries:

$$w_i \frac{(p_1 - p_2)}{\rho} \triangleq w_i \left(\frac{\Delta p}{\rho}\right)_i = F_i v_{p_i}$$

with $w = \rho \bar{v} A_p$

since F_i usually is given as

$$F_i \triangleq \frac{1}{2g_c} C_D \rho v_{p_i}^{\,2} A_{p_i} N_i$$

where

C_D = Drag coefficient
A_{p_i} = Projected area of pins
N_i = Number of pins in i^{th} group.

Thus we have:

$$w_i \left(\frac{\Delta p}{\rho}\right)_i = \rho \bar{v}_i A_i \left(\frac{\Delta p}{\rho}\right)_i = \frac{1}{2g_c} C_{D_i} \rho v_{p_i}^3 A_{p_i} N_i$$

so that

$$\left(\frac{\Delta p}{\rho}\right)_i = \frac{1}{2g_c} C_{D_i} v_{p_i}^2 \left(\frac{A_{p_i} v_{p_i}}{A_i \bar{v}_i}\right) N_i \qquad (1)$$

The total energy loss per second for N groups of pins is

$$\left(\frac{\Delta p}{\rho} \bar{w}\right)_N = \sum_{i=1}^{N} \left(\frac{\Delta p}{\rho} w\right)_i = \sum_{i=1}^{N} N_i \left(C_D \frac{v_p^2}{2g_c}\right)_i \left(V_p \rho A_p\right)_i . \qquad (2)$$

where the total N pins are comprised of i groups, each group containing N_i pins and having each pin having a projected area of A_p. Friction factors are defined such that the total energy loss per pound of total fluid flow in a channel section of length L containing N pins is

$$\left(\frac{\Delta p}{\rho}\right)_t \bar{w} = \left(\frac{\Delta p}{\rho}\right)_c \bar{w} + \left(\frac{\Delta p}{\rho} \bar{w}\right)_N = \frac{(f_c + f_p) \bar{v}^2 L}{2g_c D_h} \bar{w} \qquad (3)$$

with $\Delta p_t = \Delta p_c + \Delta p_N$

where

- t = Total
- c = Clean Channel (no pins)
- f_p = Effective Friction Factor for N pins
- f_c = Clean Channel Friction Factor
- D_h = Hydraulic diameter for clean channel
- v = Mean Velocity in the Total Flow Area of a Channel
- Δp_N = Pressure Loss Due to Pins Based on Total Flow

The definition for a clean channel is

$$\left(\frac{\Delta p}{\rho}\right)_c = \frac{f_c \bar{v}^2 L}{2g_c D_h} \qquad (4)$$

so that

$$\frac{\Delta p_N}{\rho} \bar{w} = \left(\frac{\Delta p}{\rho} w\right)_N = \frac{f_p \bar{v}^2 L}{2g_c D_h} \bar{w} . \qquad (5)$$

combining Equations (2) and (5) gives

$$\frac{f_p L}{D_h} = \frac{1}{\bar{v}^2 \bar{w}} \sum_{i=1}^{N} N_i (C_D v_p^2)_i (v_p \rho A_p)_i . \qquad (6)$$

since $\bar{w} = \bar{v}\rho A_t$, this becomes by rearrangement

$$\frac{f_p L}{D_h} = \sum_{i=1}^{N} C_{D_i} \left(\frac{v_{p_i}}{\bar{v}}\right)^3 \frac{N_i A_{p_i}}{A_t} \cdot \tag{7}$$

For a single spacer pin in a circular tube in turbulent flow, Equation (7) reduces to

$$\frac{f_p L}{D_h} = C_D \left(\frac{v_p}{\bar{v}}\right)^3 \left(\frac{A_p}{A_t}\right) \cdot$$

v_p may be expressed in terms of the velocity profile as

$$v_p(y) = \bar{v}\, K(1 - 2y/D_h)^{1/7}$$

where:

$K = v_{\mathcal{L}} / \bar{v}$

y = Eccentricity of the Pin Location

Thus,

$$\frac{f_p L}{D_h} = C_D K^3 \left(1 - \frac{2y}{D_h}\right)^{3/7} (A_p/A_t)$$

If C_D is defined by the local velocity in the obstructed flow area instead of the upstream area, then

$$\bar{v}' = \bar{v} \frac{A_t}{(A_t - A_p)} = \frac{\bar{v}}{(1 - A_d/A_t)} \cdot$$

Hence:

$$v_p'(y) = \frac{\bar{v}}{(1 - A_p/A_t)} K (1 - 2y/D_h)^{1/7}$$

and so

$$\frac{f_p L}{D_h} = C_D' K^3 \frac{(1 - 2y/D)^{3/7}}{(1 - A_p/A_t)^3} (A_p/A_t) \cdot$$

which is the form recommended by Idelchik.[22] In our investigation, the drag coefficient was based on the upstream local velocity v in order to use standard C_D data.

The method actually used was to estimate local pin velocities, determine a drag coefficient from the local velocities, and then calculate an effective friction factor f_p. This friction factor was plotted versus the mean channel Reynolds number, which yielded a suitable curve to evaluate the total pressure drop due to the spacer pins. The pressure drop in the "clean" channel (without pins) was then calculated by subtracting the calculated pin loss from the total loss due to friction.

Preliminary calculations using mean channel velocity were considered too approximate, as actual runs showed variations in mean subchannel velocity of almost 2:1 in the subchannels (1), (2), and (3) in Figure C-1. Therefore, the 24 pins at each elevation were divided into four "mean local velocity" groups. These groups are identified as A through D in Figure C-1, with the following numbers of pins in each group;

Velocity group	Number of pins	Location	Projected area, A_p (in.^{2})
A	8	Corner (short)	0.0169
B	4	Sides (short)	0.0169
C	8	Interior Corners (long)	0.0210
D	4	Center (long)	0.0210

The relations between the "mean local velocity" at a pin and the mean velocity in the entire channel were based on actual measurements of subchannel mass flux. The results of this are given in Table C-1.

Table C-1
MASS FLUX RATIOS

Mass Flux [(lb/ft^2-h) $\times$ 10^{-6}]		Mass Flux Ratio $\left(\frac{\text{Sub Channel Mass Flux}}{\text{Total Channel Average Mass Flux}}\right)$		
		Sub Channel		
		Corner (1)	Side (2)	Center (3)
0.25		0.704	0.968	1.12
0.50		0.678	0.948	1.15
1.0		0.696	0.948	1.15
1.5		0.660	0.948	1.15
2.0		0.700	0.950	1.14
	Averages:	0.690	0.950	1.14

It should be noted, the sub-channel mass-flux ratios in Table C-1 are affected very little by Reynolds number. Hence the average value was used in subsequent calculations.

The average velocity ratios from Table C-1 were applied to the different pin locations, shown in Figure C-1, to obtain local velocities at the pins. The ratio of local mean velocities to the total mean velocity over the various pins then were estimated as shown in Table C-2.

The local velocity ratios $v_p/\bar{v}$, were used to calculate local pin Reynolds numbers from average channel Reynolds numbers. The local pin Reynolds numbers were then used to evaluate local drag coefficients[22] from which the effective friction factor and the total pressure loss due to the pins were calculated by Equation (7). The tabulation of local Reynolds numbers and drag coefficients for nominal, average channel Reynolds numbers is shown in Table C-3.

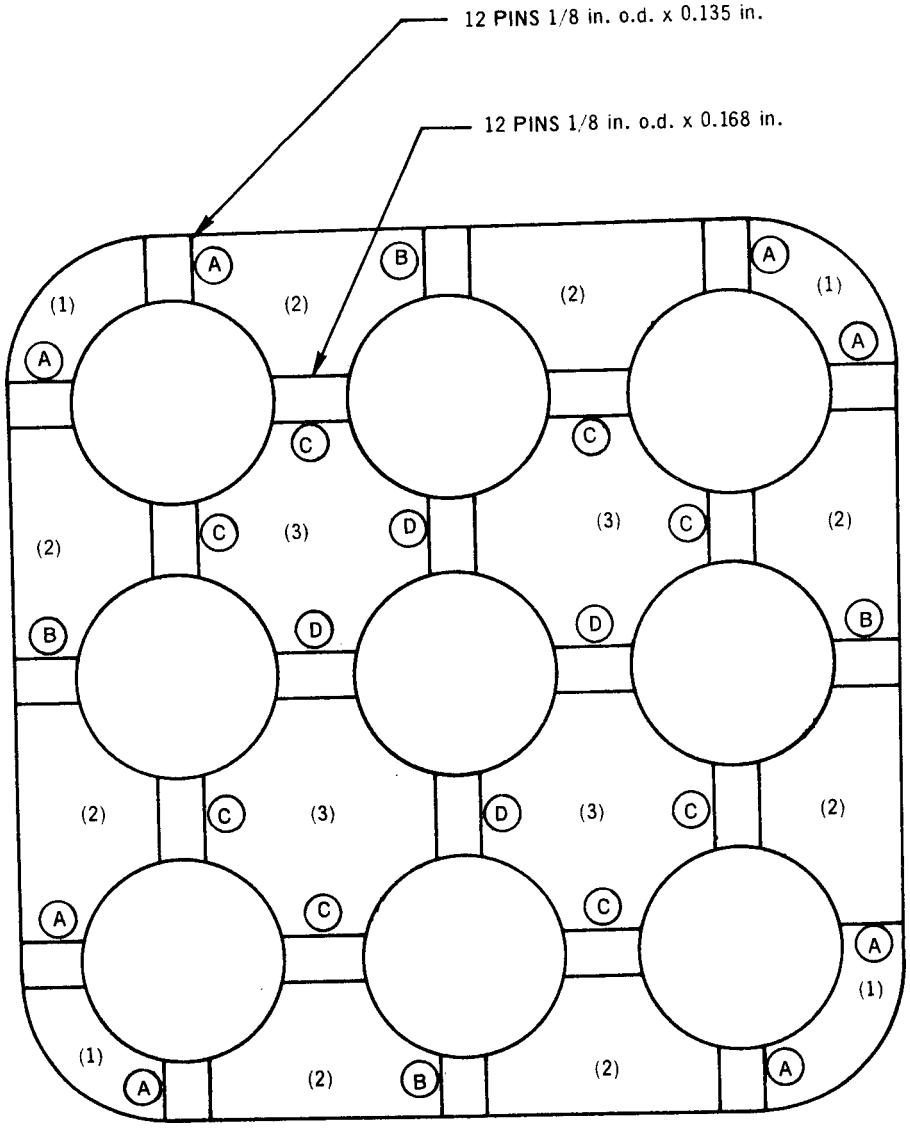

SUBCHANNELS

(1) CORNER

(2) SIDE

(3) CENTER

PINS

(A) CORNER–SIDE

(B) SIDE–SIDE

(C) SIDE–CENTER

(D) CENTER–CENTER

Figure C-1. Typical Spacer Pins

Table C-2
ESTIMATION OF VELOCITY RATIOS

Velocity Group (Figure C-1)	No. of Pins	Velocity Ratio, $v_p/\bar{v}$	Pin Area Fraction, A_p/At
A(short)	8	$\frac{0.69 + 0.95}{2} = 0.82$	$\frac{0.0169}{2.93} = 0.00577$
B(short)	4	$\frac{0.95 + 0.95}{2} = 0.95$	$\frac{0.0169}{2.93} = 0.00577$
C(long)	8	$\frac{0.95 + 1.14}{2} = 1.04$	$\frac{0.0210}{2.93} = 0.00717$
D(long)	4	$\frac{1.14 + 1.14}{2} = 1.14$	$\frac{0.0210}{2.93} = 0.00717$

The sample calculation below illustrates the calculation of the effective friction factor for 24 pins in 1 foot of channel length at a channel mass flux of $G = 1.0 \times 10^6$ lb/ft^2-h at 70°F - 75°F water temperature with a channel Reynolds number of 17,750. By Equation (7)

$$\frac{f_p L}{D_h} = \left(\frac{A_p}{A_t}\right)_{A,B} \left[C_{p_A} N_A \left(\frac{v_p}{\bar{v}}\right)_A^3 + C_{D_B} N_B \left(\frac{v_p}{\bar{v}}\right)_B^3\right]$$

$$+ \left(\frac{A_p}{A_t}\right)_{C,D} \left[C_{D_C} N_C \left(\frac{v_p}{\bar{v}}\right)_C^3 + C_{D_D} N_D \left(\frac{v_p}{\bar{v}}\right)_D^3\right]$$

Insertion of values from Tables C-2 and C-3 results in

$$\frac{f_p (12)}{(0.475)} = (0.00577) \left[(0.93)(8)(0.82)^3 + (0.92)(4)(0.95)^3\right]$$

$$+ (0.00717) \left[(0.92)(8)(1.04)^3 + (0.95)(4)(1.14)^3\right] = 0.1414$$

so that

$$f_p = 0.0056.$$

Plots of the pin friction factors against the mean channel Reynolds numbers are shown in Figure C-2.

2. Two-Phase Flow

The friction pressure drop caused by the pins in two-phase flow was calculated by using the local homogeneous density at the location of the pins. By Equation (5) the effective pin pressure drop for N pins in length L with saturated fluid at density ρ_f, is

$$(\Delta p_N)_f = \frac{\rho_f f_p \bar{v}_f^2 L}{2 g_c D_h} . \quad (8)$$

Table C-3
LOCAL REYNOLDS NUMBERS AND DRAG COEFFICIENTS

		Pin Type			
		A	B	C	D
		Velocity Ratio, V_p/V_i			
		0.82	0.95	1.04	1.14
Mass Flux (lb/ft^2-h $\times 10^{-6}$)	Mean Channel Reynolds Number	Pin Reynolds Number, and Pin Drag Coefficient (C_D)			
0.25	4,440	960	1,110	1,220	1,330
		(1.0)	(1.0)	(0.97)	(0.95)
0.50	8,875	1,920	2,220	2,440	2,660
		(0.92)	(0.90)	(0.92)	(0.90)
1.0	17,750	3,840	4,440	4,880	5,320
		(0.93)	(0.92)	(0.92)	(0.95)
1.5	26,600	5,760	6,660	7,320	7,980
		(0.95)	(1.0)	(1.0)	(1.0)
2.0	35,500	7,680	8,880	9,760	10,640
		(1.0)	(1.1)	(1.15)	(1.20)
	50,000	10,800	12,500	13,700	15,000
		(1.10)	(1.15)	(1.20)	(1.20)
	100,000-400,000	21,600-86,400	25,000-100,000	27,400-109,600	30,000-120,000
		(1.27)	(1.27)	(1.27)	(1.27)

Viscosity = 2.23 lbm/ft-h
Pin Diameter = 0.125 in.
Hydraulic Diameter of Channel = 0.475 in.
Total Channel Flow Area = 2.93 $in.^2$

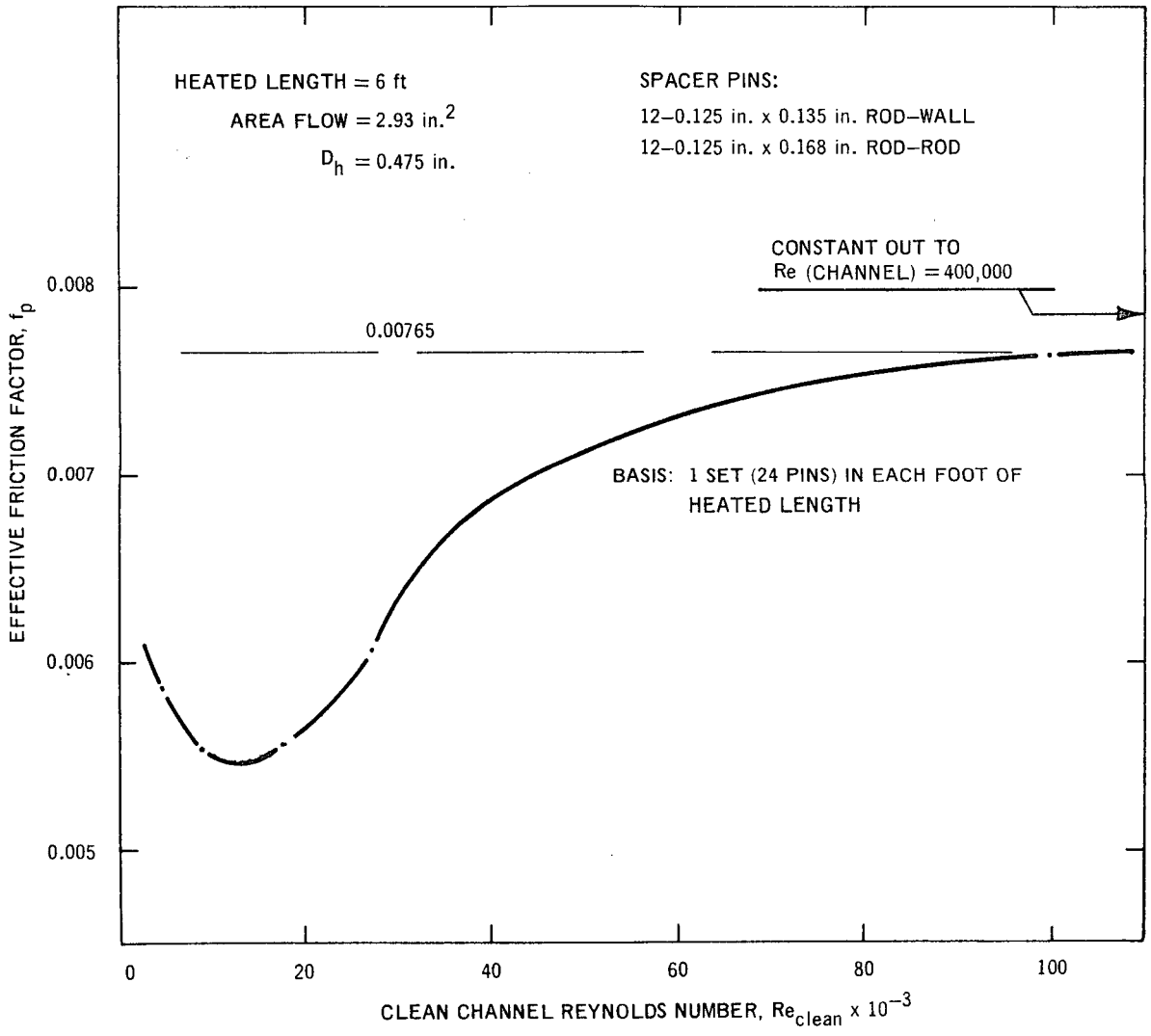

Figure C-2. Effective Friction Factor for Pins in Nine-Rod Subchannel Test Section

For a set of pins exposed to steam quality x_i, the homogeneous density is given by

$$\rho_h = \frac{1}{\left[\frac{1 - x_i}{\rho_f} + \frac{x_i}{\rho_g}\right]}$$

or

$$\frac{1}{\rho_h} = v_f + x_i v_{fg} \tag{9}$$

consequently,

$$(\Delta p_N)_{x_i} = \frac{f_p G^2 L}{2 g_c D_h} (v_f + x_i v_{fg}) \cdot \tag{10}$$

When several sets of N spacers per length L, are exposed in a boiling length $L_b > L$, then the total two-phase pressure loss due to all the sets will be

$$(\Delta p_N)_{L_b} = \left(\frac{f_p G^2 L}{2 g_c D_h}\right) \sum_{i}^{L_b} (v_f + x_i v_{fg}) \cdot \tag{11}$$

APPENDIX D

ERROR IN THE ESTIMATION OF CROSSFLOW ENTHALPY

As in Appendix B, a Kline and McClintock type error analysis was employed to estimate the error in crossflow enthalpy measurements. The crossflow enthalpy is given by

$$H_x = \frac{d\,(G_{ch}\,H_{ch})}{d\,G_{ch}}$$

$$H_x = \frac{G_{ch_1}\,H_{ch_1} - G_{ch_2}\,H_{ch_2}}{G_{ch_1} - G_{ch_2}}\,. \tag{1}$$

The error may be estimated as follows:

$$[\Delta H_x]^2 = \left[\left(\frac{\partial H_x}{\partial G_{ch}}\right)\ \Delta G_{ch_1}\right]^2 + \left[\left(\frac{\partial H_x}{\partial H_{ch_1}}\right)\ \Delta H_{ch_1}\right]^2 + \left[\left(\frac{\partial H_x}{\partial G_{ch_2}}\right)\ \Delta G_{ch_2}\right]^2 + \left[\left(\frac{\partial H_x}{\partial H_{ch_2}}\right)\ \Delta H_{ch_2}\right]^2$$

Performing the differentiation using Equation (1) gives:

$$[\Delta H_x]^2 = \Delta G_{ch_1}^2 \left[\frac{H_{ch_1}}{G_{ch_1} - G_{ch_2}} - \frac{(G_{ch_1} H_{ch_1} - G_{ch_2}\,H_{ch_2})}{(G_{ch_1} - G_{ch_2})^2}\right]^2 + \Delta H_{ch_1}^2 \left[\frac{G_{ch_1}}{G_{ch_1} - G_{ch_2}}\right]^2$$

$$+ \Delta G_{ch_2}^2 \left[\frac{H_{ch_2}}{G_{ch_1} - G_{ch_2}} - \frac{(G_{ch_1}\,H_{ch_1} - G_{ch_2}\,H_{ch_2})}{(G_{ch_1} - G_{ch_2})^2}\right]^2 + \Delta H_{ch_2}^2 \left[\frac{G_{ch_2}}{G_{ch_1} - G_{ch_2}}\right]^2 \tag{2}$$

Then

$$[\Delta H_x]^2 \cong 2\Delta G_{ch}^2 \left[\frac{\bar{H}_{ch} - H_x}{G_{ch_1} - G_{ch_2}}\right]^2 + 2\Delta H_{ch}^2 \left[\frac{\bar{G}_{ch}}{G_{ch_1} - G_{ch_2}}\right]^2$$

where

$$\bar{G}_{ch} = \frac{1}{2}\left[G_{ch_1} + G_{ch_2}\right],\ \bar{H}_{ch} = \frac{1}{2}\left[H_{ch_1} + H_{ch_2}\right]$$

or,

$$[\Delta H_x]^2 \cong \frac{2}{(G_{ch_1} - G_{ch_2})^2} \left\{\left[\Delta G_{ch}\,(\bar{H}_{ch} - H_x)\right]^2 + \left[\Delta H_{ch}\,\bar{G}_{ch}\right]^2\right\} \tag{3}$$

The following are typical values for insertion into Equation 3 (from Figures 50 and 51, and the calibration curves).

$$G_{ch_1} = 0.9 \times 10^6 \text{ lb/ft}^2\text{-h}$$

$$G_{ch_2} = 1.1 \times 10^6 \text{ lb/ft}^2\text{-h}$$

$$\bar{G}_{ch} = 1/2\,[0.9 \times 10^6 + 1.1 \times 10^6] = 1.0 \times 10^6 \text{ lb/ft}^2\text{-h}$$

$$\Delta G_{ch} \cong \pm 10^4 \text{ lb/ft}^2\text{-h}$$

$$\Delta H_{ch} \cong \pm 5 \text{ Btu/lb}$$

$$H_x - \bar{H}_{ch} = 20 \text{ Btu/lb}$$

$$[\Delta H_x]^2 = \frac{2}{(0.9 \times 10^6 - 1.1 \times 10^6)^2}\,[(10^4 \times 20)^2 + (5 \times 10^6)^2]$$

$$\Delta H_x = \pm 35 \text{ Btu/lb}$$

ACKNOWLEDGEMENTS

The data reported in this report were taken under Task-C of AT(04-3)-189 P.A. 44: "Two-Phase Flow and Heat Transfer in Multirod Geometries," sponsored by the U.S. Atomic Energy Commission. The authors wish to express their appreciation to all those at APED who have contributed to the success of this program. Specifically, the following individuals made direct contribution to the subject study, and their work is gratefully acknowledged.

PROJECT ENGINEER: E. Janssen

SUBSECTION MANAGER: F. A. Schraub

TEST OPERATIONS AND ASSEMBLY:
B. Duncan
V. Levesque
P. Daly
V. Horn
D. A. Wilhelmson
C. H. McCubbin
J. Karnofel

ANALYSIS OF DATA: E. E. Polomik

DATA REDUCTION: Y. H. Kong
S. Kiernan

DISTRIBUTION

Aerojet-General Corporation
Nuclear Products and Services Group
P.O. Box 77
San Ramon, California 94583
Attn: H. Jaffe — 1

Argonne National Laboratory
Reactor Engineering Division
9700 South Cass Avenue
Argonne, Illinois 60439
Attn: Dr. Paul Lottes — 1

Argonne National Laboratory
Reactor Engineering Division
9700 South Cass Avenue
Argonne, Illinois 60439
Attn: M. Petrick — 1

Atomics International
P.O. Box 309
Canoga Park, California 91305
Attn: L. Bernath — 1

Babcock & Wilcox Company
Atomic Energy Division
P.O. Box 1260
Lynchburg, Virginia 24505
Attn: D.F. Judd — 1

Brookhaven National Laboratory
Chemical Engineering Division
Upton, New York 11973
Attn: Dr. O.E. Dwyer — 1

Columbia University
Department of Chemical Engineering
New York, New York 10027
Attn: J. Casterline — 1

Combustion Engineering, Inc.
Nuclear Division
P.O. Box 500
Windsor, Connecticut 06095
Attn: Dr. P. Zmola — 1

E.I. du Pont de Nemours and Company
Wilmington, Delaware 19898
Attn: J.S. Neill — 1

Dynatech Corporation
17 Tudor Street
Cambridge, Massachusetts 02139
Attn: A. Bergles — 1

General Electric Company
Research and Development Center
P.O. Box 8
Schenectady, New York 12301
Attn: Fred Staub — 1

Knolls Atomic Power Laboratory
General Electric Company
P.O. Box 1072
Schenectady, New York 12301
Attn: Document Librarian — 1

Geoscience Limited
410 South Cedros
Solano Beach, California
Attn: H. Poppendick — 1

Massachusetts Institute of Technology
Department of Mechanical Engineering
Cambridge, Massachusetts 02139
Attn: Dr. W. Rohsenow — 1

Massachusetts Institute of Technology
Department of Mechanical Engineering
Cambridge, Massachusetts 02139
Attn: Dr. P. Griffith — 1

New York University
Department of Mechanical Engineering
University Heights
New York, New York 10453
Attn: Dr. Novak Zuber — 1

North Carolina State University
Department of Chemical Engineering
Raleigh, North Carolina 27607
Attn: Dr. J.K. Ferrell — 1

Oak Ridge National Laboratory
P.O. Box X
Oak Ridge, Tennessee 37830
Attn: H.W. Hoffman — 1

University of Michigan
Department of Chemical and Metallurgical Engineering
Ann Arbor, Michigan 48103
Attn: R. Balzhiser — 1

Westinghouse Electric Corporation
Atomic Power Division
Box 355
Pittsburgh, Pennsylvania 15230
Attn: L.S. Tong — 2

Westinghouse Electric Corporation
Bettis Atomic Power Laboratory
P.O. Box 79
West Mifflin, Pennsylvania 15122
Attn: S. Green — 1

National Aeronautics & Space Admin.
Lewis Research Center
21000 Brookpark Road
Cleveland, Ohio 44135
Attn: R. Weltmann (SEPO) — 2

DISTRIBUTION—(Continued)

Pacific Northwest Laboratory
P.O. Box 999
Richland, Washington 99352
Attn: F. R. Zalouder — 1

Rutgers, The State University
College of Engineering
New Brunswick, New Jersey 08903
Attn: Dr. R.L. Peskin — 1

Stanford University
Department of Mechanical Engineering
Stanford, California 94305
Attn: Dr. G. Leppert — 1

TRW, Inc.
TRW Systems Group
One Space Park
Redondo Beach, California 90278
Attn: S.M. Zivi — 1

National Aeronautics & Space Admin.
Lewis Research Center
21000 Brookpark Road
Cleveland, Ohio 44135
Attn: Librarian — 3

A. Amorosi, Director
LMFBR Program Office
Argonne National Laboratory
9700 South Cass Avenue
Argonne, Illinois 60439 — 1

Atomic Energy of Canada Limited
Chalk River, Ontario, Canada
Attn: G.A. Wikhammer — 1

U.S. Atomic Energy Commission
Division of Reactor Development and Technology
Washington, D.C. 20545
Attn: R.M. Scroggins — 2

U.S. Atomic Energy Commission
Division of Reactor Development and Technology
Washington,D.C. 20545
Attn: N. Todreas — 1

U.S. Atomic Energy Commission
Division of Reactor Development and Technology
Washington, D.C. 20545
Attn: Water Projects Branch — 1

U.S. Atomic Energy Commission
Division of Reactor Development and Technology
Washington, D.C. 20545
Attn: Research & Development Branch — 1

U.S. Atomic Energy Commission
Division of Safety Standards
Washington, D.C. 20545
Attn: R. Impara — 1

Atomic Energy Commission
DTIE
P.O. Box 62
Oak Ridge, Tennessee — 3

Centre d'Etudes Nucleaires
Chemin des Martyrs
Grenoble (Isere)
France
Attn: M. Mondin — 1

CISE
Casella Postale 3986
Milano (Segrate)
Italy
Attn: Prof. M. Silvestri — 1

MAN
Abholfach
Nurnberg 2
Germany
Attn: Dr. Mayinger — 1

SNECMA
Division Atomique
22, Quai Gallieni
Suresnes (Seine)
France
Attn: M. Foure — 1

Technische Hogeschool Eindhoven
P.O. Box 313
Eindhoven
Netherlands
Attn: Prof. Dr. M. Bogaardt — 11

AEG-Kernenergieversuchsanlage
8752 Grosswelzheim (Unterfranken)
Germany
Attn: Dr. Kirchenmayer — 1

CNEN
Rome
Via Belisario, 15
Italy
Attn: M. Bianchi — 1

Alsthom
38 avenue Kleber
Paris 16e
France
Attn: M.P. Domenjoud — 1

DISTRIBUTION—(Continued)

Centre d'Etudes Nucleaires de Saclay
B.P. no 2
Gif-sur-Yvette (S&O)
France
Attn: M.J. Horowitz
1

FIAT
Sezione Energia Nucleare
Via Settembrini 235
Torino
Italy
Attn: M.G. Cesoni
1

Reactor Centrum Nederland
112 Scheveningseweg
's Gravenhage
Netherlands
Attn: Prof. Dr. M. Bogaardt
1

ANSALDO
Direzione Generale
Piazza Carignano 2
Genova
Italy
Attn: Dr. F. Cristofori
1

EURATOM
Direction Generale R&E
51, rue Belliard
Bruxelles
Belgium
Attn: Dr. P. Kruys
2

EURATOM
Casella Postale 1
Ispra (Varese)
Italy
Attn: M.R. Morin
1